Experimental Investigation of Post-Dryout Heat Transfer and Corresponding Flow Behavior

Zur Erlangung des akademischen Grades eines
DOKTORS DER INGENIEURWISSENSCHAFTEN (Dr.-Ing.)

von der KIT-Fakultät für Maschinenbau des
Karlsruher Instituts für Technologie (KIT)
angenommene

DISSERTATION

von

M. Sc. Ludwig Köckert

Tag der mündlichen Prüfung:	19.12.2025
Hauptreferent:	Prof. Dr.-Ing. Xu Cheng
Korreferent:	Prof. Dr.-Ing. Thomas Schulenberg

Declaration

Ich versichere wahrheitsgemäß, die vorliegende Arbeit selbstständig angefertigt, alle benutzten Hilfsmittel vollständig und genau angegeben und alles kenntlich gemacht zu haben, was aus Arbeiten anderer unverändert oder mit Abänderungen entnommen wurde.

Leipzig, den 23.10.2026

_____

Ludwig Köckert

Acknowledgements

I am deeply thankful to everyone who has supported me professionally, personally, and in every conceivable way during my work.

I would like to express my profound gratitude to Prof. Dr.-Ing. Xu Cheng for his exemplary supervision, unwavering support, professional and personal guidance, and constant encouragement throughout the preparation of this thesis.
I would also like to thank Prof. Dr.-Ing. Thomas Schulenberg for taking over the co-examiner, his insightful comments, and the constructive dialogues.

I am very thankful to all current and former colleagues at the IATF for the pleasant atmosphere, valuable discussions, and shared experiences. I would particularly like to thank Meiqi Song, Zihan Xia, Dali Yu, and Nikolai Rensch for their close, trusting, and enriching collaboration on joint projects, which contributed to the success of this work.
In addition, I would like to thank Florian Feuerstein and Denis Klingel for introducing me to the experimental activities, their valuable insights and continuous support, and the enriching discussions. I would also like to express my special thanks to Fanli Kong, Xing Cheng, Fabian Wiltschko, Yihui Wu and the colleagues from Research Center Jülich for their collaboration and the time we spent working together on different projects. Additionally, I thank Dr. Florin Badea for the excellent collaboration and discussions over the past few years.
I am especially thankful to Moritz Schenk for the time we spent together, the valuable discussions, and his corrections to my thesis.
It is also important to acknowledge the consistent and friendly support in all administrative matters provided by Isolde Stamm and Marina Djordjevic over the years.

I would like to express my gratitude to my students who accompanied me during my time at the institute and contributed to the success of this work with their support. By name, I would like to mention Timo Kaiser, Julius Stier, Jonas Mohacsi, and Arash Beyrami.

For the financial support of the project MOPOW II (reference number 1501544), I would like to extend my gratitude to the former Federal Ministry for Economic Affairs and Energy (BMWi).

I would like to express my special thanks to my family and friends for their constant support and encouragement over the years.

My final thanks go to my wife Charlotte for her endless patience, support, understanding, encouragement, and her corrections to my work.

Kurzfassung

Dryout- und Post-Dryout-Wärmeübergang spielen eine wesentliche Rolle bei Dampferzeugern oder in der nuklearen Sicherheit und sind somit von großer Relevanz für industrielle Anwendungen. Da ein mögliches Materialversagen fatale Folgen haben kann, müssen die zugrunde liegenden Wärmeübertragungsmechanismen und das Strömungsverhalten verstanden werden, um die Betriebs- und Unfallbedingungen genau vorhersagen zu können. Ziel dieser Arbeit ist es daher, das Verständnis des Wärmeübergangs nach dem Dryout zu verbessern und Wissenslücken über das Tropfenverhalten und das thermische Nicht-Gleichgewicht zu schließen. Zu diesem Zweck werden Experimente in zwei verschiedenen Teststrecken mit dem Modellfluid R-134a durchgeführt und analysiert.

Im Rahmen der Untersuchung wurden stationäre Versuchsreihen in einem gleichmäßig beheizten Rohr durchgeführt, mit dem Ziel, eine umfassende Datenbasis für den Wärmeübergang nach dem Dryout zu erstellen. Dabei konnten zwei charakteristische Temperaturverteilungen identifiziert werden. Die erste zeigt einen kontinuierlichen Temperaturanstieg nach dem Dryout, während die zweite nach Erreichen eines lokalen Maximums abnehmende Temperaturen aufweist. Der Einfluss von Eingangsdampfqualität, Wärme- und Massenstromdichte und Druck wird eingehend untersucht. Dabei zeigt sich, dass insbesondere die beiden letztgenannten Parameter einen signifikanten Einfluss auf die Temperaturverteilung und die Dampfqualität am Dryout-Punkt haben. Neben dem Aufheizvorgang wird auch die Wiederbenetzung der beheizten Wand untersucht, wobei sich bei den stationären Experimenten kein Unterschied im Verhalten zeigt.

Weitere Versuchsreihen werden mit einem quadratischen Strömungskanal durchgeführt, in dessen Mitte sich ein beheiztes Rohr befindet. Diese konzentrieren sich auf die optische Untersuchung des Strömungsverhaltens nach dem Dryout sowie auf Dampftemperaturmessungen. Die Versuchsmatrix ist daher auf Bedingungen beschränkt, unter denen diese Aspekte untersucht werden können. Die optischen Untersuchungen werden mittels einer Hochgeschwindigkeitskamera durchgeführt. Der Fokus liegt auf der Messung der Tröpfchengröße sowie der vertikalen und lateralen Tropfengeschwindigkeit. Die Größenverteilung folgt in etwa einer Gamma-Verteilung, während die laterale Geschwindigkeit einer Gaußschen Normalverteilung ähnelt. Beide Parameter zeigen nur eine geringe Empfindlichkeit gegenüber Variationen der Messparameter, während die vertikale Geschwindigkeit in signifikanter Weise vom Druck abhängt und ein abnehmendes Verhalten bei steigendem Druck aufweist. Zudem ist bei kleineren Tröpfchengrößen eine deutlich höhere Streuung bei beiden Geschwindigkeiten festzustellen. Mittels einer optischen Faser wird die Temperaturverteilung des Dampfes über eine bestimmte axiale Länge gemessen. Die

ausgewählten Datenpunkte zeigen signifikante Unterschiede zwischen Gleichgewichts- und tatsächlicher Dampfqualität, was ein Nachweis von signifikantem thermischen Nicht-Gleichgewicht bei den gegebenen Testbedingungen ist.

Im Rahmen der vorliegenden Arbeit erfolgt eine Bewertung von häufig verwendeten Modellen und Korrelationen anhand der in dieser Arbeit gewonnenen Wärmeübergangs- und optischen Daten. Dabei zeigt sich, dass insbesondere die Modellierung des thermischen Nicht-Gleichgewichts weiteres Verbesserungspotenzial aufweist.

Abstract

Dryout and post-dryout heat transfer play a major role in e.g., once through steam generators and nuclear safety and thus are of great importance in industrial applications. Since possible material failure can have fatal consequences, the underlying heat transfer mechanisms and the flow behavior need to be understood to accurately predict operating and accident conditions.
This thesis therefore aims to enhance the understanding of post-dryout heat transfer and fill gaps in knowledge about droplet behavior and thermal non-equilibrium by conducting and analyzing experiments in two different test sections using the model fluid R-134a.
Steady-state test series in a uniformly heated tubular test section are conducted to establish an extensive data base of post-dryout heat transfer data. Two characteristic temperature distributions were found. The first one shows continuous temperature increase after the point of dryout while the second shows decreasing temperatures after reaching a local temperature maximum. The influence of inlet quality, heat flux, mass flux, and pressure is thoroughly investigated. Especially the latter two parameters prove to affect the temperature distribution as well as the critical vapor quality at the point of dryout significantly. Besides dewetting, the rewetting of the heated wall is studied as well, showing no behavioral difference for the steady-state experiments.
The test series carried out with an annular test section of square geometry and a heated tube in the center of the flow channel are focused on the optical investigation of the post-dryout flow behavior and vapor temperature measurements. The test matrix is therefore limited to conditions where those subjects can be studied. The optical investigations are carried out using a high-speed camera system. They are focused on droplet size and vertical and lateral velocity. The droplet size distribution roughly follows a gamma shape distribution whereas the lateral velocity resembles a Gaussian normal distribution. While both parameters stay relatively unaffected by parameter variations, the vertical velocity strongly depends on the pressure showing decreasing behavior with increasing pressure. Both velocities show significantly higher scatter at lower droplet sizes. An optical fiber is used to measure the vapor temperature distribution over a certain axial length. The selected data points exhibit significant differences between equilibrium and actual vapor quality, proving severe thermal non-equilibrium at the given test conditions.
Eventually, commonly used models and correlations are assessed using the heat transfer and optical data obtained in this thesis. Especially the correct prediction of the thermal non-equilibrium thereby shows further room for improvement.

Outline

Declaration ..... **III**

Acknowledgements ..... **V**

Kurzfassung ..... **VIII**

Abstract ..... **XI**

Outline ..... **XIII**

Nomenclature ..... **XVI**

1. Introduction **1**

1.1 Scientific Background 3
1.2 Objective and Structure 4

2. State of Science **6**

2.1 Heat Transfer Mechanisms 6
2.2 Boiling Crisis 7
2.3 Post-Dryout Flow and Heat Transfer Regime 9
2.3.1 Boiling Curve 9
2.3.2 Post-Dryout Flow Behavior and Heat Transfer Mechanisms 10
2.3.3 Rewetting 16
2.4 Literature Review of Post-Dryout Experimental Work 17
2.4.1 General Studies on PDO Heat Transfer 17
2.4.2 Studies of PDO Heat Transfer in Different Geometries and Spacer Influence 21
2.4.3 Optical Investigations under PDO Conditions 22
2.4.4 Vapor Temperature Measurements under PDO Conditions 24
2.4.5 Studies on Rewetting Behavior 25
2.5 Literature Review of Post-Dryout Heat Transfer Modeling 26
2.5.1 General Modeling Approaches of the Post-Dryout Heat Transfer 26
2.5.2 Selected Theoretical Models for Post-Dryout Heat Transfer and Droplet Behavior 29
2.6 Summary and definition of research needs 30

3. Experimental Set-up and Techniques **32**

3.1 Description of the KIT Model Fluid Facility 32
3.2 Test Sections 33

3.2.1 Uniformly Heated Tube ... 33
3.2.2 Annular Flow Channel ... 35
3.3 Properties of the Working Fluid R-134a ... 37
3.4 Measurement Techniques ... 39
3.4.1 Conventional Measurement Devices ... 40
3.4.2 Measurement of Vapor Temperature ... 42
3.4.3 Optical Measurement of Droplet Behavior ... 43
3.5 Test Procedure and Data Analysis ... 44
3.5.1 Experimental Procedure ... 44
3.5.2 Experimental Parameter Range ... 45
3.5.3 Test Data Reduction ... 49
3.5.4 Heat Balance Measurements ... 54
3.5.5 Uncertainty Analysis ... 55

4. Experimental Results and Discussion in the Tube Test Section ... 60

4.1 General Observations Regarding the Post-Dryout Heat Transfer in Steady-State Experiments ... 60
4.1.1 Temperature Distribution ... 60
4.1.2 Reproducibility of Experiments ... 62
4.1.3 Abnormalities in the Investigations ... 63
4.2 Parameter Influence on the Post-Dryout Heat Transfer ... 64
4.2.1 Inlet Vapor Quality ... 64
4.2.2 Heat Flux ... 65
4.2.3 Mass Flux ... 66
4.2.4 Pressure ... 67
4.3 Investigation of the Rewetting Behavior in the Steady-State Experiments ... 69
4.4 Assessment of Theoretical Prediction Models ... 71

5. Experimental Results and Discussion in the Annular Test Section ... 77

5.1 Droplet Behavior Analysis ... 77
5.1.1 Analysis Methods of High-Speed Camera Footage ... 77
5.1.2 General Characteristics and Distinctive Features of the Measurements ... 79
5.1.3 Droplet Size ... 82
5.1.4 Droplet Velocity ... 84
5.1.5 Investigation of the Connection between Droplet Velocity and Diameter ... 90
5.1.6 Assessment of Theoretical Prediction Models ... 93
5.2 Analysis of Thermal Non-Equilibrium ... 99
5.2.1 General Observations Regarding the Vapor Temperature Measurements and Data Point Selection Criterion ... 100
5.2.2 Results and Discussion of Vapor Temperature Data Points ... 102

5.2.3 Assessment of Theoretical Prediction Models ... 106

6. Description and Assessment of the KIT Models ... 109

6.1 Description of the KIT Correlation and Mechanistic Model ... 109
6.1.1 Introduction of the KIT PDO Correlation ... 109
6.1.2 Introduction of the KIT Mechanistic PDO Model ... 110
Assessment of the KIT PDO Models ... 112
6.1.3 Assessment of the KIT PDO Correlation ... 112
6.1.4 Assessment of the KIT Mechanistic PDO Model ... 113

7. Conclusion and Outlook ... 117

Appendix ... 122

A. Set-up and Functionality of an Optical Fiber for Temperature Measurements ... 122
B. Selected Theoretical Models for Post-Dryout Heat Transfer and Droplet Behavior ... 123
B.1 Equilibrium PDO Heat Transfer Correlations ... 123
B.2 Non-Equilibrium PDO Heat Transfer Models ... 127
B.3 KIT Mechanistic PDO Model ... 130
B.4 Validity Range of the PDO Heat Transfer Models ... 135
B.5 Modeling of the Droplet Diameter ... 137
B.6 Modeling of the Droplet Velocity ... 139
C. Further Results of Optical Investigations ... 140

Publication Bibliography ... 144

List of Own Publications ... 161

List of Figures ... 162

List of Tables ... 165

Nomenclature

Latin Symbols

Symbol	Dimensions	Description
a	m^2/s	thermal diffusivity
A	m^2	area
Bo	-	Boiling number
C_d	-	drag coefficient
c_p	J/(kg·K)	specific heat capacity
d	m	droplet diameter
D	m	diameter / characteristic length
d_{zchf}	m	distance to point of CHF
dev	-	deviation
f	-	Fanning friction factor
f	-	function
f_{TNE}	-	thermal non-equilibrium factor
g	m/s^2	gravity acceleration
G	$kg/(m^2s)$	mass flux
h	J/kg	specific enthalpy
I	A	current
$I_{1,2}$	-	constant
$i_{v\text{-}d}$	J/kg	latent heat of vaporization
L	m	length
$\dot{m}$	kg/s	mass flow
n_{eff}	-	impressed refractive index
N	-	number of pixels
Nu	-	Nusselt number
p	bar	pressure
P	-	input parameter
Pr	-	Prandtl number
$\dot{q}/q$	W/m^2	heat flux
$\dot{q}_{loss}$	W/m^2	heat loss flux
$\dot{q}_V$	W/m^3	volumetric heat flux
$\dot{Q}$	W	heat flow

r	m	radius
$\overline{R}$	m	average droplet extension radius
Re	-	Reynolds number
S	-	slip ratio
S_f	-	shielding factor
t	s	time
T	°C	temperature
u	m/s	lateral velocity
U	V	voltage
v	m/s	vertical velocity/flow velocity
We	-	Weber number
x	-	vapor quality
x	-	relative length
x	m	radial channel position/general position
x_A	-	vapor quality at the onset of annular flow

Greek Symbols

Symbol	Dimensions	Description
α	$W/(m^2K)$	heat transfer coefficient
α	1/K	thermal expansion coefficient
α_v	-	void fraction
β	-	coefficient for consideration of superheating effect
λ	m	wave length of light
λ	W/(mK)	thermal conductivity
Λ	m	Bragg grating period (fringe distance)
μ	$kg/(m^2s)$	dynamic viscosity
ν	m^2/s	kinematic viscosity
ξ	1/K	thermo-optic coefficient
ρ	kg/m^3	density
σ	N/m	surface tension
σ	-	Standard deviation

Subscripts

Symbol	Description
a	actual

am	ambient
B	Bragg
bins	bin as a droplet diameter size classification
c	critical
calc	calculated
Cam	camera
ch	characteristic
d	droplet
dev	developing
do	dryout
e	equilibrium
f	film temperature/flow
f	flow
fiber	fiber
fl	fluid
he	heated
hom	homogeneous
hy	hydraulic
i	inner
in	inlet
l	liquid
lf	liquid film
L	loss
low	lower limit in integration
m	mean
max	maximum
meas	measured
MFB	Minimum Film Boiling
mp	most probable
NB	Nucleate Boiling
non-tube	non-tubular geometry
o	outer
ob	obstacle
out	outlet
PH	Pre-heater
poi	point of interest
rel	relative
RMS	Root Mean Square
rt	region transition

S	saturation
sub	subcooling
TP	two-phase
tube	tubular geometry
upper	upper limit in integration
v	vapor
V	volume
va	actual vapor conditions
vb	bulk vapor conditions
vcr	vapor at core region conditions
ve	equilibrium vapor conditions
vf	vapor at film temperature conditions
vfr	vapor at film region conditions
vs	saturated vapor conditions
vw	vapor at wall temperature conditions
v-d	vapor to droplet
W	wall
w-v	wall to vapor
w-v,2	wall to vapor in fully developed PDO region (2)
x, y, z	coordinates

Abbreviations

Abbreviation	**Description**
ATHLET	Analysis of Thermal Hydraulics of Leaks and Transients (thermal hydraulic code developed by GRS gGmbH)
BWR	Boiling Water Reactor
CFD	Computational Fluid Dynamics
CHF	Critical Heat Flux
DFFB	Dispersed Flow Film Boiling
DNB	Departure from Nucleate Boiling
DP	Data Point
DTG	Draw Tower Gratings
HTC	Heat Transfer Coefficient
IAEA	International Atomic Energy Association
IAFB	Inverted Annular Film Boiling
IATF	Institute for Applied Thermofluidics
IEA	International Energy Agency

JAERI	Japan Atomic Energy Research Institute
KAIST	Korea Advanced Institute of Science and Technology
KIMOF	KIT Model Fluid Facility
KIT	Karlsruhe Institute of Technology
KTH	Royal Institute of Technology
LCS	Local Conditions Solution
LED	Light Emitting Diode
LIF	Laser-Induced Fluorescence
LOCA	Loss of Cooling Accident
LUT	Look-Up Table
LWR	Light Water Reactor
ML	Machine Learning
NB	Nucleate Boiling
NIST	National Institute of Standards and Technology
NUTHOS	International Topical Meeting on Nuclear Reactor Thermal-Hydraulics, Operation, and Safety
PDA	Phase-Doppler Analyzer
PDF	Probability Density Function
PDO	Post-Dryout
PRIS	Power Reactor Information System
PWR	Pressurized Water Reactor
REFPROP	Reference Fluid Thermodynamic and Transport Properties Database
RMS	Root Mean Square
ROI	Region of Interest
SPWR	Super Pressurized Water Reactor
SWINTH	Specialist Workshop on Advanced Instrumentation and Measurement Techniques for Nuclear Reactor Thermal-Hydraulics and Severe Accidents 2024
TNE	Thermal non-equilibrium
USAEC	U.S. Atomic Energy Commission

1. Introduction

The demand for power and electricity worldwide is rapidly increasing. Based on data from the International Energy Agency (IEA), (McKinsey & Company 2024) predict an overall growth in primary energy demand of 11% from 2023 to 2050. Annual power consumption increase is expected to be at 3.5% according to the same report. In the IEA's "Electricity 2025" report ((International Energy Agency 2025a)), a rise in electricity demand of 4.3% was observed globally in 2024, with an expectation of further annual increase of around 4% until 2027. The report announces a new age of electricity due to the growing electricity demand that is driven by industrial production, higher demand of air conditioning, and a growing number of data centres among other factors.

To meet the high and growing energy demand, steam-electric power plants are still an important part of the energy mix, as they are less volatile than renewable energy sources. The basic and simplified principle of those power plants is to produce steam that drives a turbine which is connected to a generator. Typical steam generator types are drum boilers and once-through steam generators. In drum boilers, water is only partially evaporated, and the generated steam needs to be separated in the large and thermally slow drum. Once-through steam generators on the other hand evaporate the water entirely so that smaller steam separators are only needed for certain low power operation modes. Due to thinner walls and an overall more compact design, the once-through steam generators show higher operation flexibility ((Siemens AG Power Generation 2006; Strauss 2016)). The basic schematic principle is illustrated in Figure 1.1a). The figure shows an application as a heat recovery steam generator e.g., in a combined cycle power plant. The exhaust gas of the first process is used to evaporate and superheat water in a subsequent process.

In order to evaporate the entire liquid, the once-through steam generator passes a critical point that needs to be considered in the design of the steam generator. In the course of evaporation, the water first starts to boil which is accompanied by a very effective heat transfer from the heated walls to the fluid. Subsequently, the amount and quality of vapor increase until the liquid only covers the heated walls as a thin film. Further evaporation finally causes the liquid film on the walls to dryout entirely, leaving the remaining liquid in form of entrained droplets in the vapor flow. This can be schematically observed in Figure 1.1b). This depletion of the liquid film marks the transition to a significantly less effective heat transfer regime, which means that the corresponding wall temperature shows a strong and sudden increase. The further course of the temperature development depends on the operating conditions. Passing the point of dryout however, is necessary to evaporate the liquid entirely. Once-through steam generators need to ensure on one hand enough heat transfer to fully evaporate the liquid, even at low mass flows. On the other hand, the significant increase in temperature at dryout and beyond need to be considered in order to prevent failure of the tube. Possible adjustments can be made to e.g., the heated length and the number and arrangement of evaporation tubes, the tube design like the

use of rifled tubes (e.g., (Siemens AG Power Generation 2006)) or the mass flux ((Strauss 2016)).

Once-through steam generators have been widely applied in steam-electric power plants as well as in the aforementioned combined cycle power plants as heat recovery steam generators ((Effert and Brückner 2021)). The Babcock-Brown Boveri Reaktor GmbH even designed a concept for use in nuclear power plants as an alternative to the conventional U-tube steam generators ((U.S. Nuclear Regulatory Commission)). (Schulenberg and Czifrus 2025) presented the basic design principle as they picked up the concept for their design proposal of a Super Pressurized Water Reactor (SPWR).

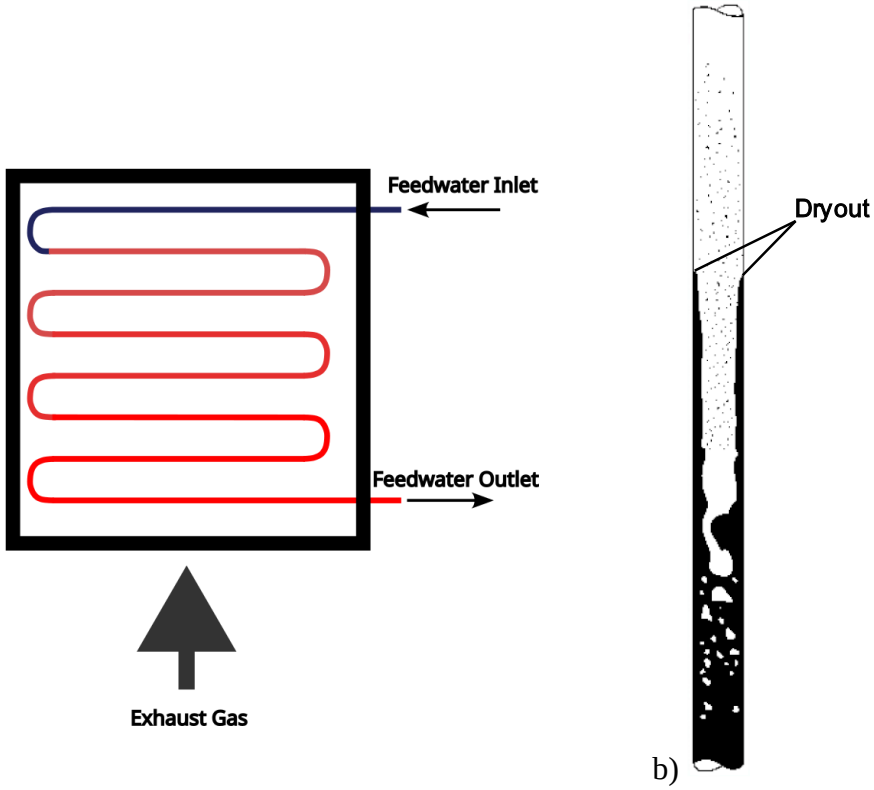


Figure 1.1: a) Basic principle of once-through steam generator applied as heat recovery steam generator with horizontally installed evaporator tubes (according to: (Schlund et al. 2021)), b) dryout in an evaporator tube with liquid in dark and vapor in white (adapted from: (Ghiaasiaan 2007), originally published in: (Collier and Thome 1994))

In the course of the expected energy demand growth while simultaneously trying to reduce CO_2 emissions, nuclear power experiences increasing interest in order to meet this energy demand. According to the IEA, nuclear energy interest level is at its highest point in about 50 years, with over 40 countries agreeing to extend their nuclear power usage ((International Energy Agency 2025b)). Currently, according to the International Atomic Energy Agency's (IAEA) Power Reactor Information System (PRIS), 416 Nuclear Power Reactors worldwide are in operation

(IAEA 2025). Around 84% of the nuclear power plants in operation are so called light water reactors (LWR) which can be subdivided into pressurized water reactor (PWR) and boiling water reactor (BWR). Also in future Small Modular Reactor (SMR) concepts, light water reactor design concepts are taken into consideration (Nuclear Energy Agency 2023).
Due to the possibly devastating consequences of a reactor accident, reactor safety and the understanding of the heat transfer and flow behavior in the reactor core in case of an accident play a major role in the design and operation of a nuclear power plant. In a light water reactor, the reactor core consists of fuel rods in which the fission process takes place. These fuel rods are assembled in fuel elements. The water flowing through the reactor core transports the heat, produced in the fuel rods by nuclear fission, away from the reactor core. In an accident scenario, in which the water rushes out of the reactor or the pressure drops quickly, leading to a rapid evaporation of the water, the cladding outer surface of the fuel rods may dry out. In that case, the heat transfer and flow mechanisms change drastically, as described before, initially leading to a strong rise in fuel rod cladding temperature. The further temperature development after dryout in the so called post-dryout (PDO) depends on different factors like mass flux or pressure. The cladding is usually made of a zirconium alloy in case of LWRs. This material is strongly oxidized at temperatures above 1000 °C while in the course of this reaction, hydrogen is generated ((Filburn and Bullard 2016)). If the admissible temperature limit of the cladding material is exceeded for too long, structural damage of the fuel rod cladding leads to the release of fission material into the reactor core. Simultaneously, if the accumulation of the generated hydrogen exceeds a certain point, a strong and uncontrolled explosion could occur. This could be observed in the Fukushima Daiichi accident in 2011 ((Filburn and Bullard 2016)).

While dryout and post-dryout conditions are necessary in once-through steam generators but need to be considered in the design, they form a scenario that must be avoided in the context of nuclear safety. A profound understanding of the phenomena and the corresponding heat transfer mechanisms and flow behavior is therefore mandatory to ensure the safe operation of power plants and other industrial applications.

1.1 Scientific Background

As indicated before, the point of dryout marks the transition point at which a heated wall that is fully wetted by a liquid film, dries out and no direct, lasting contact of liquid and heated wall can be established anymore.
The flow regime before dryout is annular flow at which the heated wall is covered by a liquid film, and liquid droplets are entrained in the core gas flow. At the point of dryout it changes to the so called mist flow where vapor covers the heated wall and droplets are entrained in this gas flow. The heat transfer transitions from the nucleate boiling to the film boiling regime. The latter is far less effective in heat transfer and therefore leads to a sudden and strong rise in wall temperature, as described. Further temperature distribution beyond this point in the PDO region

is influenced by different factors and remains subject to further investigations. The heat transfer in the film boiling regime is mainly driven by the convective heat transfer from the heated wall to the vapor, but also the behavior of the entrained droplets plays a key role through evaporation and direct interaction with the heated wall ((Schnittger 1982)). The heat transfer from wall to vapor leads to a superheating of the vapor, which causes a thermal non-equilibrium under PDO conditions.

Due to its outstanding importance regarding nuclear safety as well as designing steam generators, expansive research has been performed over the past decades to fully understand the mechanisms present in the PDO area. Models and correlations were developed to predict the heat transfer and thereby the expected wall temperatures. Those models needed to be validated by experiments that were conducted in different geometries from tube to rod bundle (e.g., (Becker et al. 1983) or (Loftus et al. 1980)) and different fluids. In practical applications, usually water is used as fluid. However, in fundamental research, often model fluids are used to investigate those phenomena as they can be conducted at lower pressure and temperatures and are therefore less demanding in regard to the experimental requirements and more cost effective. For practical applications, they need to be scaled to water conditions.

1.2 Objective and Structure

Despite the extensive research in the field of PDO heat transfer, not all involved mechanisms are fully understood and, as a consequence, can be modeled appropriately. This is especially true regarding the droplet behavior and the determination of the thermal non-equilibrium. The experimental results are scarce in those fields due to the complexity of measurements in two-phase flow. In an attempt to close this gap in knowledge, experiments in two different geometries, i.e. tube and annulus, are conducted using the model fluid R-134a. The experimental pressure range covers the range present in LWRs and also considers the parameters used in available water experiments. A comprehensive data base in R-134a is built that takes into account the influence of different parameters and could be used for further fluid-to-fluid scaling investigations. Special attention is paid to the investigation of flow behavior and determination of the thermal non-equilibrium in the annular test section, that allows optical access to the flow channel. The obtained data are used to assess widely used models and disclose further potential for improvement. The thesis is structured in the following way.

For a better understanding of the content of this thesis, the basic heat transfer mechanisms are introduced briefly, followed by the two types of boiling crisis, and the flow and heat transfer regime present in the post-dryout area. The experimental work conducted in the past decades as well as different modeling approaches are discussed. The chapter is concluded by summarizing the current state of science on PDO and identifying the research needs that build the basis of this thesis.

Chapter 3 presents the experimental set-up and the utilized measurement techniques. The experimental facility is introduced, along with the test sections that were used in this study. Measurement devices are presented from the conventional measurement techniques to the more advanced devices for the optical measurement of flow behavior and vapor temperature. Lastly, the experimental procedure and the test data reduction are shown as well as the uncertainty analysis of the obtained experimental results.

Chapters 4 and 5 contain the actual measurement results and their discussion. The fourth chapter is dedicated to the results obtained with the uniformly heated tube. General observations are presented, and the influence of the adjustable parameters is discussed. The results of the rewetting are presented and set in context. Selected models and correlations are assessed with the experimental results and potential aspects of improvement are identified. The fifth chapter is divided into two main parts. The first part is dedicated to the optical investigation of flow behavior in PDO. Analysis procedure and observed characteristics and difficulties of the measurements are discussed. The droplet behavior is analyzed regarding the droplet size, vertical and horizontal velocity, and the position in the flow channel. These data are used to validate available prediction models too. The second part contains the presentation and discussion of the vapor temperature measurements and the assessment of two models predicting the thermal non-equilibrium.

The following chapter describes a correlation and a mechanistic model, developed by (Yu 2019) and (Song 2021) at the Institute for Applied Thermofluidics (IATF) at the Karlsruhe Institute of Technology (KIT), to predict the PDO heat transfer, separately. They are also validated, using the test data from this thesis.

The last chapter comprehensively summarizes the results of this thesis and provides an outlook on further possible research and improvements.

2. State of Science

This chapter first introduces the general heat transfer mechanisms. It focuses on convective heat transfer as this represents the main mechanism encountered in this study. The different types of boiling crisis are introduced before the mechanisms of post-dryout flow patterns and heat transfer as well as the rewetting process are explained. Furthermore, the experimental progress in the field of PDO investigations is examined with respect to different aspects of the experimental research. A general overview of the available theoretical models to describe PDO heat transfer is given. The chapter concludes with a summarization and the identification of aspects that need to be addressed to enhance the understanding of post-dryout behavior.

2.1 Heat Transfer Mechanisms

This subchapter provides a brief overview over the general heat transfer mechanisms relevant to the present study. A more comprehensive description of the single mechanisms and the corresponding dimensionless numbers can be found in e.g., ((v. d. VDI e.V. 2013), chapters A2, B1, and F2) or in ((Bejan and Kraus 2003), chapters 5, 6, and 7). This section merely provides a summary that supports a better understanding of the following content.
Three different main mechanisms of heat transfer are distinguished: i) heat conduction, ii) convection, and iii) radiation. This study focuses on convection as the main heat transfer mechanism in the conducted investigations. Generally, convection describes the heat transfer in a flowing fluid. It can be divided into free, mixed, and forced convection.
Free or natural convection is caused by e.g., temperature gradients that lead to density differences and subsequently result in buoyance forces that govern the fluid movement. Forced convection on the other hand is induced by external forces e.g., a pump. Mixed convection is a superposition of both forms (v. d. VDI e.V. 2013).

Dimensionless numbers are used to compare different systems regarding defined parameters. In that regard, the Nusselt number Nu describes the ratio of convective and conductive heat transfer and was introduced as an indicator for the similarity of heat transfer in different systems or fluids. It is defined in the following equation with the heat transfer coefficient α and the characteristic length D as well as the thermal conductivity λ. The characteristic length equals the inner diameter in case of a tubular flow channel.

$$Nu = \frac{\alpha\, D}{\lambda} \tag{2.1}$$

The heat transfer coefficient is used to describe the ability of a fluid to remove orthogonally directed energy from surfaces, in this case heat from a tube wall. A formal definition is given in chapter 3.5.3, equation (3.1).
The Reynolds number Re describes the ratio of inertial and viscous forces. It is used to determine the flow characteristic at forced convection whereas the Grashof number Gr is applied in cases of free convection. The Reynolds number is described as follows:

$$Re = \frac{\rho\, v\, D}{\mu} = \frac{G\, D}{\mu} \tag{2.2}$$

where ρ is the density, v is the flow speed, and μ is the dynamic viscosity. The mass flux G describes the ratio of mass flow rate to flow cross section A_f:

$$G = \frac{\dot{m}}{A_f} \tag{2.3}$$

The Prandtl number Pr is defined as the ratio of momentum to thermal diffusivity:

$$Pr = \frac{\nu}{a} = \frac{\mu\, c_p}{\lambda} \tag{2.4}$$

with the kinematic viscosity ν, the thermal diffusivity a and the specific heat capacity c_p. Reynolds or Grashof number in combination with the Prandtl number can be used in relation to describe the Nusselt number for forced and free convection, respectively (v. d. VDI e.V. 2013). Eventually, the Weber number is used in two-phase flows e.g., in droplet flows and describes the relation of drag and cohesion forces. Depending on whether the droplet or the channel Weber number is defined, the characteristic length can be the droplet diameter or the channel geometry. The same is valid for the velocity. The surface tension is given by σ.

$$We = \frac{\rho\, v^2\, D}{\sigma} = \frac{G^2\, D}{\rho\, \sigma} \tag{2.5}$$

2.2 Boiling Crisis

In evaporation processes, the boiling crisis marks the point at which the contact of liquid flow and heated wall can no longer be preserved. The corresponding heat flux is called Critical Heat Flux (CHF) and marks the onset of a sudden and strong rise of the wall temperature as the

applied heat cannot be conveyed away as efficient as before. Therefore, this phenomenon represents an important mark in the construction and design of evaporation apparatuses such as once through steam generators or nuclear power plants. Two different kinds of boiling crisis are known that mainly depend on the vapor fraction of the flow. They are depicted in Figure 2.1 below.

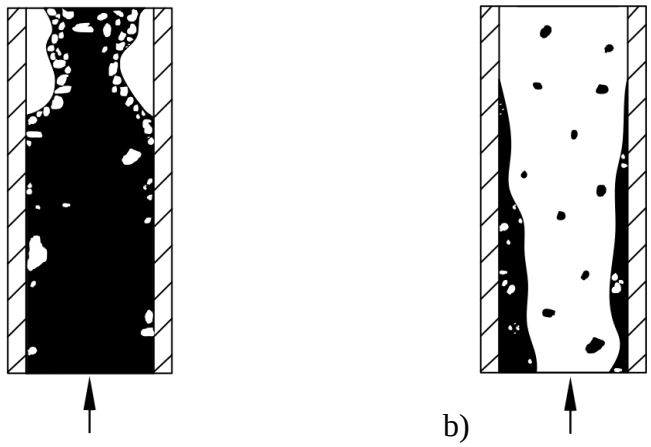


Figure 2.1: Types of boiling crisis; a) DNB and b) Dryout with liquid in dark and vapor in white in a uniformly heated tube (according to: ((v. d. VDI e.V. 2013) chapter 3.5))

Lower vapor fractions lead to the so called “Departure from Nucleate Boiling” (DNB). The vapor bubbles which form in small cavities in the heated surface coalesce eventually to a vapor blanket as heat flux is increased. In that case, the liquid fluid bulk flow is separated from the heated wall causing a rapid and strong temperature rise since the heat transfer is greatly deteriorated because of the low thermal conductivity of the vapor film (((v. d. VDI e.V. 2013) chapter H3.5), (Bejan and Kraus 2003)). The volume vapor fraction, also referred to as void fraction α_v, leading to DNB is often defined as below 0.5 (Hammouda et al. 1996; Groeneveld 1975).

Higher void fractions ((Groeneveld 1975) or (Hammouda 1996) define this value as > 0.8) on the other hand cause the dryout boiling crisis as the liquid film that covers the heated wall is gradually depleted by the increasing applied heat until it no longer wets the wall. The following rapid temperature rise is significant but less pronounced than in case of DNB since the high vapor fraction allows for convective heat transfer. Entrained liquid droplets can touch the wall again when only small heat fluxes are applied ((v. d. VDI e.V. 2013), chapter 3.5).

It should be noted that DNB was not investigated in this thesis and that related phenomena are only described briefly in the further course of this script, whenever necessary or for the sake of completeness.

2.3 Post-Dryout Flow and Heat Transfer Regime

The following subchapters focus on the flow patterns and heat transfer mechanisms encountered in the PDO. First, the boiling curve is introduced. Further, a physical description of the processes around and beyond dryout is given, followed by a discussion of the droplet initiation and their contribution to the PDO heat transfer by direct interaction with the heated wall. Also, the convective heat transfer is contemplated, and the thermal non-equilibrium is introduced. This chapter closes with the discussion of the rewetting process.

2.3.1 Boiling Curve

Figure 2.2 shows the concept of a typical boiling curve that was first introduced by (Nukiyama 1966) for pool boiling investigations. Later, it was adapted for flow boiling purposes as well and is widely used in that context. The depicted boiling curve shows the heat flux vs. the wall temperature. Under flow boiling conditions, the shape of the boiling curve depends on the mass flux. (Ma and Chung 2001) and (Stosic 2005) showed that increased mass flux results in higher CHF and distinctly flattens the N-shaped curve. As can be taken from the boiling curve, the heat transfer before CHF is generally very effective proven by a slow wall temperature increase at simultaneously high rise in heating power.

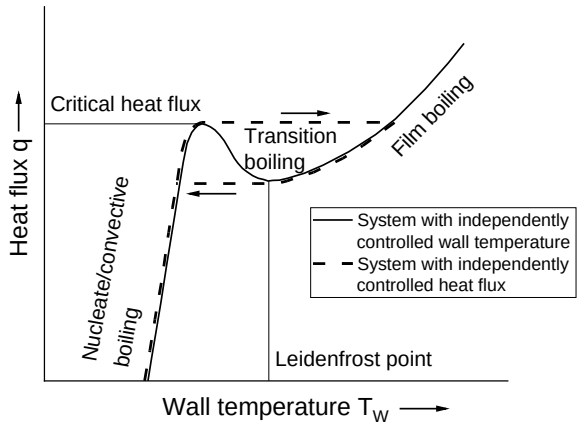


Figure 2.2: Typical boiling curve with heat transfer mechanisms (adapted from: (VDI-Gesellschaft Verfahrenstechnik und Chemieingenieurwesen 2010))

The mechanisms following the exceedance of CHF depend on how the heat is supplied to the heated surface. In heat flux controlled cases such as electrically heated wall or nuclear fuel rods, the process follows the horizontal line in Figure 2.2 and reaches the film boiling regime. It is obvious that the wall temperature increases strongly whereas the heat flux remains constant. On the other hand, when a wall temperature controlled system is of interest, a transition state

called “Transition Boiling” follows the boiling crisis in which the heated surface is alternately wetted by liquid and dried by vapor. After reaching the Leidenfrost or minimum film boiling temperature, the heat transfer mechanism transitions over to film boiling as well. The investigations and observations made in this thesis are based on heating power driven systems, so the mechanisms associated with transition boiling are not considered any further. In the film boiling regime, heat flux and temperature follow the depicted curve. Further increase of heat flux in the first case leads to further increasing wall temperatures with a slope less steep than at the point of CHF. The temperature decreases when the heat flux is decreased, and full rewetting occurs at the verge from film to transition boiling in the case of heat flux driven systems.

The area downstream of the boiling crisis is called post-CHF. The corresponding heat transfer regime is entitled film boiling, as mentioned above. It should be noted that the term “film boiling” is used differently in the literature. (Celata and Mariani 2003) or Herbst in (v. d. VDI e.V. 2013) for example, apply it solely to the heat transfer regime following DNB. In this thesis, it is used as a collective term that describes the heat transfer regime following CHF in general, independent of the type of boiling crisis. This definition was applied by e.g., (Hammouda 1996). Depending on the kind of boiling crisis, two sorts of film boiling are distinguished.
Following DNB, inverted annular film boiling (IAFB) occurs. The corresponding flow regime is characterized by a vapor film on the heated wall and a liquid flow core with bubbles of which droplets could be entrained into the vapor stream (Groeneveld 1975). However, as mentioned before, DNB and subsequent mechanisms are not subject to research in this thesis and are therefore only mentioned here for the sake of completeness.
Dryout is followed by the dispersed flow film boiling (DFFB) regime. The region following dryout is referred to as post-dryout. The PDO can be divided again into a developing and a fully developed region (Yu et al. 2018). While vapor is the main flow, entrained liquid droplets take part in the heat transfer mechanisms as well. According to (Ganić and Rohsenow 1977), the heat transfer in the DFFB regime is mainly characterized by i) convective heat transfer from heated wall to vapor, ii) heat transfer between vapor and entrained liquid droplets, iii) heat transfer between wall and droplets, iv) heat radiation from the heated surface. The last phenomenon has a significant influence only at very high wall temperatures and is therefore often neglected in the literature (see (Schnittger 1982)). The following subsection will discuss the flow pattern and the heat transfer mechanisms corresponding to the DFFB regime more detailed.

2.3.2 Post-Dryout Flow Behavior and Heat Transfer Mechanisms

Figure 2.3 displays the flow regimes along the flow channel starting from single-phase liquid flow up to dispersed flow in the PDO area. Also depicted are the corresponding heat transfer regimes as well as wall and vapor temperature.

In case of high void fractions and moderate heat fluxes, the flow develops from single-phase liquid flow to bubbly, slug, churn, and annular flow before reaching CHF. Flow and heat transfer regimes are exemplary illustrated for a uniformly heated tube. However, Azzopardi and Hills concluded in (Bertola 2003) that the flow patterns in annuli are very similar to the ones in single tubes, especially when it comes to annular and dispersed flow, sometimes also referred to as mist flow. They based their description on the experimental observations by (Caetano et al. 1992; Das et al. 1999; Kelessidis and Dukler 1989; Sadatomi et al. 1982) for concentric, partially, and fully eccentric annular test sections.

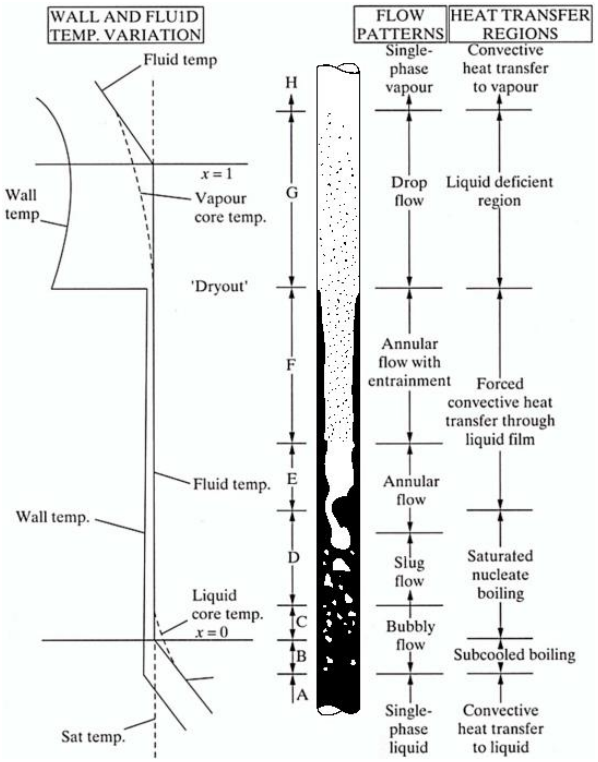


Figure 2.3: Flow patterns and heat transfer regimes as well as wall and vapor temperature for a vertically installed tube and moderate heat flux (adapted from: (Ghiaasiaan 2007), originally published in: (Collier and Thome 1994))

The physical mechanisms in the vicinity and beyond dryout are well described by (Styrikovich et al. 1980). In the annular flow regime just before dryout, the wall temperature lies slightly above saturation temperature. According to (Styrikovich et al. 1980), this is due to a metastable superheating of the liquid film leading to a small non-equilibrium. The saturation temperature is also slightly reduced by the pressure gradients in radial direction which leads to a superheating of the vapor as well. The superheating is reduced by continuous vapor generation in this area and the intense heat and mass exchange along the wavy interface between the liquid film on the wall and the vapor flow in the core. It is therefore a valid assumption that vapor and liquid are at thermal equilibrium at the point of dryout (Groeneveld 1972).

When dryout is reached, the liquid film on the heated wall depletes and the wall is covered by vapor. This leads to a drastically decreased heat transfer coefficient (HTC) which results in a sudden and strong wall temperature rise. In the vicinity of the dryout point in the dispersed flow regime, the vapor was little superheated which limits the heat transfer from vapor to droplets so that most of the heat in this area is transferred from wall to vapor. This results in a significant thermal non-equilibrium further downstream from the dryout, which is described later. The following evaporation of droplets increases the amount of vapor in the flow channel and accelerates the vapor flow. Depending on the parameters, the wall temperature increase either slows down or the temperature even decreases again after reaching a local maximum. Experimental investigations (e.g., by (Becker et al. 1983) or (Köhler 1984)) proved that the temperature starts to increase again with further increasing vapor quality after reaching a certain value. The figure illustrates a slow but continuous vapor temperature increase in the PDO region which is accelerated at the so mentioned vapor quality.

As mentioned before, four heat transfer mechanisms need to be considered in the DFFB regime. Special attention is paid to the role of droplets as the investigation of droplet behavior represents an important topic in this thesis.

The droplets found in the dispersed flow present in the PDO area are initiated in the annular flow regime. (Berna et al. 2014) elaborate comprehensively on the mechanisms and the existing correlations to describe the entrainment of liquid droplets. With increasing velocity difference between the liquid phase on the heated surface and gas core of the flow, the interface between both phases becomes wavier. At a certain point called the “onset of entrainment”, parts of the liquid phase are dragged by the faster flowing gas core. (Ishii and Grolmes 1975) named 4 different initiation types of entrainment in concurrent flow: i) the turbulent gas flow shears off the top of the rolling wave crests which were formed by the Helmholtz instabilities, ii) the liquid film is undercut by the gas flow, iii) nucleate boiling (NB) in the liquid film producing bubbles that burst at the two-phase interface, iv) impingement of liquid mass to the liquid film by either existing droplets or roll wave crests. The processes are depicted in Figure 2.4. (Berna et al. 2014) state that the rolling wave (first type) is the dominant mechanism for low viscous fluids such as water. The initiation mechanism directly influences the diameter of the droplets which marks an important parameter in the heat transfer calculations for PDO. In many models that consider the influence of heat transfer through direct contact of heated surface and droplet or through evaporation, the droplet size at an initial point along the flow has to be known. Usually, the point of dryout is chosen for such a reference point (Yu 2019). The droplet size at the point of dryout is not only influenced by its initiation mechanism but also the flow behavior (Varone 1990). Droplet break up due to velocity differences between the two phases influence the droplet size as well as droplet deposition. According to (Yu 2019), capillary and aerodynamic break up were observed with the latter one being the most influential break up process. The deposition of entrained droplets back onto the liquid film decreases the number of droplets that actually reach the point of dryout or the dispersed flow regime.

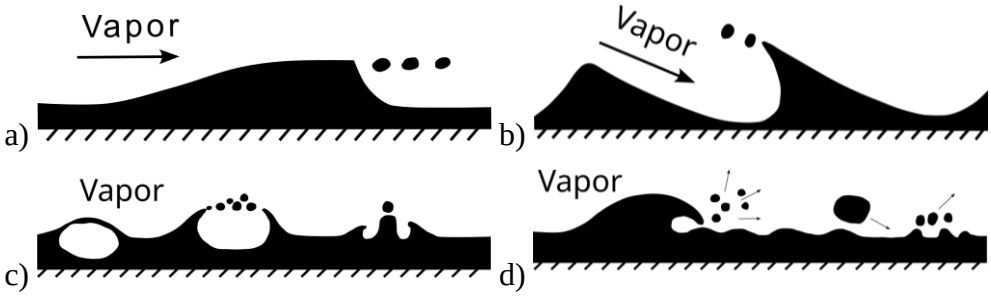


Figure 2.4: Initiation types of entrained droplets; a) Roll wave, b) Wave undercut, c) Bubble burst, d) Liquid impingement (adapted from: (Ishii and Grolmes 1975))

The direct heat transfer from the heated surface to the droplets follows one of two mechanisms. Depending on the distance to the point of dryout, the entrained droplets might touch the wall directly which in the literature is described as wet collisions (e.g., (Groeneveld 1975)). This mechanism is usually encountered in the vicinity of the dryout point. Chen and Costigan in (Hewitt et al. 1992) cited the experiments of (Evans et al. 1983) that indicate that vapor superheating occurs approximately 0.3 m after dryout. This implicates a very effective evaporation of liquid droplets in the area between dryout and vapor superheating. Since the vapor superheat in this region is apparently small they concluded that most of the evaporation occurs by direct contact of droplets and heated wall. When the Leidenfrost temperature is exceeded, no direct contact of droplet and wall is possible anymore. In that case however, the droplets are still able to enter the thermal layer at the wall. This behavior is usually referred to as dry collisions. Although the heat transfer in that scenario is less significant due to the lack of direct contact, dry collisions lead to a disturbance in the boundary layer which subsequently improves the wall to vapor heat transfer (Groeneveld 1975). In his dissertation the mechanism of dry collision is described as an approach of the liquid interface to the heated surface which increases the evaporation rate since the insulating vapor layer covering the heated wall is thinned (Groeneveld 1972). While further approaching the heated surface, this increasing evaporation rate eventually exceeds the liquid forces (i.e. liquid pressure and inertia forces caused by liquid-vapor interface oscillations) so that the liquid is forced back by the vapor thrust force. Besides the described wall temperature, (Schnittger 1982) names the droplet size, evaporation rate and therefore flow acceleration, and the relative velocity between the liquid and the vapor phase as important parameters in determining the form of droplet contact. Due to a higher „deposition energy“ of bigger droplets there exists a minimum droplet diameter below which no droplet deposition is possible anymore. Researchers ((Forslund and Rohsenow 1968; Ganić and Rohsenow 1977; Kendall and Rohsenow 1978; Guo and Mishima 2002) among others) have investigated the heat transfer from wall to droplets experimentally and analytically to quantify the contribution to the overall heat transfer. (Kendall and Rohsenow 1978)

numeralized the overall heat transfer contribution below 5%. (Yu 2019) claimed in his thesis that the amount of heat transferred differs between developing and fully developed post-dryout region. Furthermore, he distinguished between high and low pressure influence. For the analyzed test cases he found the heat transfer from wall to droplets to be bigger than 20% in the developing region in high pressure cases in water and dropping to around 10% for the fully developed region. At low pressures, the amount lies around 5% and decreases only slowly with increasing axial distance from the point of dryout. It can be concluded that the overall contribution in the fully developed PDO area is very limited. However, the contribution of the direct heat transfer from wall to droplets is more significant in the developing PDO region.

The heat transfer in PDO is mainly governed by the convective heat transfer from wall to vapor and the convective, interfacial heat transfer from vapor to droplets. In ((v. d. VDI e.V. 2013), chapter 3.6) and (Varone 1990), two limiting cases for the calculation of the PDO heat transfer are distinguished. They are depicted in Figure 2.5a) and b).

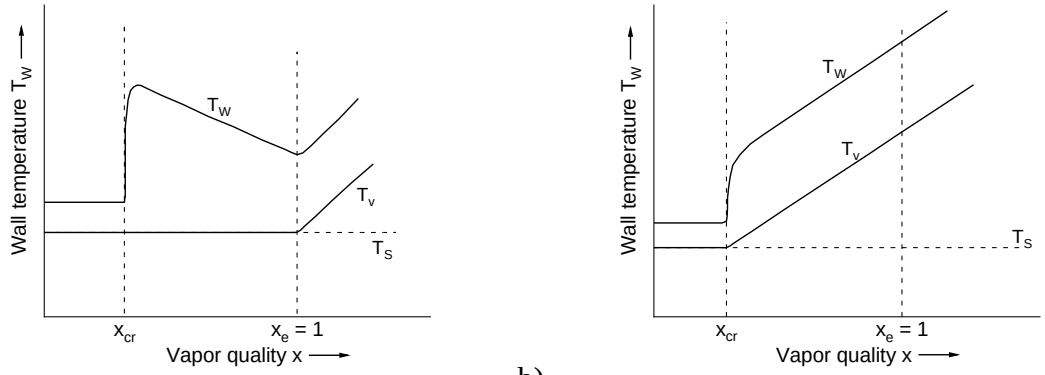


Figure 2.5: Wall and vapor temperature T_W and T_v vs. vapor quality for a) thermal equilibrium and b) thermal non-equilibrium (adapted from: (VDI-Gesellschaft Verfahrenstechnik und Chemieingenieurwesen 2010))

Thermal equilibrium

Both, droplets and vapor are assumed to be at saturation which means that the liquid and the vapor phase are at thermal equilibrium. In this case that marks the lower temperature limit for the PDO wall temperatures, all the heat transferred from the heated surface to the flow is used for droplet evaporation only ((v. d. VDI e.V. 2013), chapter H3.6, (Groeneveld 1975)). That leads to a vapor acceleration which subsequently improves the heat transfer and thus lowers the wall temperature. It therefore marks the lower limit of the PDO temperature distribution. Homogeneous flow is assumed in correlations using these assumptions (Dougall and Rohsenow 1963) or slip ratio correlations are in use (e.g., (Quinn 1966)). The actual vapor quality x_a in

that case equals the equilibrium vapor quality x_e. As soon as this value reaches 1, it is assumed that all the liquid is evaporated and the behavior changes to that of single-phase vapor flow. The assumption of thermal equilibrium has a very limited validity and is usually encountered only at high pressures and high mass fluxes ((Collier 1976; Bergles et al. 1981; Hetsroni 1982; Katsaounis)) or close to the point of dryout (Groeneveld 1975).

Thermal non-equilibrium

At total thermal non-equilibrium, it is assumed that no or only a very small portion of the heat is used for evaporation while the vast majority goes into the superheating of the vapor phase. The liquid phase remains at a saturated state. This leads to a continuous temperature increase and marks the upper limitation of temperature distribution in the PDO. In that case, the actual vapor quality is always lower than the equilibrium vapor quality as the superheated vapor enthalpy exceeds the vapor enthalpy at saturation ((v. d. VDI e.V. 2013), chapter H3.6, (Groeneveld 1975)). This relation is given by the following equation:

$$\left(x_e = \frac{h_{poi} - h_l}{i_{v-d}}\right) > \left(x_a = \frac{h_{poi} - h_l}{h_{va} - h_l}\right) \tag{2.6}$$

whereas h_{poi} is the enthalpy at the investigated point of interest, h_l the enthalpy at liquid saturation, h_{va} the enthalpy of the superheated vapor, and i_{v-d} the latent heat.

The assumption of thermal non-equilibrium delivers better results over a wider parameter range when compared to experimental investigations. Wall temperature and actual vapor quality are found to be in between the two described limiting cases ((Hill and Rohsenow 1982; Varone 1990)). According to (Hynek et al. 1969), the degree of thermal non-equilibrium mainly depends on the mass flux. The thermal non-equilibrium is more significant for lower mass fluxes since high mass fluxes cause higher flow turbulence which improves the convective heat transfer. When $x_e > 1$, the thermal non-equilibrium gradually disappears ((Groeneveld 1975; Varone 1990)).

(Chen 1986) concluded that the driving force for the convective heat transfer from wall to vapor is the difference of wall and vapor temperature (T_W - T_v) rather than the difference of wall and saturation temperature (T_W - T_S) as it was used in earlier theoretical models that neglected the thermal non-equilibrium. Since the difference to vapor temperature is smaller due to vapor superheating, he concluded that the driving force for the convective heat transfer from wall to vapor is less than assumed before. Furthermore, with more energy going into superheating of the vapor, less energy is spent on the evaporation of the liquid phase, leading to less actual vapor mass flux than assumed with thermal equilibrium.

2.3.3 Rewetting

Rewetting describes the mechanism at which a dried out heated surface is wetted again by the liquid phase. The temperature corresponding to the point of rewetting is at the minimum film boiling temperature, T_{MFB}. If a heat flux controlled system is in use, this point marks the temperature and corresponding heat flux at which a surface wetting and therefore a more efficient heat transfer from wall to fluid can be re-established. In wall temperature controlled systems, this point is the transition from the transition boiling to the film boiling regime and the other way around and is therefore the highest admissible transition boiling temperature. The minimum film boiling temperature is sometimes referred to as the Leidenfrost temperature. According to (Carbajo 1985), this is only true for isothermal surfaces in combination with saturated liquid. In measurements of the maximum transition boiling temperature, it was found that this temperature might exceed the Leidenfrost temperature. Katsaounis and Kind explain that with possibly different thermo-physical properties from fluid to wall as well as with the influence of surface roughness, flow velocity, and liquid temperature in the flow ((v. d. VDI e.V. 2013), chapter H3.6). The influence of different parameters on the minimum film boiling temperature was surveyed by (Groeneveld and Snoek 1986) among others. Based on different experiments (e.g., (Bennett et al. 1966; Groeneveld and Stewart 1982; Laperrière 1983)), they found that an increase in flowrate does not necessarily increase T_{MFB}. Increasing pressure usually leads to an increase of T_{MFB}, although it should be noted that not a wide pressure range was covered in the available data base at that time. (Peterson and Bajorek 2002) also queried this lack of data and extended the pressure range in their own experiments. The influence of vapor quality is not well understood whereas an increased fluid subcooling as well as an increase of heater surface roughness or an oxidization layer usually increase the minimum film boiling temperature.

When looking at the boiling curve, the transition from the film boiling regime back to the nucleate boiling regime can happen in one of two ways (Plummer 1974). First, the temperature follows the same path as it did when heating up, only in the opposite direction. Second, the temperature follows the path further down the boiling curve until it reaches the point where the transition happens to the transition boiling regime. This second process leads to a hysteresis as the heat flux and/or the temperature corresponding to the point of rewetting differs from the one that marked the maximum nucleate boiling heat flux and temperature. According to Plummer, the second option only occurs in either a temperature controlled system or in a heat flux controlled system in which no other liquid wall contact happens.

Different types or controlling mechanisms of rewetting have been identified in the literature. They are mainly distinguished by the previous flow and heat transfer regime leading to the rewetting. Additionally, the presence or absence of a propagating quench front plays a crucial role in this classification. The type encountered in the experiments of this thesis is called “Dispersed Flow Rewet” ((Iloeje et al. 1975)) or “Rewetting following dispersed droplet cooling” ((Groeneveld and Snoek 1986)). Without a propagating rewetting front, the heated

surface is cooled by the entrained droplets that eventually touch the wall leading to rewetting ((Groeneveld and Snoek 1986)). ((Iloeje et al. 1975)) postulate that the rewetting process is controlled by two processes and their limiting effects; i.e. heat transfer to vapor without any influence of the entrained droplets and heat transfer to droplets. The effect of the second mechanism depends on the wall temperature which determines if a direct wall droplet contact is possible. Hydrodynamic aspects like droplet size and position in the channel also affect this second mechanism. Combined, the two mechanisms determine the heat flux and minimum film boiling temperature.

2.4 Literature Review of Post-Dryout Experimental Work

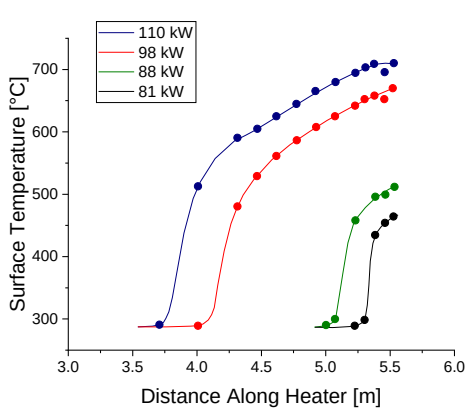
It is impossible to comprehensively present all the existing literature on experimental PDO heat transfer. A general selection of studies is therefore introduced in more detail that either shows the most important parametric trends or shows certain similarities to the experiments conducted in this study, or both. This overview is followed by experimental work in geometries other than tubes. In succession, available literature about optical investigations at PDO conditions is discussed. This chapter is concluded with the presentation of the current state of experiments to determine the thermal non-equilibrium.

2.4.1 General Studies on PDO Heat Transfer

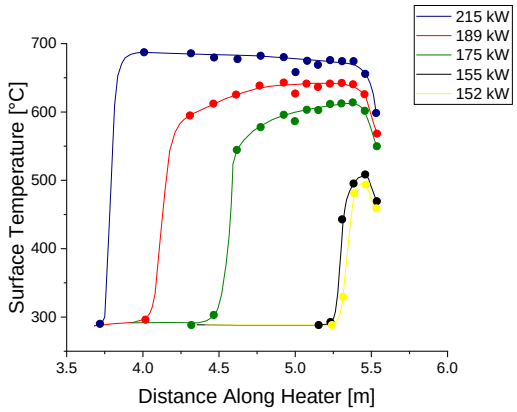
Numerous post-dryout heat transfer experiments were conducted in the past decades. However, the phenomena occurring at CHF and beyond remain object to further investigations and are not yet fully understood. Therefore, experiments are predominantly carried out in simple geometries, mostly in single tubes, to better understand the underlying phenomena. Early on, experiments were also started in different fluids. While in practical applications water is still the most important fluid, for fundamental research other fluids like nitrogen (including (Forslund and Rohsenow 1966, 1968; Hynek et al. 1969; Ganić 1976; Ganić and Rohsenow 1977)) or different sorts of refrigerants are used (e.g., (Cumo et al. 1971) and (Groeneveld 1972) in R-12, (Nishikawa et al. 1983) in R-22, (Koizumi et al. 1979) in R-113, or (Lee and Chang 2008) in R-134a). They bear the advantage of more cost effective investigations while covering the same physical phenomena, only at lower pressures and temperatures (Groeneveld et al. 1997). This reduces the costs for the required facility components as well as the necessary energy to conduct the experiments. However, in order to quantitively compare the acquired data to water conditions, they need to be scaled. Fluid-to-fluid scaling laws were developed for that purpose. The general assumption is that geometry, thermodynamic, and hydrodynamic similarity must be achieved. Some researchers proposed models based on the dimensional analysis (e.g., (Groeneveld et al. 1997; El-Nakla 2011; Yu 2019). Most models are based on the distortion approach proposed by (Ahmad 1973). (Nemitallah and El-Nakla 2013) also suggested a different approach by scaling the energy equation. As scaling PDO data is a

complex undertaking considering all the different effects, an additional degree of uncertainty is added to the data interpretation, revealing one disadvantage of the use of other fluids than water. As mentioned in the introduction, the following studies give an overview of the general trends found in the experimental investigation of PDO heat transfer. It should be noted that the presented parametric trends are derived from tube experiments. They do not necessarily occur in the same manner or to the same degree in more complex geometries.

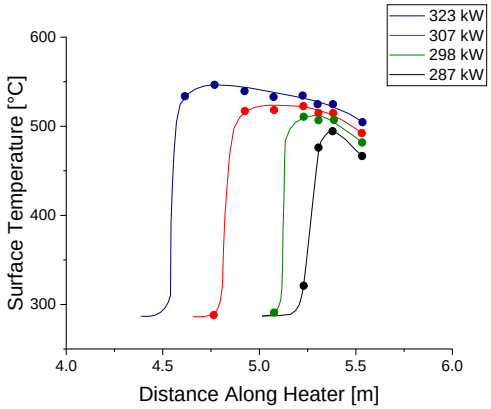
A very early study on PDO heat transfer was conducted by (Bennett et al. 1967) with water in a uniformly heated tube. Their results showed that the wall temperature increases steeply at the onset of dryout. The mass flux was proven to have a main influence on the temperature distribution in the PDO area, leading to continuously increasing wall temperatures when the mass flux is low, whereas medium mass fluxes cause the wall temperature to slowly increase or remain constant, while at high mass fluxes, the wall temperatures experience a decrease after reaching a local maximum close to the point of dryout. Figure 2.6 exemplifies the typical temperature distributions at different mass fluxes. The maximum temperature rises and the location of dryout onset is shifted further upstream as the heat flux increases. No significant hysteresis effect was found in their steady-state rewetting process. Based on their experimental findings, they developed a model to predict the wall temperature under PDO conditions taking into account the slip between vapor phase and entrained liquid phase. In their model, they assumed a two-step heat transfer process: i) from wall to vapor and ii) from vapor to droplets.



a)



b)



c)

Figure 2.6: Wall temperature vs. tube length for a) low, b) medium, and c) high mass fluxes at different heat fluxes (adapted from: (Bennett et al. 1967))

Two of the most important and comprehensive PDO heat transfer data bases for tube geometry were obtained at the Royal Institute of Technology (KTH) in Stockholm. Becker et al. first published a data base for PDO data obtained with uniformly heated tubes of different inner diameters and water as the working fluid (Becker et al. 1983). Later on, they expanded their research to non-uniformly heated tubes (Becker et al. 1992). While they did not publish a comprehensive analysis or interpretation of their data, especially of the uniformly heated tube, the parametric trends could be derived from the provided data. The results show similar tendencies to (Bennett et al. 1967) regarding the temperature distribution as well as the upstream shift of the dryout location with increasing heat flux. For lower mass flux, the temperature continues to increase after the sharp rise at the point of dryout while at higher mass flux the temperature decreases after reaching a local maximum. Those tendencies were more pronounced with a decrease and increase of mass flux, respectively. Regarding the dryout, especially at high pressures and mass fluxes, the critical vapor quality, corresponding to the point of dryout, is shifted to lower values for increasing heat flux. However, decreasing mass flux has been observed to weaken this tendency, partially prevent it, and, on rare occasions, even reverse it. Decreasing pressure pronounces this behavior and also smaller tube diameters seem to strengthen this tendency.

Nishikawa et al., as indicated above, conducted PDO heat transfer experiments with the refrigerant R-22 in uniformly heated tubes of different dimensions at high subcritical pressures (Nishikawa et al. 1983, 1986). With different inlet enthalpies they covered the range of post-dryout to an equilibrium vapor quality of unity and beyond. Their results confirmed the general temperature distributions found in water for low and high mass flux. No significant influence of the tube diameter regarding the obtained wall temperatures was observed. A correlation was developed to predict the PDO wall temperatures as none of the existing correlations could satisfactorily describe the experimental results. They introduced a non-dimensional parameter to account for the thermal non-equilibrium. Although based on high pressure data, the authors

successfully applied their model to lower pressure data from (Groeneveld 1972) and (Schnittger 1982) as well.

In his dissertation, (Schnittger 1982) investigated the PDO heat transfer in vertical and horizontal round tubes with R-12. He investigated the influence of pressure, mass flux, heat flux, and tube diameter on the wall temperature at dryout and beyond. For the vertical tube he found that the dryout vapor quality decreases with increasing mass flux as well as with increasing pressure. In the PDO region, the temperature keeps increasing for lower pressures while it decreases at higher pressure with a steeper reduction for increasing pressure. His experiments showed that increasing mass flux tends to decrease the temperature rise at the point of dryout. Increasing mass flux shows a relatively similar influence on the PDO temperature distribution as increasing pressure does. Furthermore, increasing the heat flux increases the overall level of wall temperature whereas the temperature slope shows no significant dependence on the heat flux. Based on the experiments, Schnittger developed a PDO heat transfer model paying special attention to the entrained droplet size and behavior. He concluded that droplets which enter the wall boundary layer have their most significant influence on the wall temperature by bursting. The thermal non-equilibrium was accounted for by measuring the vapor temperature with a custom-made probe.

A last study that should be mentioned in this context was proposed by (Lee and Chang 2008) conducting PDO heat transfer experiments in smooth and rifled tubes with R-134a at the Korea Advanced Institute of Science and Technology (KAIST). It represents one of the few studies under PDO conditions with R-134a. Their results in smooth tubes support the aforementioned temperature distributions at high mass fluxes. They also found that with increasing heat flux the critical vapor quality is shifted to lower values. This is pronounced with increasing pressure as observed before by Schnittger. For lower mass fluxes the maximum wall temperature decreases with increasing pressure. The strong thermal non-equilibrium effect occurring in the PDO region is significantly lowered in the rifled tubes. An empirical prediction correlation for both tube geometries was developed and compared to the available experimental data, confirming a high prediction accuracy. The correlation developed for smooth tubes is presented in Appendix B1.

Groeneveld et al. summarized several parametric trends stemming from various experiments and gave the corresponding physical background (Groeneveld 1973; Groeneveld and Delorme 1976; Groeneveld and Snoek 1986). Those conclusions are listed below. Since they partially used the HTC in their argumentation which depends on the definition, vapor superheat and wall temperature are used instead.

- Increasing mass flux G reduces vapor superheat and wall temperature.
  The slip velocity, describing the velocity difference of vapor and liquid phase, increases with increasing mass flux at equal vapor qualities since the entrained droplets are not accelerated as much as the main vapor phase. This leads to more droplet break-up and

therefore a bigger interfacial area and also to an overall higher vapor velocity which improves the heat transfer from wall to vapor.

- At low G, increasing vapor quality x increases vapor superheat and wall temperature.
  Since at lower G, most of the heat applied to the flow is used for vapor superheating, increasing x leads to a continually increasing vapor superheat.
- At high G, increasing vapor quality x reduces the wall temperature.
  Increasing x leads to an increasing vapor velocity at a constant mass flow which improves the heat transfer from wall to vapor.
- Non-equilibrium disappears gradually for x_e bigger than unity.
  The driving force for droplet evaporation will increase when the vapor temperature exceeds the saturation temperature significantly and vapor to droplet heat transfer is augmented until the complete evaporation of liquid.
- Increasing pressure p reduces vapor superheat and wall temperature.
  Increasing p leads to improved heat transfer properties of the vapor and decreased surface tension σ, which causes smaller droplets and therefore an enhanced interfacial area. Close to the critical pressure, the flow becomes homogenous as the latent heat and σ approach zero and consequently, the non-equilibrium disappears.

2.4.2 Studies of PDO Heat Transfer in Different Geometries and Spacer Influence

Besides the most common tubular test section, more complex geometries are investigated as well. Numerous studies were conducted in, mostly concentric, annular test sections (e.g., (Polomik et al. 1961; Koizumi et al. 1987; Anghel 2013). Figure 2.7 illustrates some typical PDO temperature distributions for different heat fluxes in an annular flow channel. They are depicted as the difference of wall and saturation temperature vs. the axial distance from test section inlet and include the influence of pin spacers as will be described later. Besides the influence of spacers that are usually necessary if the test section exceeds a certain length, it is obvious that the depicted temperature distribution at the heated rod wall is quite similar to the ones observed in tube geometry. However, (Koizumi et al. 1987) pointed out that in case of an annulus with single heating of the rod, the HTC for annuli exceeds the one for tube geometry as liquid of the unheated inner wall of the outer annulus channel is consistently applied to the dried out heated surface of the inner rod.

The investigation of rod bundles is of special interest in the field of nuclear safety as this geometry is present in reactor cores. The bundle size reaches from small scale 2-rod bundles (e.g., (Hench 1964)) up to tests with e.g., typical PWR size 17 x 17 rod bundles as was conducted by Westinghouse in the “Full Length Emergency Core Heat Transfer-System Effects and Separate Effects Tests (FLECHT-SEASET)” (Loftus et al. 1980). Since rod bundles experience different phenomena regarding PDO heat transfer, they were only mentioned for the sake of completeness and will not further be assessed.

The influence of spacers on the heat transfer has been scientifically investigated for decades. Research was undertaken by (Yao et al. 1982; Kim and Korol'kov 1991; Groeneveld et al. 1999; Miller et al. 2013), to name only selected examples. Some of the mentioned studies aimed at investigating the influence of spacers on PDO heat transfer whereas others were researching single-phase heat transfer. When applying PDO conditions, only at very high void fractions the conditions are close to single-phase vapor heat transfer. Recently, the Royal Institute of Technology (KTH), by name especially Anghel and Anglart, took effort in experimentally and theoretically investigating the spacer influence on PDO heat transfer ((Anglart 2006; Anglart and Persson 2007; Anghel and Anglart 2014; Anghel 2014) among further publications). The experiments were carried out in a water loop with an annular test section of which both, outer tube and inner rod were heated. Different forms of spacers were investigated among them simple pin spacers (e.g., (Anghel 2014)) but also common BWR spacer designs (Anglart and Persson 2007). Generally speaking, a spacer independent of its form represents a blockage of the flow channel narrowing the free flow area. (Hochreiter et al. 1992) indicated that this may decrease the vapor superheating, lead to boundary layer changes, droplet break-up and increased turbulence at and downstream of the spacer. All mentioned phenomena enhance the heat transfer which leads to a decrease in wall temperature or even rewetting of the dry wall, as indicated at the highest two heat fluxes in Figure 2.7. The spacers in the diagram are marked with black crosses. (Anglart and Persson 2007) pointed out that liquid deposition is also enabled through the spacer directly leading liquid to the wall surface.

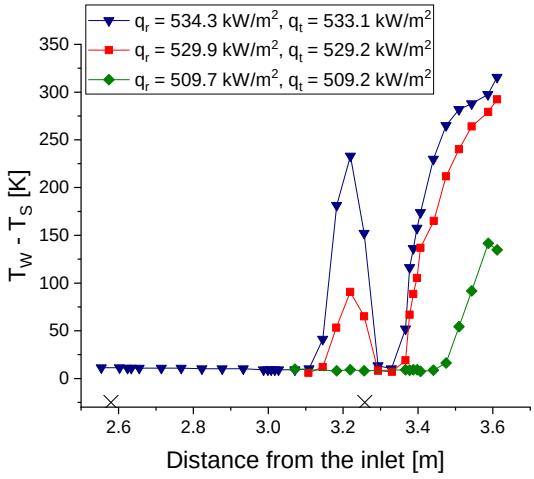


Figure 2.7: PDO temperature distribution measured at the wall surface in an annular flow channel for different heat fluxes at p = 50 bar, T_S-T_{in} = 10 °C, G = 500 kg/(m²s) (adapted from: (Anghel 2014))

2.4.3 Optical Investigations under PDO Conditions

Optical studies are conducted to investigate the flow behavior. In case of dryout and PDO conditions, the behavior of entrained droplets in the main gas flow is of special interest as

discussed before. Experimental studies, optical and non-optical, on droplet formation and droplet behavior exist in a large number in the annular flow regime (among others (Azzopardi 1985; Azzopardi et al. 1991; Trabold et al. 1999; Damsohn and Prasser 2011)). Other studies optically investigate droplet behavior or two-phase flow in general in unheated channels which lacks the influence of a constantly heated surface on the droplet behavior (e.g., (Demidovich et al. 2019)).

Under PDO conditions however, optical studies of droplet behavior in particular are scarce. One of the first studies in this context is the one carried out by (Forslund and Rohsenow 1966). They conducted experiments with liquid nitrogen in different sized tubes. The goal of their visual investigation using strobe light and microflash photography was to proof the existence of thermal non-equilibrium. They detected entrained droplets for equilibrium vapor qualities of up to x = 3 and found that the non-equilibrium strongly depends on the mass flux. (Groeneveld 1972) also conducted optical flow investigations, mainly in a transparent annular test section with the rod being indirectly heated. Although he took photos of dispersed flow conditions as well the focus lay on the investigation of the flow pattern at dryout. He used high-speed camera footage as well as still photography which was carried out using an adjustable strobe light and a Polaroid Land camera. Especially, the studies by Cumo et al. in Freon-12 (Cumo et al. 1971; Cumo et al. 1974) should be mentioned. They switched from a heated tube to a 5 x 3 mm square channel just before the optical investigation which was kept in an adiabatic state. With that set-up, they were able to carry out experiments over a broad pressure range. In their investigations, they too confirmed the existence of a thermal non-equilibrium. In fact, they could prove that the thermal non-equilibrium persists up to vapor qualities of x = 2.2 for the investigated parameter range. In addition to the distribution of droplet size, they also found that in the post-dryout region, the majority of droplets follow the vapor flow and hardly any lateral movements can be detected. They figured that the slip ratio is closed to unity in the fully developed PDO region. Furthermore, they suggested a droplet size distribution correlation which is introduced in Appendix B.5.

In recent years, studies of dispersed flow film boiling have been reported from France (Peña et al.; Oliveira et al. 2020). They investigated dispersed flow during Loss of Cooling Accident (LOCA) conditions in a tube with an inner diameter of d_i = 11.78 mm which equals the hydraulic diameter of a subchannel present in typical French PWRs. Their vertically installed test section however, shows some significant differences to the commonly used test sections. It is divided into three parts. In the unheated bottom part, superheated vapor and droplets are injected and mixed. The second part is directly heated with a DC power supply and has a length of 170 mm. The top part is once again unheated. Just before entering the second part, droplet size and velocity as well as their temperature are measured using Phase-Doppler Analyzer (PDA) and Laser-Induced Fluorescence (LIF) thermometry, respectively. Those measurements can also be performed at the top part. The wall temperature of the heated second part of the test section is monitored by an infrared camera. This wall temperature is transitionally decreased to simulate cooling processes. They found that the droplet diameter is decreased downstream of

the second part by 23 – 30% due to evaporation which does not change the droplet temperature significantly. At higher vapor flow rates, the diameter remained independent from the cooling process whereas it slightly decreases with lower flow rates. Furthermore, the droplets are accelerated along the heated section. Due to limitations of the measurement equipment, the diameter of the injected droplets does not exceed d = 300 µm.
Other flow channel geometries are rare in PDO investigations. In that context the focus of this review lay on rectangular channels as one part of the experiments in this thesis was carried out in an annulus with a rectangular flow channel. Only one channel of a similar geometry investigating steady-state PDO heat transfer phenomena is known to the author ((Lee and Chang 2010)). However, the focus in those experiments was set on the investigation of PDO heat transfer with different types of spacer grids. The optical recordings were used to merely observe the general flow pattern rather than investigating the flow pattern itself or possible droplet behavior.

2.4.4 Vapor Temperature Measurements under PDO Conditions

As the determination of the thermal non-equilibrium is crucial in the context of reliable PDO prediction models, effort was taken early on to measure either the actual vapor quality or the vapor superheat and derive the actual quality from this temperature.
(Forslund and Rohsenow 1966) identified the main problem regarding vapor temperature measurements in their investigations on liquid nitrogen. Liquid and vapor need to be separated with as little mixing of both phases in the process as possible so that the non-equilibrium state can be preserved. Otherwise, the liquid phase can influence the measurement by either wetting the measuring surface which would usually lead to determined temperatures at or close to liquid saturation or it can lead to an equalization between both phases when mixed for a longer time duration. Furthermore, the influence of the heated wall needs to be considered as well as possible radiation or heat conduction that might influence the vapor probe depending on the experimental conditions. Forslund and Rohsenow tried to avoid those difficulties in vapor temperature measurements and applied Helium to the flow. By measurement of the Helium concentration at the exhaust and comparison to the concentration at the test section exit, they tried to determine the actual flow quality. However, in such an application too the gas needs to be separated from the liquid in order to determine the right concentration. Pisoni and Tagliafico tested a calorimetric method to determine the vapor temperature in the annular flow regime that they also found applicable to mist flow conditions (ENEA 1989).
However, specially designed vapor temperature sensors are usually used in the reported literature (including (Nijhawan et al. 1980; Unal et al. 1988)). (Snoek 1990) gave an overview over different tested solutions in previous studies. The simplest sensors tested were just specially designed tubes in which the flow was led around bends before it reached the temperature sensor. Most of the sensors reported in literature however are variations of the same type of aspiration probe. A thermocouple is sheathed by two tubes that are closed at the cap.

Each include two holes on opposite sides of the tube with a 90° offset between each tube. This combination of flow deflection and small openings as well as the differential aspiration should minimize the wetting of the thermocouple.

A lot of the available studies on vapor temperature measurement stem from the US, especially under the guidance and participation of J. C. Chen. (Nijhawan et al. 1980) conducted 12 test runs measuring the vapor superheat at one location in a vertically installed tube using an aspirated thermocouple sensor. Selected theoretical prediction models performed poorly in comparison with the experimental results. (Gottula et al. 1983) managed to measure the vapor superheat at three different axial locations simultaneously. Evans followed a different approach to determine the vapor superheat at different axial positions downstream of the dryout location (Evans 1983; Evans et al. 1985). A reflood process was conducted that slowly decreased the axial distance between the measurement point and the quench front. However, the quench front propagation in this reflood process was chosen so slow that the measurements can be regarded as quasi steady-state. The obtained data indicated a transition region in the vicinity of the dryout location where the amount of liquid and the evaporation intensity is high whereas the latter one is decreased with bigger distance to dryout. Also their test data showed significant deviations to compared models although the corresponding heat flux could be predicted quite well. (Unal et al. 1988) conducted vapor temperature measurements in a 3 x 3 rod bundle. They also included the spacer effect in their investigation. It was found that wall and vapor superheat rise with increasing overall heat flux, whereas it decreases when mass flux and vapor quality are increased. The heat transfer from wall to vapor showed no real dependence on mass or heat flux. The increased heat transfer due to spacers however depend on inlet quality as well as mass flux.

Despite the introduced studies, the overall available data regarding the measurement of the thermal non-equilibrium are still scarce. This is especially true when it comes to the determination of an axial vapor temperature profile as well as a broad parameter range since the available literature is usually limited to low pressure and low mass flux conditions.

2.4.5 Studies on Rewetting Behavior

Experiments researching the minimum film boiling temperature have been reported for all kinds of geometry, from simple heated plates to horizontal or vertical tubes and rod bundles. Usually, experiments are carried out as flooding (experiments with a propagating rewetting front either from top or bottom) or spray cooling investigations in which the coolant is externally employed on to the heated surface. Only a few experiments were found that investigated the rewetting behavior by simply reducing the applied power until wetting of the surface could be detected. This is also referred to as the “true quenching phenomenon” (Lau 1983; Cheng et al. 1985). Among those experiments were the ones by (Groeneveld and Stewart 1982; Lau 1983; Cheng et al. 1985) for tube geometry. In those experiments, a stable film boiling regime was established before the power was reduced stepwise until rewetting of the heated surface was

detected. In between those steps, a steady state was established. This equals the procedure that was applied in this thesis. (Bennett et al. 1967) investigated both, the dewetting and rewetting process by stepwise increase and decrease of power. They did not find any significant difference regarding the heat flux that was found for dewetting and rewetting the heated wall. (Stosic 2005) claimed that a hysteresis effect only occurs under transient conditions and cannot be observed in steady state, based on the theoretical and experimental investigations by (Chai and Shoji 2001; Iguchi et al. 2001a, 2001b). This statement is supported by other investigations for pool boiling (Auracher and Marquardt 2002, 2004)). (Iloeje et al. 1975) carried out transient experiments by cutting off the power supply after establishing the film boiling regime and monitoring the following temperature transient. A different approach was taken by (Feng and Johannsen 1991) who would carry out temperature controlled transition boiling experiments until they reached film boiling and thus deduce the minimum film boiling temperature from the transition between both heat transfer regimes.

2.5 Literature Review of Post-Dryout Heat Transfer Modeling

In the following subchapter, a review of available literature regarding the modeling of different aspects of the PDO heat transfer is given. Numerous works have been published in the past decades. This review is therefore not meant to give a complete and exhaustive description of available models but merely focuses on a general overview and the theoretical aspects relating to the experimental investigations in this research. In addition, selected correlations and models as well as modeling approaches for certain aspects of the conducted experiments, like droplet behavior, are introduced, as they are later on compared to the obtained experimental results in this study.

2.5.1 General Modeling Approaches of the Post-Dryout Heat Transfer

Different reviews of the available correlations and models of PDO heat transfer have been given in the past decades (including earlier work by (Groeneveld 1975), later work like (Groeneveld and Snoek 1986) and (Andreani and Yadigaroglu 1994) or more recent work like (Celata and Mariani 2003; Yu 2019; Song and Liu 2021).
(Andreani and Yadigaroglu 1994) categorized the available models into correlations (equilibrium and non-equilibrium models), phenomenological, and mechanistic models. Empirical models are developed based on experimental data and bear the disadvantage that they should not be extrapolated outside their validity range, which usually is the parameter range of the experiments they were derived from. The first empirical correlations were thermal equilibrium correlations and usually represent adaptions or modifications of the well-known Dittus-Boelter form of correlation for convective heat transfer in single-phase fluids:

$$\alpha = 0.023 \cdot \frac{\lambda_{vs}}{D} \cdot Re_{vs}^{0.8} \cdot Pr_{vs}^{0.4} \tag{2.7}$$

with the thermal conductivity λ_{vs} at saturated vapor conditions, the characteristic diameter D and the Reynolds and Prandtl number at saturated vapor.

Some of the most common correlations of that kind are presented in introduced in chapter 2.5.2 and discussed in the Appendix B.1. (Andreani and Yadigaroglu 1994) stated that they might show a sufficient accuracy under certain conditions at which the thermal non-equilibrium is very low and the droplet entrainment effect is small. However, as was pointed out before, substantial thermal non-equilibrium was observed under most DFFB conditions, thus limiting the applicability of such kind of correlations.

Mainly beginning in the 1970s, researchers started to take the thermal non-equilibrium into account e.g., (Groeneveld and Delorme 1976; Plummer 1974) or later the aforementioned model by (Nishikawa et al. 1986)). Although this type of correlation was also at least partially of an empirical nature they proved to have a better agreement with the physical mechanisms encountered at PDO conditions and showed an overall wider applicability. However, under certain DFFB conditions they perform worse than the simple to use equilibrium correlations.

Another method that was not considered in the above categorization but due to its purely empirical approach should be introduced here, are Look-up tables (LUT). They are basically a normalized collection of available data throughout the literature (Groeneveld et al. 2005). A preliminary film boiling LUT was introduced by (Leung et al. 1997) and is referred to as PDO-LW-96. It contained around 15,000 data points from 16 data sets. However, (Chen 2011) queried the gaps in the low flow and medium pressure range, where thermal non-equilibrium might have a significant impact. Around the same time, (Kirillov et al. 1996) proposed a similar LUT but did not give specific deviation statistics. The PDO-LW-96 LUT was subsequently enhanced and improved and eventually resulted in the most comprehensive look-up table for vertical tube film boiling data which was compiled in 2001 at the University of Ottawa (Groeneveld 2001). However, this version was slightly further extended and improved and as of 2003 contains around 77,000 data points from 36 different data sets of which approximately 37% are in the fully developed PDO region. The parameter range covers p = 10 – 200 bar, G = 0 - 7,000 kg/(m^{2}s), x = -0.2 - 2.0, and T_W - T_S = 50 - 1200 K. The skeleton of the table was built using the results of 5 different film boiling models and correlations. To this skeleton the actual data points were added and an assessment of the quality of the different parts of the LUT was given. After a smoothening process, the LUT gave an average prediction accuracy of the heat transfer coefficient of 1.71% with a Root Mean Square (RMS) deviation of 10.58% (Groeneveld et al. 2003). It should be noted that (Groeneveld et al. 1999) proposed a diameter correction factor that was used to normalize the experimental data to a reference diameter of 8 mm. (Groeneveld et al. 2005) point out the advantages of LUTs, e.g., i) simple use, ii) no iteration necessary, iii) wide range of applications, iv) based on large data base. However, they

also mention concerns raised against LUTs, like i) fluctuation of HTC with different parameters, ii) large variations of HTC between adjacent LUT entries, iii) data scarcity at specific flow conditions. Furthermore, the necessary application of fluid-to-fluid scaling laws when using other fluids than water, possibly increases the deviation in the HTC comparison between experiments and prediction.

Phenomenological models try to avoid empirical approaches. Nonetheless, several simplifying assumptions are made in that kind of models. According to (Andreani and Yadigaroglu 1994), most models in that category do not take the heat transfer via direct wall droplet interaction into consideration. Furthermore, the radiative heat transfer is usually neglected. Widely used examples of this modeling type are the CSO model (Chen et al. 1979) and the Local Conditions Solution (LCS) model (Varone and Rohsenow 1986). The first one is presented in Appendix B.2. The original idea of the latter one was published by (Yoder and Rohsenow 1983). It was later refined and improved by Varone and Rohsenow and made the following assumptions: i) at dryout, properties are at equilibrium conditions with liquid and vapor being at saturation, ii) the temperature of the entrained liquid remains at saturation, iii) droplet size is given by one average value. This model was applied by (Yu 2019) to experimental data in water (Becker data base) and R-134a (IATF data base) and agreed well with the water data but showed less agreement with the data in R-134a (average deviation of 44.3%).

The mechanistic approach is to model the exchange of mass, momentum, and energy and, commencing at the point of dryout, trying to capture the development of flow parameters (Andreani and Yadigaroglu 1994). They reach different stages of complexity depending on whether they are attempting one dimensional or multidimensional modeling of the two phases. Recently, a mechanistic model was developed at the IATF considering the three main heat transfer mechanisms in PDO (Cheng et al. 2018). It proposed a new approach of droplet behavior in respect to droplet size and concentration, the evaporation rate of droplets at the wall, and whether a droplet can reach the wall, depending on the droplet's turbulent kinetic energy. Moreover, it was applied to boiling curve examinations, providing a hysteresis behavior as discussed before. (Guo and Mishima 2002) considered six paths of heat transfer in their model, also paying special attention to the direct heat transfer from wall to droplets. Besides the above-mentioned heat transfer mechanisms they accounted for three paths of radiative heat transfer, in fact from i) wall to vapor, ii) from wall to droplet, iii) from vapor to droplet. They found that at low pressure and mass flux conditions, radiation and wall to droplet heat transfer cannot be neglected. An example of a very complex 2D/3D model is the hybrid Eulerian-Lagrangian model developed by (Andreani and Yadigaroglu 1997). They modeled the influence of liquid on the vapor phase (2D) by attempting 3D modeling of the droplet trajectories. The mechanistic model of (Meholic 2011) also considers the six above mentioned heat transfer mechanisms. It covers a wide range of parameters and was implemented into the transient safety analysis code COBRA-TF. Also, Meholic put his focus on the direct droplet to wall heat transfer and implemented Lagrangian droplet trajectories to describe the droplet behavior in the thermal

boundary layer. His suggestion on the droplet size distribution is described in Appendix B.5 and will be compared to the results of the optical investigations.
In the past years, CFD approaches have been published on modeling dryout behavior and the PDO heat transfer (e.g., (Torfeh and Kouhikamali 2015; Li and Anglart 2016; Shi et al. 2016)). According to (Yu 2019), they show some interesting features but are computational expensive and in some cases lack equivalent experimental data. They are just mentioned for the sake of completeness and are not examined in further detail.

Despite the described efforts and the progress made over the years, certain aspects remain unclear or objects to simplifications. (Yu 2019) stated that especially the modeling of the thermal non-equilibrium due to the presence of droplets represents one of the biggest challenges. Many 1D models assume a uniform droplet distribution. CFD models have more capacity to model droplet behavior and distribution. However, they still need a comprehensive understanding of the physical mechanisms besides the above-mentioned shortcomings, as stated by Yu.
A lot of models are developed based on a specific fluid, mostly water. Their applicability to other fluids is therefore somewhat questionable which means that in addition fluid-to-fluid scaling laws have to be applied which adds another aspect of uncertainty. In order to develop suitable scaling laws, broad data bases in different fluids and different geometries are needed.

2.5.2 Selected Theoretical Models for Post-Dryout Heat Transfer and Droplet Behavior

In the following subchapters, different models are introduced that will be used in the course of this thesis to assess their performance with the obtained experimental results and possibly identify further needs of modeling. The first type are models that were used to predict the PDO heat transfer for the investigations in test section 1. They can be divided into equilibrium and non-equilibrium models. Those models are numbered and are by name the Modified Dougall-Rohsenow correlation (1), Groeneveld 5.9 (2), Condie-Bengston IV (3), Bishop I, II, III (4-6), Miropol'skiy (7), Lee and Chang correlation (8), and Groeneveld 1972 (9) for the equilibrium models and Groeneveld and Delorme (10) and the CSO (11) model for the non-equilibrium models.
Subsequently, models to describe the droplet properties and behavior such as droplet diameter and velocity were validated using the obtained data from the optical flow investigation in test section 2. They are often embedded in complete PDO heat transfer prediction models but are treated separately here. For the droplet diameter, the model of (Guo and Mishima 2002) was assessed as well as the critical We number approach by (Isshiki 1959) and e.g., (Styrikovich et al. 1980). Alternatively, the droplet distributions were compared to the ones suggested by (Cumo et al. 1974) and (Meholic 2011). The vertical droplet velocity is often modeled using the slip ratio:

$$S = \frac{v_v}{v_l} \tag{2.8}$$

with v_v and v_l being the vapor and liquid, in this case droplet, velocity, respectively. The correlations to calculate the slip ratio by (Ahmad 1970) and (Groeneveld 1972) were validated. Furthermore, the vertical velocities were compared to the values obtained from a force balance of a single droplet moving in vapor flow.

These models and their main aspects as well as their applicability range, if available, are presented and discussed in Appendix B. Additionally, a mechanistic PDO heat transfer model and a PDO heat transfer correlation were recently developed at the IATF. Both those models will be explained and assessed with the obtained experimental data more detailed in chapter 6.

2.6 Summary and definition of research needs

A lot of research has been conducted in the past decades to experimentally investigate the PDO heat transfer and try to predict the heat transfer coefficient and therefore the expected wall temperature development. However, most of the models make simplifying assumptions, especially in respect to the influence of droplets on PDO heat transfer and the determination of thermal non-equilibrium since the physical mechanisms are not fully understood and experimental investigations are scarce. Despite the progress made over the years and the identified physical trends, they lack a general applicability since many models much like experimental investigations are limited to a narrow range of parameters or a specific fluid. This is especially true regarding PDO experiments with the refrigerant R-134a.

Therefore, this study provides experimental results covering two different flow channel geometries and a broad range of parameters in R-134a, especially in tube geometry. The need for developing and improving fluid-to-fluid scaling methods was taken into account by deriving comparable parameter combinations to existing water data for tubes. The obtained data in both test sections are thoroughly analyzed with respect to the influence of mass flux, heat flux, pressure, and inlet quality and their possible affection of the local PDO conditions. The lack of experimental data regarding the droplet behavior in dispersed flow under PDO conditions was attempted to overcome with optical investigations using high-speed camera measurement techniques. Furthermore, a new method of measuring the vapor temperature and therefore determining the thermal non-equilibrium in dispersed flow film boiling was employed by integrating an optical fiber into the flow channel. The recorded data are eventually used to evaluate available models.

The obtained data expand the existing data base in R-134a under PDO conditions and provide a solid data base for fluid-to-fluid scaling methods. They furthermore enhance the

understanding of the physical mechanisms encountered in the PDO conditions and help to identify further needs of research in model development and experimentation.

3. Experimental Set-up and Techniques

The following chapter describes the test set-up for the experiments carried out as well as the measurement technology used in those experiments. First, the overall system is described, followed by the description of the two test sections that were used in the experimental investigations. Further, the main properties of the working fluid R-134a are presented. In succession, the measurement technology utilized in the conducted experiments is presented. An additional description of the test facility, parts of the measurement gear used in the experiments as well as of test section 1 is also given by (Feuerstein 2019). Moreover, the set-up was roughly described in papers published by the author (e.g., (Köckert et al. 2018; Köckert et al. 2021)). The chapter concludes with the description of the measurement procedure, the test data reduction, and the uncertainty analysis.

3.1 Description of the KIT Model Fluid Facility

The KIT Model Fluid Facility (KIMOF) is designed as a closed loop system and was constructed by ANNEN Verfahrenstechnik GmbH. A simplified schematic of the facility is displayed in Figure 3.1 and shows the primary loop as well as the necessary auxiliary loops. The main components of the primary loop are the refrigerant pump, a pre-heater and two heat exchangers for converting the coolant from a two-phase state back to a single-phase liquid state before the pump entry, the test sections as well as the pressurizer. Two test sections can be installed vertically in parallel in the test facility, each with its own aftercooling system. The smaller of the two test sections is intended for tube and annuli tests and was used in the present experiments. More detailed information about the test section geometries can be found in subchapter 3.2. The refrigerant R-134a, which is provided by Linde GmbH, is used as fluid in the conducted experiments.

For the majority of the experiments, a centrifugal pump from KSB SE & Co. KGaA was used. This pump was replaced in the course of the investigations by a hermetically sealed canned motor pump from HERMETIC-Pumpen GmbH. While the centrifugal pump was in use, bypass 1 ensured that the pump always runs at its specified working point and the mass flow through the loop is kept constant. In the course of the pump exchange, bypass 1 was shut down and its tasks were taken over by bypass 2. In both cases, bypass 2 has the additional function of feeding the subcooled liquid after the pump outlet to the heated two-phase flow downstream of the test section exit via a mixing valve, thus providing initial precooling. The pre-heater is designed as a plate heat exchanger and is utilized to control the desired test section inlet temperature. It is operated on the secondary side with water, which is heated by a gas burner. A 500 liters water tank is interconnected between the gas burner and the heat exchanger to compensate off times and possible temperature volatilities of the burner. The aftercooling heat exchangers are also constructed as plate heat exchangers. The first aftercooling stage is fed with water at ambient

temperature from a cooling tower on the secondary side. The second operates with a chiller on the secondary side. These heat exchangers ensure a subcooled state of the fluid at the pump entrance. The pressurizer consists of three piston accumulators which are operated on the secondary side by hydraulic oil. It is used to control the system pressure and compensate for pressure fluctuations.

Pressure and temperature are consistently recorded along the loop. The mass flow is determined with a Coriolis mass flow meter before entering the test section. The data acquisition is controlled using a Wago programmable logic controller. In addition, three 2640A data loggers manufactured by FLUKE Corporation, Inc are used, usually measuring at a record frequency of 2 Hz. The data can be monitored and stored on a PC using LabVIEW software.

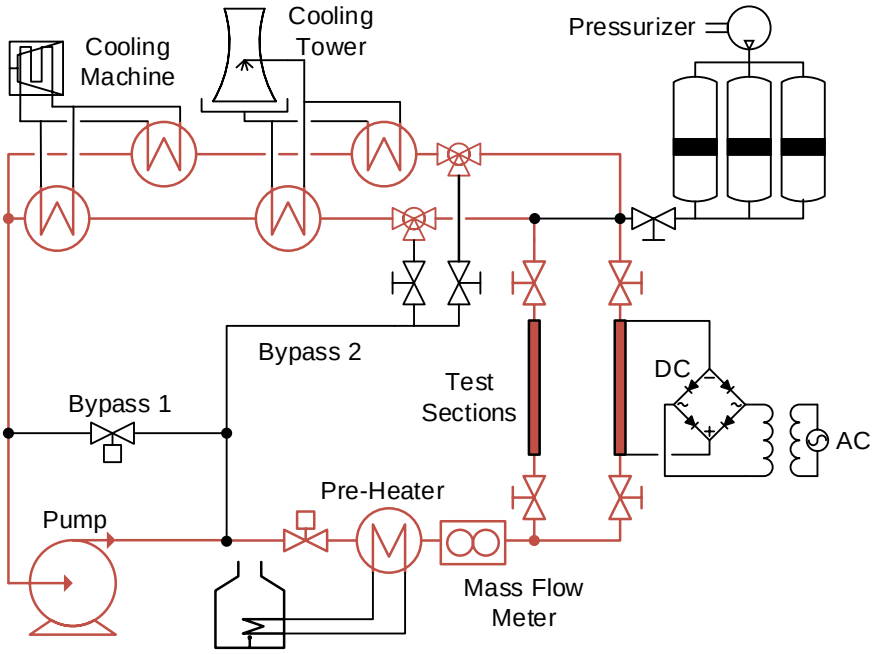


Figure 3.1: Schematic experimental set-up of the test facility KIMOF

3.2 Test Sections

Two different test sections were used to investigate the post-dryout heat transfer. The first test section is a uniformly heated tube, whereas an annular flow channel was used primarily for the flow behavior studies and provided optical access to the flow channel via windows. In the following subsections, the specifications of the two test sections are presented.

3.2.1 Uniformly Heated Tube

The first PDO test series were carried out on a vertically installed, uniformly heated tube with upflow, which will further be referred to as test section 1. The tube was manufactured by ETHEN Rohre GmbH and consists of the austenitic stainless steel X5CrNi18-10 (1.4301). A schematic representation is given in Figure 3.2. The heated length of the tube is 3100 mm.

Direct current is used for test section heating, which is applied to the test section by means of a transformer and a rectifier via two current connectors. The voltage drop can also be measured at these connectors. The test section is electrically insulated from the rest of the test facility by two insulation flanges.

The inner tube diameter is 10 mm, with an outer diameter of 12 mm. The unheated entrance length of the test section is 500 mm and therefore 50 times the inner diameter to ensure a fully developed turbulent flow at the beginning of the heated length. Temperatures on the outer wall of the tube are measured using 50 thermocouples spaced 60 mm apart, as schematically indicated in Figure 3.2. The top thermocouple is located 2 mm below the top current connector. The thermocouples are on opposite wall sides with an off-set of 180°, starting 138 mm above the start of the heated length at the lower current connector. Starting at thermocouple 12, an additional thermocouple is mounted at the same axial position but offset by 180° on the opposite side of the tube. This is repeated at intervals of 10 thermocouples. This set-up serves to investigate the radial temperature distribution and leads to an overall 55 thermocouples.

In-stream thermocouples and pressure transducers are applied at the inlet and outlet of the test section to determine pressure and fluid temperature. The test section is thermally insulated against environmental influences by two layers of mineral wool which have an overall thickness of 50 mm.

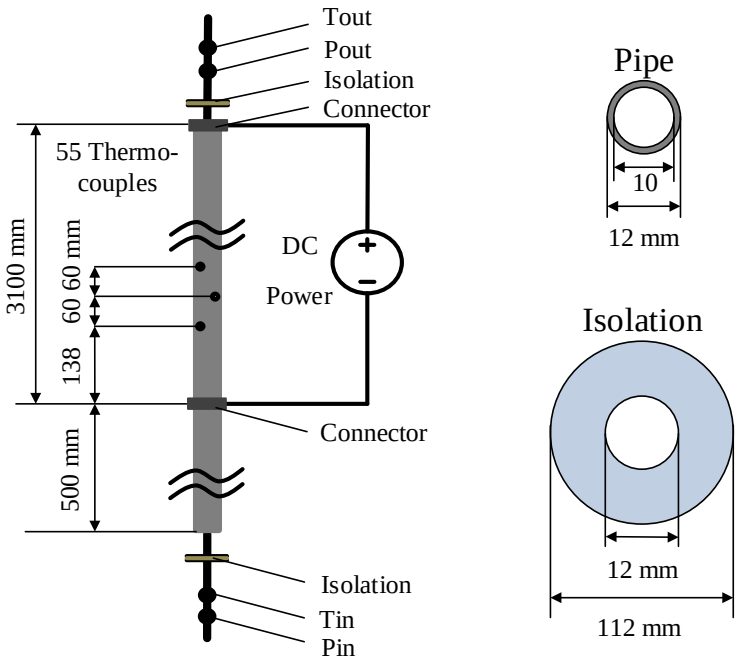


Figure 3.2: Scheme of test section 1 including cross sectional view (also used by (Feuerstein 2019))

3.2.2 Annular Flow Channel

Further PDO tests were carried out in a annular channel. This consists of a square outer channel with a heating pipe in the channel center. Throughout the further transcript, the annular flow channel will be referred to as test section 2. This test section is also installed vertically with upward flow. The schematic of the test section can be seen in Figure 3.3. The side length of the inner channel walls is 20 mm, with the outer length being 58 mm. The duct consists of three geometrically equal and therefore interchangeable modules, each having a length of 1070 mm. They are connected by flanges. One of the modules is equipped with 16 pairs of screw-in, bull's eye shaped windows. The windows of each pair are located on opposite sides of the duct. They allow visual access to the channel for investigations of the flow behavior. The windows are sealed by means of O-rings. In the tests carried out in the course of this thesis, the window module was always located in the top part of the test section. The channel is made of the stainless austenitic steel X6CrNiMoTi17-12-2 (1.4571). As can be seen in the schematic, the center point of the first window is 95 mm above the lower flange connection. The axial distances between the windows are 60 mm from center to center. Consequently, the top pair of windows is 75 mm below the top flange connection. The windows, manufactured by Herberts Industrieglas GmbH & Co. KG, are made of borosilicate glass and have a visual field diameter of 25 mm. This is thus larger than the inside length of the channel, allowing observation of the entire channel width. The thickness of the borosilicate windows is also 25 mm which allows them to withstand pressures up to p = 100 bar. The windows are flush with the inside surface of the duct, ensuring unaffected flow. Inlet and outlet of the test section are connected to the square channel via flanges.

In the center of the channel there is a directly heated tube, which was made of X5CrNi18-10 (1.4301). The heating tube was designed by the Framatome GmbH (former AREVA GmbH) and manufactured accordingly. It has an inner diameter of 7.5 mm and an outer diameter of 10 mm. This geometry results in a hydraulic diameter of the flow channel of 11,5 mm, which is approximately the hydraulic diameter of a reactor subchannel. The heated length of the pipe is 2700 mm for a total length of 4114 mm. Since the current connectors of the DC power supply already mentioned in subchapter 3.2.1 have to be placed outside the flow channel, a special copper construction was provided to allow the heated length to be placed exclusively in the channel. The heated length ends in the upper part of the field of view of the uppermost pair of windows.

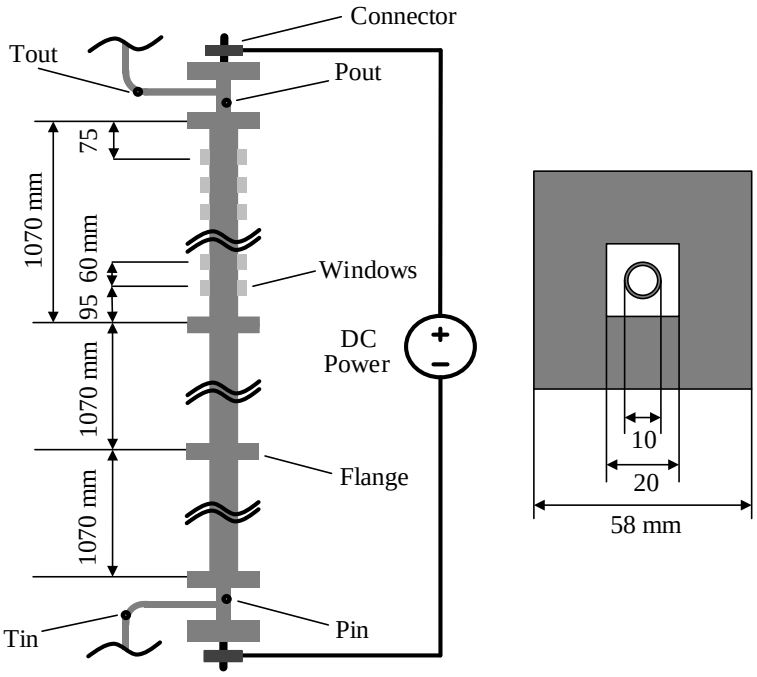


Figure 3.3: Scheme of test section 2 including a cross sectional view

Over a length of 1110 mm, starting from the top of the heated length, a total of 20 type K thermocouples are mounted on the inside of the heating tube at 12 different levels. To ensure the functionality of the thermocouples, they have been mounted on ceramic pads that are metallized with Al_2O_3. This insulates the thermocouples electrically from the heating tube and simultaneously guarantees good heat conduction. The first thermocouple level starts 20 mm below the end of the heated length. The axial distance between each level up to the sixth level is 60 mm. Between plane 6 and 11, the distance is 120 mm in each case, with the 12th plane lying 195 mm below plane 11. On each of the levels 1, 2, 4, 6, 8, 10, 11, and 12, 2 thermocouples are mounted, offset by 180°. The heating tube is fixed in the middle of the duct by the inlet and outlet flanges as well as by spacers made of the synthetic material TECASINT 1011. The sealing is made with the help of O-rings. The position of the spacers is at 855 mm, 1530 mm, 2200 mm, and 2870 mm, measured from the top of the heated length. The geometry of the spacers is illustrated in Figure 3.4. The spacers were axially fixed by means of two thin metal rings soldered on to the heating tube. Due to the material composition of the spacers as well as the O-rings, the heating tube is electrically insulated from the rest of the test section. However, the insulating flanges mentioned in subchapter 3.2.1 are also used in this test section setup to electrically insulate the test section from the rest of the facility in the event of a voltage flashover.

The positions of the pressure and temperature sensors at the inlet and outlet are indicated in Figure 3.3. Except for the respective pair of windows where the optical investigations take place, the test section is again thermally insulated with two layers of mineral wool of the same thickness as in test section 1.

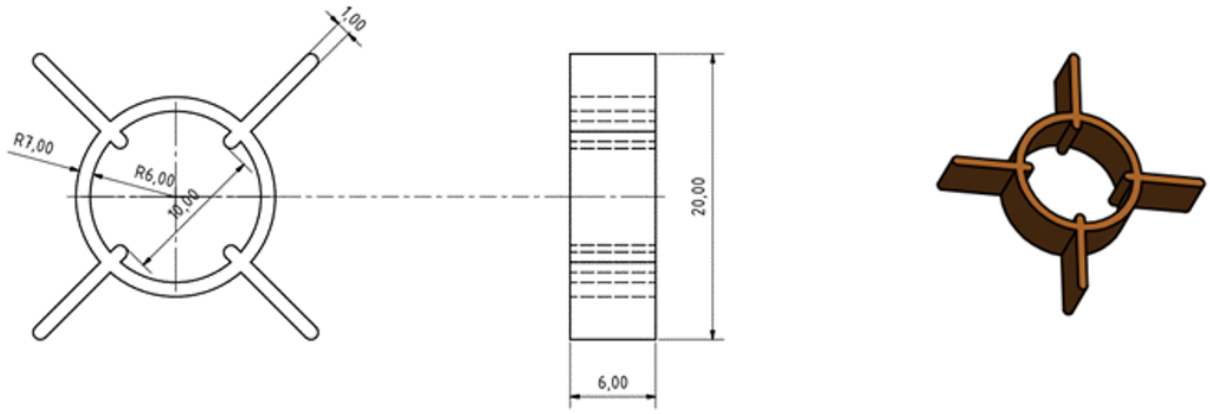


Figure 3.4: Geometry and design of the utilized spacer in test section 2

3.3 Properties of the Working Fluid R-134a

Freon R-134a, formally known as 1, 1, 1, 2 – Tetrafluoroethane, is a refrigerant that substituted R-12 as it has similar thermodynamic properties but with significantly less ozone depletion potential. It is widely used in refrigeration processes such as cooling machines, refrigerators, or air conditioners. In experimental facilities, it is used as modeling fluid for the above described reasons of reducing the costs of experimental set-up and operation (refer to chapter 2.4.1).
Some characteristic properties were retrieved from the „Reference Fluid Thermodynamic and Transport Properties Database“ (REFPROP) of the National Institute of Standards and Technology (NIST) (Lemmon et al. 2007).

- Chemical formula: CF_3CH_2F
- Normal Boiling point: -26.07 °C
- Critical pressure: 40.59 bar
- Critical temperature: 101.06 °C
- Critical density: 511.90 kg/m^3

Figure 3.5a) presents the vapor pressure curve including the critical point. The dotted line depicts the critical pressure while the critical point is marked with an x. All experiments carried out for this study were conducted at subcritical conditions. Below the saturation line, the fluid remains in vapor state while it is in liquid state above the saturation line. Furthermore, important fluid properties are depicted as a function of temperature for the entire pressure range of the conducted experiments in Figure 3.5b)-e). This includes the density, specific enthalpy, heat conductivity λ, and specific heat capacity c_p. The phase change from liquid state to vapor is illustrated with the dashed line.

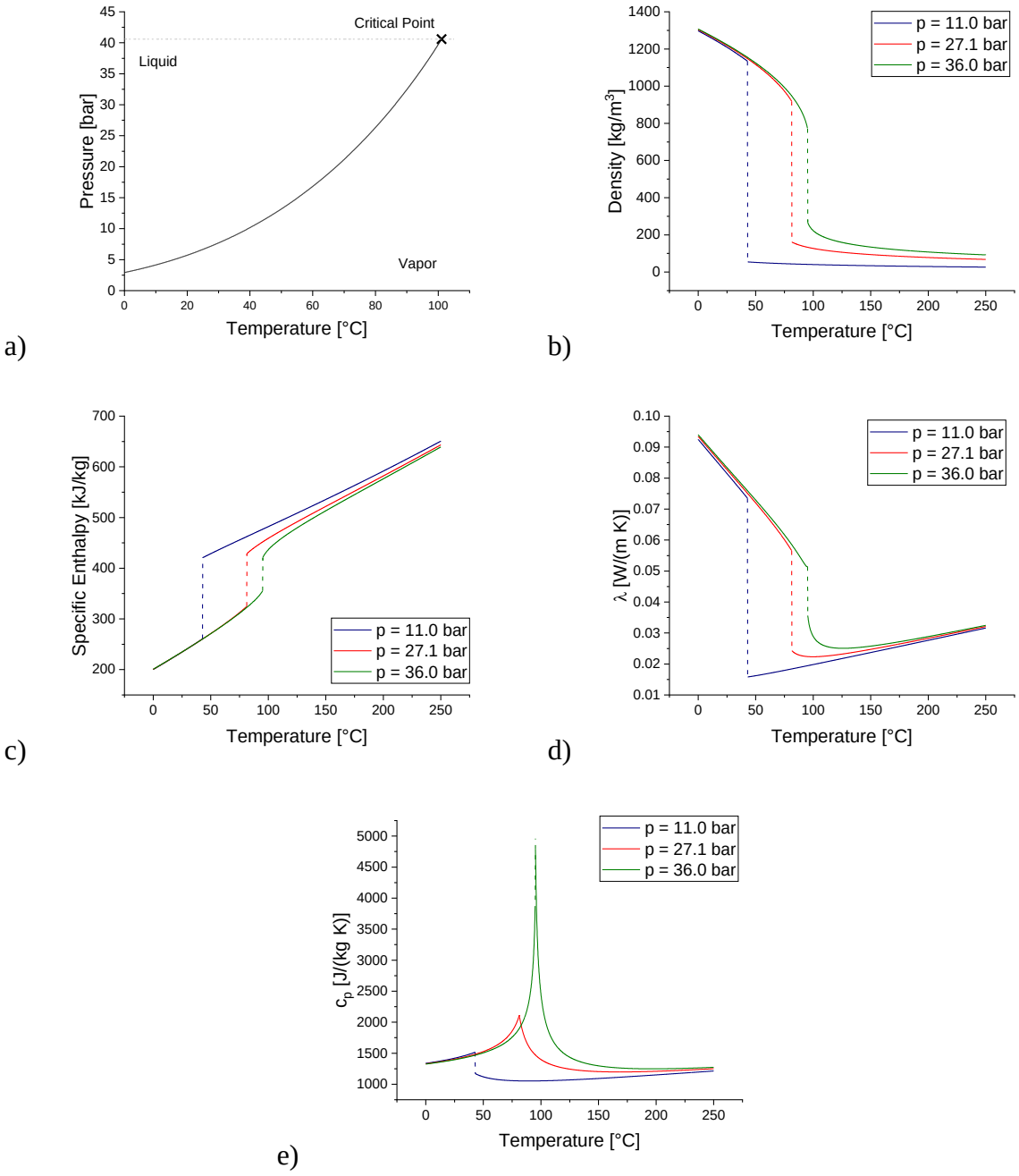


Figure 3.5: Fluid properties of R-134a with a) the vapor pressure curve, b) the density, c) the specific enthalpy, d) the heat conductivity, and e) the specific heat capacity

The properties are quite similar in liquid state. Density and thermal conductivity decrease in liquid state with increasing temperature, whereas enthalpy and specific heat capacity are increasing. Except for the specific heat capacity, the property change during the phase transition is less pronounced at higher pressures. While density and thermal conductivity drop during the phase change, the specific enthalpy increases for the entire pressure range. In all cases, the vapor properties approach a common asymptote with increasing temperature. The specific heat capacity shows a stronger dependence on the pressure. Figure 3.5e) illustrates how for the first two depicted pressures, the phase change leads to a small drop followed by a decrease in value

and an asymptotic approach. However, at the highest pressure the specific heat capacity is strongly increased following the phase change and continues to decrease directly after before it approaches the same asymptote.

According to (Preisegger and Henrici 1992), R-134a shows a good compatibility with a broad range of materials. No corrosion tracers were found when testing the compatibility with stainless steel and different elastomers which is crucial in the conducted experiments. They also mentioned the thermal stability which was tested up to temperatures of 250 °C. (Dai et al. 2018) performed their own tests on different hydrofluorocarbons, stating that decomposition of R-134a starts at temperatures above 340 to 360 °C. However, to minimize the risk of decomposition, the admissible wall temperature in the experiments of this study was limited to approximately 260 °C.

3.4 Measurement Techniques

Different sensors and measurement devices were used throughout the present investigations to measure wall and fluid temperature, mass flow and pressure as well as for the optical analysis of the flow behavior. The applied conventional measurement devices are listed in the table below and are briefly described.

This subchapter concludes with the description of the optical measurement set-up, using high-speed camera for flow investigations and an optical fiber to measure the vapor temperature.

Table 3.1: List of the utilized conventional measurement devices

Measured Variable	Measurement Device	Manufacturer
Wall Temperature	Thermocouple Type T	Omega Engineering GmbH
	Thermocouple Type K	Reckmann GmbH
Fluid Temperature	Thermocouple Type T	Omega Engineering GmbH
	Resistance Thermometer PT100	WIKA Alexander Wiegand SE & Co. KG
Pressure	Pressure Sensor 8227-5100	burster Präzisionsmesstechnik GmbH & Co KG
Mass Flow	Coriolis Flow Meter	YOKOGAWA Deutschland GmbH

3.4.1 Conventional Measurement Devices

Wall Temperature Measurement

In the experimental investigations carried out, type T and type K thermocouples were used to measure the wall temperature. Type T thermocouples generally have a lower uncertainty tolerance than type K thermocouples.
Type SA1XL-TI-3M thermocouples from Omega Engineering GmbH were used in the tests with test section 1. These type T thermocouples are designed as foil thermometers and can thus be easily attached to the tube by means of a self-adhesive film. This self-adhesive film is silicone-based and reinforced with a layer of glass fiber of several µm thickness, which ensures electrical insulation. This is necessary because current flow at the thermocouple would falsify the measurement result. The thermocouples were additionally fixed with a specially designed adhesive tape, also from Omega since the wall temperatures exceed the permissible maximum temperatures for the self-adhesive effect. The attachment is displayed in Figure 3.6 and can also be seen in (Feuerstein 2019) who used the same set-up for supercritical experiments.

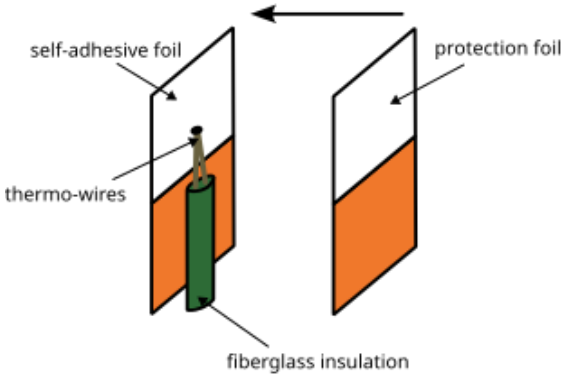
a)  b) 

Figure 3.6: a) Photo (source: (Feuerstein 2019)) and b) Schematic of a Type T self-adhesive thermocouple for wall temperature measurements (adapted from: (Feuerstein 2019))

Thermocouples of type 1R9-A050A07000K-11-Y from Reckmann GmbH were used for the wall temperature measurements of test section 2. They are designed as type K thermocouples. The reason for this is the fastening process of the thermocouples to the inner wall of the pipe. As described, the thermocouples sit on ceramic pads, which in turn are directly connected to the heating conductor. The temperatures during the necessary hard-soldering process exceed

the permissible temperatures for Type T thermocouples which made it necessary to use the less precise type K thermocouples.

Fluid Temperature Measurement

To measure the fluid temperature at the inlet and outlet of test section 1, thermocouples of the type TEK00X211027 from Tecsis GmbH were used. These thermocouples are carried out as type T and were slightly bent so that the measuring tip points into the flow. They were integrated into the primary loop via a thread connection in an SAE flange.
For the measurements in test section 2, miniature resistance thermometers of type T33-Z-P4 from WIKA Alexander Wiegand SE & Co. KG were used. With resistance thermometers, the temperature dependency of the electrical resistance of an electrical conductor is used to determine the temperature. The type used is designed as a Pt-100 model with 4-wire connection. The high measuring accuracy is counteracted by a design-related measuring inertia of approximately 4s due to the protection tube, which makes this type of temperature determination unsuitable for transient experiments.

Pressure Measurement

The static pressure over the test section was measured at the test section inlet and outlet using pressure sensors type 8227-5100 from burster Präzisionsmesstechnik GmbH & Co KG. They were, like the fluid temperature measurement sensors, integrated into the primary loop via the described SAE flange. They were calibrated upon delivery and before integration.

Mass Flow Measurement

A Coriolis flow meter was used to measure the mass flow in the primary loop. The integrated model is an RCUS34S-20TG90-0C6A-NN00-4-JA1/L005 from YOKOGAWA Deutschland GmbH. The mass flow rates applied in the conducted experiments for this thesis were in the lower measurement range of the used model. However, the manufacturer guarantees a measurement uncertainty below 0.42% for the applied range.

Heating Power Measurement

The applied heating power was calculated by multiplying voltage and current. While the current was directly measured at the transformer, the voltage was taken from two wires which were connected to the heating tube at the current connectors and were read in one of the FLUKE 2640A data logger.

3.4.2 Measurement of Vapor Temperature

The vapor temperature measurements in this thesis were carried out by using a specifically designed glass fiber. This represents a new approach in the attempt to measure the vapor temperature under PDO conditions and also offers the possibility of determining an axial vapor temperature profile. Despite the application of different techniques, most experiments so far were conducted using a modified thermocouple and no comparable approach is known to the author. The specifics of the set-up used in the present experiments are provided in this section. A summary of the general measurement principle can be found in Appendix A.

In the conducted experiments, a glass fiber manufactured by the FBGS Technologies GmbH was used. The interrogator FBG-Scan 904 was chosen as measurement device. It is based on the spectrometer technology. The applied fiber has an outer cladding diameter of 125 µm and an Ormocer-T coating, leading to an overall diameter of 195 µm. The overall length of the fiber is 2600 mm. A total of 60 Bragg gratings for temperature measurement purposes were impressed into the fiber core within the last 600 mm of the fiber length, so that the axial distance between the single grating centers is 10 mm. The width of an individual Bragg grating is 8 mm. The Fiber-Bragg-Gratings are designed as so-called Draw Tower Gratings (DTG) which are manufactured in a process that combines the drawing of the fiber and the inscription of the gratings before the coating is applied. This increases the fiber strength (see (FBGS 2020)).

In the set-up, the fiber was not directly inserted into the flow channel since the flow conditions would cause additional strain on the fiber. Instead, a special window design was constructed that allowed the insertion of a seamless drawn capillary made of stainless steel (1.4301) with an inner and outer diameter of 0.5 and 1 mm, respectively. The capillary was engaged into the channel vertically and therefore parallel to the heating tube at the top window and was fixed via a blind hole in a corresponding window (see Figure 3.7) to assure as little flow caused vibrations on the capillary and therefore on the fiber as possible. The axial length of the capillary in the flow channel is about 121 mm while the radial distance to the heating tube in the channel center lies at approximately 2.5 mm. With this set-up, 10 strain-free measurement points could be installed in the flow channel with the fiber inserted into the capillary. The positions of the individual measurement points cover an axial distance of 17 to 107 mm from the end of the heated length. The placement of the fiber in the capillary has the advantage that the error susceptibility of the measurement due to the absence of stress and the avoidance of moisture differences could be reduced (compare (Lomperski et al. 2015)). However, this is at the expense of the fiber response time. The temperature measurement uncertainty is given by the manufacturer at ± 1 °C.

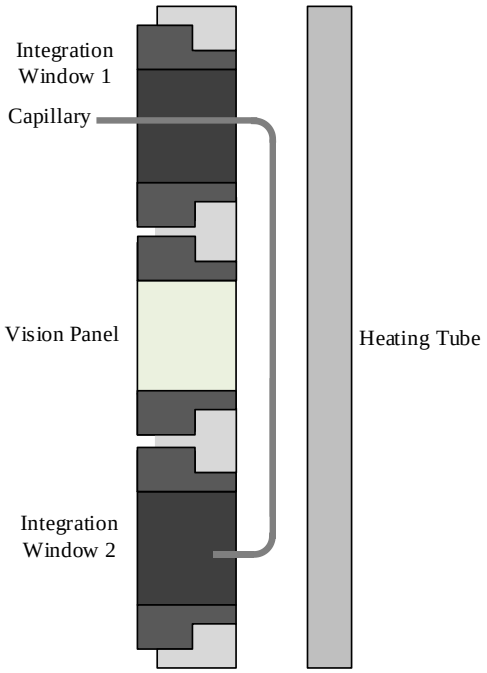


Figure 3.7: Schematic of the capillary integration into the flow channel

3.4.3 Optical Measurement of Droplet Behavior

The flow investigations were carried out using a high-speed camera. The camera chosen for the experiments was a Sprinter-FHD from the CamRecord Sprinter Series manufactured by the Optronis GmbH. This model reaches frame rates of 20 – 1980 frames per second (fps) at the maximum sensor resolution of 1920 x 1080 pixel (px). The minimum exposure time without using pulsed background light is 4 µs. The sensor diagonal lies at 22 mm. In the conducted experiments, a resolution of 1280 x 800 px at a frame rate of 2487 fps was chosen. The macro lens Sigma 150 mm f2.8 APO Macro EX DG OS HSM was added to the set-up.
The top window pair was left uninsulated in order to take camera shots and apply enough light to properly illuminate the channel. The camera was directly pointed at the windows. 3 LED light sources (model "MultiLED QT" from the GSVitec GmbH) were used for the channel illumination. In this case they are carried out as non-dimmable and non-pulsating light sources. The standard lens attachment with 30° was used. Figure 3.8 displays a top view schematic of the general set-up of the camera as well as of channel and light sources. 2 LEDs were installed on the opposite side of the camera. The third LED, which is shown here on the measurement equipment's side, was set up above the camera and was used to illuminate the heating tube directly. A simultaneous illumination of channel and heating tube could not be achieved with the test section configuration. Furthermore, due to the geometrical boundaries a comprehensive investigation of droplet behavior in the direct vicinity of the heating tube was impossible with the illumination set-up. To avoid overexposure and achieve a uniform background illumination, two glass panes were installed directly on the window on the opposite channel side of the camera. The first one was plexiglass gs white WH1010 with a thickness of 3 mm that minimized the effect of single LED light sources of the panels through light refraction. For the second one,

a Stopsol Supersilver grey pane was chosen. Both panes were manufactured by the Theodor Schmid GmbH.
The exact position of the light sources was determined in different tests by considering light refraction and scattering. Both panels on the opposite side of the camera had an incidence angle of approximately 30° on the two glass panes on the channel window whereas this angle was about 45° for the light source above the camera. Obviously, no glass panes were used on this channel side.

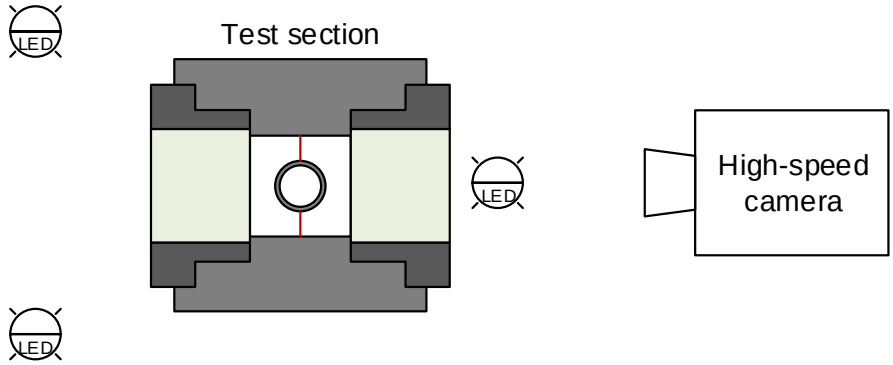


Figure 3.8: Arrangement of the experimental set-up of high-speed camera and illumination sources, including the measurement plane (marked in red)

3.5 Test Procedure and Data Analysis

The following subchapter describes the experimental process. Hereafter, the parameter range of the conducted experiments is displayed, and important analysis parameters and their derivation are introduced. The chapter continues with the description of the heat balance experiments to determine the quality of the measurement set-up. It closes with the description of the uncertainty analysis.

3.5.1 Experimental Procedure

The experiments in both test sections were carried out with a vertical upward flow of R-134a. In the experiments, the system pressure, inlet enthalpy at the test section via the inlet temperature, mass flux, and heat flux are the controllable parameters. For the conducted test runs, the system pressure as well as inlet subcooling and mass flux were set constant. Subsequently, the heat flux was increased stepwise. Dryout first occurs at the top of the heated length when CHF is reached. Once dryout appears, all parameters were kept constant and the first measurement at steady-state conditions was taken. It should be noted that the critical heat flux was only approached roughly in the experiments carried out for this thesis and no specific investigation of CHF or the point of dryout was undertaken.
To investigate the PDO heat transfer, the heat flux was increased beyond CHF. In the case of test section 1, this was carried out in pre-defined steps of 5 and 10 kW/m^2 (at high mass fluxes),

respectively, which moves the point of dryout further upstream. After each step and reaching steady-state again, a new record of the measured parameters was taken. The increase of heat flux was limited by the discussed admissible wall temperature.

Additionally, in test section 1 the rewetting behavior was investigated too. For those investigations, after reaching the highest admissible wall temperature, the heating power was decreased in the same steps as it was increased before, and steady-state measurements were taken until boiling crisis disappeared or the heated surface is completely rewetted again.

Each measurement took 60 seconds with a measurement frequency of 2 Hz to account for parameter fluctuations. During the measurements the controllable parameters were kept within defined tolerances. In fact, the mass flux was kept within 2% of the desired value, while the pressure had to be within ± 0.3 bar. Heat flux and inlet temperature were kept within ± 0.5 kW/m^2 and ± 0.5 °C, respectively. Those tolerance limits originated from experimental experiences with the test facility rather than being based on a scientific background.

The steady-state experiments with test section 2 followed the same pattern as with test section 1. However, the focus in those experiments was set on the optical investigations of the PDO flow pattern as well as the investigation of thermal non-equilibrium. The high-speed camera was positioned in a way that the measurement plane was in the center between heating tube and channel wall (as indicated by the measurement plane in Figure 3.8). The optical fiber was integrated into the channel via a capillary at the top window as described in chapter 3.4.2.

The frame rate for the high-speed camera investigations was set to 2487 fps. Each take included 1000 frames which equals a recording time of approximately 0.4 s. The corresponding 60 s parameter measurements were carried out simultaneously. The camera shots were taken at the top window pair.

The vapor temperature measurements with the optical fiber lasted between 60 s and 45 min for sporadic long-term measurements. In those measurements also, the system parameters were recorded simultaneously.

3.5.2 Experimental Parameter Range

The parameter range of the conducted experiments with both test sections are compiled in Table 3.2 to Table 3.5.

Two different approaches were taken to derive the test matrix for test section 1. Typical boiling water and pressurized water reactor pressure conditions should be covered which lie at about 70 bar and 157 bar in water according to (Ziegler and Allelein 2013). The pressures in R-134a were derived based on hydrodynamic equality regarding the density ratio of liquid and vapor. The second approach was to set conditions that can be used to evaluate fluid-to-fluid scaling methods by (Nemitallah and El-Nakla 2013) and (Yu 2019). Most of the parameters in that second approach were derived from the Becker data base (Becker et al. 1983).

Due to facility related limitations, certain parameter combinations are not possible to execute at higher pressure conditions, especially regarding selected subcooling stages at the test section

entrance. Therefore, the inlet subcooling was enhanced at those pressures. In all test runs, the heat flux was set and subsequently increased and decreased following the described process. First and last measurement point in the heating and cooling process were taken just before CHF at nucleate boiling conditions. The range of the steady-state experiments in test section 1 is presented in Table 3.2.

Table 3.2: Experimental parameters of the steady-state PDO test series (test section 1)

Pressure [bar]	**Inlet Subcooling** [°C]	**Mass Flux** [kg/(m^{2}s)]	**Heat Flux** [kW/m^2]
11.2	3.7	330 - 1980	43 - 105
	5	300 - 2000	35 - 135
	10	300 - 2000	40 - 140
16.0	5	1500	55 - 110
	10	300 - 1500	25 - 120
19.5	7	1775	64 - 101
27.1	10	500 - 2000	70 - 105
	20	300 - 2000	20 - 105
28.0	10	500 - 1500	30 - 85
	15	300	20 - 50

Furthermore, reproducibility experiments were carried out for selected parameter combinations to assure the quality of the conducted experiments. The parameter range of those test runs is compiled in Table 3.3. They cover the full pressure and a broad mass flux range.

Table 3.3: Experimental parameters of the steady-state reproducibility tests of the PDO test series (test section 1)

Pressure [bar]	**Inlet Subcooling** [°C]	**Mass Flux** [kg/(m^{2}s)]	**Heat Flux** [kW/m^2]
11.2	10	500, 1500	55 - 140
16.0	10	900, 1500	50 - 115
28.0	10	1100, 1500	40 - 85

The first steady-state test series with test section 2 was conducted for flow pattern behavior investigations using the high-speed camera. A broad pressure range could be covered with the experimental set-up. The inlet subcooling of T = 17 °C was originally chosen so that it was achievable at all different pressure stages. An additional subcooling step was added at pressures of p = 15 and 20 bar to investigate the influence of the inlet enthalpy.

Different tests at different mass fluxes were run before the actual test series. It was discovered that optical investigations of the dispersed flow were solely possible at very low mass fluxes due to the otherwise too high amount of liquid in the flow channel, especially in the areas close to the windows. A significant variation of mass flux and therefore the investigation of its influence was thus impossible. Hence, a mass flux of G = 66 kg/(m^{2}s) was chosen as this specific mass flux enables PDO investigations at different parameter variations and simultaneously provides enough flow stability for quasi steady-state experiments.

Pre-tests revealed that the sudden temperature rise at the onset of dryout is significantly more pronounced in test section 2 compared to test section 1. The actual test runs confirmed this observation. Due to the temperature limit given by R-134a in combination with partially significant flow instabilities, a distinctive variation of heat flux was impossible in the conducted experiments. The heat flux range was therefore very limited in all the test runs with test section 2.

This also prevented the conduction of rewetting experiments with the second test section. The parameter range of the first test series with test section 2 is compiled in Table 3.4.

Table 3.4: Experimental parameters of the first steady-state PDO test series for optical flow behavior investigations with the high-speed camera (test section 2)

Pressure [bar]	**Inlet Subcooling** [°C]	**Mass Flux** [kg/(m^{2}s)]	**Heat Flux** [kW/m^2]
11	17	66	48
15	12	66	43
	17	66	45
20	12	66	37 - 41
	17	66	43
27.1	17	66	38, 40
30	17	66	33, 37

Table 3.5 collects the parameters of the second test series with test section 2. This test series was carried out to determine the vapor temperature with the optical fiber.
For this test series, the aforementioned canned motor pump was used. Due to different pump characteristics, especially certain low subcooling stages could not be reached. In the second set of experiments conducted with test section 2, the specified permissible maximum temperature of the heated wall was slightly elevated from around 240 °C to improve the conditions for the measurement of vapor temperatures. Furthermore, the fiber capillary was implemented into the channel. As a consequence of this change of settings, an overall more consistent PDO regime was achieved over a longer axial distance along the heated length.
The pressure range of test section 1 was extended up to p = 36 bar and further values of q were tested within the limited applicable range. However, only in the parameter range given in Table 3.5, reliable vapor temperature measurements were observed.

Table 3.5: Experimental parameters of the second steady-state PDO test series for vapor temperature measurements (test section 2)

Pressure [bar]	**Inlet Subcooling** [°C]	**Mass Flux** [kg/(m^{2}s)]	**Heat Flux** [kW/m^2]
15	12 - 18	66	43, 44
20	14 - 18	66	40 - 44
27.1	18	66	42

3.5.3 Test Data Reduction

The following sections summarize the fundamental aspects of the analysis of the experimental investigations. Several calculations need fluid properties as input variables. Those properties were obtained from the NIST data base.

Heat Transfer Coefficient

The heat transfer coefficient was introduced already in chapter 2.1. It is obvious from the definition below that high heat fluxes in combination with small heat transfer coefficients lead to a high temperature difference. This aspect is crucial regarding the already mentioned wall temperature limitations.

$$\alpha = \frac{\dot{q}}{T_W(x) - T_{fl}(x)} \quad \left[\frac{W}{m^2\,K}\right] \tag{3.1}$$

with the heat flux $\dot{q}$ as well as the inner wall and fluid temperature, T_W and T_{fl}, in both cases at the axial position x. The calculation of wall and fluid temperature will be explained in the following sections.
The heat flux $\dot{q}$ describes the ratio of applied heating power and wetted surface:

$$\dot{q} = \frac{\dot{Q}}{A} \quad \left[\frac{W}{m^2}\right] \tag{3.2}$$

The heat flow $\dot{Q}$ on the other hand can be described as the difference of heating power and heat loss:

$$\dot{Q} = UI - \dot{Q}_L \quad [W] \tag{3.3}$$

The area of the inner tube wall is given by:

$$A = \pi L_{he} D_i \quad [m^2] \tag{3.4}$$

For the outer tube wall, necessary for the calculations with test section 2, the area is calculated as follows:

$$A = \pi L_{he} D_o \quad [m^2] \tag{3.5}$$

In both cases, L_{he} stands for the heated length of the tube.

Fluid Temperature

Since the fixed thermocouples solely measure wall temperature, the fluid temperature corresponding to the thermocouple measurement points has to be deduced from the NIST data base.
For the derivation, the measurement position and the enthalpy at this position must be known as well as the average pressure, which is determined by the conducted measurements. The simplified first law of thermodynamics results in the following form for the enthalpy:

$$h(x) = h_{in} + x \frac{\dot{Q}}{\dot{m}} \quad \left[\frac{J}{kg}\right] \tag{3.6}$$

with the relative length:

$$x = \frac{L}{L_{he}} \tag{3.7}$$

L marks the axial distance from the measurement point to the beginning of the heated length. It should be noted that the determined fluid temperature is the bulk temperature.

Inner Wall Temperature Test Section 1

In test section 1, the thermocouples solely measure the outer wall temperature along the tube. As the heat transfer from wall to fluid takes place at the inner wall, the inner wall temperature is of elementary significance.
For the simplified case of heat conduction along just one space coordinate, the following equation for the heated tube can be derived (Baehr and Stephan 2016):

$$\frac{d^2T}{dr^2} + \frac{1}{r}\frac{dT}{dr} + \frac{\dot{q}_V}{\lambda} = 0 \tag{3.8}$$

with the radius r, the heat conduction coefficient λ and the volumetric heat flux $\dot{q}_V$. For tube geometry, the latter is defined as:

$$\dot{q}_V = \frac{UI}{\frac{\pi}{4} L_{he} (D_o^2 - D_i^2)} \tag{3.9}$$

The general solution of the differential equation is given by:

$$\mathrm{T} = c_1 \ln r + c_2 - \frac{\dot{q}_V}{4\,\lambda} r^2 \tag{3.10}$$

with the constants c_1 and c_2.

This equation can be solved using two boundary conditions:

- heat loss flux at the outer wall of the tube:

$$-\lambda \left.\frac{dT}{dr}\right|_{\mathrm{r=r}_o} = \dot{q}_{loss} \tag{3.11}$$

- temperature at the outer wall of the tube:

$$\mathrm{T(r = r}_o) = T_{W,o} \tag{3.12}$$

The heat loss flux $\dot{q}_{loss}$ is defined as the ratio of heat loss at the outer tube wall and the outer tube surface:

$$\dot{q}_{\text{loss}} = \frac{\dot{Q}_L}{\pi\, L_{he}\, D_o} \tag{3.13}$$

Eventually, the inner wall temperature can be determined using the above equations and is defined as follows:

$$\mathrm{T_{W,i}} = T_{W,o} - \left(\frac{\dot{q}_V}{16\,\lambda}\right)(D_i^2 - D_o^2) + \frac{D_o}{2\,\lambda}\left[\left(\frac{\dot{q}_V\, D_o}{4} - \dot{q}_{loss}\right)\ln\left(\frac{D_i}{D_o}\right)\right] \tag{3.14}$$

Outer Wall Temperature Test Section 2

Contrary to test section 1, the inner wall temperature is measured in test section 2, using type - K thermocouples. However, since the heat transfer from heated surface to fluid takes place at the outer wall in this set-up, the heat conduction trough the heating tube needs to be calculated in order to determine the outer wall temperature. The inside of the tube is assumed to be adiabatic which provides the following two boundary conditions:

- no heat flow at the inside of the tube:

$$-\lambda \left.\frac{dT}{dr}\right|_{\mathrm{r=r}_i} = 0 \tag{3.15}$$

- inner wall temperature of the tube:

$$\mathrm{T(r = r}_i) = T_{W,i} \tag{3.16}$$

The solution to the general form of equation (3.10), solved for the outer wall temperature is given by:

$$\mathrm{T_{W,o}} = T_{W,i} + \left(\frac{\dot{q}_V}{8\,\lambda}\right) D_i^2 \left(\ln\left(\frac{D_o}{D_i}\right) + \frac{1}{2}\right) - \left(\frac{\dot{q}_V}{16\,\lambda}\right) D_o^2 \tag{3.17}$$

Heat Loss of Test Section 1

The heat loss in that set-up is driven by the temperature difference between test section and ambience. To determine the heat loss over the test section, the test section was evacuated which means that vacuum conditions were in place. This measure was taken to guarantee that no heat is lost to the fluid but the applied heat is transferred to the environment. The test section was thermally insulated during the measurements to achieve the same boundary conditions as in the actual test runs. Subsequently, small heating capacities are applied and wall temperature measurements were taken when steady-state was reached. An equilibrium state is reached between heat input and output. The wall temperature is averaged over the entire test section. The top thermocouple was excluded in those investigations since it is affected by the upper current connector which has a cooling effect on the named thermocouple through axial heat conduction. Overall, 4 measurement points were taken that can be correlated to the following heat loss equation:

$$\dot{Q}_L = 0.00097\,\Delta T^2 + 0.29\,\Delta T + 0.13 \quad [W] \tag{3.18}$$

where ΔT describes the temperature difference from outer wall and ambience.

Heat Loss of Test Section 2

The heat loss measurements in test section 2 were conducted with a slowly flowing, one-phase liquid fluid. The test section was thermally insulated as well except for the investigation window in the actual test runs to simulate once more the actual test conditions. The mass flux was fixed at G = 66 kg/(m^{2}s). The inlet enthalpy was stepwise increased by slowly increasing the temperature in the pre-heater. No additional electrical power was employed in the test section. The difference of inlet and outlet temperature had to be sufficiently big to compensate for measurement uncertainties. 3 measurement points could be achieved in this way.
Taking the origin into account, a linear function could be fitted using those 4 points. This function later on can be extrapolated to the actual PDO measurement conditions. It is given as follows:

$$\dot{Q}_L = 3.2229\,\Delta T + 6.2725 \quad [W] \tag{3.19}$$

The temperature difference is given by the difference of fluid and ambient temperature as the heat is lost via the flow channel and not the heating tube in test section 2.
Since the thermocouples are fixed in irregular axial positions, the tube was virtually divided into smaller sections from one thermocouple level to another. The heat loss was calculated for

every section separately and eventually summed up to the overall heat loss over the entire test section. The inlet temperature was taken for the calculation of the entrance section while the fluid temperature at the last thermocouple was used for the calculation of the heat loss at the exit section of the square channel. The entire heat loss calculation was processed iteratively since the heat loss needs to be known for the calculation of the fluid temperature.

3.5.4 Heat Balance Measurements

Heat balance measurements are employed to determine the quality of the measurement sensors and the experimental set-up and to detect and prevent possible failures of the general measurement set-up. They were carried out as steady-state test runs with the freon being in a single-phase liquid state. The measurements aimed at comparing the measured and the calculated enthalpy difference between inlet and outlet and determine the deviation.
Using the NIST data base, inlet and outlet enthalpy can be determined, when inlet and outlet pressure and temperature are known. The measured enthalpy difference is described by the following equation:

$$\Delta h_{meas} = h_{out} - h_{in} \tag{3.20}$$

The calculated enthalpy difference on the other hand is derived using the simplified first law of thermodynamics and is given in equation (3.21). Resolved for the enthalpy difference, the following expression is given:

$$\Delta h_{calc} = \frac{UI - \dot{Q}_L}{\dot{m}} \tag{3.21}$$

Considering the relation:

$$\Delta h_{rel} = \frac{\Delta h_{calc} - \Delta h_{meas}}{\Delta h_{calc}} \cdot 100 \tag{3.22}$$

the relative enthalpy deviation between measurement and calculation is determined in %.

Those experiments were carried out 3 times on different days with test section 1 and another time with the set-up of test section 2. The used parameters as well as the deviation region are presented in the tables stated below. The average deviations for test section 1 were 1.38%, 1.04% and 2.19%. Equation (3.21) illustrates that the calculated enthalpy difference depends on the applied heat as well as the mass flux. No noticeable trend regarding the dependency on

one of those parameters was observed. For test section 2, the average deviation lay at 1.24%. It was slightly higher at the lowest mass flux with an average deviation of 2.6%. However, also with this test section, a general trend was not observable.

Table 3.6: Parameter and deviation range of the heat balance experiments with test section 1

p [bar]	T_{in} [°C]	G [kg/(m²s)]	q [W/m²]	Δh_{rel} [%]
38	33, 35	300 - 3000	5 - 117	-4.59 - 7.44

Table 3.7: Parameter and deviation range of the heat balance experiments with test section 2

p [bar]	T_{in} [°C]	G [kg/(m²s)]	q [W/m²]	Δh_{rel} [%]
38	31	66 - 244	5 - 19	-0.58 - 3.94

3.5.5 Uncertainty Analysis

This chapter is subdivided into two main parts. First, a general description of the uncertainty analysis procedure is provided. This includes the manufacturing uncertainties of the used sensors as well as the geometrical uncertainties, all provided by the manufacturers. Subsequently, the results of the uncertainty analysis in both test sections, including both, conventional parameters as well as optical investigations are presented.

3.5.5.1 General Uncertainty Analysis Procedure

The table below lists the uncertainties of measurement sensors and the test section geometries. They were provided by the manufacturers or derived by taking the calibration data.

Table 3.8: Measurement and manufacturing uncertainties of the used sensors and geometrical parameters

Parameter	Uncertainty Test Section 1	Uncertainty Test Section 2
T_{in}, T_{out}	max(0.4%, 0.5 °C)	±(0.15 + 0.002 · T)
T_W	max(0.4%, 0.5 °C)	max(0.4%, 1.5 °C)
T_{PH}, T_{am}	max(0.4%, 0.5 °C)	max(0.4%, 0.5 °C)
T_{fiber}	-	±1 °C
Data Logger T	0.5 °C	0.5 °C
p_{in}, p_{out}, p_{PH}	0.25%	0.25%
I	1.5%	1.5%
U	0.03%	0.03%
Mass Flow	0.15 - 0.3%	0.15 - 0.3%
D_i (tube)	5%	0.4%
D_o (tube)	0.03 mm	0.08 mm
L_{he} (tube)	0.5 mm	0.5 mm
L_i (channel)	-	max. 0.82 mm
L_o (channel)	-	0.3 mm
L (channel)	-	1.2 mm

The uncertainty analysis used in this thesis is based on the processes described in the master's thesis of Coelho Silva (Coelho Silva 2015) and the bachelor's thesis of Gao (Gao 2017), both of which were carried out at the IATF. (Feuerstein 2019) adapted the proposed methods and adjusted it to test section 1. For the experiments carried out for this thesis, the methods were further adjusted by the author.

The heat transfer coefficient is calculated stepwise. Therefore, an error propagation analysis needs to be carried out, of which the stepwise solutions of the different variables serve as input values for the actual uncertainty analysis.

A sensitivity analysis determines the sensitivity of each single variable on the overall uncertainty of the investigated parameter, described by the function f, for every selected data point. The sensitivity is calculated by partial derivation of the function f. It is given in the

uncertainty calculation below by $\frac{\delta f}{\delta P_i}$, with P_i being the input variable and f being the known function to describe the investigated parameter. Multiplied with the standard deviation of each variable, the uncertainty regarding the investigated parameter of every single data point is derived.

$$\sigma_f^2 = \sum_{i=1}^{n} \left(\frac{\delta f}{\delta P_i} \sigma_i \right)^2 \tag{3.23}$$

The analysis was carried out following the basic principle of sequential perturbation, described by (Moffat 1985). Following this procedure, a perturbation of 1% for the corresponding input variable is assumed in respect to the change of the result of the function f. The above equation is valid under the assumption that the input variables are independent from each other and follow a Gaussian distribution. The PDO data point selection criterion that is introduced in chapter 4.4 was applied.

3.5.5.2 **Results of the Uncertainty Analysis of Test Section 1**

The uncertainty of different parameters was determined utilizing the above described procedure and manufacturing uncertainties. For every parameter, the relative uncertainty was derived using the unvaried value as reference. The parameter's mean uncertainty across all data points was calculated as follows:

$$\mu = \frac{1}{N} \sum_{i=1}^{N} \sigma_{f\,i} \tag{3.24}$$

with μ being the mean value, N the total number of data points and $\sigma_{f\,i}$ the value of the single data point's uncertainty.

Besides the average value, the minimum and maximum values of the relative uncertainties were determined as well to provide the range in which the uncertainties lie.

The average uncertainty of the vapor quality lies at 2.8%. It ranges from a minimum of 1.6% up to a maximum of 5.1%.

The uncertainty for the wall temperature measurement is even smaller with a mean uncertainty of 0.7%. The uncertainty ranges from 0.6 to 1.7%, corresponding to an absolute maximum uncertainty of 1.5 °C.

The Nusselt number shows an average uncertainty of 2.4% with a minimum of 1.3% and a maximum of 20.3%. However, uncertainties above 10% are connected to the developing PDO region. Only 0.4% of the overall selected data points show a Nusselt number uncertainty higher than 10%.

Minimum and maximum uncertainty for the HTC are 1.9% and 4.7%, respectively. The mean uncertainty is denoted at 2.2%.

3.5.5.3 **Results of the Uncertainty Analysis of Test Section 2**

The investigations in test section 2 were focused on the optical flow behavior analysis under PDO conditions as well as the determination of the thermal non-equilibrium. In this subchapter, first the uncertainties of the accompanying conventional heat transfer parameters are provided. Subsequently, the uncertainties of the optical measurements with the high-speed camera system are presented.

Uncertainties of the Heat Transfer Parameters

The presented measurement uncertainty is given for the high-speed camera test runs as well as for the parameters corresponding to every single selected vapor temperature measurement point.
In this second test set-up, the uncertainties of the vapor quality were also small, reaching from 1.9% to 2.5% with a mean uncertainty of 2.1%.
The average uncertainty for the wall temperatures are at 1% and in the range of 0.8% to 1.3%.
The Nusselt number uncertainty ranges from 7.6% to 9.1% with an average value of 8%. These values are comparably high to the uncertainties encountered in the first test section. This can be attributed to the relatively high manufacturing uncertainty of the inner wall side length of the channel, as presented in Table 3.8.
Minimum and maximum HTC uncertainty for this second test series lie at 2.2% and 3.9%, respectively. The mean value is denoted as 3.2%.

Uncertainties of the Optical investigations

The calculation of the uncertainties of droplet size and droplet velocities are also conducted by error propagation. The experimental set-up and test conditions encountered in the experiments (please also refer to chapter 5.1.2) required relatively high shutter times. This resulted in some amount of motion blur that is more pronounced for higher velocities and has to be considered in the determination of the measurement uncertainty. With the number N of pixels per droplet, the droplet size is given. The corresponding uncertainty for locating the position is ±0.5 px, the additional motion blur depends on the different test runs and the velocities. This is expressed in the standard deviation σ_N. The uncertainty of the droplet diameter is therefore given as in Equation (3.26).

$$d = N \tag{3.25}$$

$$\sigma_d = \sigma_N \tag{3.26}$$

The velocity is calculated as follows:

$$v = \frac{\Delta x}{\Delta t} \tag{3.27}$$

with the difference in position Δx and the time between two frames Δt.
The uncertainty of time is extremely small for the utilized camera. With the error propagation and therefore neglection of the very small second term, the uncertainty for velocity is presented as follows:

$$\sigma_{\mathrm{v}} = \frac{1}{\Delta t}\sqrt{(\sigma_x)^2 + \left(\frac{\Delta x\ \sigma_t}{\Delta \mathrm{t}}\right)^2} = \frac{\sigma_x}{\Delta t} \tag{3.28}$$

Please note that the subscript v in this case is used to denote velocity in general and not specifically the vertical velocity. The standard deviation σ_x contains the uncertainties caused by position determination and motion blur.
The uncertainties are given for the average values of droplet size and velocity of each test run as those values are further used in the validation of prediction models. The originally measured values can be found in chapter 5.1 and Appendix C.

The droplet size shows uncertainties between 8.9% and 4.3% with an average uncertainty of 5.9%.
Vertical velocity uncertainties vary between 9.8% and a maximum of 17.1% for the highest pressure where the lowest average velocity was observed. The average value lies at 12.1%.
The horizontal velocity uncertainties lie between 21.0% and 38.5% for the absolute average velocities. The average uncertainty is 27.6%.

It becomes obvious that the uncertainties are comparatively high for the horizontal velocities. This is attributed to the nature of the uncertainty determination. Since the standard deviation is a fixed value, its significance is substantially higher when the original measurement value is small. Low velocities, present at especially the horizontal velocities, therefore encounter higher uncertainties. However, in this thesis, the lateral velocities will not be used to validate theoretical models.

4. Experimental Results and Discussion in the Tube Test Section

In this chapter, the results of the experimental tests with test section 1 are presented and discussed. The main results have been made public at the NUTHOS-12 conference (Köckert et al. 2018) and in the "International Journal of Advanced Nuclear Reactor Design and Technology" (Köckert et al. 2021). Both publications are used in part in the presentation of results in this chapter. My analysis has been supported in the framework of a master's thesis by (Kaiser 2018) that I supervised.

First, the general observations on the temperature distribution of the steady-state experiments are described, including the reproducibility of the experiments and general experimental anomalies. Second, the influence of heat flux, inlet subcooling, mass flux, and pressure on the temperature distribution is investigated. Subsequently, the results of the rewetting behavior investigations are discussed. This chapter concludes with the assessment of existing models from the literature, as introduced in chapter 2.5.2 and shown in Appendix B.

It should be noted that characteristic examples of the respective observations are shown throughout the chapter. However, these examples may not necessarily reflect the same experimental conditions.

4.1 General Observations Regarding the Post-Dryout Heat Transfer in Steady-State Experiments

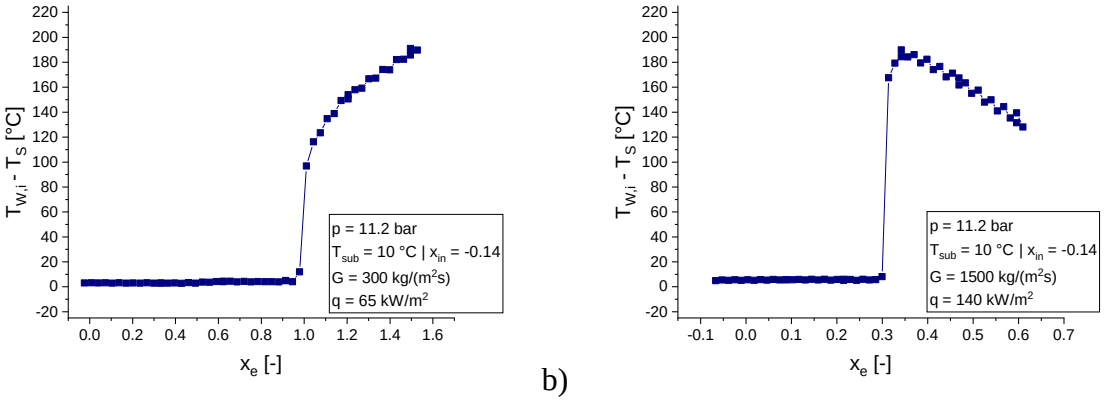
Two characteristic temperature distributions were identified in the conducted tube experiments. They are presented and discussed in the next section. Furthermore, the results of the reproducibility experiments are shown and certain irregularities in the experiments with test section 1 are discussed.

4.1.1 Temperature Distribution

The analysis of the steady-state experiments shows two characteristic temperature distributions in the post-dryout region, which depend significantly on mass flux and heat flux. These two temperature distributions are illustrated in Figure 4.1a) and b). The diagrams show the temperature difference of inner wall and saturation temperature over the equilibrium vapor quality. This is also the form of representation that will be mainly chosen in the coming subchapters. Negative vapor qualities correspond to subcooled liquid conditions, whereas vapor qualities > 1 mark the superheated vapor state according to the assumption of thermal equilibrium.

The fluid enters the test section subcooled. The subcooling stages can be taken from the test matrices in chapter 3.5.2. The point of dryout is characterized by a sharp rise in temperature,

which occurs as a result of the deteriorated heat transfer caused by the flow regime change. As discussed before, the associated vapor quality is called critical vapor quality.
The first typical temperature distribution (see Figure 4.1a)) is characterized by a degressive but steady temperature increase after the sudden and strong temperature rise at the dryout point. Thus, as the vapor quality increases, the wall temperature in the post-dryout region continues to rise steadily. This kind of distribution is typical for small mass flux and low heat fluxes.



a) b)

Figure 4.1: Characteristic PDO temperature distribution at a) small mass flux and heat fluxes, b) high mass and heat fluxes (source: (Köckert et al. 2021))

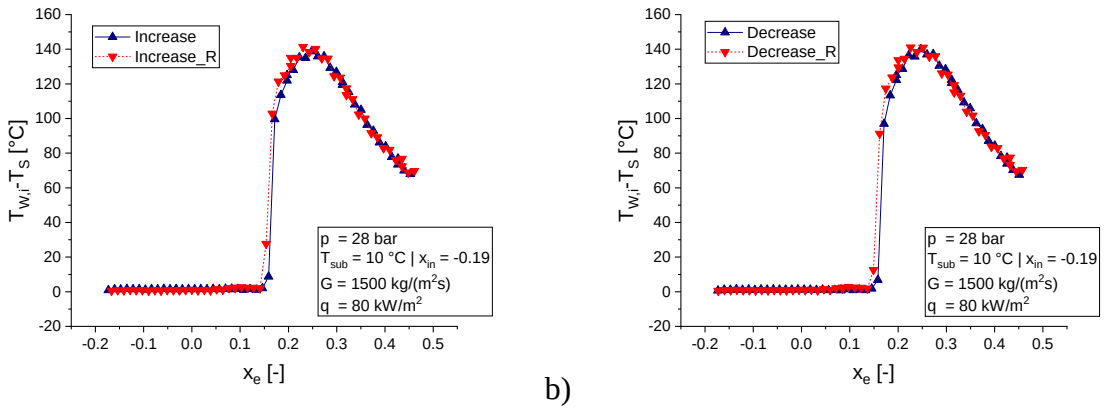
Figure 4.1b), on the other hand, shows the second characteristic temperature distribution, which can be observed at high mass and heat fluxes. After the sudden temperature rise as a result of the dryout, the wall temperature initially continues to rise, although the slope is lower than at the dryout point. After reaching a local maximum, the wall temperature decreases again as the vapor quality increases. Other experimental studies describe the wall temperature behavior at vapor qualities > 1 (including (Becker et al. 1983) and (Nishikawa et al. 1983)), as mentioned in chapter 2.3.2. In this case, the wall temperature increases again with further increasing vapor quality. This type of temperature distribution is also well described in the literature (including (Groeneveld 1975) and (v. d. VDI e.V. 2013)). Near the dryout point, the substantial part of the heat distributed by the wall is used to superheat the steam. At a certain distance from dryout, the fraction of heat transferred from vapor to droplets increases, leading to a higher evaporation rate and thus to a higher steam velocity. In succession, this leads to a lower wall temperature increase due to better heat removal or even to a decrease in wall temperature, depending on the flow conditions. The temperature decrease at high mass flux can be explained by the lower equilibrium vapor quality, which leads to an increased evaporation rate and thus greater vapor acceleration in the post-dryout region. However, at a certain point the evaporation rate decreases due to the continuously decreasing droplet surface area, leading to a steadily increasing vapor superheat and thus to a wall temperature increase above a certain vapor quality

(x = approximately 1). Due to the described limitation of the wall temperatures, those vapor qualities could not be reached in the conducted experiments with high mass fluxes.

As described in the literature review, the characteristic temperature distributions could be confirmed for different fluids by data in the literature (among others (Bennett et al. 1967), (Schnittger 1982), (Becker et al. 1983), or (Nishikawa et al. 1983)). They also confirm the assumptions in the literature that as the mass flux increases, the thermal non-equilibrium decreases ((Groeneveld 1975) or (Groeneveld and Delorme 1976)). The increase of the mass flux leads to more droplet entrainment and more droplet break-up. Consequently, the total droplet surface area in the flow is increased, which leads to better heat transfer as a result of evaporation and, ultimately, to lower thermal non-equilibrium. In addition, the increased turbulence in the flow due to higher mass fluxes and therefore higher flow velocities augments the convective heat transfer in the PDO area and contributes to the lower thermal non-equilibrium.

4.1.2 Reproducibility of Experiments

With a time difference of several weeks, a subset of experiments was repeated to ensure the reproducibility of the experiments and the corresponding results. Table 3.3 comprises the parameters covered by the reproducibility tests.



a) b)

Figure 4.2: Example of a reproducibility test run of steady-state tests with test section 1 for a) the power increase process, b) the corresponding power decrease process

Figure 4.2 depicts a comparison of an original and its reproducibility test run. For better visibility, power increase mode and power decrease mode and their corresponding reproducibility tests are shown separately. The data points obtained during the increasing heat process are denoted as “Increase” whereas the corresponding data points in the decreasing heat process are named “Decrease”. The supplement R was added for the repeated test runs. As can be taken from the diagram, an overall good reproducibility was encountered in the experimental

results. Wall temperature and critical vapor quality showed an average deviation of 2% up to 6%.
However, it was noticeable that the critical vapor quality was slightly shifted to lower values in the reproducibility experiments. A possible explanation will be provided in the following subchapter.

4.1.3 Abnormalities in the Investigations

As briefly mentioned before, the top thermocouple is influenced by the upper current connector through axial heat conduction as it is placed just below the clamp. Usually, a cooling effect is recognizable, that is differently pronounced depending on the test parameters (compare Figure 4.1 and Figure 4.4). The influence was particularly strong under vacuum conditions for the heat loss experiments, so the last thermocouple was excluded from the calculation as mentioned before.
Chapter 4.1.2 presented the results of the reproducibility experiments and mentioned a slight shift of the critical vapor quality. In fact, (Feuerstein 2019) noted local heat transfer deviations in his supercritical flow experiments that were carried out around the same time, using the same test section. Therefore, the test section was cleaned regularly by pulling a tissue through the tube. This process showed that there was deposition material on the test section wall, as can be seen in Figure 4.3.



Figure 4.3: Deposition material on a tissue after cleaning of the test section (source: (Feuerstein 2019))

(Feuerstein 2019) cut the test section at different heights after finishing of all test runs and investigated the test section thoroughly. The tube showed a deposition layer along the heated length that grows thicker towards the top of the test section. An energy-dispersive X-ray spectroscopy proved the existence of elements such as sodium or potassium that are additives of hydraulic oil used in the pressurizer. Furthermore, an increase of carbon and fluorine was

detected that could stem from the refrigerant R-134a. Although impurities or oxygen in the facility could decrease the decomposition temperature of R-134a (Dai et al. 2018), it is more likely that the deposition is caused by a small leakage of hydraulic oil into the test loop as it already decomposes at temperatures of about 120 °C (FINKE MINERALÖLWERK GMBH 2020). The investigations could exclude changes in the thermo-physical properties of the refrigerant with high certainty. However, they showed that the surface roughness slightly smoothened with increasing deposition layer thickness. It is assumed that this slightly influences the flow behavior and therefore the heat transfer and might be the reason for the critical vapor quality shift.

Furthermore, the conducted experiments showed a certain regular zig zag pattern in the temperature distribution in both, PDO and single-phase test runs. It is recognizable e.g., in Figure 4.1 for PDO conditions. This can be attributed to a small eccentricity of the tube.

4.2 Parameter Influence on the Post-Dryout Heat Transfer

In the following subchapters, the influence of the input parameters on the temperature distribution in the PDO area is discussed. First, the results of inlet quality and heat flux variations are presented. Subsequently, the influence of mass flux and pressure will be discussed.

4.2.1 Inlet Vapor Quality

Different inlet temperatures lead to different inlet enthalpies and therefore vapor qualities. The inlet subcooling was varied in two stages over a pressure from p = 11.2 up to 27.1 bar for selected test runs covering the entire mass flux range. The difference in inlet subcooling ranged from 5 °C at low and medium pressures to 10 °C at high pressure for the comparable test runs as can be taken from chapter 3.5.2.

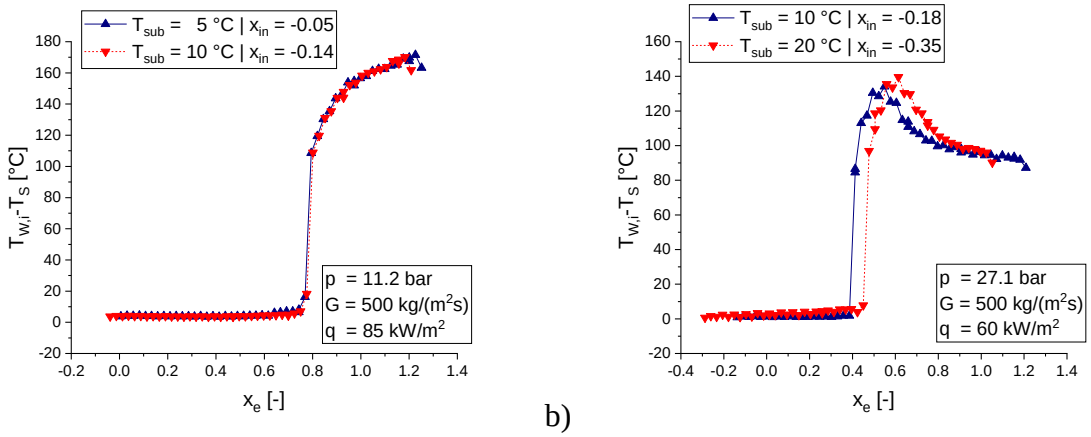


Figure 4.4: Influence of inlet subcooling on the PDO temperature distribution at a) low pressure and mass flux, b) high pressure and mass flux

The obtained data disclose that CHF increases with lower inlet qualities. This is unsurprising as more heat needs to be applied to evaporate the higher subcooled liquid to the point of dryout and beyond. However, in case of PDO conditions in comparable test runs with different inlet subcooling and therefore different inlet enthalpies, most of the tests show no differences at all along the entire test section. This is especially true for low pressure. An example is presented in Figure 4.4a). At higher pressures, certain test runs show smaller differences around the point of dryout and directly downstream of dryout. This is depicted in Figure 4.4b). This can be mainly attributed to differences in critical vapor quality between test runs of different inlet quality. These differences are usually significantly more pronounced at higher pressure except for the mass flux of G = 1000 kg/(m^{2}s). The reason is the lower latent heat at increased pressure. It is even more pronounced due to the higher differences between the inlet enthalpies at higher pressure. Regarding mass flux and heat flux, no clear dependency of the differences in critical quality was observable in the conducted experiments.

While there might exist differences around the point of dryout, the exemplary diagram proves that with increasing distance to the point of dryout, the temperature distributions follow the same asymptote for similar local vapor qualities. This is true for all test runs independent of pressure, mass flux and heat flux. (Nishikawa et al. 1983, 1986) observed the same tendency in their experiments for higher mass fluxes. However, at low mass fluxes they found significant differences in the temperature distributions for different inlet enthalpies which could not be observed in the present tests.

Based on the conducted experiments for this thesis, it can be concluded that the inlet quality has no influence on the heat transfer in the fully developed PDO region. While in certain test runs the point of dryout and the direct vicinity might be affected by inlet conditions, the PDO heat transfer further downstream depends solely on local vapor quality.

4.2.2 Heat Flux

The influence of the heat flux is shown in this subchapter as an example for high and low mass fluxes. For high mass fluxes (approximately from 1000 – 2000 kg/(m^{2}s) in the experiments performed), two effects can be observed: i) increasing heat flux leads to a stronger temperature increase at the point of dryout as well as to overall higher wall temperatures at similar local conditions, ii) increasing heat flux leads to a shift of the critical vapor quality towards smaller values. These two effects are exemplified in Figure 4.5a). For smaller mass fluxes, exemplarily represented in Figure 4.5b), the first phenomenon also occurs. However, the shift of the critical vapor quality could not be observed for low mass fluxes (in the conducted experiments G = 300 and 500 kg/(m^{2}s)).

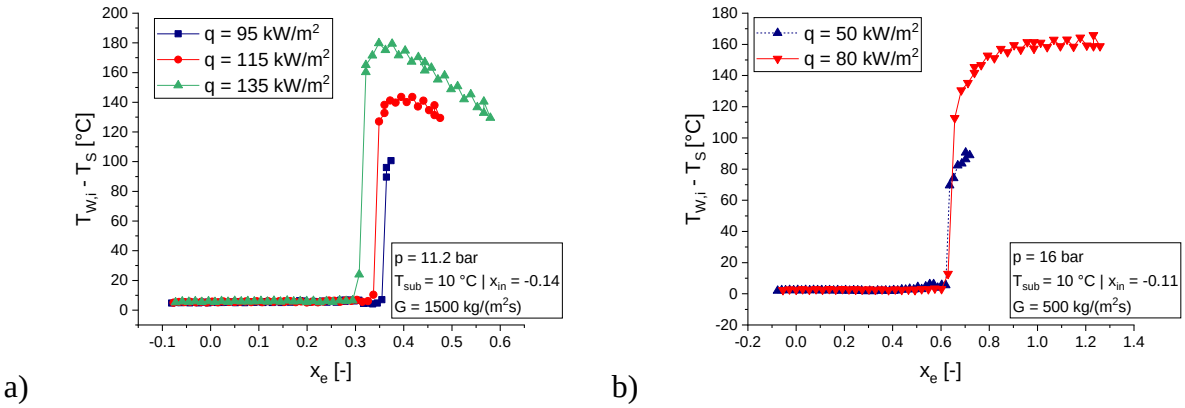


Figure 4.5: Influence of heat flux on the PDO temperature distribution at a) high mass fluxes, b) low mass fluxes (source: (Köckert et al. 2021))

Once the critical heat flux is exceeded, the heat can be transferred less effectively by vapor than by liquid before, thus leading to a sharp rise in temperature at the point of dryout, which is consequently stronger the more heat is added to the system. The difference in critical quality behavior might be attributed to different flow behavior around the point of dryout. Flow pattern maps like the one by (Hewitt and Roberts 1969) suggest that stable annular flow requires higher flow velocities. The higher shear stress and liquid momentum present at higher mass fluxes lead to a more stable liquid film on the wall. This results in the expected dryout behavior with a decrease in critical quality due to quicker film depletion at increased heat flux. Lower mass fluxes however lead to a less stable flow regime with a wavier liquid film. If flow velocities are too small the regime might even change from annular flow to other flow regimes like slug or churn flow, based on those flow pattern maps. This less stable flow behavior in combination with a high amount of vapor in the flow leads to a very early film depletion that is less sensitive to further increased heat flux.

4.2.3 Mass Flux

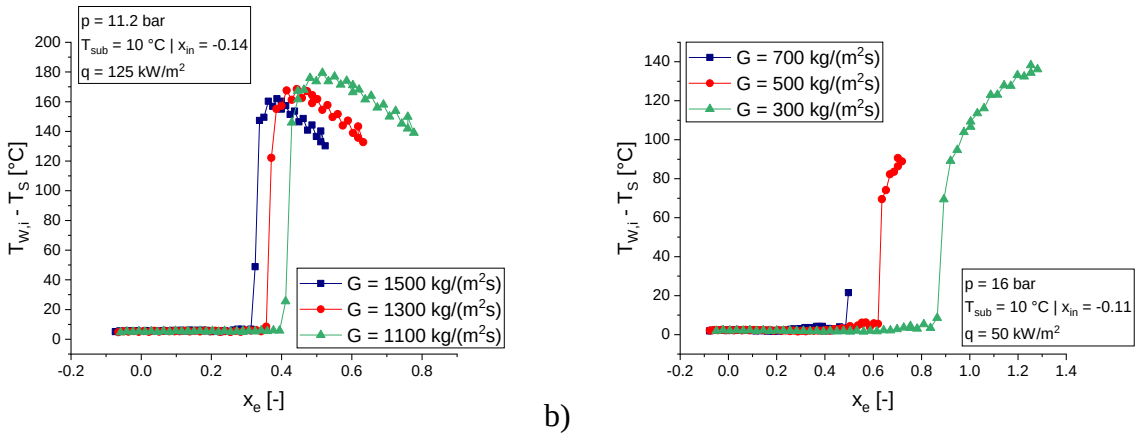
The heat flux required to achieve dryout depends very strongly on mass flux and pressure. In the experiments carried out, no overlapping heat flux for the entire parameter range could be found. Therefore, the investigation of mass flux influence is split into higher and lower mass flux ranges where comparable parameters exist.

For mass fluxes of G = 1100 - 1500 kg/(m^{2}s), the characteristic temperature distribution for high mass and heat fluxes (see Figure 4.1b) can be observed, as can be taken from Figure 4.6a). After reaching a local maximum, the wall temperature decreases with increasing vapor quality due to the increased evaporation of the entrained droplets. This leads to increased flow velocities and consequently to an improved convective heat transfer ((Lee and Chang 2008) and ((v. d. VDI e.V. 2013), chapter H3.6)). It is also noticeable that with increasing mass flux both, the temperature increase at the point of dryout and the maximum wall temperature

decrease. This can be explained by the better convective heat transfer at higher flow velocities. The negative temperature slope in the PDO region is similar for all mass fluxes, although the wall temperatures are higher at lower mass fluxes at the same local conditions.

For lower mass fluxes, the characteristic temperature distribution for low mass and heat flux (see Figure 4.1a) is observable, as illustrated in the diagram in Figure 4.6b). After the sharp rise at the point of dryout, the temperature continues to increase in the PDO region, although the slope is smaller. As the mass flux decreases, the lower flow velocity causes an increase of the critical vapor quality as well as the temperature rise at the onset of dryout.

In the experiments conducted with test section 1, it was observed that as the mass flux increases, the heat flux to reach the point of dryout increases, as does the maximum admissible heat flux (which is dictated by the maximum admissible wall temperature). Improved convective heat transfer as a result of higher flow velocities serves as an explanation.



a) b)

Figure 4.6: Influence of mass flux on the PDO temperature distribution at a) high mass fluxes, b) low mass fluxes (source: (Köckert et al. 2021))

It can be observed in the given figures that the critical vapor quality is shifted towards lower values with increasing mass flux. The entire temperature distribution is shifted to lower vapor qualities. The effect of critical quality shift is called the inverse mass flux effect and is described in the literature e.g., by (Tong and Tang 1997). The lower vapor quality at dryout and in the PDO region with increasing mass flux is caused by the enhanced flow velocities at higher mass flux, leading to more entrainment and reducing the liquid film thickness, causing an early dryout. However, the authors pointed out that this effect is only observable when the data is presented based on local conditions.

4.2.4 Pressure

In the case of pressure, the similar issue exists in regard to comparability as with the mass flux variation. Therefore, there is only a very limited number of tests for the entire pressure range, in which only the pressure varies with otherwise identical parameters.

CHF and the maximum admissible heat flux decrease with increasing pressure due to the decreasing enthalpy of evaporation. This leads to a shift of critical vapor quality to smaller values with increasing pressure. This is observable in the diagram in Figure 4.7. It can also be seen in the figure that the temperature increase at the point of dryout is much more pronounced with increasing pressure. This is possibly due to the increased vapor density at higher pressure, causing lower vapor velocities.

The pressure additionally affects the general temperature distribution. Although there is not much overlap in vapor qualities, the figure indicates a shift with increasing pressure from 16 bar to 28 bar from the characteristic distribution for low mass and heat flux to the one for high mass and heat flux. This means that in sufficient distance to the point of dryout, at lower pressure of p = 16 bar the temperature keeps increasing with increasing vapor qualities. At p = 28 bar on the other hand, the temperature decreases at similar local vapor conditions, following the behavior usually observed at high mass fluxes.

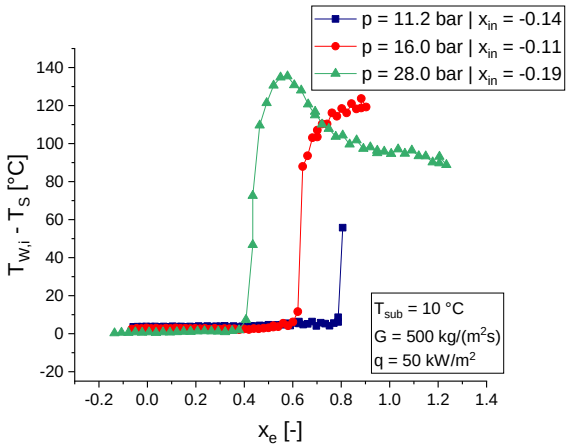


Figure 4.7: Influence of pressure on the PDO temperature distribution at otherwise constant input parameters (source: (Köckert et al. 2021))

(Schnittger 1982) made the same observation in his investigations with the simple heated tube. He claimed that two mechanisms are responsible for the development of the PDO temperature distribution. The development of thermal non-equilibrium results in an increase of wall temperature. Progressive evaporation leads to a flow acceleration, that augments the HTC and results in decreasing wall temperatures. Depending on which mechanism prevails, the wall temperatures rise or fall in PDO conditions. Since the enthalpy of evaporation decreases with increasing pressure, the evaporation rate is higher at those conditions and the wall temperature decreases. (Lee and Chang 2008) provided another possible explanation for this observation. Since the density ratio $\frac{\rho_l}{\rho_v}$ decreases significantly with increasing pressure, the void fraction also decreases. This in turn leads to less vapor superheat and thus better convective heat removal as a result of the lower thermal non-equilibrium. This effect is more pronounced at lower mass fluxes as the thermal non-equilibrium is more significant at these conditions. (Groeneveld and

Delorme 1976) argued that increasing pressure leads to improved heat transport properties and furthermore smaller droplets due to a decrease of the droplets' surface tension and therefore a bigger interfacial area. Both these effects result in a gradually disappearing thermal non-equilibrium with increasing pressure because of less vapor superheat. For the conducted experiments, it can therefore be stated that increasing pressure shifts the transition between the two characteristic temperature distributions to smaller mass and heat fluxes.

Contrary to the previously described observations from other investigations, the wall temperature does not increase at $p = 28$ bar for vapor qualities $x > 1$. Assuming thermal equilibrium, all the liquid in the flow should be completely evaporated at $x = 1$ and all the heat should be applied to superheat the vapor, resulting in an increase in wall temperature. This is opposed by the thermal non-equilibrium, which results in liquid droplets still being present in the flow even at vapor qualities of $x > 1$. As described before, droplets were found in optical studies far beyond equilibrium vapor qualities of $x = 1$. These droplets improve the heat transfer through evaporation processes and possibly cause a later onset of the expected temperature rise.

4.3 Investigation of the Rewetting Behavior in the Steady-State Experiments

The steady-state tests carried out with test section 1 did not yield any significant differences overall with regard to the temperature distribution in the power increase and decrease processes. This is exemplarily illustrated in Figure 4.8a). The heating process during power increase is labeled "Increase" in the diagrams, while the cooling process with power decrease is denominated "Decrease", as introduced in chapter 4.1.2.

In the experiments carried out in the two test series, the temperature distribution of the power decrease process at the dryout point and in the post-dryout region is sometimes slightly above or below the corresponding power increase temperature, depending on the parameter combination. However, there are no significant deviations. The same can be observed for the critical vapor quality. Apart from a few deviating temperature distributions, from which no conclusions can be drawn as to general validity and which also show only small deviations between the two temperature distributions, the temperature curves of the heating and cooling processes basically agree. As an example of a deviating temperature distribution, please refer to the diagram in Figure 4.8b). The small deviations in most cases are possibly caused by slight fluctuations of the input parameters within the tolerance range.

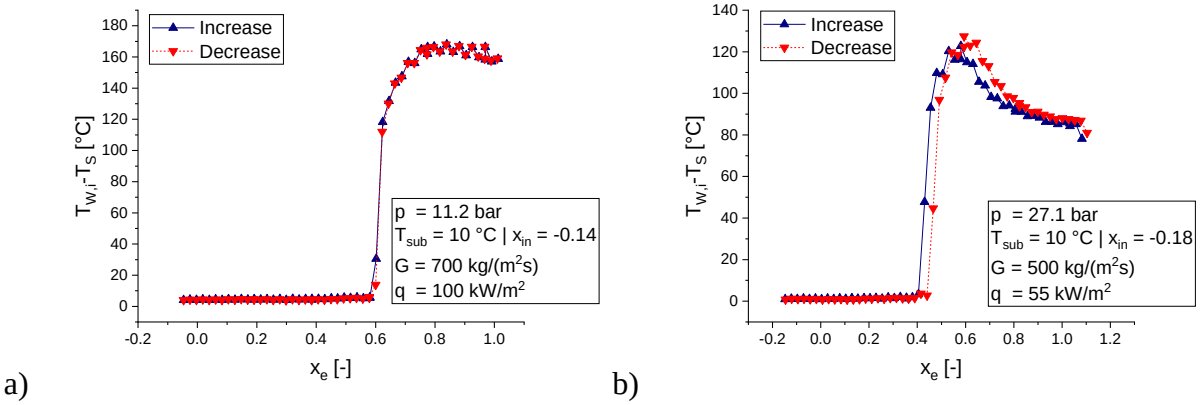


Figure 4.8: PDO temperature distributions for power increase and power decrease mode at a) very similar PDO temperature distribution; b) slight deviation in PDO temperature distribution

Theoretically, a possible hysteresis effect between power increase and decrease mode might be missed due to the axial distance between the individual thermocouple levels. Therefore, the temperature distribution over the heat flux was investigated for individual thermocouples at height levels preferably closer to the end of the heated length as those thermocouples experience distinct dryout and rewetting behavior. Representative examples at different mass fluxes are presented in Figure 4.9. It is obvious that the distribution is very similar, and that this investigation also did not yield any significant deviations between the two processes.

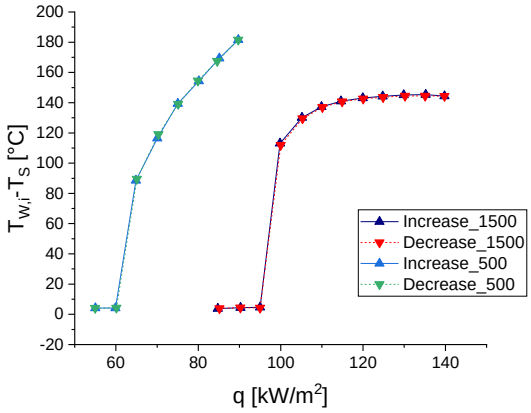


Figure 4.9: Comparison of the PDO temperature distribution for the power increase and decrease process at a representative thermocouple (TE 50) at p = 11.2 bar, ΔT_{in} = 10 °C, G = 500 and 1500 kg/(m²s) and varying heat fluxes

The experiments show the first type of cooling down and rewetting behavior distinguished by (Plummer 1974), as described in chapter 2.3.3. This means, the temperature follows the same path in the cooling process that it did when heating up, just in the opposite direction. The

experiments also confirm the findings for steady-state rewetting behavior in the discussed literature (see chapter 2.4.5). As stated above, the small deviations between the power increase and power decrease mode, that were observed in a few test runs, most likely are caused by slight parameter deviations.

4.4 Assessment of Theoretical Prediction Models

Table 4.1 comprises the results of the model comparison with the selected PDO data points obtained in the experiments. An overall of 7,825 data points was selected including both, data points obtained at power increase and decrease. Only data points with a wall temperature being 30 °C above saturation temperature in combination with a void fraction higher than 0.8 (calculated with the homogenous model) were considered to ensure PDO conditions. In the calculations, measured wall temperature data were used. The table presents the average deviation dev_m as well as standard and Root Mean Square deviation, σ and dev_{RMS}, for the selected models. These deviations are defined as follows:

$$dev_i = \frac{(\alpha_{calc} - \alpha_{meas})_i}{(\alpha_{meas})_i} \tag{4.1}$$

$$dev_m = \frac{1}{N}\sum_{i=1}^{N} dev_i \tag{4.2}$$

$$\sigma = \sqrt{\frac{1}{N-1}\sum_{i=1}^{N}(dev_i - dev_m)^2} \tag{4.3}$$

$$dev_{RMS} = \sqrt{\frac{\sum_{i=1}^{N} dev_i^2}{N}} \tag{4.4}$$

α_{calc} and α_{meas} describe the calculated and the measured heat transfer coefficient, respectively. The definition of the HTC is given in Equation (3.1).

In the iteration process to determine the vapor temperature in the CSO model, not all data points did converge. In comparison with the other correlations and models, this leads to around 350 data points less.

Furthermore, it should be noted that in all correlations and models the measured wall temperature was used when wall temperature as a parameter was part of the calculation.

Table 4.1: Assessment of the selected thermal equilibrium and non-equilibrium models with experimental data of the steady-state test series in test section 1

Correlation	**dev_m**	**σ**	**dev_{RMS}**	**Data Points**
Mod. D-R (1)	0.54	0.49	0.73	7,825
Groe 5.9 (2)	0.48	0.53	0.72	7,825
C-B IV (3)	0.74	0.31	0.80	7,825
Bishop I (4)	0.10	0.21	0.23	7,825
Bishop II (5)	0.15	0.27	0.30	7,825
Bishop III (6)	0.29	0.38	0.48	7,825
Miropol'skiy (7)	0.26	0.31	0.41	7,825
Lee&Chang (8)	0.68	0.32	0.75	7,825
Groe 1972 (9)	-0.07	0.19	0.20	7,825
Gro&Del (10)	0.44	0.28	0.52	7,825
CSO (11)	0.47	0.25	0.54	7,471

As can be seen in the table, the introduced Groeneveld 5.9 (Groe 5.9), the Modified Dougall-Rohsenow (Mod. D-R) and the Condie-Bengston IV (C-B IV) correlations which are used in ATHLET show a significant deviation, especially the Condie-Bengston IV correlation. The best fit of the empirical correlations is achieved with the first two correlations of Bishop (Bishop I and II) and the Groeneveld correlation for tubes and annuli (Groe 1972) which all cover a broad range of parameters. The last one is the only one of the selected models that underestimates the measured heat transfer coefficient and is therefore of conservative nature. Also, the Bishop III and the Miropol'skiy correlation, which is a combination of the approaches chosen by Bishop and Groeneveld in their empirical correlations, show reasonable results with average deviations below 30% and RMS deviations < 50%.

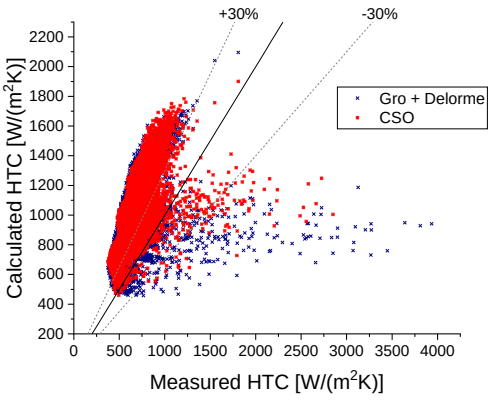
Obviously, by using the data points of the entire experimental test range, some of the empirical correlations were used outside of the parameter range they were based on (see parameter range in Appendix B.4). That might be an explanation for the particularly high deviation of some of the correlations and an advantage for the correlations that rely on a broad base range. Furthermore, most of the empirical correlations were developed by using solely water data,

which might also add to the deviation. As discussed in the general modeling approaches, most of the empirical correlations are not meant to be extrapolated outside of their original parameter range since they do not consider crucial physical mechanisms. However, some of them are applied in thermal-hydraulics codes like ATHLET and should therefore be able to predict the heat transfer over a broad range of parameters.

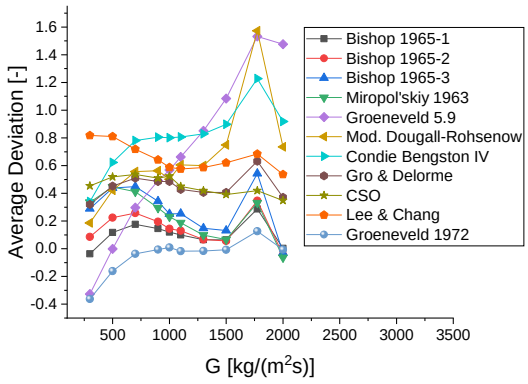
The overall high deviation of the correlation proposed by Lee and Chang is somewhat surprising since it was derived using a similar set-up at partially similar test conditions and with the same fluid as in this thesis. It was initially assumed to be caused by the correlation's dependence on the critical vapor quality and the axial distance of the particular data point to the onset of dryout. There is always an uncertainty in determining the exact critical vapor quality due to the longitudinal distance between thermocouples. In this study, the method also used by e.g., (Becker et al. 1983) sets the critical vapor quality and location in between the last thermocouple before and the first thermocouple after dryout. This method leaves an uncertainty of around 1.9% in terms of the axial position of the dryout location in relation to the overall heated length. However, an assessment with a perturbation of ±1.9% results in no significant change in the calculated deviation and could therefore not be the reason for the high deviations. The biggest difference in the experimental set-up lies in the tube diameter. The tube diameter might play an important role in CHF and PDO heat transfer and flow behavior but is discussed controversially in the literature. The KAIST experiments were conducted with a significantly larger tube regarding the inside and outside diameter, while the heated length was very similar to the test section of this thesis. (Yu 2019) claims that decreasing tube diameter increases the dryout quality which could be confirmed when comparing similar test conditions of KAIST and the present experiments. This comparison further shows that the point of dryout lies significantly further upstream for the smaller tube diameter at comparable conditions which leads to the assumption that CHF is decreased with decreased diameter. (Song 2021) argues that a decreasing tube diameter increases the droplet turbulence and therefore enhances the droplet deposition and therewith CHF, contradicting the given observation. This is contradicted again by (Celata and Mariani 2003) who claim that CHF increases with increasing diameter for fixed inlet conditions. Based on their observations of available CHF data, (Cheng and Müller 2003) conclude that there is no clear trend regarding the influence of the tube diameter. According to (Song 2021) the HTC is supposed to be higher with larger tube diameters in the PDO regime. She argues that increased tube diameter at otherwise similar conditions results in higher Re numbers and therefore higher flow turbulence which could enhance the convective heat transfer from vapor to droplets. However, (Yu 2019) says that based on the comparison of experimental data of (Becker et al. 1983) and (Era et al. 1966) with diameters of 14.9 and 6 mm, respectively, smaller tubes promote heat transfer in the fully developed PDO region. Also (Forslund and Rohsenow 1966) observed in experimental test runs that smaller tubes were closer to the equilibrium condition which would mean that heat transfer was enhanced at smaller tubes. (Nishikawa et al. 1986) found in their experiments with tubes of 9- and 13-mm inner diameter that no significant difference in wall temperature could be recognized. When comparing the

temperature distributions of both experiments, this present study and the KAIST data, the wall superheat is significantly larger for the KAIST experiments, supporting the observations presented by (Yu 2019) and (Forslund and Rohsenow 1966). Since the tube diameter goes directly into the correlation it might add to the overprediction of the HTC of the present data. Additionally, the fact that the parameter range in this thesis significantly exceeds the data base which the correlation is based on might contribute to the high overprediction of the Lee and Chang correlation.

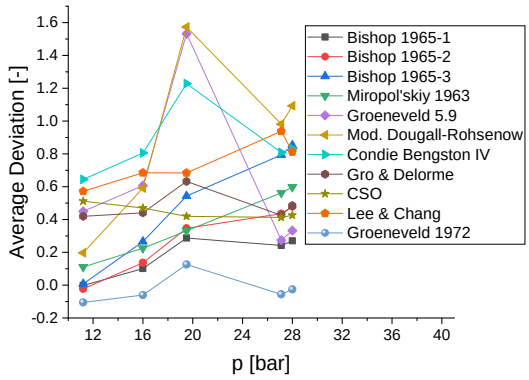
Despite taking the thermal non-equilibrium into account, the Groeneveld Delorme and CSO model significantly overpredict the measured HTCs and show worse results than some of the empirical correlations. Both models have very similar deviations. While the Groeneveld Delorme model overpredicts the measured HTC by an average of 44% with an RMS deviation of 52%, the CSO model lies slightly above that with an overprediction of 47%. The RMS deviations are 2% higher. The trend analyses, that are shown exemplarily for the two models in Figure 4.10a), illustrate that both models are unable to predict the measured HTC trend. Both models tend to significantly underpredict higher measured HTCs above ca. 1200 W/(m^{2}K). The trend analyses however indicate that some of those data points could be attributed to the developing PDO region. This might cause additional differences as the models were developed for fully developed PDO. However, the vast majority of data points lie below an HTC of 1000 W/(m^{2}K). Those data points are usually significantly overpredicted as can be taken from Figure 4.10a). Although considering the thermal non-equilibrium, important aspects of both models like the determination of the non-equilibrium were empirically derived, based on tube water data. (Groeneveld and Delorme 1976) argued themselves that the choice of a fixed α_{hom} at 0.33 as the transition point between thermal equilibrium and non-equilibrium might be questionable, since this value probably is dependent on pressure and mass flux. The CSO model proves to be highly sensitive to the iterated vapor temperature, which emphasizes the importance of correct modeling of the thermal non-equilibrium.



a)



b)



c)

Figure 4.10: a) Calculated over measured HTC for the CSO and Groeneveld and Delorme model for the steady-state test series; Average deviation for the variation of b) mass flux, c) pressure

Figure 4.10b) and c) display the influence of mass flux and pressure on the average deviation. It should be mentioned that the mass flux of G = 1775 kg/(m^{2}s) and the pressure of p = 19.5 bar include only 47 data points. This should be considered as the low number might lead to some distortion in comparison to the other parameters with significantly more data points. The diagrams show that these parameters usually lead to a peak in the average deviation. This is especially true for the Modified Dougall-Rohsenow correlation in terms of mass flux and pressure and the Groeneveld 5.9 correlation in regard to pressure. Those conditions are therefore neglected in the following discussion of the parameter influence on the correlations' performance.

Both non-equilibrium models show very similar behavior. The deviation increases for low mass fluxes up to 700 kg/(m^{2}s), before it irregularly decreases again with further increasing mass flux. However, while the CSO model shows the least deviation at the highest mass flux, the Groeneveld and Delorme model gives the best prediction at the lowest mass flux. The pressure dependency is small, within 10% deviation difference. While the Groeneveld Delorme model stays relatively constant for the entire pressure range and just shows a little increase at the highest pressure, the CSO model first decreases with increasing pressure with a slight increase again at the highest pressure. The Groeneveld and Delorme model delivers best results at the lowest pressure while the lowest deviation for the CSO model can be found at the highest pressures. Conclusively, the CSO model achieves the best prediction at low mass flux and high pressure conditions. In both those conditions, the thermal non-equilibrium is expected to be less pronounced which is an indication that the thermal non-equilibrium is not well predicted by the CSO model with the given experimental data. According to (Andreani and Yadigaroglu 1994), (Webb and Chen 1986) proved with a large data base that the Groeneveld Delorme model can significantly overpredict the vapor superheat at low pressure and low mass flux conditions by a standard deviation up to 690%. However, the model shows no pronounced dependency on

mass flux and especially pressure. In fact, the best prediction results are achieved at the lowest pressure and mass flux. Nonetheless, the current parameter range exceeds the one the model is based on, and although Groeneveld and Delorme claimed that the model can be extrapolated to data outside their original parameter range, it might cause some distortion and add to the observed overprediction.

There is no unified behavior among the other correlations and models regarding the mass flux variations. The Bishop correlations as well as Miropol'skiy follow the behavior described for the non-equilibrium models but with a steeper decrease with increasing mass flux. The deviation with the Lee and Chang correlation decreases with increasing mass flux up to $G = 1100$ kg/(m^{2}s), increases again and eventually shows the lowest value at the highest mass flux. The Modified Dougall-Rohsenow correlation as well as Condie Bengston IV show a general deviation increase with increasing mass flux while remaining almost constant after $G = 700$ kg/(m^{2}s) and at the highest mass fluxes. Also Groeneveld 1972 generally follows this deviation behavior. However, since it significantly underestimates the measured HTCs at the lowest mass flux, the correlation shows almost no deviation at all at mass fluxes of 900 kg/(m^{2}s) and higher. The Groeneveld 5.9 correlation significantly underpredicts the HTC at the lowest mass flux and shows the highest deviation of all models at the highest mass flux, continuously rising with increasing mass flux. All the models and correlations, except for Groeneveld 5.9 and Groeneveld 1972, have their lowest deviation at either the lowest or highest mass flux which means at highest or lowest expected thermal non-equilibrium.

Besides the already described non-equilibrium models, the other correlations mostly show a deviation increase with increasing pressure and have their highest deviation at the highest pressure. The only exemptions to the last point are Lee and Chang, Groeneveld 5.9, and Groeneveld 1972. Furthermore, 8 out of the 11 correlations and models have their minimum deviation at the lowest pressure which is interesting due to the higher expected thermal non-equilibrium, as discussed in chapter 2.4.1.

5. Experimental Results and Discussion in the Annular Test Section

This chapter discusses the results obtained with the second test section. It can be subdivided into two main sections. The first one analyzes and discusses the results that the optical droplet behavior investigations have yielded. This subsection also includes the methodology that was used for deriving the results from the obtained images. Furthermore, certain characteristics and abnormalities in the conducted experiments as well as limitations of the utilized image analysis software are presented and discussed as they need to be known and understood for a comprehensive evaluation of the results. The second main section presents the thermal non-equilibrium analysis using an optical fiber that was implemented in the flow channel via a stainless steel capillary.

5.1 Droplet Behavior Analysis

The following subchapters are dedicated to the analysis of the optical flow experiments in the PDO area. First, the methodology used to evaluate the high-speed camera footage is introduced. Subsequently, the limitations of the analysis software as well as general characteristics and distinctive features of the conducted experiments are discussed, as they are of importance to assess the quality of the obtained results. This subchapter concludes with the presentation and discussion of the results of the optical flow behavior analysis for the high-speed camera footage. Contents of this analysis have been published and presented at the SWINTH-2024 conference ((Köckert et al. 2024b)). My analysis has been supported in the framework of a bachelor's thesis by (Stier 2020) that I supervised.

5.1.1 Analysis Methods of High-Speed Camera Footage

The DynamicStudio software version 6.11.33 from Dantec Dynamics was used to process the camera images. This is a software package for image acquisition and image analysis, whereby only the second function was used in the experiments.
Initially, the flow images were calibrated within the software package. Various operands were subsequently used to enhance the distinction between droplets, background, and image disturbances (noise). Basically, the steps used to process the flow images can be categorized as follows:

- Creating an image section
- Image processing
- Particle tracking
- Data analysis

The challenge of the present image processing and subsequent analysis is to accurately identify droplets in the flow and differentiate them from the background, main flow, and image noise. Figure 5.1a) displays a raw image of the flow in the test section, as recorded through the display window during a test run. The heating tube, located in the center of the image, is visible in the circular display window along with the rectangular channel shape. The dark droplets should be clearly distinguishable against the gray background, which is caused by the illumination setup (refer to section 3.4.3) and the vapor flow.

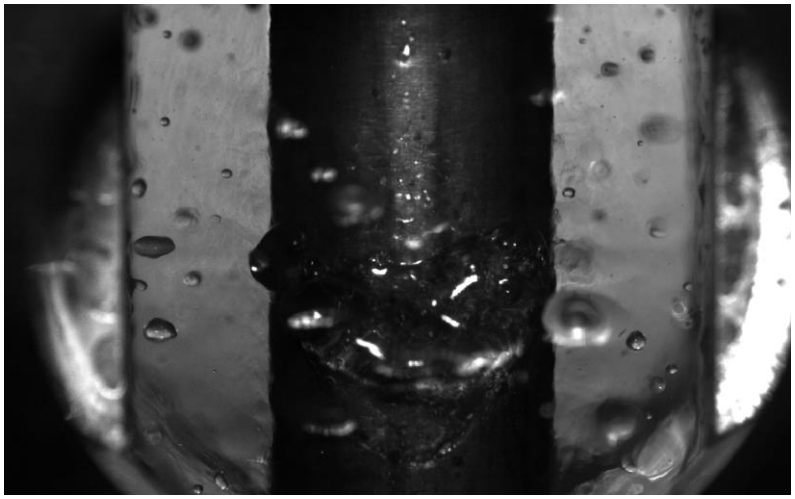
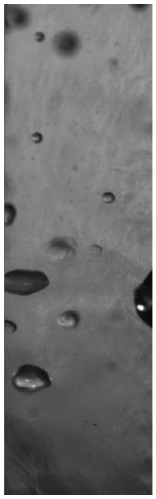
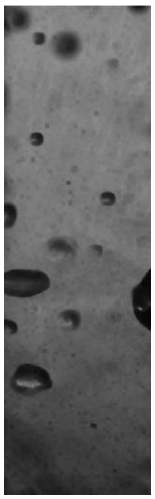
a)  b)  c) 

Figure 5.1: a) Raw flow image under PDO conditions, b) selected analysis region in left side of the flow channel, c) selected analysis region from b) after application of Opening and Erosion filter

The initial step is to create a section of the original image, the so-called region of interest (ROI). This extracted part of the image can be used to isolate interfering factors, such as the boundaries of flow channel and heating tube and their immediate surroundings. This is necessary due to the limitations of the test and illumination set-up, which make flow analyses in those areas impossible. Additionally, it at least partially allows larger areas of liquid depositions, which sometimes form on the panes of the display windows, to be masked out. In the analysis carried out in the following sub-chapters, the image section is selected so that only the region of the channel between the left-hand channel wall and the heating tube is displayed. Figure 5.1b) depicts an example of the extracted segment of the original image in Figure 5.1a). The ROI slightly differ in size and position for the different test runs due to the different flow behavior in these experiments.

The next step is to process the image section. So-called neighborhood operations, including low-pass, high-pass, and morphology filters among others, have proven effective in this regard. These functions enhance differentiation between liquid droplets, interfering objects as will be discussed later, and background by smoothing, recognizing boundaries, and increasing image

contrast, among other operations. Filters are set individually based on the flow recording. In addition, erosion and dilation filters flood bright or dark pixels with neighboring pixels to reduce the reflections in droplets, making them more distinguishable and their contours clearer, respectively. These filters also suppress local high-frequency noise. Figure 5.1c) displays an example of the opening and erosion filters usage. Multiple filters are applicable one after the other, requiring careful sequencing. The filter application generates a new image upon processing.

After image processing, the droplets undergo capture and analysis through the shadow tracking technique. This technique detects the droplets based on their shadow image, extracts relevant information including size, position and shape, and further determines their velocity by tracking the movement of the droplet shadow between two consecutively captured images. For this purpose, the ROI is transformed into a black and white version through binarization using a predetermined threshold value. Additionally, brightness gradients are used to enhance edge detection through the application of the Mexican Hat filter. In addition to recording the position in lateral and vertical direction and the velocity of the identified droplets, their equivalent diameter is determined. The equivalent diameter denotes the diameter of a spherical droplet with the same surface area as the detected object. The operation produces a numerical data table containing details on size, velocity, and location of droplets, among other variables. This table can be utilized for subsequent analysis.

5.1.2 General Characteristics and Distinctive Features of the Measurements

This subchapter discusses observed peculiarities as well as limitations regarding the conducted experiments and analysis of those experiments with test section 2.

Abnormalities during Testing

During test runs, considerable flow instabilities were observed in test section 2. These instabilities made it challenging to conduct steady-state experiments. Despite constant setting parameters during measurement recordings, larger fluctuations in wall temperature were observed during some parts of the measurement period on different occasions.

The spacers represent an obstacle of the free flow area of the channel. As discussed in chapter 2.4.2, this may increase the flow turbulence at the spacer and downstream and influence the PDO heat transfer through various effects. The last spacer is set 855 mm below the end of the heated length in this study. Several of the investigated test runs show clear influence by this spacer by decreasing wall temperatures and increased HTCs in the area downstream of the spacer. The distance of the spacer to the points of interest in the optical investigations is large as they are close to the end of the heated length. A direct influence on wall temperature or HTC could not be observed there. However, the increased turbulence by the spacers throughout the

entire flow channel might contribute to the generally observed flow instabilities in the second test section.

Chapter 3.5.2 noted the restriction on mass flux to very low values. The amount of liquid in the flow is significantly increased at higher mass fluxes. That would prevent optical investigations of the PDO flow behavior, especially in the surrounding of the heating tube in the channel center. Therefore, the previously mentioned mass flux of $G = 66\ kg/(m^2s)$ was selected for both test series. Furthermore, the limitation on heat flux was discussed, which meant that only a very limited variation of heat flux was possible at all for only a few parameter combinations, particularly in test series 1 with test section 2 (refer to section 3.5.2). In this first test series, typically only the top two thermocouple levels were in the PDO range, except for the high-pressure tests. Additionally, the low variability of the heat flux precluded the quantitative investigation of parameter influences on the PDO behavior since similar heat fluxes could not be run for a bigger pressure range. However, in the following chapters of the high-speed camera test analysis, at least a qualitative comparison with respect to pressure is made.

In the second set of experiments conducted with test section 2, the specified permissible maximum temperature of the heated wall was slightly elevated from around 240 °C to improve the conditions for the measurement of vapor temperatures. Furthermore, the fiber capillary was integrated into the flow channel. Those measures resulted in a more consistent PDO regime as indicated in chapter 3.5.2. The dryout point was noticeably moved upstream compared to the initial test series. However, precise determination of the axial position of the dryout is not possible under these conditions with the given set-up due to the significant axial distance between the start of the heated length and the first thermocouple measuring level. Furthermore, despite comparatively stable post-dryout conditions, the steady-state test runs still showed increased flow instabilities and wall temperature fluctuations and therefore limited heat flux variability.

The formation of liquid depositions on the glass windows poses challenges for optical inspections using a high-speed camera. These depositions likely consist of residual liquid fragments from the flow or condensed liquid that forms on the channel wall and window due to the lower temperature. Those act as a heat sink compared to the heating rod located in the center of the flow channel. The longer the corresponding area remains under PDO conditions, the more pronounced these depositions become. The depositions are observed to form more significantly with increasing pressure, while the weakest manifestations are noted at medium pressures of $p = 15$ and 20 bar. They are formed unevenly and may, in some instances, move slowly in countercurrent with the flow direction. The presence of liquid on the glass pane complicates the analysis of high-speed camera images since it cannot be entirely masked out, hence manifesting as interference points in the image processing.

Efforts to minimize the accumulation of liquid depositions on the window panes with the help of external heat sources were ineffective. The following section provides information about the approach taken to address these challenges in the analysis.

Characteristics and Limitations of the Software Version DynamicStudio 6.11.33

The DynamicStudio software version used for image data analysis in this thesis sums up the droplets detected per image in the data output. Consequently, previously detected droplets are identified again in subsequent images and reported as new. For instance, if a droplet is observed ascending in 80 images, its parameter values are captured as 80 unique entries in the data output. Therefore, individual droplets cannot be treated as separate entities in subsequent data analysis. The values in the histograms displayed in the following chapters therefore do not accurately represent the number of recorded droplets in the flow but rather the total summed up number across all frames. In addition, the absence of assignability complicates the filtration of interfering and noise particles from the recordings. Furthermore, this introduces a bias in the vertical velocity distribution as slower droplets are accounted for more frequently than faster ones. However, the lack of assignability makes it impossible to correctly quantify the influence of that bias.

Simultaneously, numerous droplets with zero velocity are detected. Since in a vertical upward flow, the droplets usually either follow the main flow or show turbulence or counter-current flow induced negative velocities, it is assumed that these objects are in most cases liquid depositions accumulating on the window panes. Consequently, the detected objects with zero vertical velocity are therefore disregarded in the analysis of the test results.

Additionally, numerous objects are detected with a low negative vertical velocity. These can be caused by gravity induced counter-current flow. Furthermore, flow turbulence could cause smaller droplets in particular to follow the main vapor flow and its turbulences, resulting partially in negative velocity in the vertical direction. However, when examining the images, it is more probable that these are detected areas of liquid depositions that move countercurrent to the main flow during the image acquisition. Since it is not possible, without a specific droplet assignment, to distinguish small droplets with a negative vertical velocity component from inaccurately detected particles of liquid depositions, listed droplets with a negative vertical velocity component are also not considered for further data analysis.

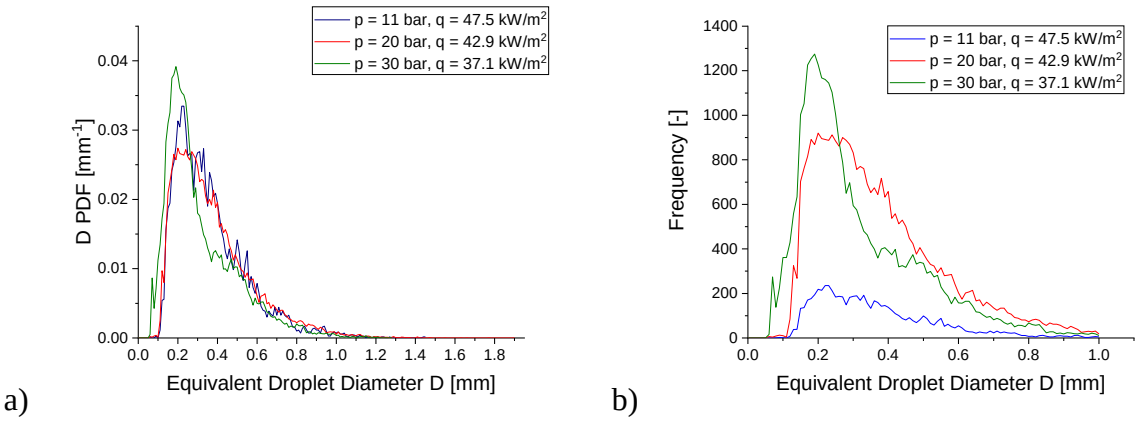
Overlapping droplets pose another challenge in particle detection since it is mainly based on brightness gradients. The overlap of two objects therefore often leads to incorrectly detected particles. Furthermore, even the software's specific functions to counteract this problem do not provide satisfactory results in most cases, leading to evaluation inaccuracies. When droplets make contact with the edge of the defined image section, an additional problem arises regarding their detection. At this point, droplets can no longer be identified.

Some droplets only appear in a very limited number of frames so that it is impossible that they could have crossed the ROI in this detected number of frames. This can happen for different reasons. First, they are incorrectly detected droplets or were picked up noise particles and disappear due to background changes in consequent images. Second, DynamicStudio sometimes loses track of particles when a specified criterion is not met in a single frame and

might pick it up later again when this specification is fulfilled again. It is also possible that a droplet is moving normal to the specified sharp image plane. On this occasion, the droplet is only detected in a few frames as it passes the sharp plane and disappears again. Due to the above-mentioned lack of assignability it is usually difficult to specify droplets that are only present in a very limited number of frames. However, whenever it was possible, those droplets were discarded from the analysis.
By utilizing erosion and dilation filters in image processing, the droplet contour is minimally altered, impacting equivalent diameter values. Nevertheless, drop contours are still occasionally not accurately recognized even after image processing, which leads to the possibility of occasionally incorrect equivalent diameters.
The issues outlined above result in some degree of inaccuracy in the analysis of the flow recordings that is almost impossible to quantify.

5.1.3 Droplet Size

The diagrams in the following subchapters usually show probability density functions (PDF) of the parameters droplet size and velocity under different conditions. The size classes are 10 µm and 0.01 m/s, respectively.
The PDF of the equivalent droplet diameter in Figure 5.2a) displays three sets of measurements indicating the equivalent droplet diameter variation at pressures of p = 11, 20, and 30 bar. The pressure comparison is carried out qualitatively using these exemplary pressures but behaves similarly for the other pressures. The minimum equivalent droplet diameter results from a minimum value defined in px in the image analysis.
It is evident from the results that all three test series display a similar distribution of droplet sizes, roughly following the shape of a gamma distribution. The majority of recorded droplets have an equivalent diameter of $d \cong 0.2$ mm.
In the two test series at p = 20 bar and p = 30 bar, remarkably more droplets were detected in the flow than at a system pressure of p = 11 bar. This is reflected in the frequency distribution in Figure 5.2b). This distribution shows the total number of detected droplets per size class on the axis of ordinate. A possible explanation for this observation is that the critical vapor quality tends to decrease with increasing pressure, resulting in a higher concentration of droplets in the PDO region. As previously noted however, the proportion of interfering particles due to liquid depositions increases with increasing pressure as well. This impact may also be observed in the high pressure measurement series.



a) b)

Figure 5.2: The equivalent droplet diameter under system pressure variation at T_S-T_{in} = 17 °C and G = 66 kg/(m²s), displayed as a) PDF distribution, b) Frequency distribution (source: (Köckert et al. 2024b))

Influence of Inlet Subcooling and Heat Flux Variation

For pressures of p = 15 and 20 bar, the influence of inlet subcooling on the droplet diameter was investigated. At p = 15 bar, the axial distance from the investigated point to dryout is the same for both subcooling conditions. The vapor quality at this point increases by approximately 1.2% in both cases compared to the vapor quality at the onset of dryout. This suggests that similar local post-dryout conditions can be assumed. On the other hand, dryout was detected one measuring level closer to the test section inlet for the larger subcooling stage at p = 20 bar. This means that in this case, the distance from the point of interest to the dryout is a maximum of 60 mm greater. The vapor quality increases by 7% with higher subcooling, compared to 3.8% with lower subcooling. Therefore, there may be slight local differences in post-dryout conditions for p = 20 bar. However, it should be noted that due to the aforementioned very limited heat flux variation, the heat flux also slightly differs at the different inlet subcooling stages so that the comparison is rather qualitative.

Regarding the PDF distributions of droplet diameters, there are only few qualitative differences between them. This is evident in the exemplary diagram in Figure 5.3a) for a pressure of p = 20 bar.

The average diameter for experiments at p = 15 bar with lower inlet subcooling is 0.344 mm, which is slightly larger than the diameter with greater subcooling (refer to Table 5.2). For a pressure of p = 20 bar, test runs with slightly different heat fluxes were conducted at lower subcooling (see Table 3.4). The diameter for these experiments varies between 0.342 and 0.357 mm but is always lower than the diameter of 0.374 mm at higher subcooling, which is displayed in Table 5.2. Direct comparison is difficult for all the described test runs due to the differences in heat flux. The small differences in diameter however, which across all cases with the same pressure lie within 35 µm, generally indicate statistical fluctuations.

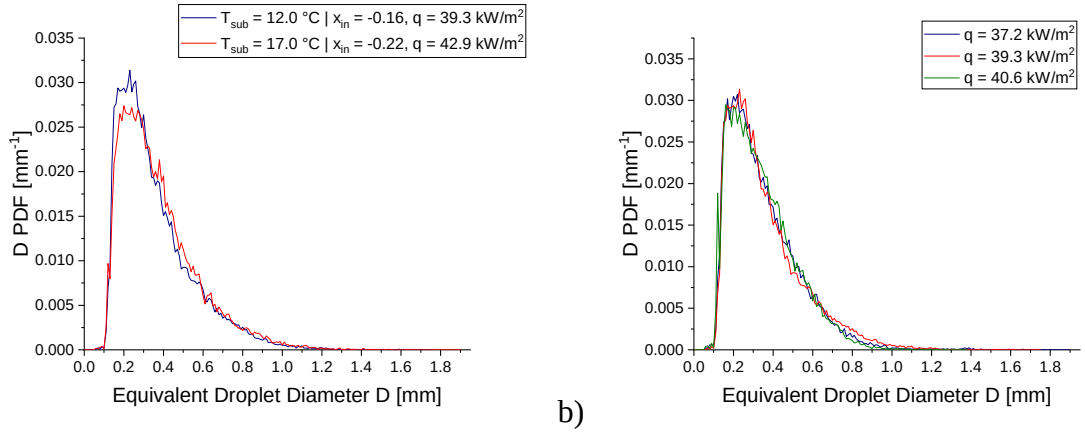


Figure 5.3: PDF of the equivalent droplet diameter at p = 20 bar and G = 66 kg/(m²s) under a) inlet subcooling variation, b) heat flux variation at T_S-T_{in} = 17 °C (source: (Köckert et al. 2024b))

This conclusion can be equally drawn for the influence of heat flux on the diameter distribution. Figure 5.3b) and an average diameter variation of 15 µm indicate that there is hardly any qualitative or quantitative difference observable due to variations in heat flux. However, regarding the very narrow heat flux variation range of only 9% from lowest to highest admissible heat flux, this conclusion might carry only limited significance.

5.1.4 Droplet Velocity

This subsection is dedicated to the investigation of the droplet velocity. First, the results of vertical velocity investigation are analyzed. This includes a comparison to the superficial vapor velocity. The section is concluded with the analysis of the horizontal velocity results and an analysis of the horizontal droplet position in the measurement plane.

5.1.4.1 Vertical Droplet Velocity

As the fluid is flowing vertically upward, an upward droplet movement is denominated positive. Detected droplets with zero or negative vertical velocities are discarded from the analysis as was discussed in chapter 5.1.2. Figure 5.4 demonstrates for the different pressures counteracting behavior regarding the vertical velocity. The number of droplets at high velocities increases for low pressures while this peak shifts to lower values with increasing pressure. This observation is also valid for the average velocities determined at the different pressure conditions. It is noteworthy that approximately 42% of the droplets at p = 30 bar were detected with vertical velocities below 0.1 m/s. As the already mentioned liquid depositions are most significant at higher pressures, the likelihood of falsely identified droplets with close to zero vertical velocities is increased at this pressure. This might add to the number of slow droplets. The general trend however is in agreement with theoretical expectations. Most of the droplets are

expected to follow the main flow, especially in the flow channel center. Since the vapor density increases with increasing pressure the vapor velocity decreases and so does the droplet velocity. The discussed bias introduced through the multiple counting of droplets, which favors slower droplets, increases the strong count of very slow droplets at high pressure as well.

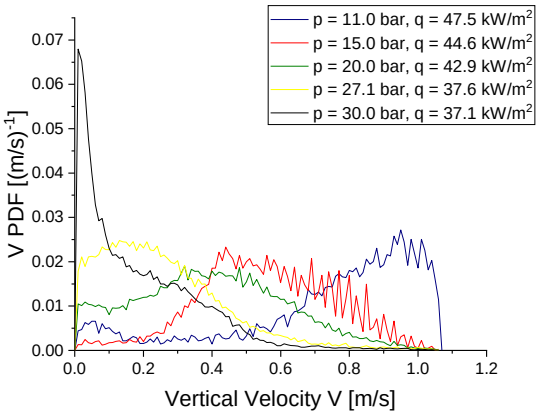
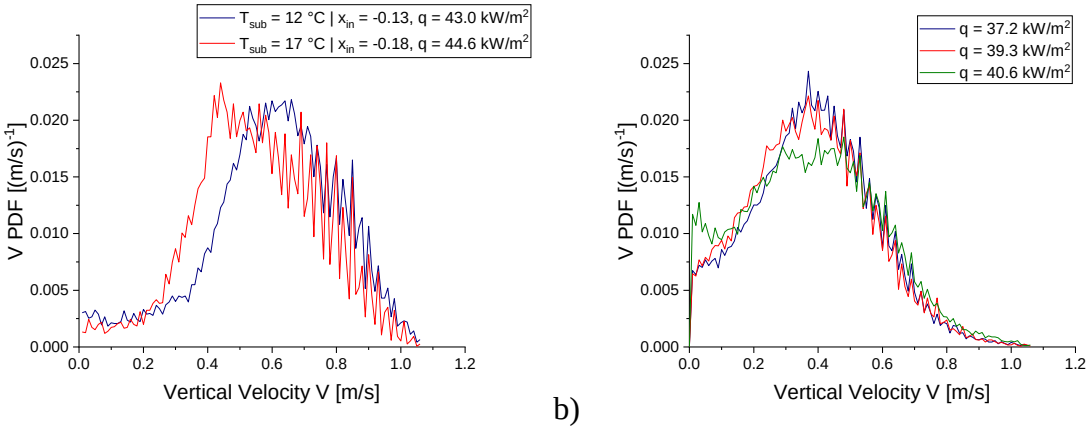


Figure 5.4: PDF of the droplet vertical velocity under system pressure variation at T_S-T_{in} = 17 °C and G = 66 kg/(m²s) (source: (Köckert et al. 2024b))

Influence of Inlet Subcooling and Heat Flux Variation

Despite variations in inlet subcooling, the local conditions are very similar, and all points of investigation are still quite close to the point of dryout. The qualitative comparison indicates a small shift in the axial velocity distribution, as displayed in Figure 5.5a). However, the average velocity shows no significant dependency on the inlet conditions and lies only 0.05 m/s lower for higher subcooling at a pressure p = 15 bar, and 0.02 m/s higher for higher subcooling at p = 20 bar, respectively.

Just as in reference to the droplet diameter, the effect of heat flux variation on the vertical velocity is negligibly small because of the very limited heat flux range, as is demonstrated in Figure 5.5b).



a) b)

Figure 5.5: PDF of the droplet vertical velocity under variation of a) inlet subcooling at p = 15 bar and G = 66 kg/(m²s) (source: (Köckert et al. 2024b)), b) heat flux at p = 20 bar, T_S-T_{in} = 12 °C, and G = 66 kg/(m²s)

Discussion of Measured Vertical Droplet Velocities, Vapor Velocity, and Slip Ratio

Table 5.1 comprises the measured average droplet velocities in vertical direction, together with the corresponding measurement parameters.

The measured droplet vertical velocities are first compared to the calculated corresponding vapor velocities. Since the actual vapor temperature in those measurements is unknown, two boundary conditions were assumed that provide a velocity range. The first limit is based on the assumption of thermal equilibrium conditions where saturated vapor properties are present. At equilibrium vapor qualities beyond 1, unity is assumed. This marks the upper limit. The lower limit is determined assuming non-equilibrium conditions using the vapor density and the actual vapor quality as defined in equation (2.6) at wall temperatures. The velocity range, based on these two boundary conditions, is also depicted in the table along with the measured slip ratio. This measured slip ratio is determined as the ratio of the calculated vapor velocity and the measured droplet velocity for the liquid phase:

$$S = \frac{v_v}{v_l} = \frac{v_{v,calc}}{v_{meas}} \tag{5.1}$$

The vapor velocity is calculated as below for saturated ($v_{v,calc,e}$) and superheated vapor at wall temperature ($v_{v,calc,W}$) conditions. In this calculation, it is assumed that the void fraction is 1, which seems reasonable as the measurements show that only very limited liquid is left in the flow.

$$v_{v,calc,e} = \min(x_e, 1) \cdot \frac{G}{\rho_{vs}}$$
$$v_{v,calc,W} = \min(x_a, 1) \cdot \frac{G}{\rho_{vw}} \quad (5.2)$$

Since the velocity is given in a range for the above assumptions, the slip ratio is also determined based on this range.

Table 5.1: Measured droplet vertical velocity in m/s obtained with the high-speed camera, corresponding calculated vapor velocities in m/s, and slip ratio based on the given values for test runs with G = 66 kg/(m²s) and T_S-T_{in} = 17 °C

p [bar]	q [kW/m²]	T_W [°C]	v_{meas} [m/s]	$v_{v,calc}$ [m/s]	S_{meas} [-]
11.0	47.5	227.5	0.75	1.05 – 1.21	1.40 – 1.62
15.0	44.6	210.5	0.55	0.76 – 0.86	1.37 – 1.55
20.0	42.9	220.2	0.40	0.56 – 0.61	1.40 – 1.53
27.1	37.6	200.1	0.26	0.39 – 0.42	1.52 – 1.62
30.0	37.1	216.3	0.19	0.34 – 0.35	1.78 – 1.83

The measured droplet velocities as well as the calculated vapor velocities tend to decrease with increasing pressure. This trend is to be expected as increasing pressure leads to an increase in vapor density, thus resulting in decreasing vapor velocities, as discussed above. The measured average droplet velocity lies consistently below the calculated range across the entire pressure range. This means that there is slip between the two phases. The measured slip between the phases, while relatively constant at low to medium pressure, increases with further increasing pressure.

This last observation is theoretically unexpected and might be influenced by different mechanisms. Possibly wrongly detected droplets decrease the average measured velocity. In addition, the described bias, that pronounces the influence of slow droplets due to the multiple counting system contributes to a reduced average velocity. Both mechanisms might be more severe at higher pressures, where more slow droplets and interfering particles are present. However, it should be noted that besides the pressure, the applied heat flux is changed as well, which makes quantitative comparisons difficult.

(Cumo et al. 1971) found for their investigations that the slip ratio in PDO is close to 1. The actual vapor temperature lies in between the two introduced limiting temperatures that define the boundaries of the vapor velocity calculations. However, the results of this study show

velocity differences between the two phases across the entire pressure range, suggesting slip between the phases for those measurements. The distance between the measurement location and the point of dryout is smaller for lower pressure which might lead to a higher slip at those conditions. Furthermore, the density ratio of liquid and vapor is big, especially at low pressures, which might support the thesis of higher slip. Nonetheless, the results suggest that a certain slip is also still present at higher pressure where the measurement location lies further away from dryout. The measurements therefore show some contradictions to the claims found by (Cumo et al. 1971), although the measured slip might be more pronounced due to the above discussed factors.

5.1.4.2 **Lateral Droplet Velocity and Distribution in the Channel**

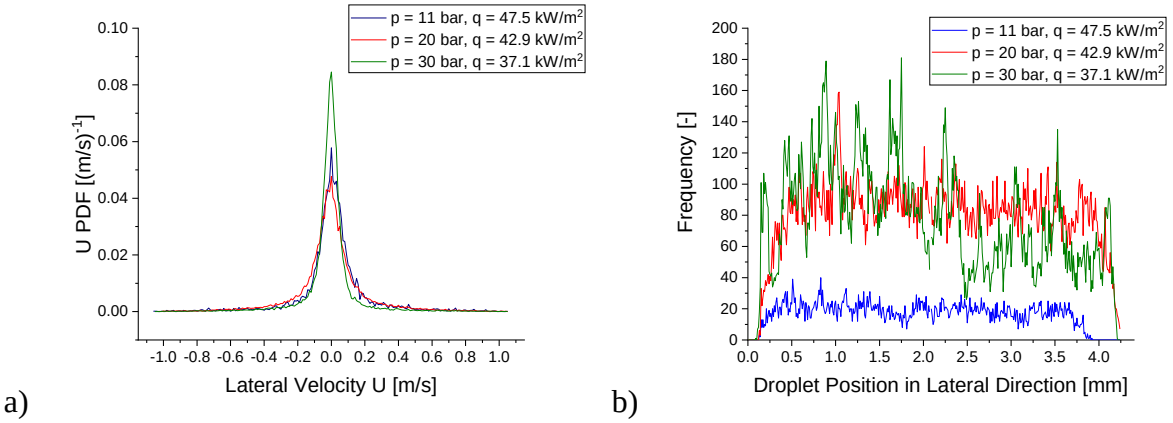
The lateral velocity in the region of interest is defined positive in the direction of the heating tube in the flow center and negative in the direction of the channel wall. The lateral velocity approximately follows a Gaussian normal distribution with a mean value of about 0 m/s. This distribution is shown for three different pressures in Figure 5.6a) but is also valid for the other conditions. Apart from the total number of detected droplets the lateral velocity is independent from the system pressure. While single droplets may reach horizontal velocities up to about 1 m/s, between 87% and 97% of the identified droplets lie within $u = \pm 0.3$ m/s for the different depicted test runs, and still between 61% and 84% within $u = \pm 0.1$ m/s. In comparison, the vertical velocities differ much more for the different test runs. Between 9% and 77% of the droplets have vertical velocities within 0.3 m/s and only 2% to 42% within 0.1 m/s, depending on the test conditions. It was observed, as discussed before, that higher pressure results in lower superficial vapor velocities and therefore vertical velocities. On the other hand, the lateral velocities do not show a clear dependency on pressure.

The channel geometry and subsequently the possible illumination of the channel made it impossible to investigate the droplet behavior in the channel center and directly at the heated wall simultaneously. Generally, the behavior directly at or in the vicinity of the heated wall could not be captured satisfactorily. However, since the vast majority of droplets were concentrated further away from the heated surface and are in fact mainly scattered across the central region of the flow channel, the focus of the investigation was therefore put on the droplet behavior in the channel and further apart from the heated wall.

For the ROI of the different test runs the lateral position of the droplets along the cross section of the flow was investigated. The exact position of the droplets in the channel depth is unknown. Although the depth of field was kept as small as possible (about 0.74 mm) some droplets that are out of focus might have been detected in the analysis as well. However, looking at the overall images it seems fair to assume that the analyzed droplets are located in the same plane in depth. This simplifies the investigation to a 2D space that is confined in the horizontal direction by the channel wall on the left side and the heating tube on the right side. In the diagram in Figure 5.6b), the position $x = 0$ mm is therefore close to the channel wall while $x >$ 4 mm is near to the heating tube. Since the ROI is not entirely the same for the different test

runs, as discussed before, the minimum and maximum droplet positions can be slightly different. Contrary to the previous diagrams, the droplet distribution across the channel is exemplarily displayed as a frequency distribution for better distinction of the curves.
It is observable in the diagram that across different pressures, the vast majority of droplets is located in the ROI center between approximately x = 0.5 and x = 4 mm. In fact, over all test cases, at least 76% of the detected droplets were found in between 0.5 and 3.5 mm, and even a minimum of 88% between x = 0.5 and x = 4 mm. The droplet number decreases against 0 when approaching the boundaries of the ROI. In the center region, fluctuations are obvious that are more pronounced at higher pressure. However, the average number of droplets remains fairly constant with a slight decrease in the direction of the heating tube. Due to the differences in temperature, the liquid portion might agglomerate a little more to the colder channel wall. The results also yield a slight increase of the average droplet diameter in the center region from about x = 0.5 - 3.5 mm. It indicates that especially most of the bigger droplets are located in that central region. The average diameter usually decreases in the direction of the heating tube as is to be expected due to higher evaporation. However, closer to the channel wall the detected diameters are also smaller which might be caused by the boundaries of the ROI. Overall it can be concluded that the droplets are evenly distributed in the center region.

The observed lateral velocities in combination with the droplet positions indicate relatively straight droplet trajectories and therefore only very limited interaction between wall and its boundary layer and the droplets. This behavior was independent of the axial position in reference to the point of dryout. The low lateral velocities and straight trajectories are in good agreement with the observations by (Cumo et al. 1971). A possible reason for this behavior might be the fact that the overall droplet size is usually small in the PDO region. (Schnittger 1982) assumed, based on the study by (Ganić 1976), that smaller droplets are less likely to develop enough lateral momentum that is necessary to reach the heated wall and its boundary layer, respectively.
(Kendall and Rohsenow 1978) quantified the contribution of direct heat transfer between wall and droplets to the overall heat transferred in the PDO area with less than 5%. (Yu 2019) distinguished between developing PDO region in which the contribution of this process is more pronounced and fully developed PDO region where the amount is yet again less than 10%. These assumptions could be supported by the investigations in this study.



a) b)

Figure 5.6: a) PDF of the droplet lateral velocity under system pressure variation at T_S-T_{in} = 17 °C and G = 66 kg/(m²s) (source: (Köckert et al. 2024b)), b) lateral droplet position in left flow channel side at the same test conditions (source: (Köckert et al. 2024b))

5.1.5 Investigation of the Connection between Droplet Velocity and Diameter

The following diagrams depict the velocity versus the droplet diameter. Every entity in the diagram represents a diameter and the corresponding velocity for an identified droplet in a frame. Due to the large number of droplets the diagrams for exemplary test runs are displayed separately. The results show some differences regarding the vertical velocity over the droplet diameter, so these results will be introduced first. Qualitatively, there are no significant differences regarding the lateral velocities versus the droplet diameter. The results will be therefore explained using only a single test run.

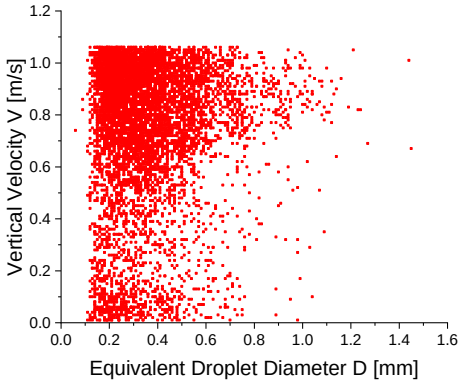
5.1.5.1 The Connection between Droplet Vertical Velocity and Diameter

The following diagrams display the distributions for the test runs at p = 11, 15, 20, and 30 bar. The first depicted test run at p = 11 bar shows a strong concentration on small to medium sized droplets with comparably high velocities. However, also the bigger droplets show an emphasis on higher velocities, but a significant lower number of droplets are identified in this size range. The velocity scatter of the smaller droplets is bigger which is generally valid for the results of the conducted experiments. However, it is noteworthy that for these particular depicted conditions only a very limited number of droplets with medium velocities between v ≅ 0.2 – 0.5 m/s was detected while the number of droplets with lower velocity at small diameters is again increased.

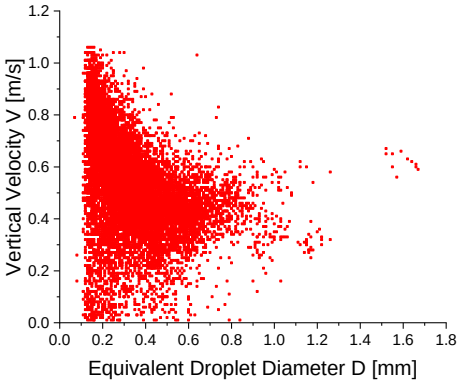
As was already mentioned before, the overall number of detected droplets is significantly increased at a higher pressures in comparison to the previous conditions. The described pattern changes with increasing pressure. The depicted trend is also valid for the distributions that are

not further displayed here. In all cases, the measured velocity amplitude is bigger for smaller droplets. As displayed, with increasing droplet size the scatter gradually diminishes, and the distribution approaches the average velocity value which in the displayed cases lies at v = 0.55 m/s and 0.4 m/s for p = 15 bar and 20 bar, respectively. It is obvious from the diagrams that a lot of droplets with velocities close to 0 were identified. This number increases with increasing pressure and shifts the distribution strongly towards small velocities. This is especially true for the depicted test run at p = 30 bar where the average velocity is even lower as already discussed before. Due to the reasons described before, this trend might be partially pronounced by possibly falsely identified objects like the liquid depositions and the velocity bias. Nonetheless, the general trend follows the expectations caused by the decreasing superficial vapor velocities with increasing pressure.

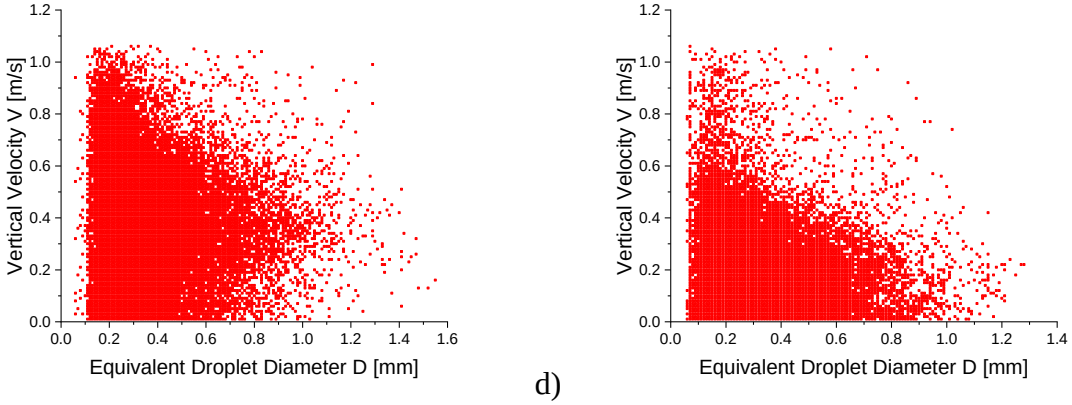
(Cumo et al. 1971) deduced from their experiments that the vertical droplet velocity is independent of their diameter. They found that there is a significant scatter but average velocities are independent of the diameter and always close to the vapor velocity, indicating very small or no slip between the two phases. These observations could not be fully confirmed with the present data sets. Looking at the mean velocities of droplets with the same diameter there is an average absolute deviation of about 16% between the overall average velocity and the average velocity of the different size classes across all test runs. The deviation differs between 9% and 23% of absolute values. While the differences are not huge, they cannot be neglected as insignificant.



a)



b)



c) d)

Figure 5.7: Droplet vertical velocity vs. equivalent diameter for a) p = 11 bar, T_S-T_{in} = 17 °C, q = 47.5 kW/m², and G = 66 kg/(m²s), b) p = 15 bar, T_S-T_{in} = 17 °C, q = 44.6 kW/m², and G = 66 kg/(m²s), c) p = 20 bar, T_S-T_{in} = 17 °C, q = 42.9 kW/m², and G = 66 kg/(m²s) (source: (Köckert et al. 2024b)), d) p = 30 bar, T_S-T_{in} = 17 °C, q = 37.1 kW/m², and G = 66 kg/(m²s)

5.1.5.2 **The Connection between Droplet Lateral Velocity and Diameter**

For the lateral velocity, the same tendencies are observable. The overall number of smaller and medium droplets is significantly higher and so is the scatter in comparison to bigger droplets. With increasing droplet size, the distribution approaches the mean velocity value close to 0. The qualitative distribution is thereby independent of pressure, inlet subcooling, and heat flux variations and is depicted in Figure 5.8.

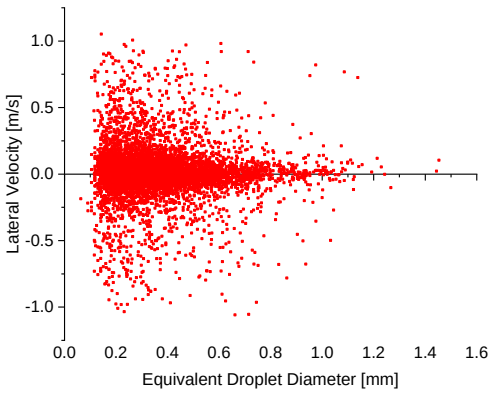


Figure 5.8: Droplet lateral velocity vs. equivalent diameter for p = 11 bar, T_S-T_{in} = 17 °C, q = 47.5 kW/m², and G = 66 kg/(m²s) (source: (Köckert et al. 2024b))

The observations partially disagree with (Schnittger 1982). He claims that the lateral velocity increases with increasing droplet size and that a more pronounced velocity profile can support

lateral movement of droplets. He explained that generally the droplets in the PDO area are comparably small and the velocity profile is relatively flat so that the lateral droplet movement is largely suppressed. For a direct wall droplet interaction or deposition, mainly the droplets in the direct vicinity of the wall can be considered, according to his explanations. (Ganić 1976) calculated that smaller droplets will be directly pushed out of the wall boundary layer due to repulsive forces caused by a stronger evaporation on the droplet side closer to the wall. Bigger droplets on the other hand have a better chance of reaching the wall and deposit due to their bigger inherent mass. (Chen et al. 1977) also assumed that only bigger droplets have the possibility to deposit on the wall. The accuracy of these statements could not be investigated since possible deposition behavior could not satisfactorily captured. However, the higher lateral velocities for smaller droplets in combination with the described observation of bigger droplets being mainly located in the center region of the flow leads to the assumption that in the investigations smaller droplets are more likely to enter the wall boundary layer.
A possible reason for the higher scatter and higher vertical and lateral velocities might be that smaller droplets are more prone to follow the turbulences of the main flow. Bigger droplets however, with more permanent weight, that therefore are expected to carry more possible momentum e.g., from the initiation process, may on the contrary behave more resilient against those turbulences.

5.1.6 Assessment of Theoretical Prediction Models

In this subchapter, the described results of the droplet behavior investigation are compared to theoretical models that are used in the literature and in some cases also in thermohydraulic system codes. The results of this comparison and possible differences are discussed. The focus lies on the droplet diameter and vertical velocity as most of the available models take those two aspects into consideration when describing droplet PDO behavior.

5.1.6.1 Comparison of Measured Equivalent Droplet Diameter and Theoretical Models

The equivalent droplet diameter average values are presented in Table 5.2 at varying system pressures. Despite increasing pressure, no significant change in the average droplet diameter is observed. It varies among different pressures but remains within a range of 0.3 to 0.4 mm. Additionally, the table indicates the calculated droplet diameters of various correlations, i.e. the model of (Guo and Mishima 2002) and the calculation of the droplet size based on the critical Weber number by (Styrikovich et al. 1980) and by (Isshiki 1959) as suggested by (Groeneveld 1972). For these models, the homogeneous assumption was used in the calculation with bulk vapor properties for data points with equilibrium qualities > 1. Furthermore, the droplet diameter as calculated in the KIT PDO mechanistic model which is described in subsection 6.1.2, is presented. Two limitations of the first three mentioned correlations should be noted. Although the correlations are officially valid in the entire PDO area, the physical properties

they are based on are taken from conditions that are actually present close to the point of dryout. However, in the conducted experiments only at low to medium pressure the window of investigation was close to the point of dryout (within 7% increase in vapor quality from the quality at dryout). With increasing pressure this number increases significantly up to 68% for a pressure of p = 30 bar. Furthermore, it is noteworthy that these correlations, contrary to the calculations in the KIT mechanistic model, do not consider the reduction of droplet size due to evaporation processes in the PDO region. However, the mechanistic model is limited in its applicability to certain experimental conditions. Therefore, only at very few test runs, the model could be used for the assessment.

The model used by Styrikovich and Isshiki calculates the droplet size solely based on a pre-determined Weber number. It is assumed that the droplet breaks up into two droplets of approximately the same size when this number is exceeded. Guo's model is more comprehensive and takes surface tension, void fraction, vapor velocity as well as density and viscosity ratio into account but also does not consider the droplet size reduction as a result of continuous evaporation with increasing distance to the onset of dryout. Nevertheless, all models describe a droplet size decrease with increasing pressure with an exemption of the pressures of p = 11 and 15 bar. This is in accordance with physical expectations as postulated e.g., by (Groeneveld and Snoek 1986) since increasing pressure results in a decrease of surface tension and therefore in smaller droplets. Furthermore, the increased pressure increases the vapor density as well, resulting in higher We numbers. This means that there is more droplet break up and thus smaller droplets. Additionally, with increasing pressure the axial distance between onset of dryout and window of investigation is increased as well. This leads to the assumption of decreasing droplet diameters due to continuous evaporation along the flow channel although this mechanism is not always taken into account, as described. However, those expectations contradict the results of the conducted measurements. Although test conditions are not entirely the same across all pressures, a decrease in average diameter is expected following the physical mechanisms. Different reasons can be found to explain this discrepancy. (Andreani and Yadigaroglu 1994) noted that in the dispersed flow film boiling regime the droplet size might be significantly influenced not only by physical properties and droplet generation mechanisms but rather by break-up mechanisms along the way. In addition, the flow behavior at the spacers could affect the droplet behavior and appearance. A possible reason might also lie in the image analysis as increasing pressure leads to an increased number of interfering objects. These objects may not have been adequately filtered, resulting in a potential distortion of the droplet spectrum. However, (Cumo et al. 1974) found in their experiments a similar trend for the influence of pressure on data points with similar vapor qualities. The vapor qualities in the present experiments are not exactly the same. However, they are close to each other, lying between about x = 1.0 and 1.2 over the entire parameter range. Cumo found that for reduced pressures below $p/p_c = 0.7$ the average diameter of the droplets remains almost constant while above this value the diameter starts to significantly decrease when approaching unity. All the conducted test runs with the exemption of p = 30 bar ($p/p_c = 0.74$) lie below the reduced pressure

of 0.7 and therefore fulfill the conditions in Cumo's observations. Across the entire parameter range, including the test runs with different inlet conditions that are not depicted in the table, the Guo correlation provides the most precise predictions compared to the measured values with an absolute average deviation of 23% and a minimum of 8% at a pressure of 20 bar. At medium and low pressures, it overestimates the droplet diameter and underestimates it at high pressures due to diameter reduction. The Styrikovich correlation however shows better agreement with the measured values in the range of higher pressures with an overall minimum deviation of 2% at p = 27.1 bar. Overall, it has an average absolute deviation of 37%. When choosing Isshiki's critical We number, the results lie in between Guo's and Styrikovich's correlations. The smallest deviation also occurs at p = 27.1 bar, where the measured diameter is underpredicted by 12%. The absolute average deviation lies at 25%. The droplet sizes calculated using the KIT model significantly exceed the droplet size in all applicable test runs, resulting in the largest average deviation of 137% across the entire pressure spectrum at a minimum of 50% at the highest pressure. This shows further potential for improvement.

Table 5.2:Measured average equivalent diameter and comparison with droplet size models

G [kg/m²s]	**T_{sub}** [°C]	**p** [bar]	**q** [kW/m²]	**d_{meas}** [mm]	**d_{Guo}** [mm]	**d_{Sty}** [mm]	**d_{Issh}** [mm]	**d_{KIT}** [mm]
66	17	11.0	47.5	0.363	0.448	0.528	0.457	0.999
		15.0	44.6	0.323	0.452	0.542	0.470	-
		20.0	42.9	0.375	0.404	0.483	0.419	-
		27.1	37.6	0.353	0.301	0.359	0.311	-
		30.0	37.1	0.314	0.236	0.278	0.241	0.470

A different approach in the existing literature is the utilization of droplet diameter distributions instead of an average diameter as discussed in chapter 2.

As indicated in the literature review, the present results were compared to the suggested droplet diameter distributions from (Cumo et al. 1974) based on the most probable diameter and (Meholic 2011) which is based on the maximum diameter. Representative examples of this comparison are given in Figure 5.9, presented as probability functions over the equivalent droplet diameter. For the Cumo distribution, two distributions besides the measured are depicted. The red curve shows the distribution when the measured most probable diameter is used, while the blue curve is based on the calculated most probable diameter, using Equation (0.45). The here called Meholic distribution (although it was also used by (Ganić and Rohsenow

1977) before) is shown in Figure 5.9c) and d). The maximum measured diameter was used to produce the distributions. As discussed in Appendix B.5, Meholic suggested to divide the distribution into five volume weighted bins, all of the same size and a correlating characteristic diameter for each bin to account for the different expected droplet sizes under PDO conditions. Those characteristic diameters can be used for further modeling. In the left exemplary diagram, the bin limits are shown with the black dashed line and the corresponding characteristic diameters for each bin with the red diamond. The concrete numbers are given in Appendix C. The sizes of the bins differ due to the volume weighting.

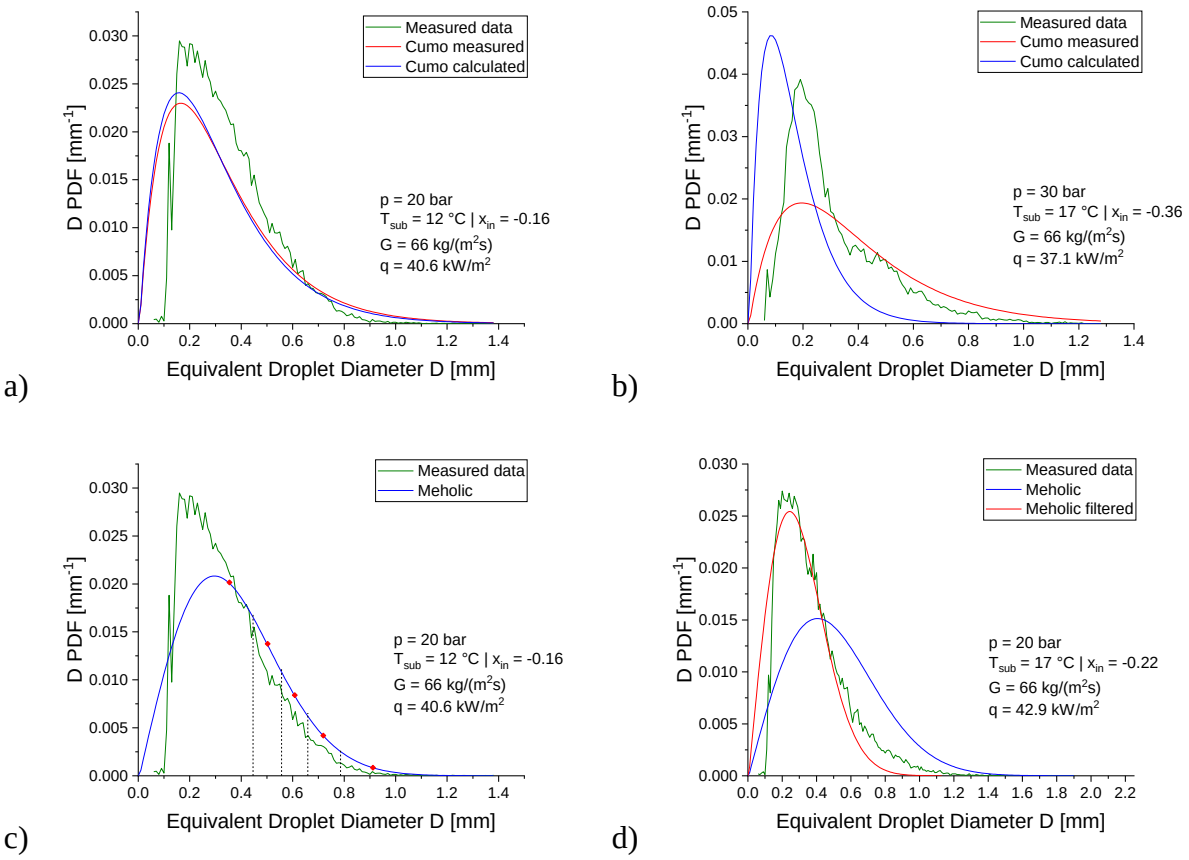


Figure 5.9: Probability distribution functions for the droplet diameter with a) and b) the Cumo model at different test conditions; c) and d) the Meholic model at different test conditions

An overall qualitative good agreement was observed across the different measurements, as is indicated in the diagrams on the left side for both distribution approaches. In case of the calculated most probable diameters by (Cumo et al. 1974), there is a decrease in diameter observable with increasing pressure. This suggests a shift of the distribution to lower diameter values as is expected from a physical understanding. However, it does not necessarily reflect the findings in their own experiments and in this thesis as discussed before. Instead, it leads to a bigger average deviation between the calculated and the measured distribution. This is shown

in the diagram in Figure 5.9b). For the Meholic distribution, the maximum measured diameter was used in the creation of the distribution. However, it was found that those diameters sometimes stand alone and are only detected on very few occasions, while the vast majority of measured data points was found having smaller diameters. This leads to the assumption that those might be incorrectly determined droplets. Due to the discussed lack of assignability, this is very difficult to verify. However, when choosing a smaller maximum diameter at the point where the majority of measured data stops, an alternative distribution, called Meholic filtered in the diagram in Figure 5.9d), shows a better agreement with the measured data and usually captures the peak quantitively better than the unfiltered distribution, as indicated in the diagram. This shows that there is further potential in the data analysis with a different software version.
In conclusion, there are obvious differences when looking at a direct quantitative comparison between measured and calculated probability density functions of the droplet size. However, qualitatively those approaches seem to be a good alternative to modeling the PDO droplet size distribution and might give a more reasonable approach to the droplet behavior than the assumption of a single average diameter.

5.1.6.2 Comparison of Measured Vertical Droplet Velocity and Theoretical Models

This subchapter discusses the comparison of the measured vertical velocity with theoretical assumptions and models. First, the measured slip ratio is compared to selected correlations. The obtained experimental values are then used to assess a force balance model to determine the vertical droplet velocity as suggested by (Cumo et al. 1971).

Comparison of Measured and Correlated Slip Ratio

Table 5.3 contains the measured slip ratios as well as suggested slip ratios from the literature by (Ahmad 1970), (Groeneveld 1972), and (Yoder and Rohsenow 1983) for the above shown test parameters. The first two correlations are described in Appendix B.6. The last correlation was adapted by (Yu 2019) in the KIT PDO mechanistic model and is described in chapter 6.1.2. The results are shown as provided by Yu's model and are therefore limited again to certain test runs. Slip ratio values by Ahmad are denoted with the subscript Ahm while Groeneveld is displayed as Gro and Yoder and Rohsenow as Yoder/Yu.
Both, measured and calculated slip ratios with the exception of the one adapted by Yu are presented again for vapor saturation and wall temperature properties. For the slip ratio ranges, the first value is given by assuming superheated wall temperature conditions while the second value is calculated at thermal equilibrium conditions. It becomes obvious from the table that for the measured slip ratio this means that the calculated vapor velocities and therefore the slip are bigger for thermal equilibrium conditions. The models by Ahmad and Groeneveld however predict higher slip for superheated wall temperature conditions. Ahmad's model takes solely

the density difference of the two phases into consideration as driver for the slip ratio. The density difference increases from saturated vapor to superheated wall temperature conditions. (Groeneveld 1972) however stated already (see also Appendix B.6) that the model was developed based on pre-dryout annular flow data where the majority of the liquid phase is on the heated wall whereas at PDO conditions the remaining liquid is entirely entrained in the gas phase. At superheated wall temperature vapor conditions such as in the present experiments, the entrained droplets are very small and it can be expected that their vertical velocity mainly depends on the main vapor phase behavior. This effect is not considered in Ahmad's model and might be an explanation for the observed discrepancy. Since Groeneveld's model adopts Ahmad's theory and only adds a correction factor, the discrepancy is observed there as well.

Table 5.3: Measured and calculated slip ratios at G = 66 kg/(m²s) and T_S-T_{in} = 17 °C

p [bar]	q [kW/m²]	T_W [°C]	S_{meas} [-]	S_{Ahm} [-]	S_{Gro} [-]	$S_{Yoder/Yu}$ [-]
11.0	47.5	227.5	1.40 – 1.62	1.86 – 1.62	1.43 – 1.31	1.18
15.0	44.6	210.5	1.37 – 1.55	1.71 – 1.49	1.35 – 1.25	-
20.0	42.9	220.2	1.40 – 1.53	1.59 – 1.37	1.29 – 1.19	-
27.1	37.6	200.1	1.52 – 1.62	1.44 – 1.24	1.22 – 1.12	-
30.0	37.1	216.3	1.78 – 1.83	1.40 – 1.18	1.20 – 1.09	1.07

Despite these described discrepancies, all the slip ratio correlations follow the expected tendency of decreasing slip with increasing pressure whereas the measured slip ratio shows an opposite trend. Possible reasons for a certain distortion of the measurements were presented in subchapter 5.1.4.1. The slip ratios suggested by (Groeneveld 1972) are generally smaller than the ones proposed by the Ahmad correlation due to the introduced correction, as is discussed in Appendix B.6. Yoder's correlation as used by Yu provides even smaller slip ratios and lies slightly below the Groeneveld correlation for the selected test runs. The Ahmad correlation agrees well with the measurements at pressures of p = 11 and 15 bar regarding assumed equilibrium conditions. Due to the opposite trend, an increasing underprediction can be observed with further increasing pressure. At superheated wall temperature conditions, Ahmad overpredicts the measured slip ratio at lower pressures but underpredicts it again with increasing pressure. Groeneveld's correlation shows good agreement for the superheated wall temperature vapor conditions at the lowest two pressures but underpredicts the measured slip at all other conditions. Yu's adaption of the Yoder correlation shows significant underprediction of the measured slip ratio across the entire parameter range.

Comparison of Measured Vertical Droplet Velocities and Force Balance Based Calculated Velocity

The investigated ROI is comparably small in size. Therefore, it seems fair to assume that in the investigated area the droplet velocity is constant, and the droplets do not undergo significant acceleration. This means that the term on the right hand side in Equation (0.51) which is time dependent can be neglected as suggested by (Cumo et al. 1971). With the droplet diameter taken from the measurements, the droplet vertical velocities are calculated as presented in Table 5.4. In the calculations, the homogeneous model was used, with void fraction and vapor qualities set to 1 when vapor quality exceeds unity. Vapor saturation properties were assumed.

Table 5.4: Comparison of measured droplet vertical velocity obtained with the high-speed camera and calculated droplet velocities in m/s

G [kg/m²s]	T_{sub} [°C]	p [bar]	q [kW/m²]	$v_{d,meas}$	$v_{d,calc}$
66	17	11.0	47.5	0.75	0.84
		15.0	44.6	0.55	0.58
		20.0	42.9	0.40	0.36
		27.1	37.6	0.26	0.24
		30.0	37.1	0.19	0.20

The force balance was set for an ideal case of straight flow in which a droplet is of spherical shape and is entrained in an otherwise pure vapor flow. Nonetheless, the table shows that the calculated droplet velocities describe the measured vertical velocity very well. Across all test runs, including the ones that are not on display here, there is an absolute average deviation of 6%, with the overprediction at p = 11 bar being the highest deviation at 13%. Usually, the droplet diameter is unknown and must be determined using correlations or distributions. (Cumo et al. 1971) claimed the independency of the velocity from the droplet diameter as discussed before. However, trying different diameters for the otherwise same test conditions shows a significant sensitivity of the calculations to the droplet diameter which is also confirmed with the measurements presented in chapter 5.1.5. Therefore, applying correlations such as the ones discussed adds an additional uncertainty and therefore might lead to higher deviations.

5.2 Analysis of Thermal Non-Equilibrium

The following chapter presents the vapor temperature investigations that were conducted in the second test series with test section 2 to determine the thermal non-equilibrium under PDO

conditions. The integration of the utilized optical fiber within a stainless steel capillary into the flow channel, the test procedure, as well as the parameter range of the vapor temperature measurements were explained in the corresponding subchapters of chapter 3.
In this chapter, general observations are described and discussed including the chosen selection criterion for vapor temperature measurement points. The analysis results are presented and contextualized in the available literature and compared to available prediction models of thermal non-equilibrium.

5.2.1 General Observations Regarding the Vapor Temperature Measurements and Data Point Selection Criterion

It was mentioned before that the highest admissible wall temperature was slightly increased in the vapor temperature measurements which, in combination with the changed set-up, led to a bigger PDO area. The intension was to enhance the PDO test conditions for the fiber measurements. As indicated in subchapter 2.4.4 the main challenge in vapor temperature measurements at two-phase flow conditions is the influence of the liquid phase through wetting of the measurement surface. It was described that specially sheathed, single thermocouples were usually chosen in an attempt to determine the vapor temperature and therewith the thermal non-equilibrium. The use of single temperature probes makes it complicated to obtain a vapor temperature profile over a determined axial distance. Hence, the idea in this work was to first establish a reliable measurement system with a new measurement approach. Secondly, with the implemented construction using an optical fiber with dozens of measurement points in a close axial distance it was the goal to obtain a vapor temperature profile over a determined axial distance. However, also in those measurements a substantial influence of the liquid phase was observed. The majority of measurements yield temperatures around or slightly above liquid saturation. This indicates a wetting of the capillary with liquid. That assumption is supported by simultaneous optical recordings of the capillary with a high-speed camera. Nonetheless, unregularly dryout of the capillary could be observed.
The quality of those obtained measurement points yields big differences. This is shown in examples in Figure 5.10a) to c) as a function of temperature over time. Besides the actual measured vapor temperature, also wall and saturation temperature are depicted. Especially at low and very high pressure, only short and sudden temperature peaks were observable (see Figure 5.10c)). At very high pressures it is noticeable that measured vapor temperatures lie regularly and uniformly above the liquid saturation temperature. The difference of measured fiber temperature and saturation temperature is thereby increasing with increasing heat flux. However, sudden and irregular temperature peaks lead to the assumption that an influence of the liquid phase is still present despite the uniform temperature distribution above saturation. Generally, most measurements show high fluctuations with unregular temperature peaks (see Figure 5.10b)). Constant vapor temperature measurements on a regular basis were only

observable at pressures of p = 20 bar. At all other pressures, the quality of the measurements was usually prone to high fluctuations.

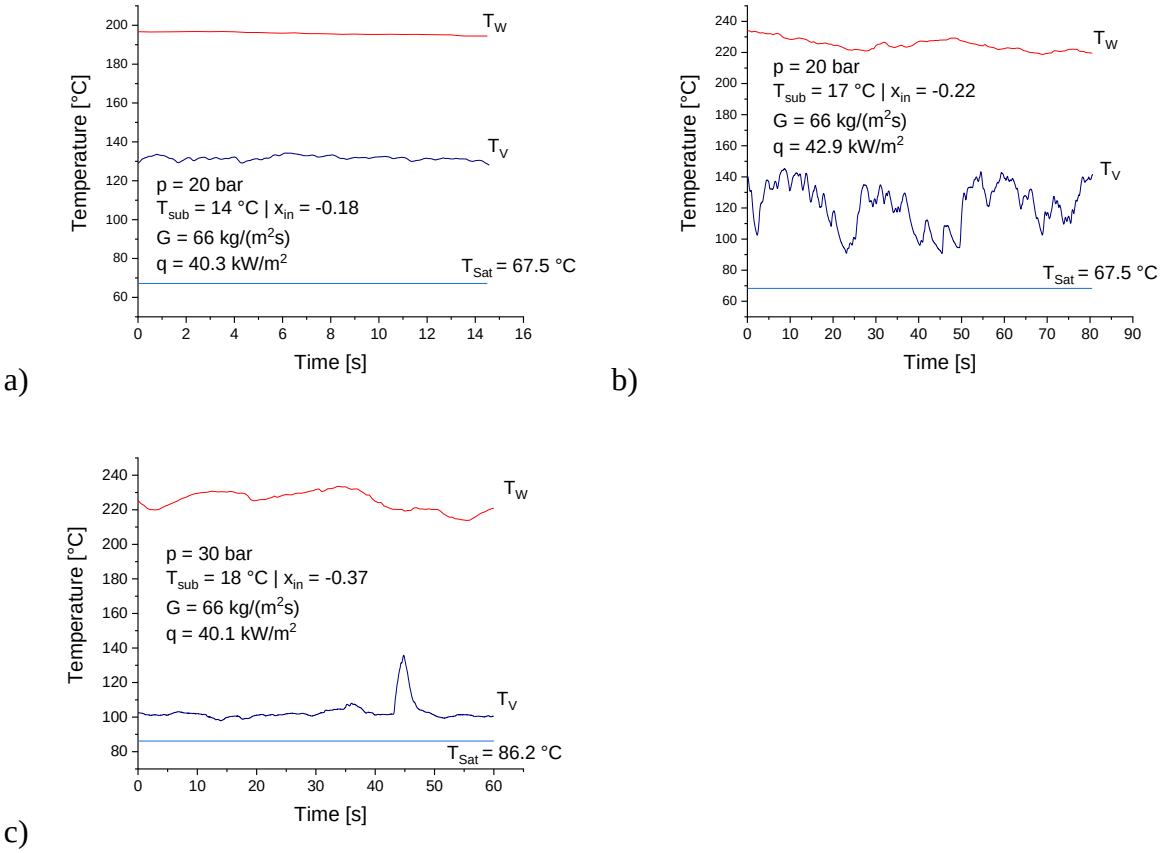


Figure 5.10: Vapor temperature measurement as a function of temperature over time including saturation and wall temperature for a) constant vapor temperature distribution, b) oscillating vapor temperature distribution, c) constant vapour temperature distribution with temperature peak

It can be found in the available literature (e.g., (Evans 1983; Unal et al. 1988)) that measurement points were categorized based on their quality. In this categorization also other factors like e.g., wall temperature were considered. (Nijhawan et al. 1980) included temperature peaks that asymptotically approach a certain value in their vapor temperature measurement analysis. When looking at the results in the present measurements, the scatter of the observed temperature peaks is too big and non-uniform, so a reliable result is not ensured. In the context of the aforementioned categorization, only measurement points of the highest category of achievable quality regarding vapor temperature measurement as well as flow stability are considered and displayed in this thesis.

Therefore, a conservative criterion for the present measurements was developed, that excluded a lot of possible data points but ensured a high quality of the eventually selected data. In subchapter 3.4.2 the time response characteristic was already mentioned. By inserting the

optical fiber into a capillary, the system is subject to a certain response inertia since the heat applied at the capillary outside needs to be transferred, mainly via heat conduction through the capillary wall, the small air gap between wall and fiber, and from the fiber outside to the fiber core, where the actual measurement takes place. The manufacturer of the fiber investigated the time response behavior of the fiber in a test using a steel capillary of 0.9 mm outer diameter with an inner diameter of 0.5 mm which equals the capillary's inside diameter in the present work. At a temperature difference of $\Delta T = 80$ °C, they measured a time delay of about 1 s. In the present work, a CFD simulation of the experimental conditions yielded a delay of max. 1.8 s for the investigated parameters. To ensure the correctness of the measured temperature, a conservative criterion was chosen that had to fulfill a max. vapor temperature amplitude of $\Delta T = 10$ °C over a minimum time frame of $\Delta t = 4 \cdot 1.8\ s = 7.2\ s$. In addition, the wall temperatures had to fulfill the same criterion. Furthermore, vapor temperatures had to exceed saturation temperatures. This guarantees data points that are based on stable measurement conditions without strong temperature changes that might be an indicator of liquid wetting behavior. The therewith selected measurement points qualitatively follow the example provided in Figure 5.10a) regarding the stability of vapor and wall temperature distribution. The axial distance to the closest thermocouple level of the heating tube differed between 2 and 28 mm, depending on the fiber measurement point position. It should be noted that this conservative approach might exclude valid data points with, in some cases, higher temperatures than the ones observed applying this criterion. Furthermore, measurement points that would fulfill the criterion but are only slightly above the saturation temperature (this includes also the above-mentioned measurements at high pressures) are neglected. Usually, sudden temperature peaks that are attached to those measurement points suggest a dryout behavior of the capillary and therefore an influence of liquid. Nonetheless, also the selected data points, fulfilling the criterion at high vapor temperatures, are occasionally preceded or succeeded by higher temperatures. However, the author believes that the chosen criterion ensures the overall highest achievable quality of the data considering the difficult measurement environment.

5.2.2 Results and Discussion of Vapor Temperature Data Points

The experiments investigating the vapor temperature yielded 285 overall data points, that fulfilled the above-described selection criterion. Seven of those data points were discarded since at least one corresponding wall temperature measurement had higher fluctuations than 10 °C during the measurement period. That leaves 278 data points at pressures of p = 15, 20, and 27.1 bar, of which 250 were generated at p = 20 bar and only one data point at p = 27.1 bar. It should be noted that a lot of those measurement points cannot be seen as independent since many were taken at the same test runs or very similar test conditions. All the data points at the different pressure conditions are displayed in Figure 5.11. The diagram shows the actual vapor quality over the equilibrium vapor quality and contains, besides the actual measurement points, also theoretical data points (black dots) at the assumption of thermal equilibrium. It can be seen

that the actual vapor quality lies in a very narrow area for p = 20 bar with one exemption that might still show a little influence of liquid, while it is further stretched for p = 15 bar. This might be caused by the different parameter range in the conducted test runs.

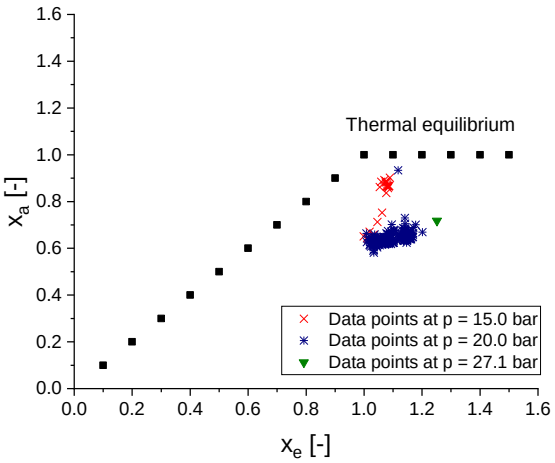


Figure 5.11: Actual vapor quality vs equilibrium vapor quality for all vapor temperature measurement points

The calculation of equilibrium and actual vapor quality was presented in Equation (2.6). With the measured vapor temperature, the enthalpy i_{va} and therewith the actual vapor quality can be determined. For the calculation of the vapor quality, using the maximum vapor temperature of the measurement points, as (Nijhawan et al. 1980) and (Unal et al. 1988) did, was compared to the utilization of the average vapor temperature of the measurement point. Due to the small admissible temperature amplitude, the difference was insignificant for the calculation of the vapor quality. Besides the temperature difference of vapor and saturated liquid, the thermal non-equilibrium is often displayed as the difference between equilibrium and actual vapor quality. The latter option is chosen for this thesis. Table 5.5 comprises the information about the test conditions as well as the overall number of measured data points, and the absolute and relative minimum, maximum, and average thermal non-equilibrium. For the relative deviation, x_a was taken as the reference value. The calculation was conducted as follows:

$$dev_i = \frac{(x_e - x_a)_i}{(x_a)_i} \tag{5.3}$$

Only absolute values were used for the considerations in the table.

Table 5.5: Parameter range of vapor temperature measurements including measured thermal non-equilibrium

G [kg/m²s]	p [bar]	T_{sub} [°C]	q [kW/m²]	Data points	x_e-x_a [-]	Rel. TNE [-]	
66	15.0	12-18	42.9-44.4	27	0.175	0.198	**Min**
					0.406	0.639	**Max**
					0.277	0.379	**Mean**
	20.0	14-19	40.2-44.2	250	0.184	0.197	**Min**
					0.532	0.838	**Max**
					0.456	0.710	**Mean**
	27.1	18	41.7	1	0.534	0.744	**Overall**

The table shows that the thermal non-equilibrium is significant throughout all test conditions. The minimum deviation lies at 20%, while the maximum and especially mean deviation are increasing with increasing pressure. This is somewhat surprising as the thermal non-equilibrium is expected to decrease with increasing pressure (compare e.g., (Lee and Chang 2008), (Yu 2019), or (Köckert et al. 2024a), among others). For a pressure comparison, it should be noted that the measurement parameters are different for these measurement points which could cause this observation. Furthermore, in those measurements the average distance from dryout to the vapor temperature measurement location increases with increasing pressure and with it the equilibrium vapor quality while the average actual vapor quality even slightly decreases (see also Figure 5.11). This means that the PDO area increases which leaves more time for the vapor to superheat and thus increase the thermal non-equilibrium.

Out of the 278 data points 93 overlapping data points were deduced which means that simultaneous vapor temperature measurements at different measurement positions were observed with a time overlap of at least 2 s which lies above the 1.8 s mentioned above. Simultaneous measurements were only observed at consecutive measurement positions. For the following observations and discussions, the vapor temperature measurement points are numerated with lower numbers being closer to the end of the heated length. This might seem counterintuitive as it means that the measurement point number increases further upstream. However, it simplifies the explanation of the generally observed trends, since the numeration remains the same for all cases, irrespective of 2, 3, or 4 overlapping measurement points. In Figure 5.12, the first measurement point in both curves is therefore the one closest to the end of the heated length.

In 21 of those 93 cases three simultaneous measurement points were observed and in one case even four. This means that in the overlapping measurements, an axial distance of 10 mm up to a maximum of 30 mm was covered, while the majority was at the lowest axial distance. Two different temperature distributions were observed for the cases with at least three overlapping measurements that are depicted in Figure 5.12. Most of the temperature distributions follow the blue pattern which means that the temperature keeps increasing with increasing distance to the end of the heated length. Occasionally however, there is a temperature extremum observable as displayed in the red curve in this figure.

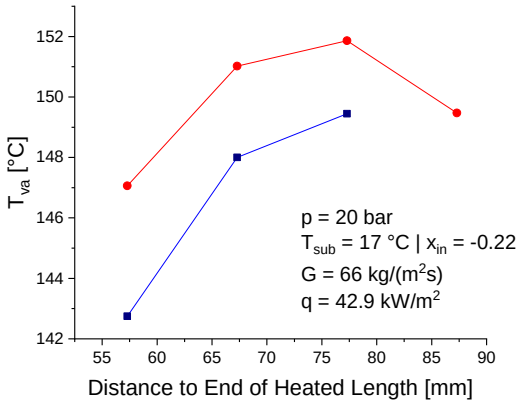


Figure 5.12: Measured vapor temperature distribution of blue: continuous temperature rise, red: with a temperature maximum

Usually, the temperature increases from the first measurement point, closest to the end of the heated length, to the next consecutive one. This temperature difference from the first to the second measurement point is more pronounced than the following consecutive temperature differences in case of three or four measurement points. In 58% of the cases, this first temperature difference is bigger than 3 °C and in 29% even bigger than 5 °C. The average lies at 4.4 °C. In only 10% of the cases, the following consecutive temperature difference is above 3 °C and not higher than 5 °C. The average drops to 1.5 °C and 2.4 °C for the case of 4 measurement points. A negative temperature difference between consecutive measurement points could be observed in only 8% between measurement point 1 and 2, but in 24% of the cases between 2 and 3 and in 100% between 3 and 4.

Some of the above-described observations may be surprising. Theoretically, it would be expected that the highest vapor temperatures are measured closest to the end of the heated length where the capillary should dry out first. All consecutive measurement points should have consistently lower temperatures than the ones above them despite the small axial distances. Different reasons can be considered for this behavior. The evaporation of droplets along the channel might lead to a cooling effect through increased vapor velocities and better heat removal. Another assumption is that the possible capillary dryout behavior might be responsible

for these observations. Based on the measured vapor temperatures, the capillary should be dried out entirely. However, it is covered by liquid most of the time and only dries out partially for unregular time periods. It is therefore assumed that the flow behavior rather than the vapor temperature is responsible for the dryout of the capillary e.g., turbulences that develop around the capillary. Since the flow is vertically upward, the chances of capillary dryout might be higher closer to the test section inlet. This is supported by the fact that 79% of the measurement points lie in the lower half of the capillary closer to the test section entrance. However, the two lowest measurement points are also barely dried out as well. Possibly, flow conditions that might lead to capillary dryout must first build up which might happen at the very beginning of the capillary. The fact that only consecutive measurement points are dried out, vapor temperatures are higher and differences between two points smaller closer to test section inlet also supports the theory that flow behavior leads to partial capillary dryout, which occurs first at the lower end of the capillary and leads to locally very similar conditions.
Nonetheless, the fact that only in one third of the cases it was at all possible to simultaneously measure vapor temperatures at different and only consecutive positions shows how difficult those measurements were and that a regular vapor temperature profile was impossible to obtain since most of the time only small parts of the fiber capillary were dewetted.

5.2.3 Assessment of Theoretical Prediction Models

The measured vapor temperature data points are used to evaluate the thermal non-equilibrium calculated by the widely used correlations of (Groeneveld and Delorme 1976) and (Chen et al. 1979). Therefore, the actual vapor qualities of those two correlations are compared to the actual measured vapor qualities. The results can be observed in Figure 5.13a) – d). Figure 5.13a) shows the calculated over the measured actual vapor quality for both correlations and all pressures. The diagrams in b) to d) show the measured as well as the correlated actual vapor qualities as a function of the equilibrium vapor quality for each pressure individually. The correlation developed by Groeneveld and Delorme is simply denoted as Groeneveld.
Different behavior can be observed for the two correlations. While the actual vapor quality remains fairly constant in the CSO correlation it shows a linear increase with increasing equilibrium vapor quality for the Groeneveld & Delorme correlation. Most of the data points of both correlations lie within a reasonable scope of 30%. However, while Groeneveld mostly overpredicts the measured actual vapor quality and increasingly does so at higher pressures, the CSO correlation shows a slight underprediction at a pressure of p = 15 bar where the measured vapor qualities have higher scatter. At p = 20 bar, it also slightly overpredicts the measured data but shows overall very good agreement. The data point at p = 27.1 bar is shown in the diagrams for the sake of completeness. However, no evident conclusion can be drawn regarding the correlation behavior at that pressure.

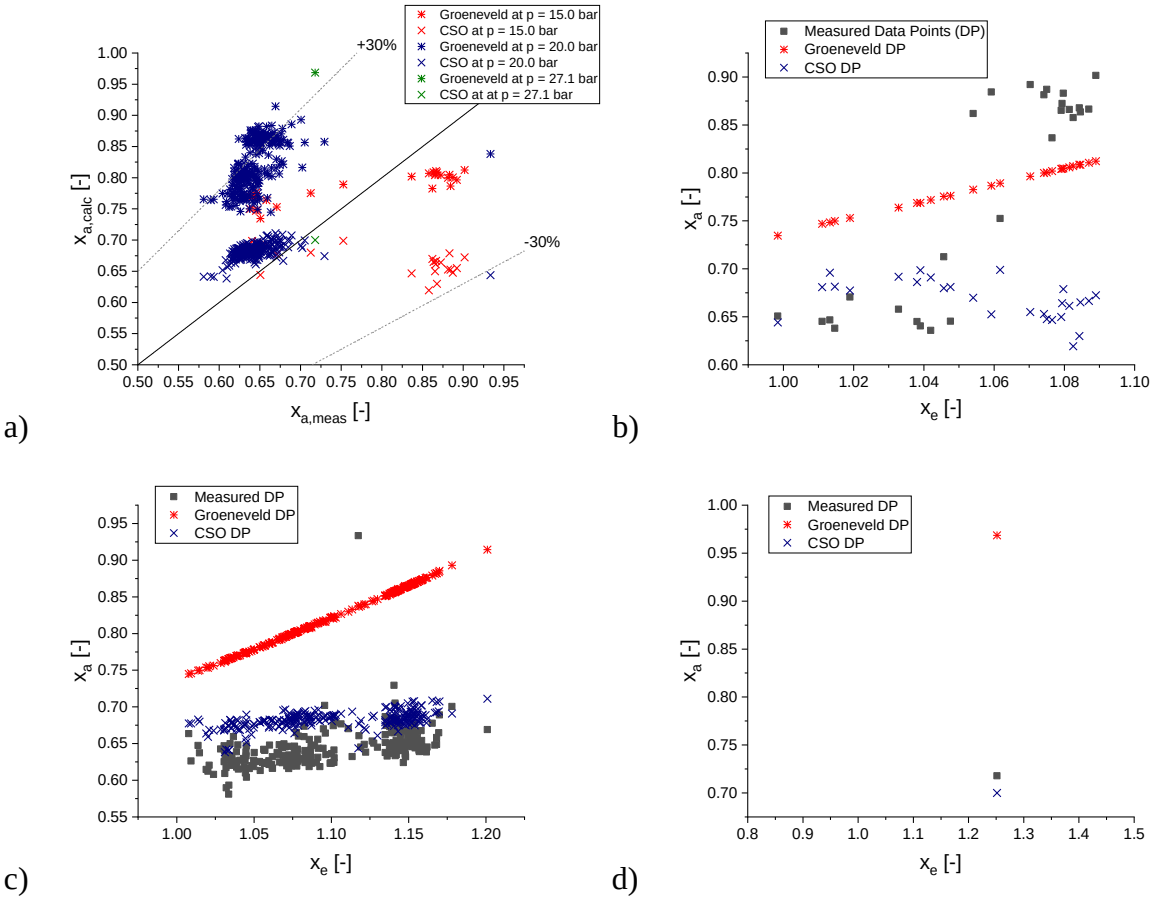


Figure 5.13: a) Calculated over measured actual vapor quality for different pressure conditions; actual over equilibrium vapor quality for measured and calculated data points at b) p = 15.0 bar, c) p = 20.0 bar, d) p = 27.1 bar

Reasons for the deviation of the correlation could be found in their partially empirical nature in combination with a lack of available data in regard to thermal non-equilibrium. Furthermore, factors like the geometry, extrapolation of data outside the original parameter range, and the assumption of homogeneous flow were discussed in previous chapters for the model of (Groeneveld and Delorme 1976). (Chen et al. 1979) added an empirical coefficient in their calculation of x_a to account for the pressure dependency. Furthermore, their correlation is based on water data.

Nonetheless, the correlations show an overall good agreement with the experimental data. This is confirmed by the average, RMS, and standard deviation compiled in Table 5.6.

Table 5.6: Model assessment with experimental data of the actual vapor quality for different pressures

G [kg/m²s]	p [bar]	T_{sub} [°C]	q [kW/m²]	Data points	Groeneveld	CSO	
66	15.0	12-18	42.9-44.4	27	0.02	-0.12	**dev_m**
					0.12	0.15	**σ**
					0.12	0.19	**RMS**
	20.0	14-19	40.2-44.2	250	0.28	0.06	**dev_m**
					0.06	0.04	**σ**
					0.28	0.07	**RMS**
	27.1	18	41.7	1	0.35	-0.02	**Overall**

As discussed before the table shows that the Groeneveld correlation usually overpredicts the actual vapor quality. However, the agreement at a pressure of p = 15 bar with a mean deviation of only 2% and an RMS deviation of 12% is very good. The overprediction increases with increasing pressure as could be seen in the diagrams above. The CSO correlation however underpredicts the vapor quality at an average of 12% at p = 15 bar, while it shows very good agreement at higher pressures where it overestimates x_a by average of only 6 and 2% for p = 20 and 27.1 bar, respectively. The RMS shows also very little variation being at 7% for p = 20 bar.

6. Description and Assessment of the KIT Models

As mentioned before, a PDO correlation as well as a mechanistic PDO model were developed at the IATF. In the course of this chapter, the general structure of the two models relevant to this investigation is described first. The second part of this chapter is used to evaluate both, the correlation as well as the mechanistic model with the data obtained in this thesis and assess their performance for the different test runs regarding the investigation of the PDO heat transfer coefficient.

6.1 Description of the KIT Correlation and Mechanistic Model

The following subchapters give an overview of the structure of the PDO correlation and an introduction of the mechanistic model. It should be noted that only the main aspects of the models and their alteration from existing models in the literature are described to provide a general understanding. For further details, it is referred to the original work performed by Meiqi Song and Dali Yu (Song 2021; Yu 2019). Preliminary versions and parts of the mechanistic model were also published in (Yu et al. 2018) and (Köckert et al. 2021).

6.1.1 Introduction of the KIT PDO Correlation

The PDO correlation developed by (Song 2021) makes use of the already described Dittus-Boelter form of the convective heat transfer correlation. It combines the two-phase Reynolds number Re_{TP}, the Prandtl number at wall temperature Pr_W, and the thermal equilibrium quality x_e. To compensate for possible inaccuracies of the constant factors, correction factors were developed by stepwise identifying relevant dimensionless numbers and their influence on the heat transfer. Eventually, 3 correction factors are introduced with the first one compensating the dependency on the two-phase Reynolds number, the second one the influence of the Prandtl number, and the third one covering the influence of the vapor quality by taking the equilibrium vapor quality into account. The final form of the PDO correlation is expressed as below:

$$Nu = F_1 \cdot F_2 \cdot F_3 \cdot (0.023\ Re_{TP}^{0.8}\ Pr_W^{0.4}) \tag{6.1}$$

with the two-phase Reynolds number being expressed as:

$$Re_{TP} = \frac{G\ D_{hy}}{\mu_{vs}}\left[x_e + \frac{\mu_{vs}}{\mu_l}(1 - x_e)\right] \tag{6.2}$$

and the correction factors:

$$F_1 = 8.346 \cdot 10^{-03}\, Re_{TP}^{0.319}$$
$$F_2 = \max(0.795\, Pr_W^{-1.752}, 0.809\, Pr_W^{1.287}) \quad (6.3)$$
$$F_3 = \min(0.715\, (1 - x_e)^{-0.678}, 1.0)$$

6.1.2 Introduction of the KIT Mechanistic PDO Model

The mechanistic model was developed to describe the heat transfer in the PDO region for tube geometry and is valid for different fluids. In this subchapter, only the main idea of the model as well as relevant sub-correlations used for the slip ratio and droplet size calculation are displayed here. A more comprehensive summary of the model can be found in Appendix B3.
The model is based on the analysis of heat as well as mass transfer mechanisms. It considers the 3 main heat transfer mechanisms in PDO: i) convective heat transfer from wall to vapor, ii) from vapor to droplets and iii) direct contact of droplet and heated wall.
The PDO area is axially divided into a developing region which marks the vicinity after the point of dryout and the fully developed region which in this case starts after a continuous vapor phase is established on the heated wall. Furthermore, the cross section of the channel is divided once more into a core region in the channel center and a film region close to the heated wall. It is assumed that most of the droplets entrained in the flow are concentrated in the core region within the fully developed PDO area due to quick evaporation of droplets in the superheated film region close to the wall. The superheating of vapor on the other hand changes vapor temperature and velocity, especially in the film region. This leads to a higher wall temperature. The division of the flow channel is illustrated in Figure 6.1.

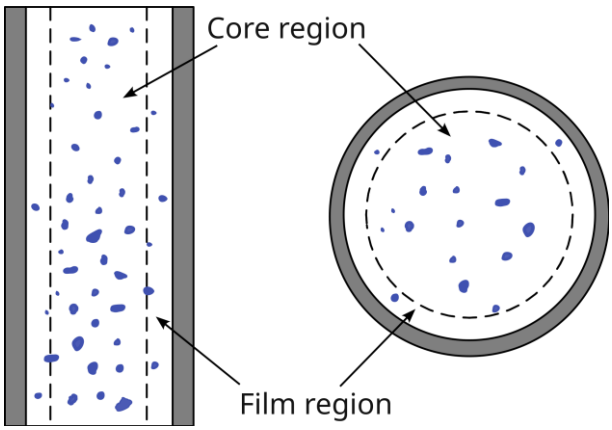


Figure 6.1: Division of a tubular flow channel into film and core region (adapted from: (Yu 2019))

For the model development only PDO data points were accepted, using the earlier described criterion of α_v > 80% established by (Groeneveld 1975). However, in this model the selection

was even more strict by including only test runs at which the dryout void fraction exceeded 0.8 already. The void fraction was thereby calculated using the following equation:

$$\alpha_v = \frac{1}{\frac{1-x_a}{x_a}\frac{\rho_v}{\rho_d}S + 1} \tag{6.4}$$

with the slip ratio S determined according to (Yoder and Rohsenow 1983):

$$S = \frac{v_v}{v_d} = 1 + 2.31\left[\frac{\rho_d}{\rho_{va}}\frac{1}{x_a}\frac{q}{G\, i_{v-d}\, C_D}\frac{d}{D_{tube}}\right] \tag{6.5}$$

The actual quality is named x_a, while ρ_{va} and ρ_d describe the actual vapor and droplet density. v_v and v_d give the vapor and droplet velocity in flow direction whereas i_{v-d}, C_D, d, and D_{tube} describe the latent heat, the droplet drag coefficient, the droplet diameter and the inner tube diameter, respectively. The wall heat flux and mass flux were already introduced.

Droplet Diameter Calculation

The droplet diameter is calculated using an average value at every axial location along the flow and considering the number of droplets constant despite possible evaporation. Furthermore, the droplets are considered as non-deformable spheres, not taking into account droplet break-up or coalescence in the PDO region. In this model, the droplet size diameter depends on the droplet size and vapor quality at dryout as well as on the actual vapor quality in the following manner:

$$\frac{d_{poi}}{d_{do}} = \left(\frac{1-x_a}{1-x_{do}}\right)^{\frac{1}{3}} \tag{6.6}$$

The droplet diameter at dryout is determined using the proposed method of (Yoder and Rohsenow 1980):

$$\frac{d_{do}}{D_{tube}} = \frac{1}{x_{do} - 0.1}\left(\frac{d_c}{D_{tube}}(x_A - 0.1) + \left(\frac{\rho_d}{\rho_v}\right)^2 \frac{We_c}{\left(S_{lf}-1\right)^2}\frac{\rho_v\,\sigma}{G^2 D_{tube}}\frac{1}{\left(\frac{\rho_d}{\rho_v}\frac{1}{S_{lf}} - 1\right)} \cdot \left[\frac{1}{1 + x_A\left(\frac{\rho_d}{\rho_v}\frac{1}{S_{lf}} - 1\right)} - \frac{1}{1 + x_{do}\left(\frac{\rho_d}{\rho_v}\frac{1}{S_{lf}} - 1\right)}\right]\right) \tag{6.7}$$

with the tube diameter D_T, the critical droplet diameter d_c, the vapor quality at the onset of annular flow x_A, and the liquid film slip ratio S_{lf}. All properties are used at saturation. The critical We number is set to 6.5. For the detailed calculation it is referred to the original source or (Yu 2019).

Assessment of the KIT PDO Models

This chapter discusses the prediction quality of both models in regard to the obtained PDO data in this thesis with test section 1. The method of comparison is the same as used before in the other HTC model assessments. Also, the selection criteria to determine PDO conditions remain the same for the KIT PDO correlation whereas the criterion described in the previous subchapter is applied to the KIT mechanistic model.

6.1.3 Assessment of the KIT PDO Correlation

Table 6.1 comprises the deviation of the KIT PDO correlation proposed by (Song 2021).
It shows very good agreement with the HTC measured in test section 1 where the mean deviation lies at only 2% and also the RMS deviation is reasonably small. This is not surprising since the data for developing this correlation partially stem from this test series. Together with the Groeneveld correlation of 1972, it is the only conservative correlation of the selected models.

Table 6.1: Assessment results of the KIT PDO correlation with the experimental data in test section 1

Test Section	dev_m	σ	dev_{RMS}	Data Points
1	-0.02	0.22	0.23	7,825

The diagram in Figure 6.2a) depicts the calculated over the measured HTC. It proves a significant underprediction of the higher measured HTCs. As mentioned before, some of those might be still in the PDO developing region which could be an explanation for the high deviation. However, for HTCs below 1300 W/(m^{2}K) it shows good agreement with the tendency of slightly underpredicting the measured HTC but with the majority of the data points being within 30% deviation.
The mass flux influence in Figure 6.2b) shows that the lowest mass flux is comparably strongly underpredicted while the highest mass flux and thus lowest expected thermal non-equilibrium shows the lowest deviation. At mass fluxes higher than 500 kg/(m^{2}s), the measured HTC is

usually overpredicted with the highest overprediction at G = 1000 kg/(m^{2}s). When neglecting G = 1775 kg/(m^{2}s) due to the comparably low number of data points the average deviation decreases from that point with further increasing mass flux. The pressure influence shows higher deviations at the highest pressures. It is also comparably high for medium pressure of p = 19.5 bar. However, at medium pressure only very few data points are available in this test series and therefore the influence is not severe. As discussed before, the thermal non-equilibrium is less pronounced at higher pressure due to enhanced heat transfer. The data show that the correlation performs better at lower pressure with higher expected thermal non-equilibrium. On the other side it is assumed that thermal non-equilibrium is most severe at low mass fluxes and therefore shows potential for further improvement of the correlation.

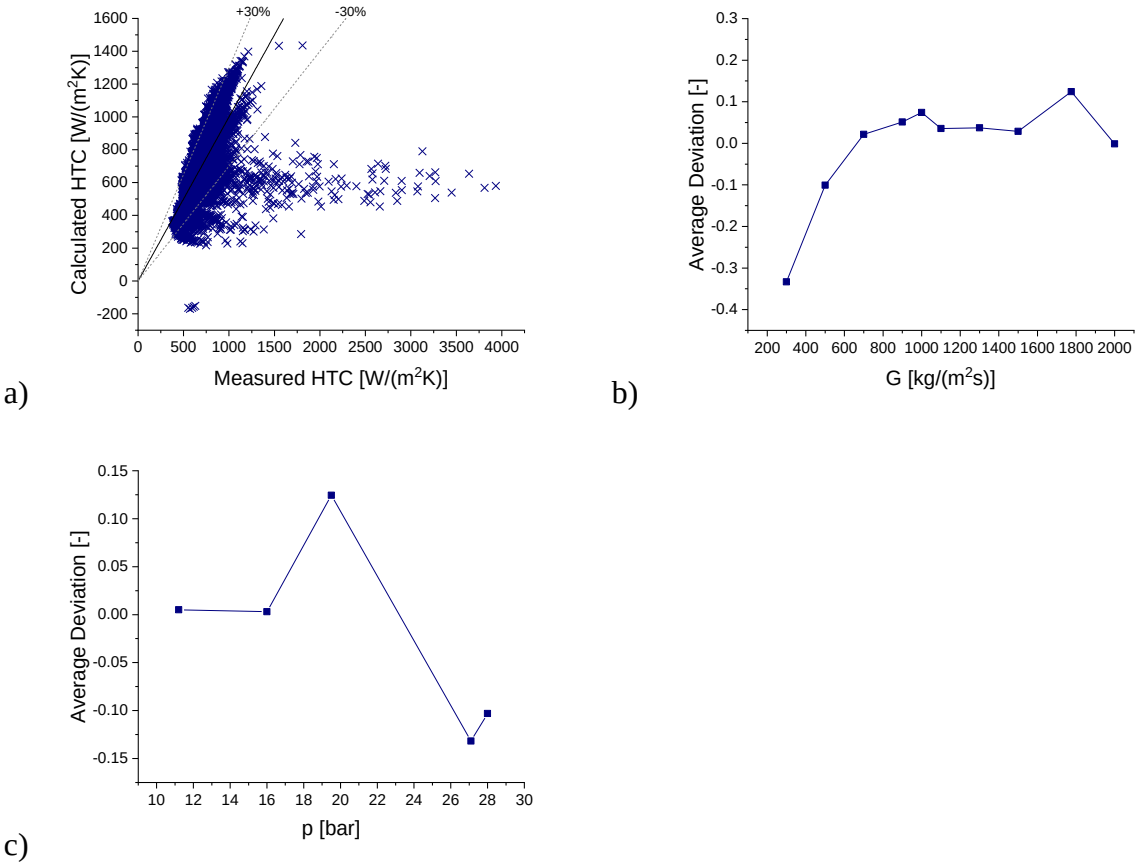


Figure 6.2: *Calculated over measured HTC for a) the steady-state test series in test section 1; Average deviation for the variation of b) mass flux, c) pressure*

6.1.4 Assessment of the KIT Mechanistic PDO Model

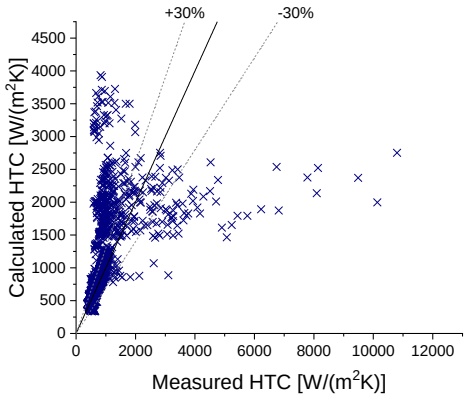
The deviations between measured and calculated HTC are presented in Table 6.2. The HTC in the model is calculated using the difference of wall and saturation temperature as by the author's suggestion.

The data point criterion in the mechanistic model was discussed in the previous chapter and leads to less selected data in all test series. The steady-state test series in test section 1 is

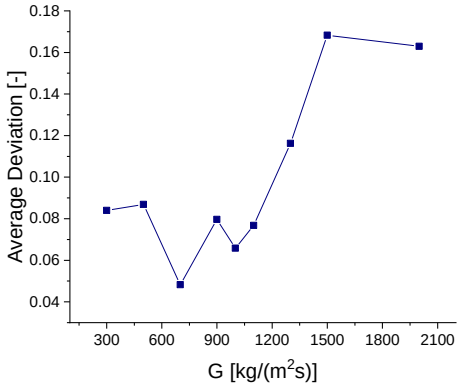
predicted very well with a slight HTC overestimation of 10% on average and RMS deviations below 40%. Parts of this test series were utilized in the model development. Nonetheless, the diagram in Figure 6.3a) shows some scatter. In the main range between 500 and 1000 W/(m^{2}K) some significant overprediction is observable. Several data points that can be attributed to the developing PDO region with HTCs significantly beyond 1000 W/(m^{2}K) are clearly underpredicted. The general overprediction at fully developed PDO while underpredicting the developing region was also found in (Yu 2019), where only parts of the data of this thesis were used for the model assessment. Nonetheless, an average deviation of 10% proves that the prediction capability for the vast majority of the data points is very good.

Table 6.2: Assessment results of the KIT PDO mechanistic model with the experimental data in test section 1

Test Section	**dev$_m$**	**σ**	**dev$_{RMS}$**	**Data Points**
1	0.10	0.34	0.36	6,461



a)



b)

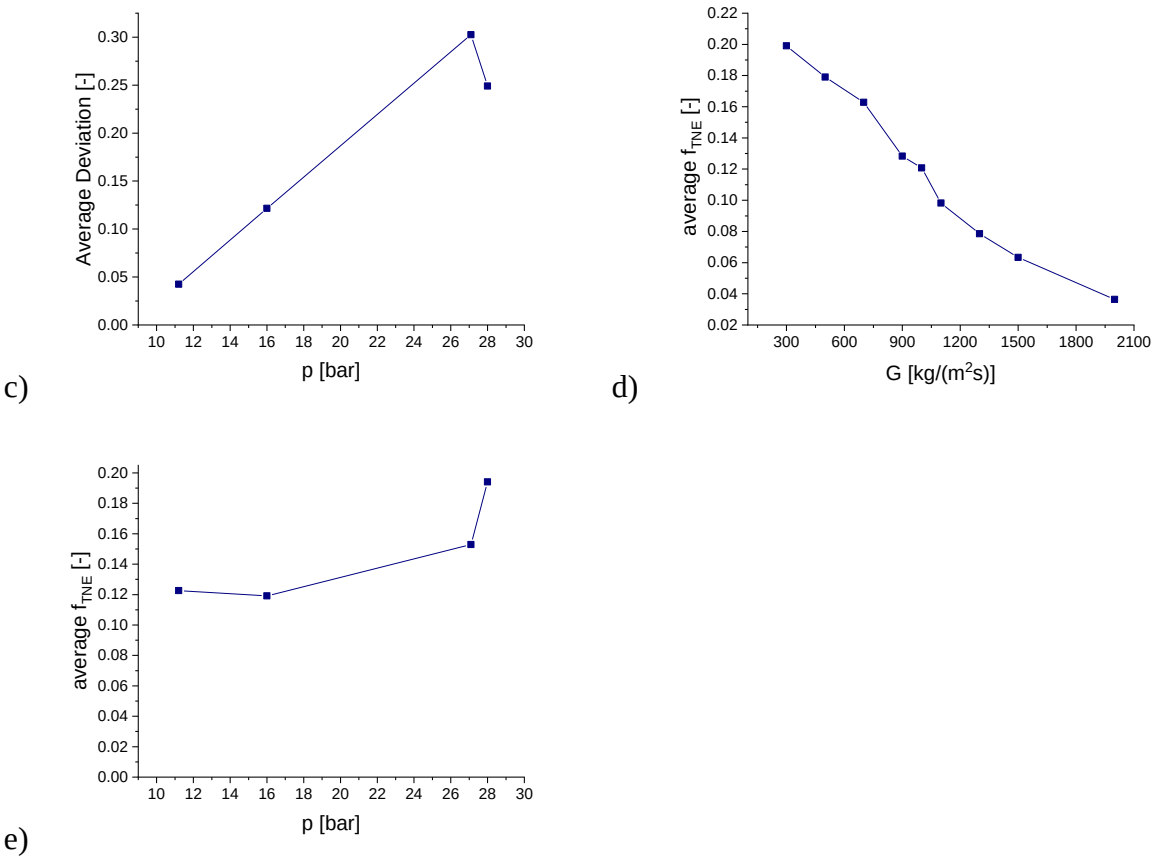


Figure 6.3: Calculated over measured HTC for a) the steady-state test series in test section 1; Average deviation for the variation of b) mass flux, c) pressure; TNE factor for the variation of d) mass flux, e) pressure

The diagrams in Figure 6.3b) and c) indicate that the model shows highest average deviations at conditions with the lowest expected thermal non-equilibrium, i.e. highest mass fluxes and pressures. On the other hand, low mass flux and pressure conditions where the thermal non-equilibrium is considered to be most pronounced are predicted very well, despite the fact that the vapor temperature calculation indicates further potential for improvement. This is proven when the HTC is determined using the calculated vapor temperature instead of the saturation temperature which leads to significantly worse results. The deviations using the saturation temperature, as mentioned above, increase with increasing pressure and reaches maxima at the highest pressures of 30% and 25%, respectively. The mass flux variation leads to diffusive behavior between 500 and 1100 kg/(m^{2}s) and increases from there to the highest mass fluxes. Nonetheless, the deviations stay within a maximum of 17%. In (Köckert et al. 2024a), a thermal non-equilibrium factor (TNE factor) was introduced as follows:

$$f_{TNE} = \frac{\mathrm{T_{v,calc}} - T_S}{\mathrm{T_{W,calc}} - T_S} \tag{6.8}$$

This factor varies between 0 (thermal equilibrium conditions with no vapor superheating) and 1 (highest thermal non-equilibrium with highest vapor superheating). It should quantify the grade of thermal non-equilibrium. The development of this factor with the given model is presented in Figure 6.3d) and e) for the variation of mass flux and pressure, respectively. A lower TNE factor can be interpreted as the result of lower vapor and wall temperatures, leading to higher HTCs. In that sense, when combining the results of Figure 6.3b) and d), it can be concluded that the model underpredicts TNE factor at the highest mass fluxes, resulting in an overprediction of the HTC. However, the general prediction trend of the thermal non-equilibrium and therefore the TNE factor is correct. This is not the case when examining the development of the TNE factor with pressure variations. As discussed before, the lowest thermal non-equilibrium is expected at the highest pressures. However, Figure 6.3e) shows highest TNE factors at the highest pressure. Simultaneously, the overprediction of the HTC is also highest at the highest pressure. Therefore, the modeling of the thermal non-equilibrium seems not to be the direct reason for the overprediction at higher pressures.

Overall, it can be concluded that the mechanistic model shows good agreement with the tube data and follows the right trend despite observed scatter and underprediction of data in the developing PDO region. The modeling of the thermal non-equilibrium proves to have further potential.

7. Conclusion and Outlook

For this thesis, PDO experiments in two different geometries were conducted with the model fluid R-134a. The experiments in circular tube geometry aimed at extending existing experimental HTC data bases by covering a broad parameter range. They were conducted as steady-state experiments and additionally considered rewetting behavior. The experiments with the annular test section focused on the optical investigation of PDO flow behavior using high-speed camera as well as the investigation of the thermal non-equilibrium with an optical fiber. The parameter range was somewhat limited due to higher flow fluctuations and bound to conditions where those optical investigations were possible.

In the experiments with the first test section, two characteristic, highly reproducible temperature distributions were found that could be confirmed by available literature (e.g., (Bennett et al. 1967; Becker et al. 1983)). The first type shows a continuous temperature increase in the PDO area with increasing vapor quality and is characteristic for low mass flux and heat flux conditions. The second type is characterized by an even PDO temperature distribution or a temperature decrease after reaching a local maximum. This second type of distribution is typical for higher mass fluxes and heat fluxes. Higher evaporation rates and therefore higher vapor acceleration are responsible for this second type behavior. The increased turbulence leads to smaller thermal non-equilibrium. The influence of adjustable experimental parameters, i.e. inlet temperature, heat flux, mass flux, and pressure was thoroughly investigated.

Higher inlet subcooling results in an increase of CHF since more heat needs to be applied to evaporate the higher subcooled liquid. However, variation in inlet subcooling and therefore inlet qualities yielded no significant influence on the temperature behavior in PDO. This is especially true for low pressure. Certain test runs show smaller differences around the point of dryout at higher pressures, subsequent to differences in the critical vapor quality. This can be attributed to the lower latent heat at increased pressure and higher inlet quality differences at those conditions in the present experiments. However, even for test runs with differences around the point of dryout, the temperature distributions of different inlet qualities fall into one asymptote in the fully developed PDO region further downstream from the point of dryout. This proves that PDO heat transfer depends on local vapor quality rather than inlet conditions.

Changes in heat flux have their most significant influence on the PDO temperature distribution at high mass fluxes where increasing heat flux causes stronger temperature rise at the onset of dryout and shifts the vapor qualities towards lower values. The latter phenomenon is not observable at low mass fluxes. This is assumed to be caused by a less stable film behavior and dryout at low mass fluxes which make this film depletion behavior less sensitive to variations in heat flux.

The big range of investigated mass fluxes prevented the direct comparison of all mass fluxes so that the influence on the PDO temperature distribution was investigated separately for high and

low to medium mass fluxes. At higher mass fluxes, increasing mass flux enhances the evaporation rate and the convective heat transfer and thus results in lower temperature rise at dryout and overall locally lower temperatures at similar temperature slopes. It also shifts the critical quality to lower values which is known as the inverse mass flux effect. Low to medium mass fluxes show the characteristic temperature distribution for low mass and heat fluxes with increased critical vapor quality and stronger temperature increase at dryout when mass flux is decreased.

The investigation of pressure influence yielded similar evidence as with the mass flux analysis. It could be observed that increasing pressure decreases CHF along with the highest admissible heat flux and shifts the critical quality to lower values. Additionally, the temperature rise at dryout is more pronounced. Increasing pressure also moves the transition point between the two characteristic temperature distributions to lower mass and heat fluxes. This phenomenon was also recognized in other studies. At high vapor qualities beyond unity, no temperature increase is observed as would be expected under thermal equilibrium conditions. This is an indicator of thermal non-equilibrium which means that even at equilibrium vapor qualities higher than 1, the liquid phase still exists in the form of entrained droplets in the vapor flow and contributes to the PDO heat transfer.

The investigation of rewetting behavior, sometimes referred to as " true quenching" (e.g., (Lau 1983)), yielded no differences between heating and cooling operation mode in steady-state conditions, confirming the rare findings in the literature (e.g., (Bennett et al. 1967)).

Two test series were carried out with the annular test section of which the first one focused on the optical flow investigation with a high-speed camera while the second one was used for vapor temperature measurements. The set-up was slightly changed in between test series by integrating a fiber capillary at the top of the test section. The amount of liquid in the flow, flow instabilities, and the strong temperature rise at dryout resulted in a very limited test matrix in which mainly the pressure could be varied.

For the optical investigations, image disturbing factors as well as limitations in the analysis software were discussed that influence the quality of the data analysis. For the mentioned reasons, most parameter influence investigations were carried out qualitatively.

The droplet size distribution follows roughly a gamma distribution and shows similar behavior across all pressures.

The camera measurements show a shift of the average and most probable vertical velocity from higher to lower values with increasing pressure which can be explained with increasing vapor density. No influence of heat flux is observable while variation in inlet subcooling yields small distribution shifts with average velocities still being within 0.05 m/s.

The lateral velocity distributions follow a Gaussian normal distribution for all test conditions with mean values close to zero. A minimum of 87% of the droplets lie within ±0.3 m/s. At least 76% of all detected droplets are located within 3 mm in the channel center between channel wall and heating tube. The location along with relatively straight trajectories and small lateral

velocities indicate that there is very limited droplet wall interaction which proves the limited contribution of direct wall droplet contact to the overall heat transfer at PDO conditions.
The investigation of the connection of droplet size and vertical velocity yields some differences in the distributions for different pressures. However, the most common distribution shows highest velocity scatter at lower droplet sizes and approaches the overall mean velocity with increasing size. Horizontal velocities follow this distribution without any exemptions. These findings partially disagree with assumptions in the literature that claim constant mean velocity values, independent from droplet size, and highest lateral movement for the biggest droplet sizes ((Cumo et al. 1971; Ganić 1976; Chen et al. 1977; Schnittger 1982)).
The measurements of vapor temperature using an optical fiber inserted in a stainless steel capillary proved to be very difficult since most of the time the influence of liquid through wetting of the capillary was observable. Therefore, a conservative data point selection criterion regarding measurement duration and temperature distribution was set to ensure high quality of the chosen data points. The greatest number of measurement points was found at p = 20 bar, further data points were found at 15 bar and one at 27.1 bar. The selected data points are not necessarily independent from each other but were often taken at the same or similar test conditions. For the selected data points, a significant thermal non-equilibrium was observable with differences between 20% and 85% between equilibrium and actual vapor quality. The measurement of a vapor temperature profile along the length of the flow channel was rare and usually limited to small axial distances. Those parallel measurements were only observable for consecutive measurement levels. This is attributed to the flow behavior being presumably responsible for the capillary dryout. With increasing distance to the end of the heated length, a temperature increase is observable. Occasionally, a temperature peak is reached, and the vapor temperature shows decreasing behavior again with further increasing distance from the end of the heated length.

All the obtained data from the experiments in this thesis were used to evaluate available prediction methods and possibly identify lacks in knowledge and improvement potential.
The HTC data were compared to the predictions of 10 empirical correlations, two thermal non-equilibrium models, and one phenomenological model for the uniformly heated tube. The best prediction accuracy in test section 1 is achieved by empirical correlations that are based on a broad data range, i.e. the Bishop I and II correlations ((Bishop et al. 1964; Bishop et al. 1965)) as well as the Groeneveld 1972 (Groeneveld 1973) and KIT correlation (Song 2021). The thermal non-equilibrium models by Groeneveld and Delorme (Groeneveld and Delorme 1976) and CSO (Chen et al. 1979) show significant deviations. This might be partially attributed to the empirical modeling approaches of the thermal non-equilibrium. Good agreement can be found with the KIT model (Yu 2019). However, parts of the data base were used for the model development.
The average droplet size results were compared to different correlations. They all undergo certain limitations like the lack of evaporation consideration. As theoretically expected, all

correlations predict a diameter decrease with increasing pressure. However, this is not reflected in the obtained results. The smallest deviation is pressure dependent, with Guo's model (Guo and Mishima 2002) showing the overall least difference. Additionally, the entire droplet distribution was compared to two correlations, proving that this approach delivers good results and shows potential for further droplet analysis improvements.
The droplet vertical velocity in PDO is usually considered via slip ratio correlations. The camera measurements show relatively stable slip across low to medium pressures that increases with further increasing pressure. However, it should be noted that with increasing pressure, the heat flux needed to be varied as well. Correlations investigated in this thesis provide a decreasing slip with increasing pressure. Therefore, they are only able to give somewhat reasonable predictions at low to medium pressures. In that sense, the correlations by (Ahmad 1970) and (Groeneveld 1972) show partially good agreement at lower pressures while all correlations underestimate the measured slip at higher pressures. As suggested by (Cumo et al. 1971), the vertical velocity measured with the high-speed camera was compared to values derived from force balance calculations. They show very good agreement throughout all test runs with an average deviation of 6%.
The actual qualities derived from the measured vapor temperatures were used to assess the determination of actual quality in the models of Groeneveld and Delorme and CSO. The CSO model shows very good agreement across all data points with the average deviation for all pressures ranging from -12% to 2%. The Groeneveld Delorme model provides very good predictions at p = 15 bar with average deviations of 2% but shows decreasing accuracy with increasing pressure.

The above described experiments significantly extend the data bases in R-134a for PDO conditions. Consideration of available water data in setting up the experimental parameter range makes this data base available for further improvement of fluid-to-fluid scaling methods that are necessary when working with a model fluid. The careful analysis of the experimental results and influential parameters helps to enhance the understanding of the physical mechanisms contributing to the heat transfer under PDO conditions. Lastly, the assessment of correlations and models for heat transfer and flow behavior showed which models are capable of predicting heat transfer and corresponding flow behavior under PDO conditions and identifies potential for further improvements.

Outlook

In the future, the work of this thesis can be continued in further research work. As discussed before the data base, especially in tube geometry, can be used for further development and refinement of existing fluid-to-fluid scaling laws since geometrical, mass flux, and pressure conditions of water data bases have been considered in the experiments. Further phenomenological modeling is necessary to improve the capability of heat transfer predictions

over a broad range of parameters. Especially the modeling of the thermal non-equilibrium as well as droplet behavior and its contribution to the PDO heat transfer need further refinement and a broader data base.

The investigations with the annular test section proved to be very difficult overall and show further improvement potential. First, the obtained data base in this geometry is comparably narrow since the focus in this thesis was the optical investigation and the test matrix was bound to conditions where those measurements were possible. This data base could be enhanced in further tests. It might be necessary to change the geometrical boundaries in order to enhance the possible parameter range. This option is already explored in another research project at IATF using a smaller flow channel to increase mass flux. However, decreasing the size of the flow channel influences the development of droplets and further complicates the optical investigations under PDO conditions. Generally, further optical investigations under PDO conditions are needed, also with other facilities, since the available data base is still scarce, and the data are needed to raise the potential of theoretical modeling. The present analysis of the droplet behavior could be run again with a different software approach to overcome the discussed deficiencies experienced in this thesis and improve the analysis quality. The use of machine learning (ML) tools in that regard gains more and more importance and shows promising results ((Hessenkemper et al. 2022)). In order to correctly model the thermal non-equilibrium, further vapor temperature measurements over a broad parameter range are necessary. The approach taken in this thesis is promising but still experiences influence of liquid. Hydrophobic coatings of the capillary might help to overcome this issue. Furthermore, to achieve a temperature profile it should be tried to extend the axial length of the vapor temperature measurements.

Appendix

A. Set-up and Functionality of an Optical Fiber for Temperature Measurements

As can be observed in Figure 0.1, the optical fiber consists of the fiber core, the cladding around the core as well as a coating, which is not shown in the schematic. The photo sensitivity of optical fiber is made use of to operate them as temperature sensors. This photo sensitivity makes it possible to integrate Fiber-Bragg-Gratings (FBG) into the fiber core. Usually, this integration process is done by exposing the desired spots of the fiber to a laser system that provides radiation in UV wavelength. At those future measurement points, the refractive index along the fiber is permanently changed and further functions as a selective mirror for pre-defined wavelengths that fulfill the required conditions of the Bragg grating at this spot (Othonos 1997). It is possible to integrate more than one Fiber-Bragg-Grating along the fiber core which enables the fiber to be used as a quasi-distributed sensor. However, it is important that the difference between the Bragg-Grating-Wavelengths is sufficient.

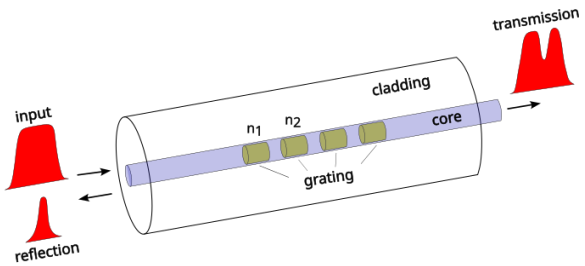


Figure 0.1: Structure and measurement principle of an optical fiber with Fiber-Bragg-Grating (adapted from: (Lomperski et al. 2015))

Figure 0.1 also displays the measuring principle of an optical fiber. A broadband light source sends a signal into the fiber. At the spot of a Fiber-Bragg-Grating the majority of the light spectrum is transmitted. Only the part of the light spectrum that fulfills the conditions of the Bragg grating is reflected and propagates in the countercurrent fiber direction. Via a coupler, the signal eventually reaches an optical spectrometer, where it is evaluated. The reflected Bragg wavelength can be described with the Bragg grating period Λ between the individual fringes of a Bragg grating and the impressed refractive index n_{eff} as follows:

$$\lambda_B = 2\, n_{eff}\, \Lambda \tag{0.1}$$

Changes in external influences, such as strain or, in this case, temperature, result in a shift of the reflected Bragg wavelength, which can be detected by the system and, by comparison with the original wavelength, allows conclusions about the influence of the interference. According to (Morey et al. 1989) this shift is defined as:

$$\frac{\Delta\lambda_B}{\lambda_B} = (\alpha + \xi)\,\Delta T \qquad (0.2)$$

with the thermal expansion coefficient α, responsible for the changes of the grating spacing and the thermo-optic coefficient ξ, which describes the changes of the refractive index. The last effect is dominant in the case of temperature influences. In this way, the fiber can be used as a temperature sensor and provides a pre-defined number of measurement points. It is important for temperature measurements that the absence of strain in the fiber is guaranteed as those superimposing effects would lead to false temperature measurements.
The temperature sensitivity, which is defined by the manufacturer as the sum of the thermal expansion and the thermo-optic coefficient (compare equation (0.2)) lies at 6.5 x 10^{-6} K^{-1} in the experimental set-up for this thesis.

B. Selected Theoretical Models for Post-Dryout Heat Transfer and Droplet Behavior

Subchapter 2.5.2 introduced the correlations that are validated in this thesis. The following subsections present the models and discuss their main aspects. The numeration for the heat transfer models equals the ones introduced in the above chapter.

B.1 Equilibrium PDO Heat Transfer Correlations

The first 3 presented correlations are adapted and applied in the widely used thermal-hydraulic system code “Analysis of Thermal Hydraulics of Leaks and Transients” (ATHLET) (Austregesilo et al. 2012) to describe the film boiling heat transfer in dispersed flow conditions. They are of a purely empirical nature and do not consider the thermal non-equilibrium. However, as discussed before, this kind of correlation is easy to handle, and they deliver reasonable results in certain parameter ranges and are therefore still enabled in system thermal-hydraulic codes. The first correlation on display is the modified Dougall-Rohsenow correlation (Liesch et al. 1975). In the above mentioned ATHLET manual, the second one is named Groeneveld 5.9 correlation, found in (Groeneveld and Moeck 1968). However, it seems like in ATHLET a simplified version of the 5.9 correlation is used. The 5.9 correlation found in the original paper is similar to the correlation named Groeneveld 1972 (9) in this thesis. It was

decided to keep the name as it is used in the ATHLET modeling. The third model to calculate film boiling heat transfer in ATHLET is the Condie-Bengston IV correlation (Vojtek 1978).

Modified Dougall-Rohsenow correlation (1):

$$\alpha = 0.023 \cdot \frac{\lambda_{vb}}{D} \cdot Re^{0.8} \cdot Pr_{vb}^{0.4} \cdot \left(\frac{T_{vb}}{T_W}\right)^{0.5} \tag{0.3}$$

Groeneveld 5.9 correlation (2):

$$\alpha = 0.00327 \cdot \frac{\lambda_{vb}}{D} \cdot Re^{0.901} \cdot Pr_{vw}^{1.32} \cdot (Y)^{-1.5} \tag{0.4}$$

$$Y = 1 - 0.1 \cdot \left[\left(\frac{\rho_l}{\rho_{vs}}\right) - 1\right]^{0.4} \cdot (1 - x_e)^{0.4} \tag{0.5}$$

Condie-Bengston IV correlation (3):

$$\alpha = 0.05345 \cdot \left[\frac{\lambda_{vb}^a \, Pr_{vw}^b \, Re^c}{D^d \, (x_e + 1)^e}\right] \tag{0.6}$$

with the constant coefficients in the Condie-Bengston IV correlation defined as $a = 0.4593$, $b = 2.2598$, $c = 0.6249 + 0.2043 \cdot \ln(x_e + 1)$, $d = 0.8095$, and $e = 2.0514$.
In all cases, the Reynolds number is determined with the following expression at bulk vapor conditions:

$$Re = \frac{G \, D}{\mu_{vb}} \tag{0.7}$$

While Pr_{vw} is calculated at wall temperature conditions, all the other properties use the bulk vapor temperature for their calculations. In the above equations, α is the heat transfer coefficient, D is the characteristic diameter and x_e describes the equilibrium vapor quality. The saturated liquid and vapor density are given by ρ_l and ρ_{vs}, respectively, whereas λ_v expresses the thermal conductivity of vapor. The dynamic viscosity is denoted by μ_v.

(Bishop et al. 1964; Bishop et al. 1965) suggested a series of simple to use PDO correlations, covering a broad range of low to very high subcritical pressure and medium to high mass fluxes. They are listed below as

Bishop I (4):

$$\alpha = 0.0193 \cdot \frac{\lambda_{vf}}{D} \cdot Re_{vf}^{0.8} \cdot Pr_{vf}^{1.23} \cdot \left(\frac{\rho_{vs}}{\rho_l}\right)^{0.068} \cdot F_1^{0.68} \qquad (0.8)$$

Bishop II (5):

$$\alpha = 0.033 \cdot \frac{\lambda_{vf}}{D} \cdot Re_{vw}^{0.8} \cdot Pr_{vw}^{1.25} \cdot \left(\frac{\rho_{vs}}{\rho_l}\right)^{0.197} \cdot F_1^{0.739} \qquad (0.9)$$

Bishop III (6):

$$\alpha = 0.098 \cdot \frac{\lambda_{vw}}{D} \cdot \left[Re_{vw} \cdot \left(\frac{\rho_{vs}}{\rho_l}\right) \cdot F_1\right]^{0.8} \cdot Pr_{vw}^{0.83} \cdot \left(\frac{\rho_{vs}}{\rho_l}\right)^{0.5} \qquad (0.10)$$

with

$$F_1 = x_e + \left(\frac{\rho_{vs}}{\rho_l}\right) \cdot (1 - x_e)$$

The subscript vf describes the properties at film vapor temperature, which is the average value of wall and bulk vapor temperature.

(Miropol'skiy 1963) proposed the following correlation with a similar validity range as Bishop et al., also for tubes.

Miropol'skiy (7):

$$\alpha = 0.023 \cdot \frac{\lambda_{vb}}{D} \cdot [Re \cdot F_1]^{0.8} \cdot Pr_{vw}^{0.8} \cdot Y \qquad (0.11)$$

Another approach was taken in the correlation developed by (Lee and Chang 2008) which is based on their experimental results as discussed in chapter 2.4.1. For comparison with the experimental results obtained for this thesis, only the correlation for smooth tubes is considered.

The correlation takes into account the critical vapor quality at the point of dryout x_c. Furthermore, the axial distance of the point of interest to the onset of dryout $dzchf$ is considered. The heat transfer coefficient of the presented form is derived using the inner wall and saturated vapor temperature.

Lee and Chang (8):

$$Nu = 0.2935 \cdot \frac{x_c^{0.568} \left\{ Re_{vs} \left[x_e + \frac{\rho_{vs}}{\rho_l} (1 - x_e) \right] \right\}^{0.645} Pr_{vf}^{0.854}}{x_e^{0.715} \left(1 + \frac{dzchf}{D} \right)^{0.088}} \qquad (0.12)$$

Reynolds number and vapor density are considered at vapor saturation whereas the Prandtl number is calculated using film vapor temperature.
In their study, (Lee and Chang 2008) applied their correlation to data sets in R-12 and R-22, coming from experiments conducted by (Groeneveld 1972) and (Nishikawa et al. 1983). It shows a slight underprediction of the measured wall super heat in both presented cases. Regarding their own experiments in smooth tubes, the correlation also slightly underpredicts the measured wall superheat with an average deviation of -5.4% at an RMS deviation of 28%. It is within the range of the later presented CSO correlation by (Chen et al. 1979) which overpredicts the wall superheat on average by 5.7% with a slightly higher RMS deviation of 35.5%.

Groeneveld published a report in which he was investigating different aspects of the PDO heat transfer at reactor operating conditions including the PDO heat transfer in general as well as the effects of surface roughness and other flow turbulence enhancers on CHF and PDO, and general aspects of rewetting behavior (Groeneveld 1973). He therefore analyzed available data from different research facilities that were obtained in tube and annuli geometry. Based on the available data, he derived another equilibrium correlation. 6 different sets of constants with best-fit to the different geometry data sets were derived, partially including and excluding the dependence on heat flux. The U.S. Atomic Energy Commission (USAEC) recommended the form below (U.S. Atomic Energy Commission 1971).

Groeneveld 1972 (9):

$$\alpha = 0.00327 \cdot \frac{\lambda_{vs}}{D_{hy}} \cdot \left\{ Re_{vs} \cdot \left[x_e + \frac{\rho_{vs}}{\rho_l}(1 - x_e) \right] \right\}^{0.901} \cdot \left[1 - 0.1 \cdot \left(\frac{\rho_l}{\rho_{vs}} - 1 \right)^{0.4} \cdot (1 - x_e)^{0.4} \right]^{-1.5} \cdot Pr_{vw}^{1.32} \quad (0.13)$$

with the hydraulic diameter D_h. It is very similar to the above introduced Groeneveld 5.9 correlation (Equation (0.4)).

This widely used form ((Koizumi et al. 1987)) was recommended by USAEC not only for tube and annuli geometry from which it was derived but also for rod bundles. However, Groeneveld was cautious recommending the correlation for bundle geometry due to the scarcity of available validation data as well as the previously mentioned reason of irregular temperature distributions. He also noted, although the correlation performed well in comparison with others, it might underpredict the temperatures in the PDO further away from the point of dryout and at low mass fluxes as it is based on the assumption of thermal equilibrium.

B.2 Non-Equilibrium PDO Heat Transfer Models

Groeneveld and Delorme Model

(Groeneveld and Delorme 1976) developed a model that takes the thermal non-equilibrium into account. This model is numbered as (10). It is developed as a combination of a thermal non-equilibrium prediction correlation and a superheated steam correlation. The first one was derived using around 1,400 data points obtained from different research facilities in tube geometry. Three simplifying assumptions were made for the prediction of thermal non-equilibrium: i) the entrained droplets are not involved in the cooling process at the heated wall, ii) heat radiation is neglected, and iii) the flow is assumed to be homogenous.

The second assumption was discussed before. Groeneveld and Delorme based their third simplification on the introduced experimental investigations of (Cumo et al. 1971) who obtained slip ratios close to unity in the fully developed PDO area. The same study was used, among others, to justify the first simplification regarding the role of droplets in PDO heat transfer. As discussed in chapters 2.4.3 and 5.1.4.2, trajectories parallel to the channel wall and no significant lateral velocities were observed in that study. So, they concluded that droplets do not contribute to the cooling process at the heated wall. This first assumption limits the correlation to fully developed PDO conditions, excluding e.g., developing PDO conditions.

The following correlation was proposed to predict the actual vapor quality x_a:

$$\frac{h_{va} - h_{ve}}{i_{v-d}} = \exp[-tan\Psi] \cdot \exp\left[-\left(3 \cdot \alpha_{\mathrm{v,hom}} \right)^{-4} \right] \quad (0.14)$$

with

$$\Psi = 0.13864 \cdot Pr^{0.2031} \cdot Re_{hom}^{0.20006} \cdot \left(\frac{q\ D\ c_{p,ve}}{\lambda\ i_{v-d}}\right)^{-0.09232} \cdot (1.3072 - 1.0833 \cdot x_e + 0.8455 \cdot x_e^2) \tag{0.15}$$

The homogeneous Reynolds number is defined as

$$Re_{hom} = \frac{G\ D\ x_1}{\mu_{ve}\ \alpha_{v,hom}} \tag{0.16}$$

with the homogeneous void fraction

$$\alpha_{v,hom} = \frac{x_1}{x_1 + \frac{\rho_{vs}}{\rho_l}(1 - x_1)} \tag{0.17}$$

Ψ is defined as the thermal non-equilibrium parameter ($0 < \Psi < \frac{\pi}{2}$). The equilibrium mass vapor quality x_1 is defined in the following boundaries:

$$\begin{aligned} x_1 &= 0, \quad x_e < 0 \\ x_1 &= x_e, \quad 0 \le x_e \le 1 \\ x_1 &= 1, \quad x_e > 1 \end{aligned} \tag{0.18}$$

The vapor enthalpies in equation (0.14) for equilibrium and actual vapor properties are denoted by h_{ve} and h_{va}, respectively. Generally, the subscript ve and va mark equilibrium and actual vapor conditions throughout the model. The latent heat of evaporation is given by i_{v-d}. $c_{p,ve}$ describes the specific heat.

Using the above equations, the actual vapor quality x_a can be calculated:

$$x_a = \frac{i_{v-d}}{h_{va} - h_{ve}} x_e \tag{0.19}$$

Eventually, the superheated steam correlation by (Hadaller and Banerjee 1969) was chosen to calculate the HTC as follows:

$$\alpha = 0.008348 \cdot \frac{\lambda_f}{D_{hy}} \cdot \left[\frac{G\ D_{hy}}{\mu_f} \cdot \left(x_a + \frac{\rho_v}{\rho_l}(1 - x_a)\right)\right]^{0.8774} \cdot Pr_f^{0.6112} \qquad (0.20)$$

The subscript f denotes the vapor film temperature which is defined as the average of the wall and the bulk vapor temperature $T_f = (T_W + T_{vb})/2$.
It should be noted that the quality at dryout is not necessary to be known. However, the authors argue that a more precise prediction is possible when knowing the dryout quality. In that case, the condition $x_a \geq x_{do}$ can be introduced which means that the actual vapor quality can be set to the dryout vapor quality in case the calculated x_a is exceeded by the dryout quality. They justify this condition with the fact that just downstream of dryout, the heat transfer from vapor to liquid is negligibly small.
Groeneveld and Delorme applied the model also to data outside the parameter range that was used for the development of the correlation. Despite its empirical character, the correlation showed a good agreement with the experimental data with an overall RMS deviation of 6.9% and therefore shows potential for being extrapolated. According to the authors this is attributed to the correct predictions of trends corresponding to the underlying physical mechanisms.

CSO Model

Another thermal non-equilibrium model that is widely used was proposed by (Chen et al. 1979) and is known as the CSO model (11). Like the model of Groeneveld and Delorme, the dryout quality and location do not need to be known but the model is rather based on local conditions. The thermal non-equilibrium is expressed as the ratio of actual and equilibrium vapor quality, as can be seen below:

$$\frac{x_a}{x_e} = 1 - B(p) \cdot \frac{T_{va} - T_S}{T_W - T_{va}} \qquad (0.21)$$

with the empirical correlation B(p) being defined as:

$$B(p) = \frac{0.26}{1.15 - \left(\frac{p}{p_c}\right)^{0.65}} \qquad (0.22)$$

where (p/p_c) marks the ratio of system pressure and critical pressure.
With solving the heat balance in equation (0.19) and solving equation (0.21) simultaneously, the actual vapor temperature can be determined.

The authors used explicit approximation of Beattie's implicit form for calculating the Fanning friction factor f:

$$f = 0.037 \cdot \left[\frac{G\ D_{hy}}{\mu_{va}}\left(x_a + \frac{\rho_v}{\rho_l}(1 - x_a)\right)\right]^{-0.17} \tag{0.23}$$

which is used to eventually calculate the heat transfer coefficient given by the following expression:

$$\alpha = G\ x_a\ c_{p,f}\ Pr_f^{-\frac{2}{3}}\frac{f}{2} \tag{0.24}$$

Also here, the subscript f expresses vapor film temperature which is defined in the same way as described above.
The model was derived and compared to approximately 2,850 data points from 8 different sources. With the assumption that in the region of interest (fully developed PDO), the total measured heat flux approximately equals the heat flux from dry wall to vapor, an average deviation of 14.9% was achieved for all the data points by the authors when comparing calculated and measured heat fluxes.

B.3 KIT Mechanistic PDO Model

The following explanations continue the description of the mechanistic model.
The definition of the slip ratio given in Equation (6.5) is used in this model throughout the entire PDO area except for the point of dryout itself at which the following form applies:

$$S_{do} = \frac{1 + \sqrt{1 - \left(1 - \frac{4}{3}\frac{\rho_d\,\rho_v\,g\,\left(1 - \frac{\rho_v}{\rho_d}\right)}{G^2\,C_D}\,d_c\left(\frac{\alpha_{v,do}}{x_{do}}\right)^2\right)\left(1 - \frac{16}{3}\frac{q}{G\,i_{v-d}\,C_D}\frac{d_c}{D_{tube}}\frac{\rho_v}{\rho_d}\frac{1}{x_{do}}\right)}}{1 - \left(1 - \frac{4}{3}\frac{\rho_d\,\rho_v\,g\,\left(1 - \frac{\rho_v}{\rho_d}\right)}{G^2\,C_D}\,d_c\left(\frac{\alpha_{v,do}}{x_{do}}\right)^2\right)} \tag{0.25}$$

The subscript do stands for dryout whereas d_c marks the critical droplet diameter.
Yu used the drag coefficient for dispersed flow suggested by (Groeneveld 1972):

$$C_D = \frac{27}{Re_d^{0.84}} \qquad Re_d < 150$$
$$C_D = 0.4 \qquad Re_d \geq 150 \tag{0.26}$$

Re_d marks the Reynolds number of the droplets and is defined as follows:

$$Re_d = \frac{\rho_v \, (v_v - v_d) \, d}{\mu_v} \tag{0.27}$$

The Developing Region Length

According to (Yu 2019), the developing PDO region in the literature is often defined as either a constant distance from the point of dryout (Chen 1986) or as the distance from dryout to a point where vapor Graetz number is very small (Nguyen and Moon 2015). In the presented model, an empirical correlation was developed that determines the developing PDO region as the difference of quality using a big amount of data in water and R-134a (Becker et al. 1983; Köckert et al. 2021). It is eventually defined as below as it turned out that Reynolds and Boiling number Re and Bo, as well as the viscosity ratio $\frac{\mu_d}{\mu_{vs}}$ have a significant influence on the developing region length L_{dev}:

$$L_{dev} = x_{rt} - x_{do} = 900 \, Re^{-0.08} \, (Bo + 10^{-4}) \left(\frac{\mu_d}{\mu_{vs}}\right)^{-0.55} \tag{0.28}$$

with the Boiling and Reynolds number:

$$Re = \frac{G \, D_{tube}}{\mu_{vs}}$$
$$Bo = \frac{q}{G \, i_{v-d}} \tag{0.29}$$

The transition between developing and developed region is given by x_{rt}, while x_{do} describes the vapor quality at the point of dryout. The saturated dynamic viscosity of droplets and vapor is given by μ_d and μ_{vs}.

The Convective Heat Transfer from Wall to Vapor

The convective heat transfer over the entire PDO region in this model is regarded as a transient, entrance region problem that considers the axial distance to the position of dryout. It is therefore defined as the combination of convective heat transfer in the developed PDO region and at the point of dryout.
The heat transfer coefficient in this model is considered stable in the fully developed region. The correlation of (Forslund and Rohsenow 1966), originally developed based on liquid nitrogen data, was modified in the present model to account for different fluids. It describes the heat transfer in the fully developed region as follows:

$$\alpha_{w-v,2} = 0.03675 \frac{\lambda_{vb}}{D_{tube}} Re_{vb}^{0.743} Pr_{vb}^{0.4} \left(\frac{\mu_{vb}}{\mu_{vw}}\right)^{0.1} \tag{0.30}$$

where λ_{vb} describes the thermal conductivity of the bulk vapor. A constant coefficient of 1.05 multiplied with the original version of the correlation as well as the viscosity ratio with empirically determined exponent were introduced to account for the significant fluid property changes across the tube cross section. The subscript vb is assigned to the bulk vapor temperature whereas vw marks the vapor temperature conditions at the wall surface. Reynolds and Prandtl number at vapor conditions are generally defined as below:

$$Re_v = \frac{G\ x_a\ D_{tube}}{\mu_v\ \alpha_v}$$
$$Pr_v = \frac{c_{p,v}\ \mu_v}{\lambda_v} \tag{0.31}$$

The model of Yu considers the overall convective heat transfer from wall to vapor in the PDO area as the sum of the heat transfer at the point of dryout and the above described heat transfer in the fully developed region. It is defined as follows:

$$\alpha_{w-v} = (1 - K_1)\alpha_{w-v,2} + K_1 \alpha_{w-v,NB} \tag{0.32}$$

The Chen correlation (Chen 1966) at saturated nucleate boiling is used to determine the HTC at the dryout point. Yu introduces the dimensionless weighting factor K_1 which ranges from 1 at the point of dryout to 0 in the fully developed region. The structure was adapted from (Nguyen and Moon 2015).

$$K_1 = \frac{1}{1 + \left(\frac{10^4}{Re_{vb}^{\frac{1}{6}}}\right)\left(\frac{L_{poi}}{L_{dev}}\right)^{2.5}} \tag{0.33}$$

The constants were derived from comparison of theoretical and experimental wall superheat distributions. Re_{vb} describes the Reynolds number at bulk vapor temperature while L_{poi} gives the distance of the point of interest to the dryout location.

The Heat Transfer from Wall to Droplets

In the present model, the heat transfer from wall to droplets is characterized by the so-called effectiveness. It is based on (Kendall and Rohsenow 1978) and describes the ratio of actually transferred heat by wall-droplet contact and the heat that is necessary to completely evaporate the deposited droplets. The effectiveness is calculated as below. For the detailed calculation it is referred to the original work of (Kendall and Rohsenow 1978) or to the thesis of (Yu 2019).

$$\varepsilon = 2.6\left(\frac{\rho_{vb}}{\rho_d}\right)^{\frac{1}{2}}\left(\frac{\bar{R}}{d}\right)^{\frac{1}{8}}\left[\frac{\beta_2\lambda_{vb}(T_W - T_S)}{i_{v-d}(\rho_{vb}\sigma d)^{0,5}}\right]^{\frac{1}{2}}\left[I_2\frac{\mu_{vb}i_{v-d}}{\beta\lambda_{vb}(T_W - T_S) + I_1}\right]^{-\frac{1}{4}} \tag{0.34}$$

with $\bar{R}$ being the average droplet extension radius, σ being the surface tension, I_1 and I_2 being constants, and β being a coefficient to consider the superheating effect on the vapor temperature distribution.

The Heat Transfer from Vapor to Droplets

The model considers the heat transfer from vapor to droplets as the second biggest source of heat removal in the PDO region and the main source of thermal non-equilibrium. It assumes that droplets are mainly concentrated in the turbulent flow core and can only reach the film region near the wall through sufficient lateral velocity. This assumption is based on the investigations by (Hagiwara et al. 1980), (Ganić and Rohsenow 1979), and (Lee 1982). Furthermore, it considers the idea of (Hull and Rohsenow 1982) and (Varone 1990) that the vapor temperature curve flattens with increasing distance to the heated wall and the evaporation rate of the droplets is a function of their radial position.
These assumptions led to the above described division of the tube cross section into the center core region and the film region close to the heated wall. Therefore, the vapor temperature was defined differently for the core (subscript vc) and the film region (subscript vf):

$$T_{vcr} = \frac{T_{vb} + T_S}{2} \tag{0.35}$$

$$T_{vfr} = \frac{T_{vb} + T_W}{2} \tag{0.36}$$

T_S and T_W describe the saturation and the wall temperature, respectively.
The calculation of the HTC is based on the Hughmark correlation (Hughmark 1967) and is enhanced with a shielding factor S_f based on (Yuen and Chen 1978).
If $0 \leq Re_d < 776.06$ and $0 \leq Pr_v < 250$

$$\alpha_{v-d} = S_f \frac{\lambda_v}{d}\left(2 + 0.6 Re_d^{0.5} Pr_v^{0.33}\right) \tag{0.37}$$

If $Re_d \geq 776.06$ and $0 \leq Pr_v < 250$

$$\alpha_{v-d} = S_f \frac{\lambda_v}{d}\left(2 + 0.27 Re_d^{0.62} Pr_v^{0.33}\right) \tag{0.38}$$

with

$$S_f = \frac{1}{\left[1 + \frac{c_{p,v}(T_v - T_S)}{i_{v-d}}\right]} \tag{0.39}$$

The interfacial HTCs are separately determined for the core and the film region using the characteristic vapor temperature conditions in that region.
To determine the overall transferred heat through this form of heat transfer, a correction factor K_2 is introduced as the total heat is a combination of core and film region heat transfer. It was mainly derived from investigation of the PDO temperature slope and represents the influence of drag, evaporation, and turbulent dispersion force. According to Yu, those forces mark the main influence the droplet exchange between both divisions. With K_2 being:

$$K_2 = 4500\ \alpha_v^2 \left(\frac{Re_d}{Re_{vb}}\right)^{1.5} \left(\frac{D_{tube}}{d}\right)(x_e - x_{do})^2 \tag{0.40}$$

the overall interfacial heat transferred is given by:

$$q_{v-d} = (1 - K_2)\alpha_{v-d,vcr}(T_{vcr} - T_S) + K_2\alpha_{v-d,vfr}(T_{vfr} - T_S) \quad (0.41)$$

B.4 Validity Range of the PDO Heat Transfer Models

Table 0.1 contains applicable validity ranges of the utilized PDO heat transfer models in this thesis. The data these correlations were usually based on, were mostly obtained in water. Only the Lee and Chang and partially the Song correlation were based on the refrigerant R-134a, respectively. As becomes obvious, some of the correlations do not provide valid information regarding the validity range. Additional information will be given in the section below the table.

Table 0.1: Validity range of the utilized PDO heat transfer models

Correlation	Geometry	p [bar]	G [kg/(m²s)]	x [-]	q [kW/m²]
Mod. D-R (1)	-	-	-	-	-
Groe 5.9 (2)	-	-	-	-	-
C-B IV (3)	-	4.2 - 221.5	40 - 3939	0.00 - 1.00	-
Bishop I (4)	tube	40.8 - 219.0	700 - 3400	0.07 - 1.00	-
Bishop II (5)	tube	40.8 - 219.0	700 - 3400	0.07 - 1.00	-
Bishop III (6)	tube	168.0 - 219.0	1350 - 3400	0.19 - 1.00	-
Miropol'skiy (7)	tube	40.5 - 223.0	700 - 2000	0.06 - 1.00	-
Lee&Chang (8)	tube	13.0 - 24.0	70 - 800	-	24 - 240
Groe 1972 (9)	tube + annuli	34.4 - 218.0	700 - 5300	0.10 - 0.90	-
Gro&Del (10)	tube	< 205.0	> 270	-	-
CSO (11)	-	< 195.1	-	-	-
Song (water)	tube	10.0 - 215.0	500 - 3500	-	90 - 3060
Song (R-134a)	tube	11.0 - 28.0	300 - 1500	0.26 - 1.76	25 - 140
Yu	tube	-	-	-	-

An approved validity range could not be found for the Modified Dougall-Rohsenow correlation. The original version of the correlation was developed by (Dougall and Rohsenow 1963) and compared to their own experimental data in two tube test sections of 4.6 and 10.4 mm inner diameter. The mass flux ranged from G = 450 to 1110 kg/(m^{2}s) while heat fluxes covered a range from q = 45.4 – 131.8 kW/m^2 and pressure lay between 1.2 and 1.6 bar. The vapor qualities lay below 0.5. However, these data were applied to the original version of the correlation. No proof of a concrete validity range for the modified version could be found.

Also for the Groeneveld 5.9 (2) correlation as used in ATHLET, no direct applicability range could be found. Since it is a modified form of the Groeneveld 1972 (9) correlation, one can assume that the validity range might be similar to the range given for the Groeneveld 1972 correlation. However, using the correlation in ATHLET to predict the film boiling heat transfer in a reactor, it has to cover a wide range of parameters.

The Groeneveld and Delorme model was developed based on 1,402 PDO data points (Groeneveld and Delorme 1976). In their publication they do not provide the concrete parameter range except for the information provided in the table and the additional fact that wall temperatures had to exceed 375 °C to prevent the use of transition boiling date. They did however give the parameter range of 1,852 data points to which the model was originally compared to. Those data points include the 1,402 data points the model is based on and extends the data base to investigate the performance outside the original scope and therefore potential extrapolation. This parameter range covers pressures of p = 7 – 215 bar, mass fluxes of G = 130 – 4000 kg/(m^{2}s), and qualities of x = -0.12 – 3.09. Although the model is based on and was originally compared to tube data only, (Groeneveld and Delorme 1976) claimed that it could be applied to e.g., rod bundles as well provided that imbalances of flow and enthalpy are small between subchannels.

There is no direct parameter range provided for the CSO model and given that it tries to phenomenologically model the important heat transfer aspects it should be applicable in a wide range of parameters. However, in the model development a data base of 2,854 data points was used to assess different parts of the model. The pressure limit given in the table is dictated by the empirical modeling approach to determine the actual vapor quality. The mentioned data base covers p = 4.2 – 195.1 bar, G = 17 – 3011 kg/(m^{2}s), and x = 0.502 – 1.728 (Chen et al. 1979).

The Song correlation, introduced as KIT PDO correlation, covers a broad range of parameters as can be taken from the table. Data in water and R-134a were used which explains the two listed ranges that can be found in (Song 2021; Song et al. 2022).

The KIT Mechanistic PDO Model, addressed in the table as “Yu” was developed for tube data. No further restrictions as to the validity range except for the geometry were given.

B.5 Modeling of the Droplet Diameter

As discussed before, droplets have a significant influence on the heat transfer in the PDO area. Modeling of the droplets is therefore an important feature in reliable heat transfer models.
There are different approaches on how to model the droplet diameter. One of the simplest methods found in existing models was the use of the maximum stable diameter above which droplet break-up is assumed. The calculation of the droplet diameter d is conducted by determining the critical Weber number We_c:

$$We_c = \frac{\rho_v \, (v_v - v_l)^2 \, d}{\sigma} \tag{0.42}$$

With a given critical Weber number, the equation is solved for d. Different We numbers were assumed by researchers in the past. (Isshiki 1959) suggested $We_c = 6.5$ based on his experimental results. Many researchers like (Forslund and Rohsenow 1966; Ganić and Rohsenow 1977) or (Styrikovich et al. 1980) used $We_c = 7.5$.
(Guo and Mishima 2002) used the following correlation, originally proposed by (Kataoka et al. 1983), in their PDO heat transfer model:

$$d = 7.96 \cdot 10^{-3} \cdot \frac{\sigma}{\rho_v \, (\alpha \, v_v)^2} \cdot Re_v^{\frac{2}{3}} \cdot \left(\frac{\rho_v}{\rho_l}\right)^{-\frac{1}{3}} \cdot \left(\frac{\mu_v}{\mu_l}\right)^{\frac{2}{3}} \tag{0.43}$$

Besides one single average diameter, often diameter distributions are implemented in theoretical models which better fit the experimental results. Normal and log-normal distributions are quite popular. For this study, two different distributions are used to compare the experimental results with. The first one was used by (Cumo et al. 1974):

$$P(d) = \frac{d}{d_{mp}^2} \cdot e^{-\frac{d}{d_{mp}}} \tag{0.44}$$

with d_{mp} being the most probable diameter.
To calculate d_{mp}, they suggested a correlation based on their optical flow investigation results that was also used later on by e.g., (Chen et al. 1979). It is defined as:

$$d_{mp} = \frac{\mu_l}{G \, x} \cdot 123.1 \cdot \left(1 - \frac{p}{p_c}\right)^{0.31} \tag{0.45}$$

so bringing the most probable diameter in relation to the normalized pressure.
If one wants to derive a mean droplet diameter d_m from the distribution, the following relation is used:

$$d_m = \frac{\int_0^\infty P(d)\ d\ \delta d}{\int_0^\infty P(d)\ \delta d} \tag{0.46}$$

The other distribution tested in this study was utilized in the before mentioned model of (Meholic 2011) as well as in the model of (Ganić and Rohsenow 1977). It is given as follows:

$$P(d) = 4 \cdot \frac{d}{d_m^2} \cdot e^{-2 \cdot \left(\frac{d}{d_m}\right)^2} \tag{0.47}$$

The mean droplet size in this distribution is calculated with the maximum droplet diameter d_{max}:

$$d_m = 0.422\ d_{max} \tag{0.48}$$

This relation was calculated by integrating to the inclusion of 99.9% of the overall droplet volume. In his model, Meholic divided the droplet size distribution into several bins with each bin having the same volume and calculated a characteristic diameter for each bin representing all the droplets within that bin. He therewith accounted for the different droplet sizes present in the PDO area. The boundaries for these volume weighted bins are determined iteratively:

$$\frac{1}{N_{bins}} = \frac{\int_{d_{low}}^{d_{upper}} \left\{ \frac{\pi}{6}\ d^3 \left[4 \frac{d}{d_m^2}\ exp\left(-2\ \left(\frac{d}{d_m^2} \right)^2 \right) \right] \right\} \delta d}{\int_0^{d_{max}} \left\{ \frac{\pi}{6}\ d^3 \left[4 \frac{d}{d_m^2}\ exp\left(-2\ \left(\frac{d}{d_m^2} \right)^2 \right) \right] \right\} \delta d} \tag{0.49}$$

The characteristic diameter d_{ch} is derived as follows:

$$d_{ch} = \frac{\int_{d_{low,ch}}^{d_{upper,ch}} \left\{ \frac{\pi}{6}\, d^4 \left[4 \frac{d}{d_m^2}\, exp\left(-2 \left(\frac{d}{d_m^2} \right)^2 \right) \right] \right\} \delta d}{\int_{d_{low,ch}}^{d_{upper,ch}} \left\{ \frac{\pi}{6}\, d^3 \left[4 \frac{d}{d_m^2}\, exp\left(-2 \left(\frac{d}{d_m^2} \right)^2 \right) \right] \right\} \delta d} \tag{0.50}$$

B.6 Modeling of the Droplet Velocity

(Cumo et al. 1971) in their paper on droplet behavior used the force balance of an upward flow to describe the flow behavior of a droplet. They identified the drag force, the weight force, and the buoyancy force as the main forces that affect the droplet movement. The force balance for an ideal straight flow case is developed as below:

$$\begin{aligned} \frac{1}{2}\, C_d\, \rho_{vs}\, (v_{vs} - v_d)^2 \frac{\pi}{4}\, d^2 + \frac{\pi}{6}\, d^3\, g\, (\rho_{vs} - \rho_l) \\ = \frac{\partial}{\partial t}\, (v_d \frac{6}{\pi}\, d^3\, \rho_l) \end{aligned} \tag{0.51}$$

The first term marks the drag force. The second term denotes the buoyance force minus the weight force, which counteracts the buoyance force due to the mass of the droplet. The gravity acceleration is given by g. In cases where the droplet velocity is constant or nearly constant, the term on the right hand side can be dropped.
In that equation, the droplet diameter d is given by an average value and the droplet is assumed to have a spherical shape.
The definition of the drag coefficient C_d was taken from (Quinn 1963-68):

$$C_d = \left(0.63 + 4.8\, Re^{-\frac{1}{2}} \right)^2 \tag{0.52}$$

with the Reynolds number

$$Re = \frac{\rho_{vs}\, (v_{vs} - v_d)\, d}{\mu_{vs}} \tag{0.53}$$

Besides that, there is very little to be found in terms of correlations modeling the vertical droplet velocity in the PDO area. Often, the slip ratio is used to describe the connection of vapor velocity and liquid velocity, i.e. droplet velocity at dryout and beyond. (Ahmad 1970) suggested a slip ratio correlation as follows:

$$S = \frac{v_v}{v_l} = \frac{\left(\frac{\rho_l}{\rho_v}\right)^{0.205}}{\left(\frac{G\ D_{hy}}{\mu_l}\right)^{0.016}} \tag{0.54}$$

(Groeneveld 1972) argued that this calculation was based on void fraction data that were obtained in conditions before dryout. Since at dryout and in PDO the liquid is entirely entrained in the vapor flow the average liquid velocity is higher and the slip ratio is therefore decreased in those areas. He argues that an overestimated slip ratio leads to an underestimation of the droplet size when using the correlation in Equation (0.42). When following this argument, the expected thermal non-equilibrium is lower than in reality since smaller droplets lead to a bigger surface area and therefore improved heat transfer from vapor to droplets. To compensate for this overprediction he therefore proposed, based on his own experimental data, to assume a slip ratio as the average value of homogeneous flow with no slip and the slip ratio provided by Ahmad at the point of dryout.

C. Further Results of Optical Investigations

Table 0.2: Measured average equivalent diameter and comparison with droplet size models for all selected test runs

G [kg/m²s]	T_{sub} [°C]	p [bar]	q [kW/m²]	d_{meas} [mm]	d_{Guo} [mm]	d_{Sty} [mm]	d_{Issh} [mm]	d_{KIT} [mm]
66	17	11.0	47.5	0.363	0.448	0.528	0.457	0.999
	12	15.0	43.0	0.344	0.448	0.535	0.464	-
	17	15.0	44.6	0.323	0.452	0.542	0.470	-
	12	20.0	37.2	0.349	0.439	-	-	-
		20.0	39.3	0.357	0.419	0.508	0.440	-
		20.0	40.6	0.342	0.410	0.492	0.427	-
		20.0	42.9	0.375	0.404	0.483	0.419	-
	17	27.1	37.6	0.353	0.301	0.359	0.311	-
		30.0	37.1	0.314	0.236	0.278	0.241	0.470

Table 0.3: Measured average equivalent diameter and comparison with droplet size models for all selected test runs

G [kg/m²s]	T_{sub} [°C]	p [bar]	q [kW/m²]	d_{meas} [mm]	d_{Guo} [mm]	d_{Sty} [mm]	d_{Issh} [mm]	d_{KIT} [mm]
66	17	11.0	47.5	0.363	0.448	0.528	0.457	0.999
	12	15.0	43.0	0.344	0.448	0.535	0.464	-
	17	15.0	44.6	0.323	0.452	0.542	0.470	-
	12	20.0	37.2	0.349	0.439	-	-	-
		20.0	39.3	0.357	0.419	0.508	0.440	-
		20.0	40.6	0.342	0.410	0.492	0.427	-
	17	20.0	42.9	0.375	0.404	0.483	0.419	-
		27.1	37.6	0.353	0.301	0.359	0.311	-
		30.0	37.1	0.314	0.236	0.278	0.241	0.470

Table 0.4: Measured average lateral velocities

G [kg/m²s]	T_{sub} [°C]	p [bar]	q [kW/m²]	u_{meas} [m/s]
66	17	11.0	47.5	0.01
	12	15.0	43.0	0.00
	17	15.0	44.6	-0.01
	12	20.0	37.2	0.00
		20.0	39.3	0.00
		20.0	40.6	-0.01
	17	20.0	42.9	0.00
		27.1	37.6	0.00
		30.0	37.1	-0.01

Table 0.5: Measured average vertical velocities with the high-speed camera and comparison with force balance based calculated velocities

G [kg/m²s]	T_{sub} [°C]	p [bar]	q [kW/m²]	v_{cam} [m/s]	v_{calc} [m/s]
66	17	11.0	47.5	0.75	0.84
	12	15.0	43.0	0.60	0.57
	17	15.0	44.6	0.55	0.58
	12	20.0	37.2	0.39	0.37
		20.0	39.3	0.38	0.37
		20.0	40.6	0.39	0.37
	17	20.0	42.9	0.40	0.36
		27.1	37.6	0.26	0.24
		30.0	37.1	0.19	0.20

Table 0.6: Slip ratios at the conditions provided in above tables and displayed wall temperatures and vapor qualities; first range value at superheated wall temperature vapor conditions, second value at thermal equilibrium conditions

T_W [°C]	x_e [-]	x_a [-]	S_{meas}	S_{Ahm}	S_{Gro}	$S_{Yoder/Yu}$
227.5	1.004	0.442	1.40 – 1.62	1.86 – 1.62	1.43 – 1.31	1.18
203.0	1.035	0.481	1.29 – 1.43	1.70 – 1.49	1.35 – 1.25	-
210.5	1.026	0.463	1.37 – 1.55	1.71 – 1.49	1.35 – 1.25	-
184.0	0.993	0.477	1.39 – 1.58	1.56 – 1.38	1.28 – 1.19	1.12
215.5	1.056	0.445	1.45 – 1.63	1.59 – 1.38	1.29 – 1.19	-
224.9	1.103	0.448	1.45 – 1.58	1.59 – 1.37	1.30 – 1.19	-
220.2	1.089	0.450	1.40 – 1.53	1.59 – 1.37	1.29 – 1.19	-
200.1	1.122	0.453	1.52 – 1.62	1.44 – 1.24	1.22 – 1.12	-
216.3	1.226	0.428	1.78 – 1.83	1.40 – 1.18	1.20 – 1.09	1.07

Table 0.7: Upper bin limits and characteristic bin diameters for the Meholic droplet diameter distributions in chapter 5.1.6.1

G [kg/m²s]	**T_{sub}** [°C]	**p** [bar]	**q** [kW/m²]	**Bin limit** [mm]	**d_{char}** [mm]
66	17	11.0	47.5	0.368; 0.460; 0.545; 0.649; 1.140	0.293; 0.416; 0.502; 0.594;0.754
	12	15.0	43.0	0.507; 0.633; 0.750; 0.894; 1.570	0.403; 0.573; 0.691; 0.818; 1.038
	17	15.0	44.6	-	-
	12	20.0	37.2	0.614; 0.766; 0.908; 1.082; 1.900	0.488; 0.693; 0.836; 0.990; 1.256
		20.0	39.3	0.565; 0.706; 0.836; 0.997; 1.750	0.449; 0.638; 0.770; 0.911; 1.157
		20.0	40.6	0.446; 0.557; 0.659; 0.786; 1.380	0.354; 0.503; 0.608; 0.719; 0.912
	17	20.0	42.9	0.614; 0.766; 0.908; 1.082; 1.900	0.488; 0.693; 0.836; 0.990; 1.256
		27.1	37.6	0.717; 0.895; 1.061; 1.264; 2.220	0.570; 0.810; 0.977; 1.156; 1.467
		30.0	37.1	0.413; 0.516; 0.612; 0.729; 1.280	0.328; 0.467; 0.564; 0.667; 0.846

Publication Bibliography

Ahmad, S. Y. (1970): Axial Distribution of Bulk Temperature and Void Fraction in a Heated Channel With Inlet Subcooling. In *Journal of Heat Transfer* 92 (4), pp. 595–609. DOI: 10.1115/1.3449729.

Ahmad, S. Y. (1973): Fluid to fluid modeling of critical heat flux: A compensated distortion model. In *International Journal of Heat and Mass Transfer* 16 (3), pp. 641–662. DOI: 10.1016/0017-9310(73)90229-9.

Andreani, M.; Yadigaroglu, G. (1994): Prediction methods for dispersed flow film boiling. In *International Journal of Multiphase Flow* 20, pp. 1–51. DOI: 10.1016/0301-9322(94)90069-8.

Andreani, M.; Yadigaroglu, G. (1997): A 3-D Eulerian-Lagrangian model of dispersed flow film boiling including a mechanistic description of the droplet spectrum evolution—I. The thermal-hydraulic model. In *International Journal of Heat and Mass Transfer* (Vol. 40, No.8), pp. 1753–1772. Available online at https://www.semanticscholar.org/paper/A-3-D-Eulerian-Lagrangian-model-of-dispersed-flow-a-Andreani-Yadigaroglu/afb228a66ea4fb17d1fc5c234d753be990b88d3d.

Anghel, I. G. (2013): Experimental and theoretical study of post-dryout heat transfer in annuli with flow obstacle. Stockholm: Engineering Sciences, KTH Royal Institute of Technology (TRITA-FYS, 2013:60).

Anghel, I. G. (2014): Experimental and theoretical study of post-dryout heat transfer in annuli with flow obstacle. Dissertation. KTH Royal Institute of Technology. Available online at http://kth.diva-portal.org/smash/record.jsf?pid=diva2%3A706045&dswid=-9726.

Anghel, I. G.; Anglart, H. (2014): On post-dryout heat transfer in channels with flow obstacles. In *Nuclear Engineering and Design* 270, pp. 351–358. DOI: 10.1016/j.nucengdes.2014.02.005.

Anglart, H. (2006): Modeling of Spacer Influence on Post-Dryout Heat Transfer in Heated Channels. In: Proceedings of the 14th International Conference on Nuclear Engineering - 2006. Presented at 14th International Conference on Nuclear Engineering, July 17-20, 2006, Miami, Florida, USA. 14th International Conference on Nuclear Engineering. Miami, Florida, USA, 7/17/2006 - 7/20/2006. ICONE; International Conference on Nuclear Engineering. New York, NY: ASME, pp. 747–753.

Anglart, H.; Persson, P. (2007): Experimental investigation of post-dryout heat transfer in annulus with spacers. In *International Journal of Multiphase Flow* 33 (8), pp. 809–821. DOI: 10.1016/j.ijmultiphaseflow.2007.02.006.

Auracher, H.; Marquardt, W. (2002): Experimental studies of boiling mechanisms in all boiling regimes under steady-state and transient conditions. In *International Journal of Thermal Sciences* 41 (7), pp. 586–598. DOI: 10.1016/S1290-0729(02)01352-2.

Auracher, H.; Marquardt, W. (2004): Heat transfer characteristics and mechanisms along entire boiling curves under steady-state and transient conditions. In *International Journal of Heat and Fluid Flow* 25 (2), pp. 223–242. DOI: 10.1016/j.ijheatfluidflow.2003.11.011.

Austregesilo, H.; Bals, C.; Hora, A.; Lerchl, G.; Romstedt, P.; Schöffel, P. et al. (2012): Athlet mod 3.0 Cycle A: Models and methods. Edited by Gesellschaft für Anlagen- und Reaktorsicherheit (GRS) (Technical Report GRS-P-1 Vol. 3).

Azzopardi, B. J. (1985): Drop sizes in annular two-phase flow. In *Experiments in Fluids* 3 (1), pp. 53–59. DOI: 10.1007/BF00285271.

Azzopardi, B. J.; Piearcey, A.; Jepson, D. M. (1991): Drop size measurements for annular two-phase flow in a 20 mm diameter vertical tube. In *Experiments in Fluids* 11-11 (2-3), pp. 191–197. DOI: 10.1007/BF00190300.

Baehr, H. D.; Stephan, K. (2016): Wärme- und Stoffübertragung. 9., aktualisierte Auflage. Berlin, Heidelberg: Springer Berlin Heidelberg.

Becker, K. M.; Askeljung, P.; Hedberg, S.; Söderquist, B.; Kahlbohm, U. (1992): An experimental investigation of the influence of axial heat flux distributions on PDO heat transfer for flow of water in vertical tubes. Royal Inst. of Tech., Stockholm (Sweden). Dept. of Reactor Technology. Sweden (KTH-NEL-54).

Becker, K. M.; Ling, C. H.; Hedberg, S.; Strand, G. (1983): An experimental investigation of post dryout heat transfer. Royal Inst. of Tech., Stockholm (Sweden). Dept. of Reactor Technology. Sweden (KTH-NEL--33(V.1,2)). Available online at https://inis.iaea.org/collection/NCLCollectionStore/_Public/15/049/15049472.pdf?r=1.

Bejan, A.; Kraus, A. D. (2003): Heat Transfer Handbook: Wiley (Heat Transfer Handbook). Available online at https://books.google.de/books?id=XbUgEAAAQBAJ.

Bennett, A. W.; Hewitt, G. F.; Kearsey, H. A.; Keeys, R. K. F. (1966): The wetting of hot surfaces by water in a steam environment at high pressure. Atomic Energy Research Establishment (UKAEA Report, AERE-R5146).

Bennett, A. W.; Hewitt, G. F.; Kearsey, H. A.; Keeys, R. K. F. (1967): Heat Transfer to Steam-Water Mixtures Flowing in Uniformly Heated Tubes in which the Critical Heat Flux has been Exceeded. Atomic Energy Research Establishment. Harwell, Berkshire (AERE-R5373).

Bergles, A. E.; Collier, G.; Delhaye, M.; Hewill, G. F.; Mayinger, F. (1981): Two-phase flow and heat transfer in the power and process industries. Washington: Hemisphere Publishing Corp.

Berna, C.; Escrivá, A.; Muñoz-Cobo, J. L.; Herranz, L. E. (2014): Review of droplet entrainment in annular flow: Interfacial waves and onset of entrainment. In *Progress in Nuclear Energy* 74, pp. 14–43. DOI: 10.1016/j.pnucene.2014.01.018.

Bertola, V. (Ed.) (2003): Modelling and Experimentation in Two-Phase Flow. Vienna: Springer Vienna (International Centre for Mechanical Sciences).

Bishop, A.; Sandberg, R. O.; Tong, L. S.; American Society of Mechanical Engineers. (1965): Forced convection heat transfer at high pressure after the critical heat flux. 65-HT-31. New York N.Y: ASME. Available online at http://worldcatlibraries.org/wcpa/oclc/272397023.

Bishop, A. A.; Sandberg, R. O.; Tong, L. S. (1964): High Temperature Supercritical Pressure Water Loop. Part V. Forced Convection Heat Transfer to Water After the Critical Heat Flux at High Subcritical Pressures (Westinghouse Electric Corp. Atomic Power Div., Pittsburgh, WCAP-2056; (Pt.V)). Available online at https://www.osti.gov/biblio/4668675-high-temperature-supercritical-pressure-water-loop-part-forced-convection-heat-transfer-water-after-critical-heat-flux-high-subcritical-pressures.

Caetano, E. F.; Shoham, O.; Brill, J. P. (1992): Upward Vertical Two-Phase Flow Through an Annulus—Part I: Single-Phase Friction Factor, Taylor Bubble Rise Velocity, and Flow Pattern Prediction. In *Journal of Energy Resources Technology* 114 (1), pp. 1–13. DOI: 10.1115/1.2905917.

Carbajo, Juan J. (1985): A study on the rewetting temperature. In *Nuclear Engineering and Design* 84 (1), pp. 21–52. DOI: 10.1016/0029-5493(85)90310-3.

Celata, G. P.; Mariani, A. (2003): Critical Heat Flux, Post-CHF Heat Transfer and Their Augmentation. In V. Bertola (Ed.): Modelling and Experimentation in Two-Phase Flow: Springer-Verlag, pp. 325–382. Available online at https://www.researchgate.net/publication/300452465_Critical_Heat_Flux_Post-CHF_Heat_Transfer_and_Their_Augmentation.

Chai, L. H.; Shoji, M. (2001): Boiling curves – bifurcation and catastrophe. In *International Journal of Heat and Mass Transfer* 44 (21), pp. 4175–4179. DOI: 10.1016/S0017-9310(01)00059-X.

Chen, J. C. (1966): Correlation for Boiling Heat Transfer to Saturated Fluids in Convective Flow. In *Industrial & Engineering Chemistry Process Design and Development* 5 (3), pp. 322–329. DOI: 10.1021/i260019a023.

Chen, J. C. (1986): A short review of dispersed flow heat transfer in post-dryout boiling. In *Nuclear Engineering and Design* 95, pp. 375–383. DOI: 10.1016/0029-5493(86)90062-2.

Chen, J. C.; Ozkaynak, F. T.; Sundaram, R. K. (1979): Vapor heat transfer in post-CHF region including the effect of thermodynamic non-equilibrium. In *Nuclear Engineering and Design* 51 (2), pp. 143–155. DOI: 10.1016/0029-5493(79)90086-4.

Chen, J. C.; Sundaram, R. K.; Ozkaynak, F. T. (1977): A phenomenological correlation for post-CHF heat transfer. United States. Available online at http://inis.iaea.org/search/search.aspx?orig_q=RN:09365532.

Chen, Y. (2011): Heat Transfer in Film Boiling of Flowing Water. In Aziz Belmiloudi (Ed.): Heat Transfer - Theoretical Analysis, Experimental Investigations and Industrial Systems: InTech.

Cheng, S. C.; Lau, P.W.K.; Poon, K. T. (1985): Measurements of true quench temperature of subcooled water under forced convective conditions. In *International Journal of Heat and Mass Transfer* 28 (1), pp. 235–243. DOI: 10.1016/0017-9310(85)90025-0.

Cheng, X.; Feuerstein, F.; Klingel, D.; Yu, D. L. (2018): Mechanistic prediction of post dryout heat transfer and rewetting. In *Kerntechnik* 83 (3), pp. 203–207. DOI: 10.3139/124.110872.

Cheng, X.; Müller, U. (2003): Review on critical heat flux in water cooled reactors. Karlsruhe: Forschungszentrum Karlsruhe GmbH (Forschungsbericht FZKA 6825).

Coelho Silva, A. (2015): Versuche zum Wärmeübergang mit überkritischem R134a an der KIMOF. Master's thesis. Karlsruhe Institute of Technology, Karlsruhe (Germany).

Collier, J. G. (1976): Post-dryout heat transfer - a review of the current position. Advanced Study. Institute on Two-Phase Flows and Heat Transfer. Istanbul.

Collier, J. G.; Thome, J. R. (1994): Convective Boiling and Condensation. 3rd ed.: Clarendon Press.

Cumo, M.; Farello, G. E.; Ferrari, G.; Palazzi, G. (1974): On Two-Phase Highly Dispersed Flows. In *J. Heat Transfer* 96 (4), pp. 496–503. DOI: 10.1115/1.3450235.

Cumo, M.; Ferrari, G.; Farello, G. E. (1971): A photographic study of two-phase highly dispersed flows. Comitato Nazionale per l'Energia Nucleare (CNEN). Italy. Available online at https://inis.iaea.org/collection/NCLCollectionStore/_Public/02/014/2014128.pdf?r=1.

Dai, X.; Shi, L.; An, Q.; Qian, W. (2018): Thermal stability of some hydrofluorocarbons as supercritical ORCs working fluids. In *Applied Thermal Engineering* 128, pp. 1095–1101. DOI: 10.1016/j.applthermaleng.2017.09.046.

Damsohn, M.; Prasser, H.-M. (2011): Droplet deposition measurement with high-speed camera and novel high-speed liquid film sensor with high spatial resolution. In *Nuclear Engineering and Design* 241 (7), pp. 2494–2499. DOI: 10.1016/j.nucengdes.2011.04.016.

Das, G.; Das, P. K.; Purohit, N. K.; Mitra, A. K. (1999): Flow Pattern Transition During Gas Liquid Upflow Through Vertical Concentric Annuli. In *Journal of Fluids Engineering* 121 (4), pp. 895–907.

Demidovich, A. V.; Kralinova, S. S.; Tkachenko, P. P.; Shlegel, N. E.; Volkov, R. S. (2019): Interaction of Liquid Droplets in Gas and Vapor Flows. In *Energies* 12 (22), p. 4256. DOI: 10.3390/en12224256.

Dougall, R. S.; Rohsenow, W. M. (1963): Film boiling on the inside of vertical tubes with upward flow of the fluid at low qualities. With assistance of Engineering., Massachusetts Institute of Technology. Dept. of Mechanical, Laboratory., Massachusetts Institute of Technology. Heat Transfer. Cambridge, Mass.: Dept. of Mechanical Engineering, Massachusetts Institute of Technology, [1963] (Cambridge, Mass.: Dept. of Mechanical Engineering, Massachusetts Institute of Technology, [1963]). Available online at https://dspace.mit.edu/handle/1721.1/62142.

Effert, M.; Brückner, J. (2021): Benson low mass flux vertically-tubed evaporators in the power market. A status update. Edited by Siemens Energy Global GmbH & Co. KG Generation. Reprint - Originally published in MPS 04/2017 - Modern Power Systems, page 26-28 and 30-31.

El-Nakla, M. (2011): On fluid-to-fluid modeling of film boiling heat transfer using dimensional analysis. In *International Journal of Multiphase Flow* 37 (2), pp. 229–234. DOI: 10.1016/j.ijmultiphaseflow.2010.09.004.

ENEA (1989): Thermal Non-Equilibrium in Two-Phase Flow. 7th EUROTHERM Seminar. Rome, March 23-24. INIS-mf-11484.

Era, A.; Gaspari, G. P.; Hassid, A.; Milani, A.; Zavattarelli, R. (1966): Heat transfer data in the liquid deficient region for steam-water mixtures at 70 kg/m² flowing in tubular and annular conduits. Centro Informazioni Studi Esperienze. Italy (Technical Report CISE R-184).

Evans, D.; Chen, J. C.; Webb, S. (1983): Experimental measurement of axially varying vapor superheats in convective film boiling. In *Interfacial Transport Phenomena* ASME, HTD-VOL. 23, pp. 85–92. Available online at https://www.osti.gov/biblio/5339575.

Evans, D.; Webb, S. W.; Chen, J. C. (1985): Axially Varying Vapor Superheats in Convective Film Boiling. In *Journal of Heat Transfer* 107 (3), pp. 663–669. DOI: 10.1115/1.3247475.

Evans, D. G. (1983): Measurement of thermal nonequilibrium in post-CHF convective film boiling. Master's thesis. Lehigh University, Bethlehem (USA). Available online at https://www.semanticscholar.org/paper/Measurement-of-thermal-nonequilibrium-in-post-CHF-Evans/36cba2a33e11911d60ad72f24bbb1b7b671ff8d4.

FBGS (2020): DTG® & FSG® Technologie - FBGS. Available online at https://fbgs.com/de/technology/dtg-fsg-technology/, updated on 4/13/2020, checked on 6/14/2021.

Feng, Q.; Johannsen, K. (1991): Experimental results of maximum transition boiling temperature during upflow in a circular tube at medium pressure. In *Experimental Thermal and Fluid Science* 4 (1), pp. 90–102. DOI: 10.1016/0894-1777(91)90023-k.

Feuerstein, F. (2019): Investigation of heat transfer near the critical point of R134a. Dissertation. Karlsruhe Institute of Technology, Karlsruhe (Germany).

Filburn, T.; Bullard, S. (2016): Nuclear Fuel, Cladding, and the “Discovery” of Zirconium. In: Three Mile Island, Chernobyl and Fukushima: Springer, Cham, pp. 105–114. Available online at https://link.springer.com/chapter/10.1007/978-3-319-34055-5_10.

FINKE MINERALÖLWERK GMBH (2020): Sicherheitsdatenblatt gemäß Verordnung (EG) Nr. 1907/2006. AVIATICON HLP-D 46 ((pp. 1 - 9)).

Forslund, R. P.; Rohsenow, W. M. (1966): Thermal non-equilibrium in dispersed flow film boiling in a vertical tube. Massachusetts Institute of Technology. Cambridge (USA) (Technical Report No. 75312-44).

Forslund, R. P.; Rohsenow, W. M. (1968): Dispersed Flow Film Boiling. In *Journal of Heat Transfer* 90 (4), pp. 399–407. DOI: 10.1115/1.3597531.

Ganić, E. N. (1976): Post critical heat flux heat transfer. Massachusetts Institute of Technology, Cambridge (USA). Available online at https://dspace.mit.edu/handle/1721.1/98595.

Ganić, E. N.; Rohsenow, W. M. (1977): Dispersed flow heat transfer. In *International Journal of Heat and Mass Transfer* 20 (8), pp. 855–866. DOI: 10.1016/0017-9310(77)90115-6.

Ganić, E. N.; Rohsenow, W. M. (1979): On the Mechanism of Liquid Drop Deposition in Two-Phase Dispersed Flow. In *Journal of Heat Transfer* 101 (2), pp. 288–294. DOI: 10.1115/1.3450962.

Gao, Y. (2017): Messfehlerberechnung für Wärmeübergangsversuche mit überkritischen R134a an der KIMOF. Bachelor's thesis. Karlsruhe Institute of Technology, Karlsruhe (Germany).

Ghiaasiaan, S. M. (2007): Two-phase flow, boiling and condensation in conventional and miniature systems. New York: Cambridge University Press. Available online at https://www.researchgate.net/publication/266503594_Two-Phase_Flow_Boiling_and_Condensation_In_Conventional_and_Miniature_Systems.

Gottula, R. C.; Nelson, R. A.; Chen, J. C.; Neti, S.; Sundaram, R. K. (1983): Forced-convective nonequilibrium post-CHF heat-transfer experiments in a vertical tube. (EG and G Idaho, Inc., Idaho Falls (USA), EGG-M-13782; CONF-830301-16). Available online at https://www.osti.gov/biblio/6210518.

Groeneveld, D. C. (1972): The thermal behaviour of a heated surface at and beyond dryout. Dissertation. University of Western Ontario, London (Canada). Chalk River Nuclear

Laboratories (AECL). Available online at https://inis.iaea.org/collection/NCLCollectionStore/_Public/04/089/4089003.pdf?r=1.

Groeneveld, D. C. (1973): Post-dryout heat transfer at reactor operating conditions. Presented at the National Topical Meeting on Water Reactor Safety, American Nuclear Society, Salt Lake City, Utah, March 26-28, 1973. Atomic Energy of Canada Limited (AECL). Chalk River (Canada) (AECL-4513).

Groeneveld, D. C. (1975): Post-dryout heat transfer: Physical mechanisms and a survey of prediction methods. In *Nuclear Engineering and Design* 32 (3), pp. 283–294. DOI: 10.1016/0029-5493(75)90099-0.

Groeneveld, D. C. (2001): Look-Up Table for Fully Developed Film-Boiling Heat-Transfer Coefficients for Light Water.

Groeneveld, D. C.; Delorme, G.G.J. (1976): Prediction of thermal non-equilibrium in the post-dryout regime. In *Nuclear Engineering and Design* 36 (1), pp. 17–26. DOI: 10.1016/0029-5493(76)90138-2.

Groeneveld, D. C.; Doerffer, S.; Tain, R. M.; Hammouda, N. (1997): Fluid-to-fluid modelling of the critical heat flux and post-dryout heat transfer. In M. Giot, F. Mayinger, G. P. Celata (Eds.): Experimental heat transfer fluid mechanics and thermodynamics. Proceedings of the 4th World Conference on Experimental Heat Transfer, Fluid Mechanics and Thermodynamics, Brussels, June 2-6, 1997. Pisa: Edizioni ETS, pp. 859–866.

Groeneveld, D. C.; Leung, L. K. H.; Guo, Y.; Vasic, A.; El Nakla, M.; Peng, S. W. et al. (2005): Lookup Tables for Predicting CHF and Film-Boiling Heat Transfer: Past, Present, and Future. In *Nuclear Technology* 152 (1), pp. 87–104. DOI: 10.13182/NT152-87.

Groeneveld, D. C.; Leung, L.K.H.; Vasic', A. Z.; Guo, Y. J.; Cheng, S. C. (2003): A look-up table for fully developed film-boiling heat transfer. In *Nuclear Engineering and Design* 225 (1), pp. 83–97. DOI: 10.1016/S0029-5493(03)00149-3.

Groeneveld, D. C.; Leung, L.K.H.; Zhang, J.; Cheng, S. C.; Vasić, A.Z (1999): Effect of appendages on film-boiling heat transfer in tubes. In: Proceedings of the Ninth International Topical Meeting on Nuclear Reactor Thermal Hydraulics (NURETH-9). San Francisco (California), October 3–8, Log #235, 17 pp.

Groeneveld, D. C.; Moeck, E. O. (1968): An Investigation of Heat Transfer in the Liquid Deficient Regime (Atomic Energy of Canada Ltd., Chalk River (Ontario). Chalk River Nuclear Labs, AECL-3281(Rev.)). Available online at https://www.osti.gov/biblio/4747993.

Groeneveld, D. C.; Snoek, C. W. (1986): A Comprehensive Examination of Heat Transfer Correlations Suitable for Reactor Safety Analysis. In *MultScienTechn* 2 (1-4), pp. 181–274. DOI: 10.1615/MultScienTechn.v2.i1-4.30.

Groeneveld, D. C.; Stewart, J. C. (1982): The Minimum Film Boiling Temperature for Water During Film Boiling Collapse. In: Proceeding of International Heat Transfer Conference 7. International Heat Transfer Conference 7. Munich, Germany, 06.09.1982 - 10.09.1982. Connecticut: Begellhouse, pp. 393–398.

Guo, Y.; Mishima, K. (2002): A non-equilibrium mechanistic heat transfer model for post-dryout dispersed flow regime. In *Experimental Thermal and Fluid Science* 26 (6-7), pp. 861–869. DOI: 10.1016/S0894-1777(02)00195-4.

Hadaller, G.; Banerjee, S. (1969): Heat transfer to superheated steam in round tubes. AECL Report.

Hagiwara, Y.; Suzuki, K.; Sato, T. (1980): An experimental investigation on liquid droplets diffusion in annular-mist flow. In *Multiphase Transport: Fundamentals, Reactor Safety, Applications* 1, pp. 111–131.

Hammouda, N. (1996): Subcooled film boiling in non-aqueous fluids. Université D'Ottawa / University Of Ottawa, Ottawa.

Hammouda, N.; Groeneveld, D. C.; Cheng, S. C. (1996): An experimental study of subcooled film boiling of refrigerants in vertical up-flow. In *International Journal of Heat and Mass Transfer* 39 (18), pp. 3799–3812. DOI: 10.1016/0017-9310(96)00062-2.

Hench, J. E. (1964): Multirod (Two-Rod) Transition and Film Boiling in Forced Convection to Water at 1000 psia (General Electric Co., San Jose, Calif. Atomic Power Equipment Dept, GEAP-4721; EURAEC-1262). Available online at https://www.osti.gov/biblio/4616262-multirod-two-rod-transition-film-boiling-forced-convection-water-psia.

Hessenkemper, H.; Starke, S.; Atassi, Y.; Ziegenhein, T.; Lucas, D. (2022): Bubble identification from images with machine learning methods. In *International Journal of Multiphase Flow* 155, p. 104169. DOI: 10.1016/j.ijmultiphaseflow.2022.104169.

Hetsroni, G. (1982): Handbook of multiphase systems: McGraw-Hill Book Co.,New York, NY. Available online at https://www.osti.gov/biblio/5474196.

Hewitt, G. F.; Delhaye, J. M.; Zuber, N. (Eds.) (1992): Post-Dryout Heat Transfer. First edition. Boca Raton, Fl (USA): CRC Press.

Hewitt, G. F.; Roberts, D. N. (1969): Studies of two-phase flow patterns by simultaneous x-ray and flash photography (Atomic Energy Research Establishment, Harwell, England (United Kingdom), AERE-M--2159). Available online at https://www.osti.gov/biblio/4798091.

Hill, W. S.; Rohsenow, W. M. (1982): Dryout droplet distribution and dispersed flow film boiling. Massachusetts Institute of Technology (Report No. 85694-105).

Hochreiter, L. E.; Loftus, M. J.; Erbacher, F. J.; Ihle, P.; Rust, K. (1992): Post CHF Effects of Spacer Grids and Blockages in Rod Bundles. In G. F. Hewitt, J. M. Delhaye, N. Zuber (Eds.):

Post-Dryout Heat Transfer. First edition. Boca Raton, Fl (USA): CRC Press, pp. 185–269. Available online at https://www.taylorfrancis.com/chapters/edit/10.1201/9780203742754-3/post-chf-effects-spacer-grids-blockages-rod-bundles-hochreiter-loftus-erbacher-ihle-rust.

Hughmark, G. A. (1967): Mass and heat transfer from rigid spheres. In *AIChE J.* 13 (6), pp. 1219–1221. DOI: 10.1002/aic.690130638.

Hull, L. M.; Rohsenow, W. M. (1982): Thermal boundary layer development in dispersed flow film boiling. Heat Transfer Laboratory, Dept. of Mechanical Engineering, Massachusetts Institute of Technology. Cambridge (USA). Available online at https://dspace.mit.edu/handle/1721.1/61440.

Hynek, S. F.; Rohsenow, W. M.; Bergles, A. E. (1969): Forced-convection, dispersed-flow film boiling. Massachusetts Institute of Technology (Technical report No. DSR 70586-63). Available online at https://www.semanticscholar.org/paper/Forced-convection%2C-dispersed-flow-film-boiling-Hynek-Rohsenow/f6181acc63958653df583a84d480387ba20f5ac9.

IAEA (2025): Power Reactor Information System. International Atomic Energy Agency. Available online at https://pris.iaea.org/pris/home.aspx, updated on 10/23/2025, checked on 10/24/2025.

Iguchi, T.; Stosic, Z. V.; Iwaki, C. (2001a): Experimental Investigation of Boiling Curve in Vicinity of CHF and Rewetting Conditions Part 1: Boiling Curve, Experiments and Post-CHF Test Results. In G. P. Celata (Ed.): Experimental heat transfer, fluid mechanics and thermodynamics, 2001. Proceedings of the Fifth World Conference on Experimental Heat Transfer, Fluid Mechanics and Thermodynamics, Thessaloniki, Greece, 24 - 28 September, 2001. Pisa: ETS (Experimental heat transfer, fluid mechanics and thermodynamics), pp. 227–236.

Iguchi, T.; Stosic, Z. V.; Iwaki, C. (2001b): Experimental Investigation of Boiling Curve in Vicinity of CHF and Rewetting Conditions Part 2: Reflood Test Results and Comparison to Post-CHF Test Results. In G. P. Celata (Ed.): Experimental heat transfer, fluid mechanics and thermodynamics, 2001. Proceedings of the Fifth World Conference on Experimental Heat Transfer, Fluid Mechanics and Thermodynamics, Thessaloniki, Greece, 24 - 28 September, 2001. Pisa: ETS (Experimental heat transfer, fluid mechanics and thermodynamics), pp. 237–244.

Iloeje, O. C.; Plummer, D. N.; Rohsenow, W. M.; Griffith, P. (1975): An Investigation of the Collapse and Surface Rewet in Film Boiling in Forced Vertical Flow. In *J. Heat Transfer* 97 (2), pp. 166–172. DOI: 10.1115/1.3450336.

International Energy Agency (2025a): Electricity 2025. Analysis and forecast to 2027. Available online at https://www.iea.org/news/growth-in-global-electricity-demand-is-set-to-accelerate-in-the-coming-years-as-power-hungry-sectors-expand, checked on 2/28/2025.

International Energy Agency (2025b): The Path to a New Era for Nuclear Energy. Available online at https://www.iea.org/reports/the-path-to-a-new-era-for-nuclear-energy, checked on 2/28/2025.

Ishii, M.; Grolmes, M. A. (1975): Inception criteria for droplet entrainment in two-phase concurrent film flow. In *AIChE J.* 21 (2), pp. 308–318. DOI: 10.1002/aic.690210212.

Isshiki, N. (1959): Theoretical and experimental study on atomization of liquid drop in high speed gas stream. Transportation Technical Research Institute. Tokyo (Japan) (Report No. 35). Available online at http://worldcatlibraries.org/wcpa/oclc/250873253.

Kaiser, T. (2018): Experimentelle Untersuchungen zum post-dryout Wärmeübergang und Rewetting an der Modellfluidanlage KIMOF. Master's thesis. Karlsruhe Institute of Technology, Karlsruhe (Germany).

Kataoka, I.; Ishii, M.; Mishima, K. (1983): Generation and Size Distribution of Droplet in Annular Two-Phase Flow. In *Journal of Fluids Engineering* 105 (2), pp. 230–238. DOI: 10.1115/1.3240969.

Katsaounis, A.: Post-dryout correlations and models compared to experimental data from different fluids. In: Proceedings of the XVIII International Symposium on Heat and Mass Transfer in Cryoengineering and Refrigeration, Hemisphere Publishing Corp., Washington; ICHMT-Symposium, Sept. 1986, Dubrovnik, Yugoslavia. Preprint GKSS 86/E/41.

Kelessidis, V. C.; Dukler, A. E. (1989): Modeling flow pattern transitions for upward gas-liquid flow in vertical concentric and eccentric annuli. In *International Journal of Multiphase Flow* 15 (2), pp. 173–191. DOI: 10.1016/0301-9322(89)90069-4.

Kendall, G. E.; Rohsenow, W. M. (1978): Heat transfer to impacting drops and post critical heat flux dispersed flow. Massachusetts Institute of Technology. Cambridge (USA) (Technical Report No. 85694-100).

Kim, I. G.; Korol'kov, B. P. (1991): Enhancement of steady-state postdryout heat transfer in an annulus with spacers. Heat Transfer Soviet Res. In *Heat Transfer Soviet Research* 23 (5), pp. 649–657.

Kirillov, P. L.; Smogalev, I. P.; Ivacshkevitch, A. A.; Vinogradov, V. N.; Sudnitsina, M. O.; Mitrofanova, T. V. (1996): The Look-Up Table for Heat Transfer Coefficient in Post-Dryout Region for Water Flowing in Tubes (the 1996-Version). Institute of Physics and Power Engineering. Obninsk (Russia) (Preprint FEI-2525).

Köckert, L.; Badea, A. F.; Cheng, X.; Yu, D.; Klingel, D. (2021): Studies on post-dryout heat transfer in R-134a vertical flow. In *International Journal of Advanced Nuclear Reactor Design and Technology* 3, pp. 44–53. DOI: 10.1016/j.jandt.2021.05.001.

Köckert, L.; Feuerstein, F.; Yu, D.; Klingel, D.; Cheng, X. (2018): Experimental Study of Post-Dryout Heat Transfer and Rewetting in an R-134a Cooled Vertical Tube at Comparable

Water-Cooled Reactor Pressure Conditions. In: The 12th International Topical Meeting on Reactor Thermal-Hydraulics, Operation, and Safety (NUTHOS-12), Qingdao (China).

Köckert, L.; Liu, W.; Cheng, X. (2024a): Post-dryout heat transfer in circular tubes using R-134a: experiment and correlation assessment. In *Wärme - und Stoffübertragung* 60 (8), pp. 1453–1466. DOI: 10.1007/s00231-024-03498-5.

Köckert, L.; Rensch, N.; Badea, A. F.; Cheng, X. (2024b): Experimental investigation of the post-dryout heat transfer and droplet behavior with R-134a. In: Specialist Workshop on Advanced Instrumentation and Measurement Techniques for Nuclear Reactor Thermal-Hydraulics and Severe Accidents 2024 (SWINTH-2024). Dresden (Germany).

Köhler, W. (1984): Einfluß des Benetzungszustandes der Heizflache auf Wärmeübergang und Druckverlust in einem Verdampferrohr. Dissertation. Technical University Munich, Munich.

Koizumi, Y.; Kumamaru, H.; Yonomoto, T.; Tasaka, K. (1987): Post-dryout heat transfer of high-pressure steam-water two-phase flow in single rod channel and multi rod bundle. In *Nuclear Engineering and Design* 99, pp. 157–165. DOI: 10.1016/0029-5493(87)90117-8.

Koizumi, Y.; Ueda, T.; Tanaka, H. (1979): Post dryout heat transfer to R-113 upward flow in a vertical tube. In *International Journal of Heat and Mass Transfer* 22 (5), pp. 669–678. DOI: 10.1016/0017-9310(79)90115-7.

Laperrière, A. (1983): An analytical and experimental investigation of forced convection film boiling. An analytical and experimental investigation of forced convection film boiling. Université D'Ottawa / University Of Ottawa. Available online at https://ruor.uottawa.ca/handle/10393/3837.

Lau, P. W. K. (1983): Rewetting phenomena and measurements of true quench temperature. Université D'Ottawa / University Of Ottawa. Available online at https://ruor.uottawa.ca/handle/10393/3566?mode=full.

Lee, K. L.; Chang, S. H. (2010): Experimental investigations of the post-CHF heat transfer of R-134a flow boiling in an annulus with spacer grids. In *Nuclear Engineering and Design* 240 (10), pp. 3397–3404. DOI: 10.1016/j.nucengdes.2010.07.013.

Lee, R. (1982): Droplet deposition above a quench front during reflood after a large break LOCA. United States. Available online at http://inis.iaea.org/search/search.aspx?orig_q=RN:16078119.

Lee, S. K.; Chang, S. H. (2008): Experimental study of post-dryout with R-134a upward flow in smooth tube and rifled tubes. In *International Journal of Heat and Mass Transfer* 51 (11-12), pp. 3153–3163. DOI: 10.1016/j.ijheatmasstransfer.2007.08.026.

Lemmon, E. W.; Huber, M. L.; McLinden, M. O. (2007): NIST Standard Reference Database 23, Version 8.0 - Reference Fluid Thermodynamic and Transport Properties (REFPROP). Gaithersburg.

Leung, L.K.H.; Hammouda, N.; Groeneveld, D. C. (1997): A look-up table for film-boiling heat-transfer coefficients in tubes with vertical upward flow. In: Proceedings of the Eighth international topical meeting on nuclear reactor thermal-hydraulics (NURETH-8), Kyoto (Japan), 30 Sep - 4 Oct, pp. 671–678. Available online at http://inis.iaea.org/search/search.aspx?orig_q=RN:30016288.

Li, H.; Anglart, H. (2016): Prediction of dryout and post-dryout heat transfer using a two-phase CFD model. In *International Journal of Heat and Mass Transfer* 99, pp. 839–850. DOI: 10.1016/j.ijheatmasstransfer.2016.04.021.

Liesch, K.; Raemhild, G.; Hofmann, K. (1975): Zur Bestimmung des Wärmübergangs und der kritischen Heizflächenbelastung im Hinblick auf besondere Verhältnisse in den Kühlkanälen eines DWR bei schweren Kühlmittelverlustunfällen. Laboratorium für Reaktorregelung und Anlagensicherung (MRR 150).

Loftus, M. J.; Hochreiter, L. E.; Conway, C. E.; Dodge, C. E.; Tong, A.; Rosal, E. R. et al. (1980): PWR flecht seaset unblocked bundle, forced and gravity reflood task data report. Volume 1. Edited by USNRC, EPRI, Westinghouse (FLECHT SEASET Program - NRC/EPRI/Westinghouse Report No. 7).

Lomperski, S.; Gerardi, C.; Pointer, W. D. (2015): Fiber optic distributed temperature sensor mapping of a jet-mixing flow field. In *Experiments in Fluids* 56 (3). DOI: 10.1007/s00348-015-1918-6.

Ma, Yue; Chung, J. N. (2001): An experimental study of critical heat flux (CHF) in microgravity forced-convection boiling. In *International Journal of Multiphase Flow* 27 (10), pp. 1753–1767. DOI: 10.1016/S0301-9322(01)00031-3.

McKinsey & Company (2024): Global Energy Perspective 2024. Available online at https://www.mckinsey.com/industries/energy-and-materials/our-insights/global-energy-perspective#/, checked on 2/28/2025.

Meholic, M. J. (2011): The Development of a Non-Equilibrium Dispersed Flow Film Boiling Heat Transfer Modeling Package. Available online at https://etda.libraries.psu.edu/catalog/11651.

Miller, D. J.; Cheung, F. B.; Bajorek, S. M. (2013): On the development of a grid-enhanced single-phase convective heat transfer correlation. In *Nuclear Engineering and Design* 264, pp. 56–60. DOI: 10.1016/j.nucengdes.2012.11.023.

Miropol'skiy, Z. L. (1963): Heat Transfer in Film Boiling of a Steam-Water Mixture in Steam Generating Tubes. In *Teploenergetika* 10, pp. 49–53.

Moffat, R. J. (1985): Using Uncertainty Analysis in the Planning of an Experiment. In *Journal of Fluids Engineering* 107 (2), pp. 173–178. DOI: 10.1115/1.3242452.

Morey, W. W.; Meltz, G.; Glenn, W. H. (1989): Fiber Optic Bragg Grating Sensors. In Ramon P. DePaula, Eric Udd (Eds.): Fiber Optic and Laser Sensors VII. OE/FIBERS '89. Boston, Tuesday 5 September 1989: SPIE (SPIE Proceedings), p. 98.

Nemitallah, M.; El-Nakla, M. (2013): Fluid to Fluid Modeling for Post Dry Out Using Dimensional Analysis and Energy Scaling. In *AMM* 302, pp. 42–48. DOI: 10.4028/www.scientific.net/AMM.302.42.

Nguyen, N. H.; Moon, S.-K. (2015): An improved heat transfer correlation for developing post-dryout region in vertical tubes. In *Nuclear Engineering and Technology* 47 (4), pp. 407–415. DOI: 10.1016/j.net.2015.04.004.

Nijhawan, S.; Chen, J. C.; Sundaram, R. K.; London, E. J. (1980): Measurement of Vapor Superheat in Post-Critical-Heat-Flux Boiling. In *Journal of Heat Transfer* 102 (3), pp. 465–470. DOI: 10.1115/1.3244324.

Nishikawa, K.; Yoshida, S.; Mori, H.; Takamatsu, H. (1983): An experiment on the heat transfer characteristics in the post-burnout region at high subcritical pressures. In *Nuclear Engineering and Design* 74 (2), pp. 233–239. DOI: 10.1016/0029-5493(83)90060-2.

Nishikawa, K.; Yoshida, S.; Mori, H.; Takamatsu, H. (1986): Post-dryout heat transfer to Freon in a vertical tube at high subcritical pressures. In *International Journal of Heat and Mass Transfer* 29 (8), pp. 1245–1251. DOI: 10.1016/0017-9310(86)90157-2.

Nuclear Energy Agency (2023): The NEA Small Modular Reactor Dashboard (NEA No. 7650). Available online at https://www.oecd-nea.org/jcms/pl_78743/the-nea-small-modular-reactor-dashboard, checked on 2/28/2025.

Nukiyama, S. (1966): The maximum and minimum values of the heat Q transmitted from metal to boiling water under atmospheric pressure. In *International Journal of Heat and Mass Transfer* 9 (12), pp. 1419–1433. DOI: 10.1016/0017-9310(66)90138-4.

Oliveira, A.V.S.; Peña Carrillo, J. D.; Labergue, A.; Glantz, T.; Gradeck, M. (2020): Experimental study of dispersed flow film boiling at sub-channel scale in LOCA conditions: Influence of the steam flow rate and residual power. In *Applied Thermal Engineering* 172, p. 115143. DOI: 10.1016/j.applthermaleng.2020.115143.

Othonos, A. (1997): Fiber Bragg gratings. In *Review of Scientific Instruments* 68 (12), pp. 4309–4341. DOI: 10.1063/1.1148392.

Peña, J. D.; Oliveira, A.; Labergue, A.; Glantz, T.; Gradeck, M.: Experimental thermal-hydraulic study of a steam-droplets flow inside a vertical pipe during the cooling phase in LOCA conditions -effect of the steam flow rate. In: 10th International Conference on Multiphase Flow, ICMF 2019, Rio de Janeiro, Brazil, May 19 – 24, 2019. Available online at https://hal.archives-ouvertes.fr/hal-02433931, checked on 1/9/2020.

Peterson, L. J.; Bajorek, S. M. (2002): Experimental Investigation of Minimum Film Boiling Temperature for Vertical Cylinders at Elevated Pressure. In: 10th International Conference on Nuclear, April 14–18, 2002, Arlington, Virginia (USA), Volume 3, pp. 883–892.

Plummer, D. N. (1974): Post critical heat transfer to flowing liquid in a vertical tube. Dissertation. Massachusetts Institute of Technology, Cambridge (USA). Department of Mechanical Engineering.

Polomik, E. E.; Levy, S.; Sawochka, S. G. (1961): Heat Transfer Coefficients with Annular Flow During "One-Through" Boiling Water to 100 Per Cent Quality at 800, 1100, 1400 PSI. General Electric Company. Atomic Power Equipment Department (GEAP-3703). Available online at https://digital.library.unt.edu/ark:/67531/metadc101060/m1/20/.

Preisegger, E.; Henrici, R. (1992): Refrigerant 134a: The first step into a new age of refrigerants. In *International Journal of Refrigeration* 15 (6), pp. 326–331. DOI: 10.1016/0140-7007(92)90014-L.

Quinn, E. P. (1963-68): Transition Boiling Heat Transfer Program (General Electric Co. Atomic Power Equipment Dept., San Jose, Calif). Available online at https://www.osti.gov/biblio/4034958-transition-boiling-heat-transfer-program-quarterly-progress-report-april-june.

Quinn, E. P. (1966): Physical Model of Heat Transfer Beyond the Critical Heat Flux, GEAP-5093.

Sadatomi, M.; Sato, Y.; Saruwatari, S. (1982): Two-phase flow in vertical noncircular channels. In *International Journal of Multiphase Flow* 8 (6), pp. 641–655. DOI: 10.1016/0301-9322(82)90068-4.

Schlund, G.; Schulze, T.; Brückner, J.; Thomas, F. (2021): New Benson evaporator for vertical HRSGs exceeds expectations. Heat recovery steam generators. Edited by Siemens Energy Global GmbH & Co. KG Generation. Reprint - Originally published in MPS 10/2019 - Modern Power Systems, page 39-41.

Schnittger, R.-B. (1982): Untersuchungen zum Wärmeübergang bei vertikalen und horizontalen Rohrströmungen im Post-Dryout-Bereich. Dissertation. Universität Hannover, Hannover.

Schulenberg, T.; Czifrus, S. (2025): Design Concept of a Super Pressurized Water Reactor.

Shi, J.; Sun, B.; Zhang, G.; Song, F.; Yang, L. (2016): Prediction of dryout and post-dryout wall temperature at different operating parameters for once-through steam generators. In *International Journal of Heat and Mass Transfer* 103, pp. 66–76. DOI: 10.1016/j.ijheatmasstransfer.2016.07.027.

Siemens AG Power Generation (Ed.) (2006): BENSON® Once-trough heat recovery steam generator (Order No. A96001-S90-A496-X-4A00).

Snoek, C. W. (1990): A selection of new developments in multiphase flow measurement techniques. In *Experimental Thermal and Fluid Science* 3 (1), pp. 60–73. DOI: 10.1016/0894-1777(90)90101-C.

Song, M. (2021): Modelling of CHF and Post-CHF Heat Transfer for Trans-critical Transients. Dissertation. Karlsruhe Institute of Technology, Karlsruhe (Germany). Available online at https://publikationen.bibliothek.kit.edu/1000139979.

Song, M.; Liu, X. (2021): Assessment of CHF and Post-CHF Heat Transfer Models for High-Pressure Condition. In *Front. Energy Res.* 9, p. 768. DOI: 10.3389/fenrg.2021.782086.

Song, M.; Liu, X.; Cheng, X. (2022): A new correlation for post-dryout heat transfer in upward vertical flow. In *Nuclear Engineering and Design* 392, p. 111747. DOI: 10.1016/j.nucengdes.2022.111747.

Stier, J. (2020): Optische Strömungsuntersuchung unter post-dryout Bedingungen. Bachelor's thesis. Karlsruhe Institute of Technology, Karlsruhe (Germany).

Stosic, Z. V. (2005): On the frontier of boiling curve and beyond design of its origin. In. Proceedings of the International Conference Nuclear Energy for New Europe 2005. Slovenia. Slovenia: Nuclear Society of Slovenia. Available online at http://inis.iaea.org/search/search.aspx?orig_q=RN:37104705.

Strauss, Karl (2016): Kraftwerkstechnik. Berlin, Heidelberg: Springer Berlin Heidelberg.

Styrikovich, M. A.; Leontiev, A. I.; Polonsky, V. S.; Malashkin, I. I. (1980): Analytical study of heat transfer in the post dry-out region in smooth and rough vaporization channels. In *International Journal of Heat and Mass Transfer* 23 (8), pp. 1045–1053. DOI: 10.1016/0017-9310(80)90169-6.

Tong, L. S.; Tang, Y. S. (1997): Boiling Heat Transfer and Two-Phase Flow. 2nd ed. Washington D.C. (USA): Taylor & Francis.

Torfeh, S.; Kouhikamali, R. (2015): Numerical investigation of mist flow regime in a vertical tube. In *International Journal of Thermal Sciences* 95, pp. 1–8. DOI: 10.1016/j.ijthermalsci.2015.03.015.

Trabold, T. A.; Kumar, R.; Vassallo, P. F. (1999): Experimental Study of Dispersed Droplets in High-Pressure Annular Flows. In *Journal of Heat Transfer* 121 (4), pp. 924–933. DOI: 10.1115/1.2826083.

U.S. Atomic Energy Commission (1971): Criteria for Emergency Core Cooling Systems for Light Water Power Reactors. Interim Policy Statement. Federal Register, 36, No. 125, pp. 12247-12250.

U.S. Nuclear Regulatory Commission: Part I - Introduction to Reactor Technology - PWR. Chapter 4.0 Babcock & Wilcox Plant Description. Edited by U.S. Nuclear Regulatory Commission Technical Training Center.

Unal, C.; Tuzla, K.; Badr, O.; Neti, S.; Chen, J. (1988): Parametric Trends for Post-CHF Heat Transfer in Rod Bundles. In *Journal of Heat Transfer* 110 (3), pp. 721–727. DOI: 10.1115/1.3250551.

v. d. VDI e.V., I. (2013): VDI-Wärmeatlas. Mit 320 Tabellen. 11th ed. Berlin, Heidelberg: Springer Berlin / Heidelberg (VDI-Buch Ser).

Varone, A. F. (1990): The influence of the dispersed phase on the convective heat transfer in dispersed flow film boiling. Diss. Massachusetts Institute of Technology. Available online at http://dspace.mit.edu/handle/1721.1/13996.

Varone, A. F.; Rohsenow, W. M. (1986): Post dryout heat transfer prediction. In *Nuclear Engineering and Design* 95, pp. 315–327. DOI: 10.1016/0029-5493(86)90057-9.

VDI-Gesellschaft Verfahrenstechnik und Chemieingenieurwesen (2010): VDI heat atlas. 2nd ed. Berlin, New York: Springer (VDI-Buch).

Vojtek, I. (1978): Auswertung der 25-Stabbündel-Versuche mit dem Rechenprogramm BRUDI-VA (GRS-A-208).

Webb, S. W.; Chen, J. C. (1986): Evaluation of Convective Film Boiling Models with Nonequilibrium Data in Tubes. In: Proceeding of International Heat Transfer Conference 8. International Heat Transfer Conference 8. San Francisco, USA, 1986. Connecticut: Begellhouse, pp. 2233–2238.

Yao, S. C.; Hochreiter, L. E.; Leech, W. J. (1982): Heat-Transfer Augmentation in Rod Bundles Near Grid Spacers. In *Journal of Heat Transfer* 104 (1), pp. 76–81. DOI: 10.1115/1.3245071.

Yoder, G. L.; Rohsenow, W. M. (1980): Dispersed Flow Film Boiling. Department of Mechanical Engineering, Massachusetts Institute of Technology. Cambridge (USA) (85694-103).

Yoder, G. L.; Rohsenow, W. M. (1983): A Solution for Dispersed Flow Heat Transfer Using Equilibrium Fluid Conditions. In *Journal of Heat Transfer* 105 (1), pp. 10–17. DOI: 10.1115/1.3245528.

Yu, D. (2019): Analysis and Modelling of Full-Range Post-Dryout Heat Transfer in Vertical Tubes. Dissertation. Karlsruhe Institute of Technology, Karlsruhe (Germany).

Yu, D.; Feuerstein, F.; Koeckert, L.; Cheng, X. (2018): Analysis and modeling of post-dryout heat transfer in upward vertical flow. In *Annals of Nuclear Energy* 115, pp. 186–194. DOI: 10.1016/j.anucene.2018.01.026.

Yuen, M. C.; Chen, L. W. (1978): Heat-transfer measurements of evaporating liquid droplets. In *International Journal of Heat and Mass Transfer* 21 (5), pp. 537–542. DOI: 10.1016/0017-9310(78)90049-2.

Ziegler, A.; Allelein, H.-J. (2013): Reaktortechnik. Physikalisch-technische Grundlagen. 2., neu bearb. Aufl. Berlin, Heidelberg: Springer Vieweg. Available online at http://gbv.eblib.com/patron/FullRecord.aspx?p=1317011.

List of Own Publications

Köckert, L.; Feuerstein, F.; Yu, D.; Klingel, D.; Cheng, X. (2018): Experimental Study of Post-Dryout Heat Transfer and Rewetting in an R-134a Cooled Vertical Tube at Comparable Water-Cooled Reactor Pressure Conditions. In: The 12th International Topical Meeting on Reactor Thermal-Hydraulics, Operation, and Safety (NUTHOS-12), Qingdao (China).

Köckert, L.; Badea, A. F.; Cheng, X.; Yu, D.; Klingel, D. (2021): Studies on post-dryout heat transfer in R-134a vertical flow. In International Journal of Advanced Nuclear Reactor Design and Technology 3, pp. 44-53. DOI: 10.1016/j.jandt.2021.05.001.

Köckert, L.; Liu, W.; Cheng, X. (2024): Post-dryout heat transfer in circular tubes using R-134a: experiment and correlation assessment. In Wärme - und Stoffübertragung 60 (8), pp. 1453-1466. DOI: 10.1007/s00231-024-03498-5.

Köckert, L.; Rensch, N.; Badea, A. F.; Cheng, X. (2024): Experimental investigation of the post-dryout heat transfer and droplet behavior with R-134a. In: Specialist Workshop on Advanced Instrumentation and Measurement Techniques for Nuclear Reactor Thermal-Hydraulics and Severe Accidents 2024 (SWINTH-2024). Dresden (Germany).

Yu, D.; Feuerstein, F.; Köckert, L.; Cheng, X. (2018): Analysis and modeling of post-dryout heat transfer in upward vertical flow. In Annals of Nuclear Energy 115, pp. 186-194. DOI: 10.1016/j.anucene.2018.01.026.

IAEA (2020): Understanding and Prediction of Thermohydraulic Phenomena Relevant to Supercritical Water Cooled Reactors (SCWRs). Final Report of a Coordinated Research Project. Vienna: IAEA (IAEA TECDOC Series, v.1900).

Rensch, N.; Köckert, L.; Klingel, D.; Badea, A.; Cheng, X. (2023): Experimental Investigation of the Post-Dryout Heat Transfer with R-134a at High Pressures. In Raymond Furstenau, Bao-Wen Yang, Elia Merzari, Yassin Hassan, Hisashi Ninokata, Fan-Bill Cheung et al. (Eds.): 20th International Topical Meeting on Nuclear Reactor Thermal Hydraulics (NURETH-20). 20th International Topical Meeting on Nuclear Reactor Thermal Hydraulics (NURETH-20). Washington, D.C, 8/20/2023 - 8/25/2023. Illinois: American Nuclear Society, pp. 2296-2309.

Rensch, N.; Köckert, L.; Badea, A. F.; Cheng, X. (2025): Experimental Investigation of Post-Dryout Heat Transfer with R-134a at High Pressures. In Nuclear Science and Engineering 199 (10), pp. 1659-1678. DOI: 10.1080/00295639.2024.2403890.

List of Figures

Figure 1.1: a) Basic principle of once-through steam generator applied as heat recovery steam generator with horizontally installed evaporator tubes (according to: (Schlund et al. 2021)), b) dryout in an evaporator tube with liquid in dark and vapor in white (adapted from: (Ghiaasiaan 2007), originally published in: (Collier and Thome 1994)) 2
Figure 2.1: Types of boiling crisis; a) DNB and b) Dryout with liquid in dark and vapor in white in a uniformly heated tube (according to: ((v. d. VDI e.V. 2013) chapter 3.5)) 8
Figure 2.2: Typical boiling curve with heat transfer mechanisms (adapted from: (VDI-Gesellschaft Verfahrenstechnik und Chemieingenieurwesen 2010)) 9
Figure 2.3: Flow patterns and heat transfer regimes as well as wall and vapor temperature for a vertically installed tube and moderate heat flux (adapted from: (Ghiaasiaan 2007), originally published in: (Collier and Thome 1994)) 11
Figure 2.4: Initiation types of entrained droplets; a) Roll wave, b) Wave undercut, c) Bubble burst, d) Liquid impingement (adapted from: (Ishii and Grolmes 1975)) ... 13
Figure 2.5: Wall and vapor temperature T_W and T_v vs. vapor quality for a) thermal equilibrium and b) thermal non-equilibrium (adapted from: (VDI-Gesellschaft Verfahrenstechnik und Chemieingenieurwesen 2010)) 14
Figure 2.6: Wall temperature vs. tube length for a) low, b) medium, and c) high mass fluxes at different heat fluxes (adapted from: (Bennett et al. 1967)) 19
Figure 2.7: PDO temperature distribution measured at the wall surface in an annular flow channel for different heat fluxes at p = 50 bar, T_S-T_{in} = 10 °C, G = 500 kg/(m²s) (adapted from: (Anghel 2014)) 22
Figure 3.1: Schematic experimental set-up of the test facility KIMOF 33
Figure 3.2: Scheme of test section 1 including cross sectional view (also used by (Feuerstein 2019)) 34
Figure 3.3: Scheme of test section 2 including a cross sectional view 36
Figure 3.4: Geometry and design of the utilized spacer in test section 2 37
Figure 3.5: Fluid properties of R-134a with a) the vapor pressure curve, b) the density, c) the specific enthalpy, d) the heat conductivity, and e) the specific heat capacity 38
Figure 3.6: a) Photo (source: (Feuerstein 2019)) and b) Schematic of a Type T self-adhesive thermocouple for wall temperature measurements (adapted from: (Feuerstein 2019)) 40
Figure 3.7: Schematic of the capillary integration into the flow channel 43
Figure 3.8: Arrangement of the experimental set-up of high-speed camera and illumination sources, including the measurement plane (marked in red) 44
Figure 4.1: Characteristic PDO temperature distribution at a) small mass flux and heat fluxes, b) high mass and heat fluxes (source: (Köckert et al. 2021)) 61
Figure 4.2: Example of a reproducibility test run of steady-state tests with test section 1 for a) the power increase process, b) the corresponding power decrease process 62

Figure 4.3: Deposition material on a tissue after cleaning of the test section (source: (Feuerstein 2019)) 63
Figure 4.4: Influence of inlet subcooling on the PDO temperature distribution at a) low pressure and mass flux, b) high pressure and mass flux 64
Figure 4.5: Influence of heat flux on the PDO temperature distribution at a) high mass fluxes, b) low mass fluxes (source: (Köckert et al. 2021)) 66
Figure 4.6: Influence of mass flux on the PDO temperature distribution at a) high mass fluxes, b) low mass fluxes (source: (Köckert et al. 2021)) 67
Figure 4.7: Influence of pressure on the PDO temperature distribution at otherwise constant input parameters (source: (Köckert et al. 2021)) 68
Figure 4.8: PDO temperature distributions for power increase and power decrease mode at a) very similar PDO temperature distribution; b) slight deviation in PDO temperature distribution 70
Figure 4.9: Comparison of the PDO temperature distribution for the power increase and decrease process at a representative thermocouple (TE 50) at p = 11.2 bar, ΔT_{in} = 10 °C, G = 500 and 1500 kg/(m^2s) and varying heat fluxes 70
Figure 4.10: a) Calculated over measured HTC for the CSO and Groeneveld and Delorme model for the steady-state test series; Average deviation for the variation of b) mass flux, c) pressure 75
Figure 5.1: a) Raw flow image under PDO conditions, b) selected analysis region in left side of the flow channel, c) selected analysis region from b) after application of Opening and Erosion filter 78
Figure 5.2: The equivalent droplet diameter under system pressure variation at T_S-T_{in} = 17 °C and G = 66 kg/(m^2s), displayed as a) PDF distribution, b) Frequency distribution (source: (Köckert et al. 2024b)) 83
Figure 5.3: Frequency distribution of the equivalent droplet diameter at p = 20 bar and G = 66 kg/(m^2s) under a) inlet subcooling variation, b) heat flux variation at T_S-T_{in} = 17 °C (source: (Köckert et al. 2024b)) 84
Figure 5.4: Frequency distribution of the droplet vertical velocity under system pressure variation at T_S-T_{in} = 17 °C and G = 66 kg/(m^2s) (source: (Köckert et al. 2024b)) ... 85
Figure 5.5: Frequency distribution of the droplet vertical velocity under variation of a) inlet subcooling at p = 15 bar and G = 66 kg/(m^2s) (source: (Köckert et al. 2024b)), b) heat flux at p = 20 bar, T_S-T_{in} = 12 °C, and G = 66 kg/(m^2s) 86
Figure 5.6: a) Frequency distribution of the droplet lateral velocity under system pressure variation at T_S-T_{in} = 17 °C and G = 66 kg/(m^2s) (source: (Köckert et al. 2024b)), b) lateral droplet position in left flow channel side at the same test conditions (source: (Köckert et al. 2024b)) 90
Figure 5.7: Droplet vertical velocity vs. equivalent diameter for a) p = 11 bar, T_S-T_{in} = 17 °C, q = 47.5 kW/m^2, and G = 66 kg/(m^2s), b) p = 15 bar, T_S-T_{in} = 17 °C, q = 44.6 kW/m^2, and G = 66 kg/(m^2s), c) p = 20 bar, T_S-T_{in} = 17 °C, q = 42.9 kW/m^2, and G = 66 kg/(m^2s) (source: (Köckert et al. 2024b)), d) p = 30 bar, T_S-T_{in} = 17 °C, q = 37.1 kW/m^2, and G = 66 kg/(m^2s) 92

Figure 5.8: Droplet lateral velocity vs. equivalent diameter for p = 11 bar, T_S-T_{in} = 17 °C, q = 47.5 kW/m^2, and G = 66 kg/(m^{2}s) (source: (Köckert et al. 2024b)) 92
Figure 5.9: Probability distribution functions for the droplet diameter with a) and b) the Cumo model at different test conditions; c) and d) the Meholic model at different test conditions..... 96
Figure 5.10: Vapor temperature measurement as a function of temperature over time including saturation and wall temperature for a) constant vapor temperature distribution, b) oscillating vapor temperature distribution, c) constant vapour temperature distribution with temperature peak 101
Figure 5.11: Actual vapor quality vs equilibrium vapor quality for all vapor temperature measurement points 103
Figure 5.12: Measured vapor temperature distribution of blue: continuous temperature rise, red: with a temperature maximum..... 105
Figure 5.13: a) Calculated over measured actual vapor quality for different pressure conditions; actual over equilibrium vapor quality for measured and calculated data points at b) p = 15.0 bar, c) p = 20.0 bar, d) p = 27.1 bar..... 107
Figure 6.1: Division of a tubular flow channel into film and core region (adapted from: (Yu 2019))..... 110
Figure 6.2: Calculated over measured HTC for a) the steady-state test series in test section 1; Average deviation for the variation of b) mass flux, c) pressure..... 113
Figure 6.3: Calculated over measured HTC for a) the steady-state test series in test section 1; Average deviation for the variation of b) mass flux, c) pressure; TNE factor for the variation of d) mass flux, e) pressure..... 115
Figure 0.1: Structure and measurement principle of an optical fiber with Fiber-Bragg-Grating (adapted from: (Lomperski et al. 2015))..... 122

List of Tables

Table 3.1: List of the utilized conventional measurement devices 39
Table 3.2: Experimental parameters of the steady-state PDO test series (test section 1) 46
Table 3.3: Experimental parameters of the steady-state reproducibility tests of the PDO test series (test section 1)..... 47
Table 3.4: Experimental parameters of the first steady-state PDO test series for optical flow behavior investigations with the high-speed camera (test section 2) 48
Table 3.5: Experimental parameters of the second steady-state PDO test series for vapor temperature measurements (test section 2)..... 49
Table 3.6: Parameter and deviation range of the heat balance experiments with test section 1 55
Table 3.7: Parameter and deviation range of the heat balance experiments with test section 2 55
Table 3.8: Measurement and manufacturing uncertainties of the used sensors and geometrical parameters..... 56
Table 4.1: Assessment of the selected thermal equilibrium and non-equilibrium models with experimental data of the steady-state test series in test section 1 72
Table 5.1: Measured droplet vertical velocity in m/s obtained with the high-speed camera, corresponding calculated vapor velocities in m/s, and slip ratio based on the given values for test runs with G = 66 kg/(m^{2}s) and T_S-T_{in} = 17 °C..... 87
Table 5.2:Measured average equivalent diameter and comparison with droplet size models . 95
Table 5.3: Measured and calculated slip ratios at G = 66 kg/(m^{2}s) and T_S-T_{in} = 17 °C 98
Table 5.4: Comparison of measured droplet vertical velocity obtained with the high-speed camera and calculated droplet velocities in m/s 99
Table 5.5: Parameter range of vapor temperature measurements including measured thermal non-equilibrium 104
Table 5.6: Model assessment with experimental data of the actual vapor quality for different pressures 108
Table 6.1: Assessment results of the KIT PDO correlation with the experimental data in test section 1 112
Table 6.2: Assessment results of the KIT PDO mechanistic model with the experimental data in test section 1 114
Table 0.1: Validity range of the utilized PDO heat transfer models 135
Table 0.2: Measured average equivalent diameter and comparison with droplet size models for all selected test runs 140
Table 0.3: Measured average equivalent diameter and comparison with droplet size models for all selected test runs 141
Table 0.4: Measured average lateral velocities 141
Table 0.5: Measured average vertical velocities with the high-speed camera and comparison with force balance based calculated velocities 142

Table 0.6: Measured and calculated slip ratios at the conditions provided in above tables and displayed wall temperatures; first range value at superheated wall temperature vapor conditions, second value at thermal equilibrium conditions 142
Table 0.7: Upper bin limits and characteristic bin diameters for the Meholic droplet diameter distributions in chapter 5.1.6.1 143